January 2015

An Experimental Characterization of Tip Leakage Flows and Corresponding Effects on Multistage Compressor Performance

Reid Adam Berdanier
Purdue University

Recommended Citation

Berdanier, Reid Adam, "An Experimental Characterization of Tip Leakage Flows and Corresponding Effects on Multistage Compressor Performance" (2015). *Open Access Dissertations*. 1167.
https://docs.lib.purdue.edu/open_access_dissertations/1167

Graduate School Form 30
Updated 1/15/2015

PURDUE UNIVERSITY
GRADUATE SCHOOL
Thesis/Dissertation Acceptance

This is to certify that the thesis/dissertation prepared

By Reid Adam Berdanier

Entitled

An Experimental Characterization of Tip Leakage Flows and Corresponding Effects on Multistage Compressor Performance

For the degree of Doctor of Philosophy

Is approved by the final examining committee:

Nicole L. Key Chair	Patricia Davies
Hyoun-Woo Shin	
Guillermo Paniagua	
Aaron J. King	

To the best of my knowledge and as understood by the student in the Thesis/Dissertation Agreement, Publication Delay, and Certification Disclaimer (Graduate School Form 32), this thesis/dissertation adheres to the provisions of Purdue University's "Policy of Integrity in Research" and the use of copyright material.

Approved by Major Professor(s): Nicole L. Key

Approved by: Ganesh Subbarayan 7/15/2015

Head of the Departmental Graduate Program Date

AN EXPERIMENTAL CHARACTERIZATION OF TIP LEAKAGE FLOWS AND CORRESPONDING EFFECTS ON MULTISTAGE COMPRESSOR PERFORMANCE

A Dissertation

Submitted to the Faculty

of

Purdue University

by

Reid Adam Berdanier

In Partial Fulfillment of the

Requirements for the Degree

of

Doctor of Philosophy

August 2015

Purdue University

West Lafayette, Indiana

To my family of yesterday, today, and tomorrow.

ACKNOWLEDGMENTS

I am very thankful to all of the people who contributed to facilitate my success throughout this program. I am grateful every day for the superior mentorship that I have received from my advisor, Nicole Key. The significant intellectual and professional growth that I have enjoyed throughout the past few years is due in great part to her unbelievable leadership and selfless guidance. This research was funded primarily by NASA and Rolls-Royce, but financial support from the National Science Foundation Graduate Research Fellowship Program is also gratefully acknowledged.

I would like to thank Professor Patricia Davies and Professor Guillermo Paniagua, as well as Dr. Hyoun-Woo Shin from GE Aviation (retired) and Dr. Aaron King from Rolls-Royce for their valuable feedback and support as members of my advisory committee. Technical advice and guidance from John Fabian is also gratefully acknowledged as an essential contribution to these results. The assistance provided by the support staff at Zucrow Laboratories was crucial to this project, especially the technical skills and generous feedback provided by Rob McGuire.

All of the students with whom I have had the pleasure of working in the past five years have undoubtedly helped to shape the researcher that I have become. Special thanks are due to Dr. Natalie Smith for everything she has taught me and her teamwork when solving seemingly impossible problems. The assistance of Dr. Anna Young from

Cambridge University is also acknowledged for her assistance with the acquisition and preliminary analysis of stall data for this project.

My parents, Bruce and Melinda Berdanier, and my older brother Aaron, have always been a great resource and support network throughout my education, and I am unable to express the importance that each of them holds in my life. I love all of you dearly. Most important, I am thankful to my beautiful wife, Catherine, for all of her unseen sacrifices, support, and enduring love. I am truly blessed to have you in my life.

TABLE OF CONTENTS

Page

APPENDICES

LIST OF TABLES

LIST OF FIGURES

Figure Page

Figure Page

Appendix Figures

LIST OF SYMBOLS

Symbol	Description
A	Geometric Flow Area
B	Blockage
c	Chord
D	Diameter
E	Wire Voltage
h	Enthalpy
H	Blade Span/Annulus Height
$\dot{m}$	Mass Flow Rate
Ma	Mach Number
N	Rotational Speed
P	Pressure
r	Radial Coordinate
R	Resistance
Re	Reynolds Number
s	Blade Pitch
t	Blade Thickness, Time
T	Temperature

Symbol	Description
U_t	Blade Tip Speed
V	Absolute Velocity
W	Relative Velocity
x	Axial Coordinate

Greek

α	Absolute Flow (Yaw) Angle
β	Relative Flow (Yaw) Angle
γ	Ratio of Specific Heats
δ	Clearance Derivative for Stall Margin (Flow Range)
δ_η	Clearance Derivative for Isentropic Efficiency
δ_ψ	Clearance Derivative for Peak Pressure Rise Difference
δ_ξ	Clearance Derivative for Leakage Flow Trajectory Angle
δ^*	Velocity Density Deficit
η	Isentropic Efficiency
ω	Vorticity
Ω	Blade Angular Velocity
ϕ	Pitch Angle
Φ	Flow Coefficient
Ψ	Total-to-Static Pressure Rise Coefficient
ρ	Density

Symbol	Description
Greek	
σ	Wire Slanting Angle
τ	Tip Clearance Height
θ	Tangential Coordinate
ξ	Leakage Flow Trajectory Angle
Subscripts	
AA	Radial and Circumferential Area Average
amb	Ambient reference pressure
act	Actual Condition
c	Corrected Condition
CA	Circumferential Average
eff	Effective
leak	Leakage
LN	Normalized Leakage
m	Meridional Direction
mech	Mechanical
o	Stagnation Condition
pk	Peak Value
r	Radial Direction
RA	Radial Area Average

Symbol	Description
Subscripts	
ref	Reference Condition
s	Isentropic Condition
SM	Stall Margin (Flow Range)
st	Streamwise Direction
stall	Stall Condition
stg	Stage
x	Axial Direction
w	Wire
θ	Tangential Direction
$1 \cdots 9$	Measurement Positions
Accents	
$\langle \quad \rangle$	Ensemble Average

LIST OF ABBREVIATIONS

Abbreviation	Description
AIP	Aerodynamic Interface Plane
BPP	Blade Passing Period
CFD	Computational Fluid Dynamics
DCA	Double Circular Arc
EA	Ensemble Average
HL	High Loading
HPC	High Pressure Compressor
IBR	Integrally Bladed Rotor
IGV	Inlet Guide Vane
LDV	Laser Doppler Velocimetry
LL	Low Loading
LSRC	Low-Speed Research Compressor
NB	Number of Blades
NL	Nominal Loading
NS	Near Stall
OPR	Overall Pressure Ratio
PE	Peak Efficiency

Abbreviation	Description
PIV	Particle Image Velocimetry
RMS	Root-Mean-Square
RRf	Rotor Revolution Frequency
SFW	Subsonic Fixed Wing
SLE	Special Limits of Error
SM	Stall Margin
TC	Tip Clearance
TPR	Total Pressure Ratio
TTL	Transistor-Transistor-Logic
TTR	Total Temperature Ratio

ABSTRACT

Berdanier, Reid Adam. Ph.D., Purdue University, August 2015. An Experimental Characterization of Tip Leakage Flows and Corresponding Effects on Multistage Compressor Performance. Major Professor: Dr. Nicole L. Key, School of Mechanical Engineering.

The effect of rotor tip clearances in turbomachinery applications has been a primary research interest for nearly 80 years. Over that time, studies have shown increased tip clearance in axial flow compressors typically has a detrimental effect on overall pressure rise capability, isentropic efficiency, and stall margin. With modern engine designs trending toward decreased core sizes to increase propulsive efficiency (by increasing bypass ratio) or additional compression stages to increase thermal efficiency by increasing the overall pressure ratio, blade heights in the rear stages of the high pressure compressor are expected to decrease. These rear stages typically feature smaller blade aspect ratios, for which endwall flows are more important, and the rotor tip clearance height represents a larger fraction of blade span. As a result, data sets collected with large relative rotor tip clearance heights are necessary to facilitate these future small core design goals.

This research seeks to characterize rotor tip leakage flows for three tip clearance heights in the Purdue three-stage axial compressor facility (1.5%, 3.0%, and 4.0% as a percentage of overall annulus height). The multistage environment of this compressor provides the unique opportunity to examine tip leakage flow effects due to stage matching, stator-rotor interactions, and rotor-rotor interactions. The important tip leakage flow effects which develop as a result of these interactions are absent for previous studies which have been conducted using single-stage machines or isolated rotors.

A series of compressor performance maps comprise points at four corrected speeds for each of the three rotor tip clearance heights. Steady total pressure and total temperature measurements highlight the effects of tip leakage flows on radial profiles and wake shapes throughout the compressor. These data also evaluate tip clearance effects on efficiency, stall margin, and peak pressure rise capability. An emphasis of measurements collected at these part-speed and off-design conditions provides a unique data set for calibrating computational models and predictive algorithms. Further investigations with detailed steady total pressure traverses provide additional insight to tip leakage flow effects on stator performance.

A series of data on the 100% corrected speedline further characterize the tip leakage flow using time-resolved measurements from a combination of instrumentation techniques. An array of high-frequency-response piezoresistive pressure transducers installed over the rotors allows quantification of tip leakage flow trajectories. These data, along with measurements from a fast-response total pressure probe downstream of the rotors, evaluate the development of tip leakage flows and assess the corresponding effects of upstream stator wakes. Finally, thermal anemometry measurements collected using the single slanted hot-wire technique evaluate three-dimensional velocity components throughout the compressor. These data facilitate calculations of several flow metrics, including a blockage parameter and phase-locked streamwise vorticity.

CHAPTER 1: INTRODUCTION

1.1. Motivation

Rising fuel costs and environmental concerns are continuing to drive gas turbine engine development toward increased overall efficiency and decreased fuel burn. However, achieving these goals will likely lead to smaller gas turbine engine cores for two reasons. First, improvements in materials and cooling schemes allow increased turbine inlet temperatures and, thus, increased overall pressure ratios (OPR) that will allow for higher thermal efficiencies. For a given engine size, an increased OPR is most easily accommodated through added compression stages. Second, larger bypass ratios lead to increased propulsive efficiencies in turbofan engines. For large aircraft, current under-wing engine mounting arrangements are limited in their ability to accommodate larger fan diameters. For small aircraft, the nacelle is already a significant contributor to overall aircraft drag and an increased fan diameter could have an overall negative effect. As these limits for the outer diameter of a turbofan are encountered, designers are turning their attention to reducing the size of the core as a means for increasing the bypass ratio. Both of these driving factors result in smaller blading, especially in the rear stages of a high-pressure compressor (HPC).

As engine cores become smaller, the flow path area decreases, and the losses in the endwall regions become more significant as they constitute a larger percentage of the total flow field. Additionally, tip clearances will not scale with the decreased blade size because of manufacturing tolerances and the margin needed for transient operation and thermal growth. As a result, a smaller core leads to rotor tip clearance heights which are large relative to the blade size. A larger relative tip clearance height leads to increased blockage due to the associated tip leakage flows, as well as potential issues with stage matching at off-design operating conditions. Previous research has suggested an increase of tip clearance-to-span ratio causes decreased efficiency and pressure rise capability. Similarly, the ratio of clearance-to-chord may also increase, leading to a decrease in stall margin. Thus, small blade heights with increased relative clearances are expected to have a detrimental impact on HPC efficiency and operability.

However, these concerns with large tip clearance heights relative to blade size are not specific to new engine designs. Existing engine designs are also subject to these potential performance detriments as in-service deterioration results in larger clearances in compressors. The development of design technologies that are desensitized to large tip clearances would provide the ability to avoid the penalties of reduced stall margin and reduced efficiency typically associated with in-service deterioration. Ultimately, the flow physics of these tip leakage flows must be better understood in a multistage environment to generate these new technologies – an understanding which must extend beyond the design point to also improve off-design compressor performance.

1.2. Tip Leakage Flows

The presence of a rotor tip clearance creates an opportunity for interaction between the high-pressure “pressure” side and low-pressure “suction” side of the airfoil at the blade tip. This pressure difference leads to a pressure-driven flow through the clearance gap at the rotor tip. The pressure-driven fluid interacts with the bulk flow in the adjacent passage, which can lead to the formation of a shear layer and the roll up of a vortex sheet (Storer and Cumpsty, 1994; Chen, 1991). Although, recent research suggests that the structure which has often been identified by the tip leakage vortex may be instantaneously represented by vortex fragments instead of a coherent vortex structure (Tan et al., 2014). Once ensemble-averaged, these fragments may combine to form the region of high vorticity which is often identified as the tip leakage vortex. Nonetheless, the development of this tip leakage "vortex" identified by previous authors is analogous to the blade tip vortex which develops at the end of aircraft wings; however, the relative motion of the rotor blade with respect to the adjacent wall in a compressor creates a shear-driven component of the flow in addition to the pressure-driven component (Rains, 1954; Gbadebo et al., 2006).

Studies of tip clearances on the order of 3% or less are primarily present in literature since these values represent the variation of a typical design clearance under rapid throttle changes in an aircraft engine (Freeman, 1985). Experimental data corresponding to large tip clearance heights (e.g., larger than 3% relative to blade span) are less prevalent in the literature, but are particularly important for advancing product development toward smaller core sizes. Of note, Williams et al. (2010) used a cascade to investigate very large tip clearances up to 6% of annulus height, which is representative for the HPC stages of industrial gas turbines. As expected, losses increased with increasing tip clearance, however, losses leveled off for clearances larger than 4% annulus height. The authors hypothesized that for large tip clearances, the effect of the endwall became less important, and the flow through the tip gap behaved more like that of a wing tip vortex since the casing had less impact on the leakage flow.

Although the understanding of tip leakage flow effects in the context of a full-scale gas turbine is important, several fundamental studies have led to a number of valuable conclusions about the basic flow features of tip leakage flows. Of note, the point of inception for the tip leakage flow has been observed by several authors to move along the chord from the leading edge to approximately mid-span (Herzig and Hansen, 1955; Hunter and Cumpsty, 1982; Crook et al., 1993); however, the determining factor for this point of inception appears to be the location of maximum loading for the blade tip, which is often heavily dependent on the blade design family.

Further research has assessed the effects of the tip leakage flow trajectory. In some cases, the tip leakage flow may convect across the blade passage at a high trajectory angle and pass through the tip clearance of the adjacent blade (Khalsa, 1996). In this case, the low pressure fluid contained in the tip leakage flow faces potentially compounding loss as it passes through the second clearance gap. Understandably, the presence or absence of this effect is heavily-dependent on the loading of the blade row through its effect on the trajectory of the leakage flow and the solidity of the blade row (Dickens and Day, 2011).

1.3. Influence of Tip Clearance on Overall Compressor Performance

Past studies have analyzed the effect of tip clearance heights on the order of 1 to 3% relative to blade span. Many of the early tip clearance studies were aimed at studying cavitation for axial-flow pumps (Rains, 1954; Williams, 1960), but there are also some early discussions of tip clearance effects on compressors for gas turbine engines (e.g., Jefferson and Turner, 1958). A review of these early studies is given by Reeder (1968) and Peacock (1982, 1983).

Wisler (1985a) and Freeman (1985) give a thorough overview of the tip clearance effects for multistage gas turbine compressors. Using experimental data from a four-stage low-speed research compressor, Wisler suggests the compressor will face a peak efficiency penalty on the order of 1.5 points for a 1.4% increase of tip clearance height (Wisler, 1985a; 1985b), and similar predictions can be made relating to the penalties for stall margin and peak pressure rise. However, Freeman (1985) emphasizes the inability to completely predict the specific impact on a multistage machine since it depends strongly on the detailed design of the compressor and the stage matching parameters.

To date, much of the compressor performance research analyzing tip clearance effects has focused on single-stage machines or isolated rotors (e.g., Ruden, 1944; Hutton, 1956; Moore and Osborne, 1977; Inoue at al., 1986; McDougall, 1990; Goto, 1992). A review of the specifics for some of these earlier facilities is provided by Moyle (1991). The utility of results from such experimental arrangements comes from the ability to isolate the results from one particular flow effect without the contributions from other sources. A prime example of this would be the effect of rotor tip leakage flows due to an upstream stator row. However, experimental measurements in an embedded stage with propagating upstream effects yield results which are more applicable to a true engine component.

Many of the multistage compressor research studies (e.g., Wisler, 1985b; Jefferson and Turner, 1958; Lindsey, 1949; Koch, 1981; Freeman, 1985) do not include compressibility effects related to high-speed machines, incorporated limited instrumentation for inter-stage observations, or lack the stage-to-stage interactions which exist with non-repeating stages. With few exceptions (e.g., Tschirner et al., 2006), more recent results collected in multistage compressors have typically focused primarily on the unsteady flow phenomena of the tip leakage flow rather than its effect on overall compressor performance (e.g., Niehuis et al., 2003; Ernst et al., 2011).

A primary focus for earlier studies centered on analyzing effects of efficiency, pressure rise, and stall margin due to increased rotor tip clearance. Although some authors have suggested the existence of an optimal clearance height which could lead to peak efficiency (Hutton, 1956; Spencer, 1956; Wennerstrom, 1984), the very small tip clearance required to achieve an optimum is typically impractical for real machines. Thus, many studies analyzing larger clearance heights have shown a decrease of efficiency with increased clearance height (Ruden, 1944; Williams, 1960; Wisler, 1985b). Based on the existing literature, there is general agreement toward the observation that an increase of rotor tip clearance leads to a decrease of overall total pressure rise capability and work coefficient, as well as operability range (stall margin). The extent of these observed effects, though, may be dependent upon the aerodynamic loading and the design of the blade itself.

1.4. Rotor Tip Clearance Flow Measurements

1.4.1. Time-Resolved Over-Rotor Static Pressures

The application of piezoresistive pressure transducers in compressor research provides the ability to track the fluctuating characteristics of the tip leakage flow and other flow features associated with the rotor passing. As technological advances continue to drive the reduction in size and cost of these sensors, the quality of data measured from this technique is also continuously advancing. Several authors (e.g., Inoue, 1989; Moyle, 1996; Yoon, 2006; Weichert, 2011) have used these piezoresistive sensors in surface-mounted arrays over the rotor to track the motion of the tip leakage flow in the axial-circumferential plane using measured wall static pressures. In particular, the unsteadiness of the measurements represented by the root-mean squared (RMS) with respect to the phase-locked ensemble average pressure can be a useful technique to determine the leakage flow trajectory.

From these studies, some conclusions have been drawn regarding the trajectory of the tip clearance as it relates to tip clearance height and/or proximity to the stall point (Inoue, 1989; Chen, 1991; Yoon, 2006). However, these conclusions are not in agreement from all authors, therefore suggesting that fundamental differences related to the detailed design and operation of each specific compressor are likely in effect. Of note, Yoon (2006) observes and discusses a change in direction of the tip leakage flow trajectory near mid-chord when the tip leakage flow turns sharply in the circumferential direction. Chen (1991) theoretically predicts this non-linear trajectory only after the leakage flow has exited the rear of the blade passage, where the image vortices required to satisfy kinematic constraints change with the absence of the blade as an effective wall.

1.4.2. Time-Resolved Total Pressures

In addition to the application of piezoresistive pressure measurement devices for measuring surface static pressures described above, such devices are also often implemented in probes that facilitate measurements in radial-circumferential planes between adjacent blade rows. These probes have passed through significant refinement and advancement over the past decade. A thorough review of the design and application of these probes is provided by Kupferschmied et al. (2000), and additional information is given by Ainsworth et al. (2000) and Sieverding et al. (2000). Continued development and application of these probes for use in unforgiving turbomachinery environments has been led primarily by Brouckaert and colleagues (Brouckaert, 2002; Mersinligil et al., 2011; Sans et al., 2013).

The piezoresistive pressure probe method has been applied by several authors over the years (e.g., Dunker and Hungenberg, 1980; Prato et al., 2001; Neihuis et al., 2003; Ernst et al., 2011; Sans et al., 2013). Of these authors, only a few have focused specifically on investigating the tip leakage flow in a plane downstream of a rotor (Ernst et al., 2011; Sans et al., 2013). As with the surface static pressure measurements, the unsteadiness of the measured pressure represented by the RMS with respect to the ensemble average can be a useful method for highlighting the unsteady flow features present in the tip leakage flow and the rotor wake. Despite the wide application of this experimental method, however, there is a lack of literature corresponding to the application of this technique for analyzing several different tip clearance heights on the same machine.

1.4.3. Time-Resolved Velocity and Flow Angles

In addition to the high-frequency-response pressure measurements, the time-resolved velocity components are particularly valuable for determining the location, extent, and development of the tip leakage flow. Furthermore, flow velocities are a key tool for evaluating flow blockage, flow angles are often used as a calibration mechanism by comparing experimental data with computational results, and the time-resolved information that can be acquired from high-frequency-response sensors can lead to important conclusions about forcing functions related to aeromechanics.

Using thermal anemometry, the flow velocity can be measured, and several components of velocity can be determined by measuring several sensors simultaneously. Lakshminarayana et al. (1982a, 1982b, 1984) measured multiple velocity components and turbulence properties in the tip region downstream of a compressor rotor in a single stage orientation, but all tests were performed with one tip clearance. Inoue et al. (1986, 1989) utilized an isolated rotor to analyze tip leakage flow effects with three velocity components for five different clearance heights and employed relative kinetic energy defect to identify the tip leakage flow region. Inoue et al. (1986) also provide a definition of streamwise vorticity, represented by a projection of the vorticity components onto the relative flow direction exiting the rotor passage.

In addition to multi-component velocity measurements downstream of the isolated rotor, Inoue et al. (1989) also obtained hot-wire measurements in the rotor tip clearance gap. A similar procedure was developed by Weichert (2011) through the use of a miniature hot-wire to measure flow at three radial planes in the clearance gap.

Goto (1992) used a single slanted hot-wire to measure three velocity components for a low-speed single-stage compressor with three tip clearance heights less than or equal to 3% chord. Saathoff et al. (2003) used two single-wire sensors simulating an X-type probe to measure two velocity components. However, all of these studies lack multistage flow effects desirable for application to full-scale gas turbine engines.

Evaluating compressor flow features in a multistage environment is particularly important due to the communication between stages which is not appropriately captured in isolated rotor or single stage studies. Previous authors have highlighted rotor-rotor, stator-rotor, and stator-stator interactions in other studies, and their influence must also be considered for the development of rotor tip leakage flows.

1.5. Influence of Stator Wakes on Rotor Tip Leakage Flows

Measurements collected in a two-stage high-speed compressor by Ernst et al. (2011) have provided valuable insight into the stator-rotor interactions and rotor-rotor interactions associated with the tip leakage flow. However, the study was only carried out for one tip clearance. Moyle et al. (1996) used casing static pressure measurements with two tip clearances in a two-stage compressor, but the clearances evaluated were both less than one percent span. Nonetheless, the observations documented by Moyle et al. showed an important dependence of the measured wall static pressure traces on the relative position of the adjacent stator vanes

In support of research investigating tip leakage flows, other authors have also identified an interaction between the rotor tip leakage flow and wakes from upstream stator vanes (Mailach et al., 2008; Lange et al., 2012; Krug et al., 2015; Smith et al., 2015b). As the rotor passes through the velocity deficit region associated with the stator wake, the loading on the rotor momentarily increases. Because the size and location of inception of the tip leakage flow is dependent on the blade loading, the periodic changes of loading on the rotor blade due to passing through the stator wake region introduce corresponding periodic fluctuations of the tip leakage flow.

1.6. Blockage Effects

In compressors, blockage represents the reduction of flow area due to the existence of low momentum fluid. Suder (1998) outlines the definition of blockage as the relationship between the geometric flow area and the effective flow area. The effective flow area can be evaluated using a displacement thickness analogy from fundamental boundary layer theory.

Blockage will increase the velocity in the core flow region, thereby reducing the work done by the rotor on the core flow. As endwall boundary layers grow at off-design operating conditions, stage matching problems may be introduced. However, a lack of understanding for this endwall boundary layer growth in multistage axial compressors also exists at design conditions and typically forces designers to rely on correlations, as explained by Cumpsty (2004).

The effects of endwall boundary layers in an axial compressor were investigated at length by Smith (1970) in the four-stage low-speed research compressor (LSRC) at GE Aviation. These data showed that blockage was essentially unchanged across a repeating stage, and blockage was a function of tip clearance and loading condition. However, the repeating-stage model implemented by Smith is valid for multistage compressors with large aspect ratios and relatively small clearances. Furthermore, the repeating stage condition was not achieved for an aspect ratio of 1.96, the lowest aspect ratio tested by Smith. The rear stages of high pressure core compressors typically have aspect ratios on the order of unity or less. Thus, further information must be collected under these conditions to supplement the data published by Smith.

Data collected by Cumpsty (1986) in a four-stage compressor at lower Reynolds numbers showed rotor tip clearance was a critical parameter for determining the endwall boundary layer thickness. Khalid et al. (1994, 1999) developed a model to relate tip clearance flow to associated downstream blockage in an axial compressor. These authors proposed that the total pressure loss in the endwall region resulted from the interaction of tip leakage flows and passage flows, and the endwall blockage was correlated with aerodynamic loading on the blade.

Suder (1998) outlines a method for calculating blockage using axial velocity measurements. Data analyzed by Suder for an isolated transonic rotor showed that the blockage in the endwall region increased with blade loading in agreement with the correlation presented by Khalid (1994). The Rotor 37 facility utilized by Suder was specifically selected for isolation to avoid interactions from upstream or downstream stators. However, these idealized conditions are not representative of the multistage environments present in a true gas turbine compressor.

1.7. Computational Validation Using Experimental Data

The development of computational design tools has led to existing products which are fairly accurate at predicting multistage compressor performance for well-behaved flows (e.g., at the design point). However, the challenges associated with adequately modeling tip leakage flows in turbomachinery are substantial, as discussed by Denton (2010). Furthermore, at off-design operating conditions such as part-speed or high loading, these existing design tools are less capable of accurately modeling flow blockages due to endwall boundary layers, separated flow regions, and other secondary flows. As a result, there is a desire to improve these multistage computational tools for predicting off-design conditions which are critical to compressor operability and, ultimately, advance the state-of-the-art through compressor designs desensitized to tip clearance effects.

Suder and Celestina (1996) compared computational simulation results to experimental data obtained using laser Doppler velocimetry (LDV) in a single stage transonic compressor. A comparison of measurements at two loading conditions and two speeds (one transonic and one subsonic) were presented for a tip clearance height of 0.5% span (0.7% chord). At subsonic conditions, Suder and Celestina showed the radial influence of the leakage flow represented approximately five times the physical clearance (approximately a factor of four less than the extent due to the presence of shocks at transonic conditions).

The experimental data from Suder and Celestina (1996) prompted Van Zante et al. (1999) to investigate computational models of the tip leakage flow field focusing on the impact of grid topology, the numerical treatment of the tip gap, and their effects on the solution. The authors found that gridding the tip gap did not provide any advantages over using a simple tip clearance model, but the wall-bounded shear layer was an important component to the tip leakage flow, especially when the difference between the relative velocities of the leakage jet and casing was large.

The observations by Van Zante et al. (1999) and further conclusions by Gupta et al. (2003) provide a valuable example of how a quality experimental dataset can be used to calibrate CFD models. However, the isolated rotor and single stage environment does not capture all of the important flow physics present in a multistage compressor. In particular, spanwise mixing and endwall boundary layer development are influenced by upstream stages. These, in addition to the tip leakage flow, are major contributors to blockage in the endwall region and can lead to stage matching issues (Cumpsty, 2004).

1.8. Research Objectives and Methodology

Whereas the effect of rotor tip clearance in axial compressors has been documented for several decades, a deficiency exists in the open literature for data collected in a multistage environment with the presence of appreciable compressibility effects. As a result, the primary focus of this work was to characterize the fundamental flow physics and the overall performance effects due to increased rotor tip clearance heights in a multistage axial compressor.

Many previous studies of tip clearance sensitivity have implemented two tip clearances. For this study, three rotor tip clearances were investigated to assess trends of measured parameters with tip clearance which may be non-linear as the tip clearance is increased. These clearance sizes (1.5%, 3.0%, and 4.0% as a fraction of overall annulus height) were selected to represent the design intent and two larger clearances which may be defined as “large” clearances in the context of future HPC designs.

In this study, overall compressor performance is investigated at four corrected speeds for each of the three tip clearance configurations using steady pressure and temperature measurements distributed throughout the compressor. Trends for performance metrics, including efficiency and stall margin, are evaluated for varying levels of tip clearance. The operating rotor tip clearance heights are measured to allow the best comparison of measured results. The stall inception mechanisms are also investigated for each of the tip clearance configurations.

Detailed radial traverses of total pressure at the exit of each stator row provide an improved understanding of the tip leakage flow effects in a multistage environment. Detailed radial traverses of time-resolved total pressures at the exit of each rotor row are measured with a fast-response pressure probe. These data help to quantify the size of the leakage flow at different tip clearance heights and loading conditions for each rotor. Thermal anemometry is also implemented to evaluate the time-resolved three-dimensional components of velocity throughout the compressor. These measurements facilitate quantifying the effect of the tip leakage flow by calculating a blockage parameter and the streamwise vorticity.

Time-resolved static pressure measurements are collected over the rotor tips for all rotors with each of the three tip clearance configurations for up to five loading conditions along the 100% corrected speedline using fast-response piezoresistive pressure sensors. These time-resolved static pressure measurements, as well as the time-resolved total pressures and velocities reveal a profound influence of the upstream stator vane on the size and shape of the rotor tip leakage flow.

Current RANS-based computational tools commonly used in design iterations typically struggle with accurate prediction of stage matching, particularly for off-design conditions at which regions of separated flow may be significant. To accommodate new design goals and reduce such existing computational tool limitations, a specific emphasis is focused toward acquisition of several off-design conditions. Ultimately, the data collected for this project represent a unique data set which contributes to build a better understanding of the tip leakage flow field and its associated loss mechanisms. These data will facilitate future engine design goals leading to smaller blade heights in the rear stages of high pressure compressors and aid in the development of new blade designs which are desensitized to the performance penalties attributed to rotor tip leakage flows.

CHAPTER 2: EXPERIMENTAL METHODS

2.1. Research Facility

2.1.1. Integral Facility Components

The Purdue University three-stage axial compressor research facility is a geometrically-scaled design which models the rear stages of a high-pressure core compressor. The facility features engine-representative Reynolds numbers and Mach numbers, which makes it a useful vehicle for research at a high technology readiness level. Furthermore, the intermediate rotational speed regime and the multistage design of the facility create unique opportunities to analyze an “embedded” stage and complex multistage flow effects.

The Purdue three-stage compressor facility features a 6061 aluminum casing and all blading is machined from 17-4 stainless steel. The compressor comprises an inlet guide vane (IGV) followed by three stages. The inlet guide vane and the three rotor rows are double-circular arc (DCA) designs, and the three stator vane rows are NACA 65-series airfoils. All three of the rotor rows are integrated bladed rotor (IBR) “blisk” designs, such that each of the three rotor rows represents one solid piece of material. Further, each of the stationary vane rows has been created as a 180-degree monolithic segment, with vanes which are fully-shrouded at the inner and outer diameters. Specific geometric parameters for the blading in the facility are outlined in Table 2.1.

Each of the stationary vane rows are individually circumferentially indexable for up to two full stator vane passages, allowing circumferential flow variations to be measured with stationary instrumentation. Each of the vane rows is moved with a pair of linear actuators during compressor operation, and precision string potentiometers provide feedback control of the vane positions. This two-vane circumferential measurement capability was an expansion beyond previous capabilities which was made possible through the new compressor casing hardware required for this project.

Table 2.1: Purdue three-stage compressor airfoil design parameters.

Blade Row	Camber [º]		Stagger [º]		Chord [in.]		t/c	Airfoils		Ma (avg)		Re_c 10^5
	Hub	Tip	Hub	Tip	Hub	Tip		N	Type	Rel	Abs	
IGV	-12.3	-14.0	8.2	9.0	2.00	2.00	0.065	44	DCA	0.26	0.26	3.0
R	44.7	25.8	32.6	47.8	2.46	2.81	0.045	36	DCA	0.46	0.32	7.0
S1	49.5	48.3	25.6	24.0	2.11	2.11	0.065	44	65	0.35	0.35	4.4
R2	42.4	24.6	35.4	49.8	2.60	2.96	0.049	33	DCA	0.45	0.31	7.7
S2	49.7	48.4	26.1	24.6	2.22	2.22	0.065	44	65	0.33	0.33	4.6
R3	39.5	22.9	38.2	51.8	2.75	3.13	0.051	30	DCA	0.44	0.31	8.4
S3	62.4	61.2	19.7	18.1	2.35	2.35	0.065	50	65	0.31	0.31	4.8

The research compressor is driven from the rear by a 1400 hp AC motor through a 5:1 speed-increasing gearbox to provide a nominal rotational speed of 5000 rpm at the design point. A liquid-cooled variable frequency drive system paired with an encoder on the motor drive shaft provides the capability to maintain a compressor operating speed within 0.01% of the desired mechanical speed. This capability creates an especially unique opportunity to ensure confidence in the repeatability of measurements as they relate to the rotational speed of the machine. In addition to the motor encoder, an optical laser tachometer aimed at the high-speed output shaft of the gearbox creates a transistor-transistor logic (TTL) signal which is used as a once-per-revolution (1/rev) trigger for the high-frequency-response data acquisition systems.

The compressor operates with ambient, unconditioned air as the working fluid. As shown in Figure 2.1, the air is first drawn into a large settling chamber before passing through a reducing bellmouth into a two foot diameter duct. A long-form Venturi flow meter designed in accordance with ASME PTC-19.5 (2004) flow measurement standards accurately measures the mass flow rate passing through the compressor.

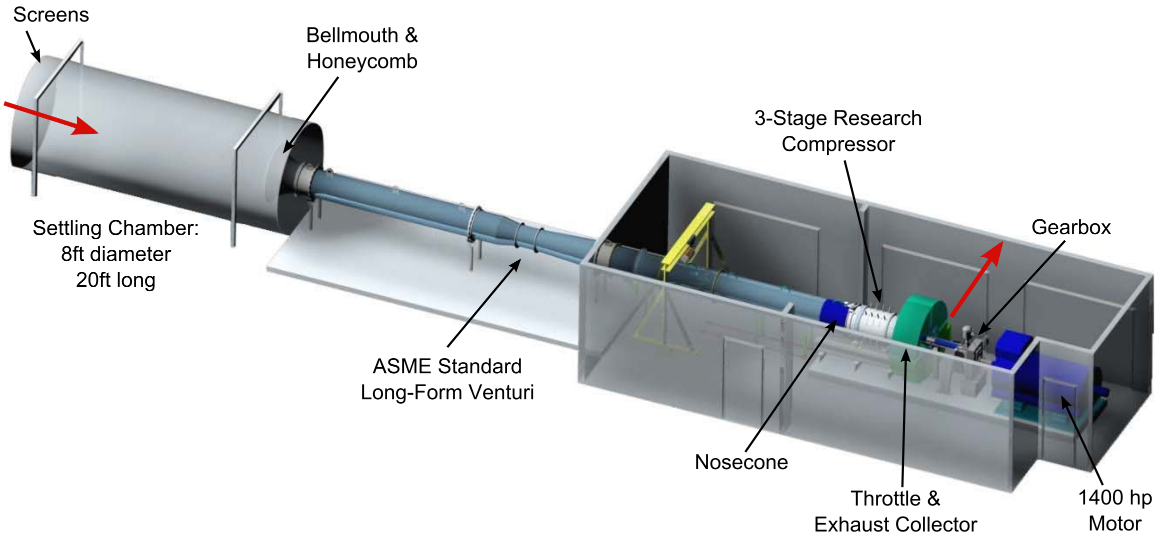

Figure 2.1: Purdue three-stage axial compressor research facility.

Two Rosemount 3051C high-accuracy pressure transmitters are installed for measuring the differential pressure across the Venturi. Because the relative uncertainty of the differential pressure measurement is dependent upon the calibration range, the two

3051C transmitters were calibrated in different pressure ranges (0 to 5 inH_2O and 0 to 8 inH_2O) and are connected via a manifold. These ranges were selected to ensure adequate coverage of the entire range of operating conditions (0 to 8 inH_2O), while maintaining a measurement near the peak efficiency point which utilizes the smallest possible measurement uncertainty. Moreover, in the low flow rate measurement range, the pair of devices provides a redundant measurement for added confidence. As a complement to the differential pressure measurements, a pitot-static pressure probe with an integrated T-type thermocouple is installed just upstream of the Venturi meter, and the measurements from this probe are used to define the density and other thermodynamic properties required for the mass flow rate calculation equations.

After passing through the Venturi meter, the air continues through an insulated duct section that is 11 duct diameters in length. A bullet-nose cone upstream of the compressor directs the airflow to the constant annulus flowpath, which is defined by a two-inch passage height with a hub-to-tip ratio of 5:6. At the exit of the compressor, a sliding-annulus throttle controls the back pressure of the machine, and a scroll collector directs the air to an exhaust plane at ambient pressure. Additional specifics defining the existing facility layout can be found in Ball (2013), and a thorough discussion of facility health monitoring systems is provided by Talalayev (2011).

2.1.2. Additional Geometry Considerations

In addition to the typical geometry parameters prescribed for the Purdue three-stage compressor flowpath, other pertinent information may be required to accurately build a computational model of the machine. Of note, the labyrinth (knife) seal clearances under the stator platforms have been measured as “cold” (static) values: 0.022 in. for the IGV, 0.035 in. for Stator 1, 0.037 in. for Stator 2, and 0.024 in. for Stator 3. Operating “hot” clearances for these seals have not been measured. Further, all of the stator vanes have fillet radii at both inner and outer diameter endwalls of 3/32 in., and the rotor hub fillet radii are all 0.150 in. The leading edges of the rotor blades have elliptical shape, and the stators have circular leading edges. An average surface roughness of 30-40 μin. has been prescribed for all of the internal flowpath surfaces, including the blades. A past analysis using an optical scan compared the design intent geometry of the rotor blisks with the as-manufactured geometry and confirmed that all measured dimensions are within the specified design tolerances of the parts. The rotor tip clearances for each defined operating condition have been measured, and the data are presented in this document.

2.1.3. Variable Tip Clearance Hardware

A series of compressor casing hardware components were required to support the tip clearance analyses desired for this project. Three tip clearance configurations were used for this study, as outlined by the information in Table 2.2. In each configuration, one discrete tip clearance height exists for all three rotor rows (i.e., no combinations of tip clearance heights were considered). The first tip clearance configuration (TC1) represents the baseline compressor configuration that has been presented by previous investigators with this facility. This baseline configuration represents a nominal 1.5% tip clearance height as a fraction of overall annulus height.

Table 2.2: Tip clearance configurations and design intent clearance heights.

Configuration	Nominal Clearance Height, τ [in]	Normalized Clearance Height, τ/H (τ/c_{R2}) [%]	Tip Clearance Representation
TC1	0.030	1.5 (1.0)	Smooth Wall
TC2	0.060	3.0 (2.0)	Casing Recess
TC3	0.080	4.0 (2.7)	Casing Recess

As outlined in Table 2.2, the two larger tip clearance configurations (TC2 and TC3) were achieved through the use of a casing recess over the rotors. These compressor configurations nominally represent 3.0% and 4.0% tip clearance height. Although the differences between casing recesses and traditional cropped rotors have been documented in the past (Wisler and Beacher, 1989), this geometry is not representative of a typical trench since the recess extends as far upstream and downstream of the rotor as possible to minimize disturbance to the tip leakage flow. Also, Brossman (2012) showed through computational simulation of the Purdue three-stage axial compressor that the overall performance and the individual stage performances of a compressor with these types of casing recesses – which are introduced as far as possible upstream and downstream of the rotor – sufficiently represent the trends of the same machine with a smooth wall and a cropped rotor. This, combined with the constraints associated with a cropped rotor study, led to the choice of using recessed casings to achieve the two larger clearance configurations.

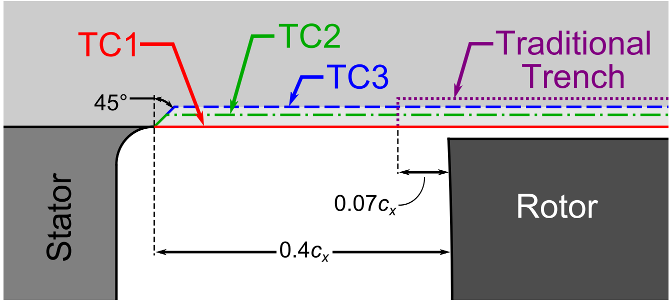

Figure 2.2: Compressor tip clearance casing geometry configurations.

Wisler and Beacher (1989) analyzed traditional trenches, similar to what may occur during a tip rub, and they extended 6% pitch upstream and downstream of the rotors (analogous to 7% Rotor 1 axial chord for this machine). Instead, the casing recesses for this study were designed to extend 40% axial chord upstream and downstream of the rotor blade so that the leakage flow would not be affected by the edges of the recess. Furthermore, 45 degree chamfers were introduced to ease the transition from the 2-inch annulus height of the baseline compressor defined by the stator vanes and the increased space over the rotors. The introduction of these angle features facilitates grid topology continuity for computational comparison studies. A schematic of the geometries for the three compressor tip clearance configurations is shown in Figure 2.2, including a comparison with a traditional trench. In addition to the cartoon of the casing configurations in Figure 2.2, a photographic example of the casing recess for TC2 is shown in Figure 2.3. It is important to note here that a manufacturing error led to the removal of the 45 degree ramp from the recess at the upstream side for Rotor 2, as shown in Figure 2.4, for both TC2 and TC3.

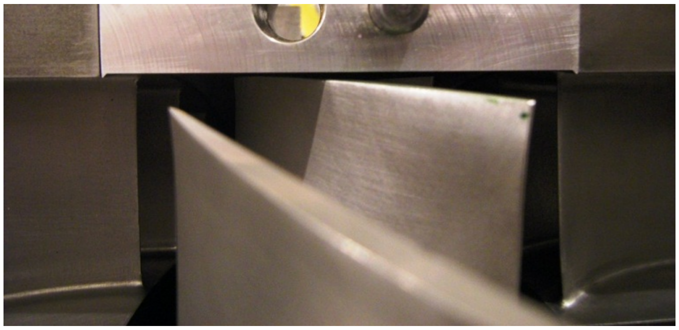

Figure 2.3: Casing recess example photograph (TC2) highlighting 45 degree angles at both ends of recess. Flow is from left to right.

Figure 2.4: Missing 45 degree ramp upstream of Rotor 2, shown here for TC2. Flow is from left to right.

To ensure that the three separate compressor casings would provide the best possible vehicle for tip clearance performance comparisons, the casing designs incorporated tight manufacturing tolerances. In addition to preventing the introduction of tip clearance non-uniformities for a given casing configuration, these tolerances also helped to ensure consistency between the three casings. The most important of these tolerances pertained to the inner diameter of the casing over the rotor tips, for which the diameter dimension was specified with a tolerance of +0.001/0.000 in., as well as geometric tolerances of 0.005 in. for the overall runout and 0.002 in. for the profile shape.

These tolerances, as well as all of the other pertinent dimensions, were verified by coordinate measuring machine (CMM) inspection processes.

2.2. Steady Compressor Performance

2.2.1. Corrected Operating Conditions for Humidity Effects

The definition of a compressor operating point is typically “corrected” to standard day conditions to ensure consistent measurements with changing inlet conditions and comparability with computational simulations. To this end, many facilities operate according to classical corrected speed and corrected mass flow rate definitions defined by turbomachinery textbooks. However, careful examination of these equations shows that they do not appropriate account for the presence of humidity in the air.

Existing compressor test codes and full engine analyses discuss the importance of humidity, and some suggest the use of conditioned or refrigerated air to avoid the potentially negative humidity effects (NACA TN-1138, 1950; Erwin, 1964). Because the Purdue three-stage compressor facility does not have the luxury of a conditioned air supply, a method of appropriately accounting for the presence of humidity is required.

Analysis of the derivation process leading to the classical equations defining corrected speed and corrected mass flow rate for a compressor highlights the assumptions of a thermally- and calorically-perfect gas which are not appropriate for a humid air mixture. Ultimately, an alternate presentation of these same equations has been derived to circumvent the need for perfect gas assumptions. These alternate equations utilize stagnation speed of sound and stagnation density in place of stagnation temperature and stagnation pressure in the classical equations. By this process, the corrected rotational speed is determined by

$$N_c = \frac{N_{\mathrm{mech}}}{a_{o,\mathrm{act}}/a_{o,\mathrm{ref}}} , \tag{2.1}$$

and the corrected mass flow rate is determined by

$$\dot{m}_c = \dot{m}_{\mathrm{act}} \left(\frac{\rho_{a,\mathrm{ref}}\, a_{o,\mathrm{ref}}}{\rho_{a,\mathrm{act}}\, a_{o,\mathrm{act}}} \right) . \tag{2.2}$$

A formal derivation of these definitions for humid air considerations is available in Berdanier et al. (2015). The results of this study showed that air conditions which are realizable in the hot and humid midwest United States summers can lead to a miscalculation of required mechanical speed on the order of 0.5% and actual mass flow rate on the order of 1.0%. Even for the intermediate-speed class of compressors encompassing the Purdue three-stage compressor, these effects are well within the measurement capabilities of existing instrumentation. Specifically, a comparison of the results using the classical equations for corrected conditions and the alternate representations of the equations is shown by the humidity zone identified in Figure 2.5.

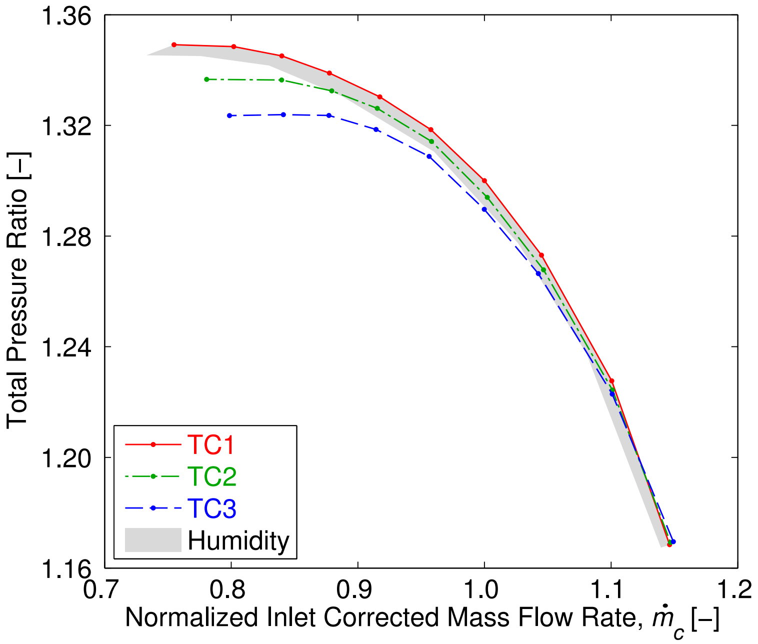

Figure 2.5: Humidity effects on measured compressor performance for a hot humid day in the context of the 100% corrected speedlines for the three tip clearance heights presented in this study.

Figure 2.5 reveals that research facilities which operate with unconditioned ambient air (such as the Purdue three-stage compressor) must carefully consider humidity effects for correcting operating conditions, particularly when measuring small-scale performance changes or attempting to compare results at the same operating condition across several seasons of the year. The desired deliverables of this project match both of these requirements, and therefore, further emphasize the importance of humid air considerations for this project.

2.2.2. Holistic Performance Measurements

For the Purdue three-stage compressor, the conditions used to calculate the corrected speed and corrected mass flow rate are measured at the Aerodynamic Interface

Plane (AIP), denoted by axial position zero in the flowpath shown in Figure 2.6. At this upstream inlet plane of the compressor, the 50% span measurements from a seven-element total pressure rake and a seven-element total temperature rake are used to calculate bulk one-dimensional flow parameters. The amount of moisture in the air is determined by an Omega HX94 thermo-hygrometer located near the inlet of the compressor, capable of measuring relative humidity with an uncertainty of ±2%. These measured parameters are used as inputs with the REFPROP thermodynamic equation program (Lemmon et al., 2013) to calculate the pertinent stagnation speed of sound and stagnation density required for Equations (2.1) and (2.2).

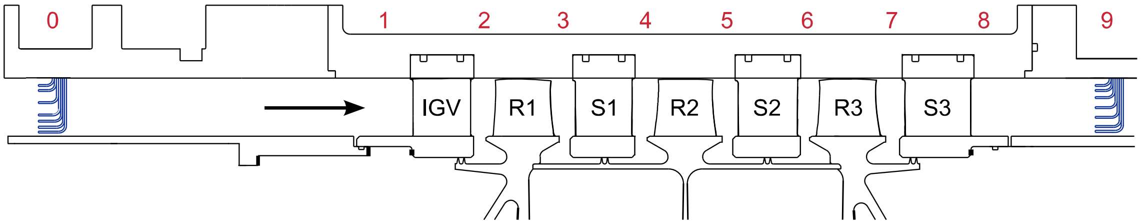

Figure 2.6: Purdue three-stage compressor facility flowpath cross section.

In addition to the seven-element total pressure and total temperature rakes installed at the AIP, 13 circumferentially-distributed static pressure taps evaluate the static pressure for this upstream inlet plane at the outer diameter of the flowpath. Great care has been incorporated to ensure circumferential uniformity of the pressures and temperatures at the inlet of the compressor, as measured by Ball (2013).

Referring again to the flowpath in Figure 2.6, the exit plane of the compressor (axial position 9) is also defined by a set of seven-element total pressure and total temperature rakes and one static pressure measurement. Separate from these upstream and downstream locations, additional seven-element total pressure and total temperature rakes are available at each of the axial positions labeled 1 through 8. Static pressures at these axial positions are evaluated by four circumferentially-distributed static pressure taps on the casing. The combination of these measurements at positions 1 through 9 provide the opportunity to define overall compressor performance and relative performance of each individual blade row or each stage. The radial position of the measurement locations for the seven-element pressure and temperature rakes at each axial position 0 through 9 are provided in Table 2.3.

Table 2.3: Radial distributions of rake measurement locations.

Ax. Pos.	Total Pressure [% annulus height]							Total Temp. [% annulus height]						
0	12	20	30	40	60	80	88	12	20	35	50	70	80	88
1 – 8	12	20	35	50	70	80	88	12	20	35	50	70	80	88
9	12	20	35	50	65	80	88	12	20	30	50	70	80	88

The axial location of the stations labeled in Figure 2.6 is halfway between the blade rows based on the mid-span geometry. The centerline of the rake coincides with the location of the axial measurement plane. The recovery factor for both the total pressure and total temperature rakes (as provided by the manufacturer) is equal to one, with three significant digits, for an angular acceptance range of ±30 degrees. The rakes are aligned with a representative mean flow angle, but this angular acceptance facilitates accurate measurements at off-design operating conditions.

Because the recessed casing geometry design (Figure 2.2) extends to the farthest axial extent, when the rakes are inserted with the TC2 or TC3 casing hardware, they are positioned within the tip clearance recess area. For this study, the rakes were radially positioned such that the measurement positions defined in Table 2.3 are consistent with the annulus height of the stator vanes (which are geometrically unaffected by the casing recesses). These rake positions are shown graphically in Figure 2.7, such that the outer edge of the rake was aligned with the 100% annulus height location, regardless of the tip clearance configuration (i.e., whether or not a casing recess was present). By this method, the detailed measurements collected at these same axial positions extend to 101.5% or 102.5% annulus height for the TC2 and TC3 tip clearance configurations, respectively. Based on this definition for Figure 2.7, the area-averaged weightings for the 88% rake positions are also varied for the three tip clearances to account for the changing flow area.

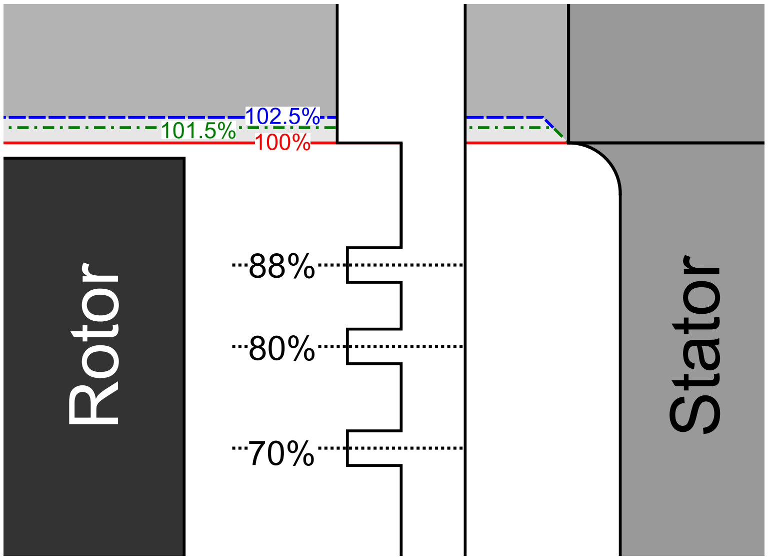

Figure 2.7: Rake positions for different tip clearance configurations.

The new variable tip clearance hardware for this project expanded the capabilities of the facility to accommodate measurement rake insertion at three or five circumferential positions (specifically for measurement plane 6, at the exit of the embedded second stage) for each of the positions 1 through 8 in Figure 2.6. These same rake insertion positions also function as locations for the installation of L.C. Smith precision probe positioners for detailed measurement traverses with a variety of instrumentation technologies.

In addition to the flow measurements, a series of surface-mounted thermocouples are installed on the outer part of the casing over each blade row to yield an axial temperature distribution. These measurements facilitate CFD analyses implementing alternate boundary condition methods, such as the isothermal boundary condition presented by Bruna and Turner (2013) for Rotor 37, instead of the more common, but significantly simplified, adiabatic boundary condition. Because the data collected from this experimental study are expected to aid in the development and calibration of computational models, it is important that these temperatures are collected with the aerodynamic performance data to appropriately define the system boundary conditions.

The total and static pressures for the facility are measured using Scanivalve 3217 and 3016 Digital Sensor Array (DSA) pressure scanner modules, each containing 16 temperature-compensated piezoresistive pressure sensors. Depending on the requirements of the specific measurement, the DSA channels are rated for differential pressure ranges of 1 psid, 2.5 psid, 5 psid, or 15 psid. These devices have been selected for their long-term accuracy ratings of 0.12% FS, 0.12% FS, 0.05% FS, and 0.05%FS, respectively. Thermal measurement drifts from these devices are prevented through regular procedures for an on-line zero calibration prior to and during compressor operation (typically every

20 minutes). The differential pressures are referred to an atmospheric reference pressure which is separately measured using a high-accuracy Setra 270 barometric pressure sensor with a range of 800-1100 mbar and an accuracy of 0.03% FS.

The temperatures for the facility are evaluated using T-type thermocouples paired with special limits of error (SLE) extension wire. A Keysight Technologies 34980A integrating voltmeter paired with 34921A/T modules and terminal blocks accommodates the measurement of these thermocouple channels. To achieve significantly reduced uncertainty contributions to the temperature measurements, Keysight Y1138A extension cables separate the terminal blocks from the measurement modules, and a 10 kΩ thermistor with an interchangeability of ±0.18 ºR provides the reference temperature for the isothermal terminal block. The temperature data reported for this study have been evaluated by an arithmetic mean of five independent measurements, each of which represents a thermocouple voltage measurement integrated over five power line cycles.

Through the use of a liquid calibration bath, the measurement chain for each of the temperature rake measurement channels was evaluated. By incorporating a high-accuracy thermistor as a reference measurement in the same calibration bath, the overall uncertainty of each individual channel was determined. These calibration results show an overall uncertainty typically less than 0.45 ºR. This value represents a conservative all-inclusive uncertainty for all temperature channels and all ranges of measured temperatures. However, the repeatability of the temperature measurements is an order of magnitude less than this value.

2.2.3. Isentropic Compressor Efficiency

For this study, the isentropic compressor efficiency will be evaluated using the formal definition,

$$\eta = \frac{h_{o2s} - h_{o1}}{h_{o2} - h_{o1}}, \tag{2.3}$$

as a function of stagnation enthalpies. Alternatively, a perfect gas assumption allows a simplification of isentropic efficiency,

$$\eta = \frac{\mathrm{TPR}^{((\gamma-1)/\gamma)} - 1}{\mathrm{TTR} - 1}, \tag{2.4}$$

which appears to be preferable due to its definition as a function of measured properties – total pressures and temperatures appearing in the total pressure ratio (TPR) and total temperature ratio (TTR). However, following an effort to minimize perfect gas simplifications, there is an inherent complication with the use of Equation (2.4), as discussed by Lou et al. (2013) and continued by Berdanier et al. (2015). Specifically, Lou et al. (2013) showed that the isentropic efficiency is always over-predicted when using Equation (2.4). This over-prediction may be less than 1 efficiency point for an overall TPR of 1.3, but it increases to over 5 efficiency points for a TPR on the order of 40 or more. The introduction of REFPROP (Lemmon et al., 2013) as an integral component of the data processing suite for this study provides the opportunity to calculate isentropic efficiency via the *definition* of the parameter shown in Equation (2.3). As with the calculation of corrected parameters introduced above, the use of REFPROP also accommodates the inclusion of humidity in the calculation of the stagnation enthalpies required to evaluate efficiency.

2.2.4. Detailed Steady Total Pressure Traverses

As described above, the steady compressor pressure rise is defined using a series of seven-element total pressure rakes distributed throughout the machine. However, these measurements inherently lack spatial resolution and a more thorough distribution of measurements closer to the endwalls. Thus, in addition to the total pressure rake measurements, a miniature Kiel head total pressure probe (United Sensor KAC-type) was traversed in small radial increments downstream of each of the stator vane rows. This probe features a 0.063 in. outer diameter Kiel head and was paired with a L.C. Smith precision probe positioner to incrementally achieve the desired plunge locations with position feedback. The probe accommodates a yaw and pitch angular acceptance cone of greater than ±40 degrees, but the probe was aligned with a representative mean flow angle.

2.3. Tip Clearance Measurement System

It is well known that static rotor tip clearances – sometimes referred to as "cold" clearances – do not typically represent the operating, or "hot" running, clearances. In general, thermal growth, pressure forces, and centrifugal effects due to high-speed rotor rotation contribute to blade growth and untwist which leads to a change of rotor tip clearances at different operating conditions and for different ambient conditions. The influence of thermal effects on the compressor casing may also contribute significantly to changing rotor tip clearances. As a result, a series of measurements have been collected to evaluate the static and operating tip clearances of the Purdue three-stage compressor.

2.3.1. Static Tip Clearance Measurements

The static “cold” tip clearances have been evaluated for each of the three tip clearance configurations. These measurements were collected by measuring the blade-to-blade variability (i.e., the run-out of the rotor blade tips) using a fixed dial indicator with a rolling tip. The manufacturing tolerances of the rotor blisk show the blade-to-blade variability at any fixed location about the circumference of the compressor, as presented in Figure 2.8. These blade-to-blade measurements were collected several times to calculate the mean values in Figure 2.8. As a result, the uncertainty of the mean value is on the order of 1×10^{-4} in.

The concentricity of the rotor with respect to the casing has also been evaluated using static tip clearance measurements collected at several positions around the circumference of the compressor casing. These measurements have shown for each tip clearance configuration that the concentricity of the rotor with respect to the casing is a less than 0.003 in. The smallest tip clearances are measured at a position of 345 degrees from the top of the compressor, in the direction of rotor rotation, as shown in Figure 2.9. The rotor concentricity can be controlled using a set of alignment bolts at both the front and rear bearing assemblies, as prescribed by Talaleyev (2011). This concentricity control is limited to within 0.008-0.012 in. based on bolt thread pitch. Thus, the measured concentricity of the rotor is confirmed to be within the adjustment capabilities of the system.

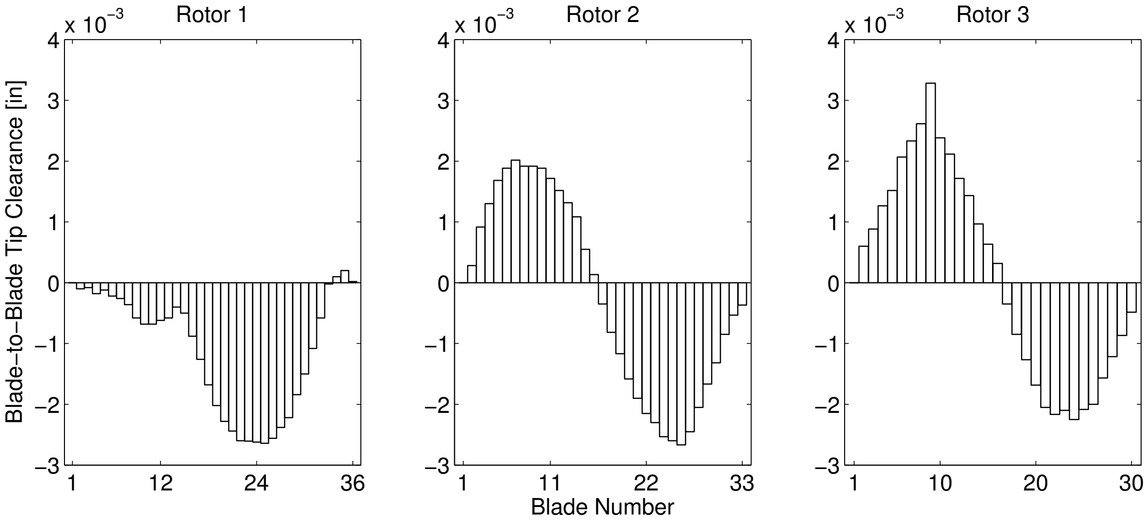

Figure 2.8: Blade-to-blade variability of tip clearance height with respect to “Blade 1” for all three rotor rows.

For this study, a facility upgrade included the introduction of a CapaciSense 5-series frequency modulated (FM) capacitance probe tip clearance measurement system (produced by Pentair Thermal Management). The system features nine available channels, allowing three probes to be installed for each of the three rotor rows. The three probes are equally-spaced circumferentially, 120 degrees apart, at positions of 105 degrees, 225 degrees, and 345 degrees – all measured from the top of the compressor in the direction of rotor rotation (see Figure 2.9). Each of the nine probes was individually calibrated using a custom-designed calibration disk which represents the tip geometry of the rotor blade through scaling techniques proven by the manufacturer. The probes were all calibrated for operation from a rub condition (0 in. clearance) to a maximum 0.2 in. clearance height.

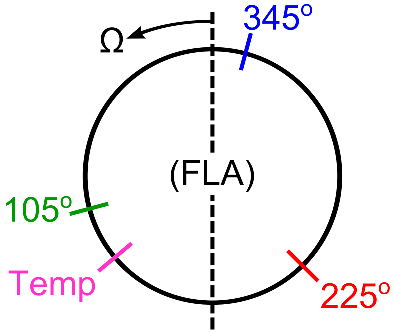

Figure 2.9: Circumferential capacitance probe measurement locations.

The electronics chain for the FM tip clearance measurement system has several key components. The probes, shown in Figure 2.10(a), were designed and built for application in this specific facility; a triaxial cable is permanently attached to the probe and provides enhanced rejection of electromagnetic interference. The use of a non-mineral-insulated cable limits the maximum operating temperature of this system to approximately 260 ºC, well above the operating limits of the Purdue three-stage compressor. The oscillator, shown in Figure 2.10(b), drives the cable with an oscillating voltage (nominally 2 MHz). As the blade passes the probe, the measured capacitance modulates the driven frequency from the oscillator. This modulation is sensed by the carrier, and the demodulator (Figure 2.10(c)) converts the modulation frequency due to the blade passing event to a DC voltage. The DC voltage is correlated to a clearance height via the individual channel calibration. This proportionality between measured capacitance, frequency modulation, voltage, and tip clearance is the heart of the FM tip clearance measurement system.

(a) (b) (c)

Figure 2.10: Capacitance tip clearance measurement system components.
(a) Probe; (b) Oscillator; (c) Demodulator.

The clearance measurement system is controlled from a set of “Control and Processing Module” (CPM) computers operating Slackware 14 Linux. Each of these computers utilizes one Advantech PCI-1714UL data acquisition card to sample four of the nine channels (three total CPMs). The three CPMs are setup in a master-slave-slave configuration communicating via Ethernet, and the master CPM utilizes a manufacturer-designed graphical user interface (GUI) to configure and operate the entire probe measurement chain (including the oscillators and demodulators). The data acquisition card is capable of sampling the four analog channels at up to 10 MHz per channel, as well as an external trigger which is linked to the 1/rev signal from the laser tachometer for the compressor. For the measurements presented in this study, all data were collected using the full 10 MHz sampling capability of the data acquisition card. Other specifications for the capacitance probe measurement system are listed in Table 2.4.

The clearance calculation process provides a blade-by-blade clearance output calculated from the peak-to-peak voltage for the typical blade pulse output signal (known as the Blade Passing Signal (BPS)). By synchronizing the measured clearances with the once-per-revolution trigger from the compressor, these calculated clearances from the

BPS output can be traced to known blade numbers. As an alternative to this BPS method, the software applies a low-pass filter to the BPS output to create a DC voltage output signal which the manufacturer refers to as a “RMS” signal, although it should be noted that the low-pass filter mechanism does not represent a true root-mean-square calculation procedure. This RMS signal serves as a representative average of the tip clearance for all blades measured by a particular probe.

Table 2.4: Capacitance probe measurements system specifications.

Parameter	Value
Operating Frequency	2 MHz nominal
Oscillator Sensitivity	100 kHz per pF
Demodulator Sensitivity	500 mV per kHz typical
Measurement Range	0.200 in. calibrated
System Resolution	$< 4\times10^{-5}$ in. (at 0.030 in. clearance)
Signal-to-Noise Ratio	30-50 typical

2.3.2. Operating Tip Clearance Measurement Uncertainty

The manufacturer of the capacitance probe measurement system claims an umbrella uncertainty on the measurement system of less than 4×10^{-4} in. This value is based on historical comparisons with other measurement techniques, including laser measurements and rub sticks, as well as careful attention to the design, manufacture, and calibration processes to ensure minimal uncertainties. However, no formal uncertainty analysis had yet been performed to validate this claim, which represents more of a repeatability, or comparability, and does not consider uncertainty contributions from the electronics components.

To overcome this limitation, an uncertainty analysis was performed based on known information about the electronic devices in the system and the calibration data. Following a method outlined by Müller et al. (1997) for a similar capacitance probe system, the uncertainty of the individual probes was evaluated to be on the order of 0.001 in. or less over the range of tip clearances investigated for this study. Additional information regarding the tip clearance system uncertainty analysis is available in Berdanier and Key (2015a).

2.4. Time-Resolved Flow Field Measurements

2.4.1. Over-Rotor Static Pressure Measurements

Time-resolved static pressures over the rotor tips were measured using a custom-designed array implementing flush-mounted fast-response pressure transducers. This array incorporates 25 Kulite XCS-062 subminiature pressure transducers (having an outer diameter of 0.066 in.) with a 5 psig range. These XCS-series transducers feature high-sensitivity piezoresistive sensing elements, maximizing the resolution of the measurements. The sensors were installed with standard B-type screens for protection of the sensing elements, but the new sensors were filled with additional silicon material to reduce the cavity size behind the screen and allow for the greatest allowable frequency response. As a result, a frequency response on the order of 30 kHz is expected for these new sensors.

During the design process, a specific effort was made to accommodate all sensors in one axial row. Some previous authors have utilized a method of offsetting sensors in two or more axial rows, separated by some angle in the pitchwise direction, to accommodate more axial resolution (Yoon et al., 2006; Shin et al., 2008; Courtiade and Ottavy, 2012). However, such sensor orientations can introduce complications in the measurements for multistage machines, as the wakes propagating from upstream stators and potential fields from downstream stators may affect the measurements. Understandably, this effect can be accounted for if the sensors are moved relative to the stator vanes, but it introduces an additional complication to the data acquisition and processing procedures. As an alternative, other authors have achieved maximum axial resolution by implementing a series of sensors at different axial positions, spaced periodically in the circumferential direction with respect to the rotor pitch (Levis, 2006; Sans et al., 2013). However, this method could be also be negatively affected by blade-to-blade non-uniformities, rotor eccentricity, and any associated flow variability.

The small diameter of the XCS-062 devices provides the ability to incorporate the maximum possible number of sensors in one axial row, thereby increasing the spatial resolution of the output results. The sensors are permanently installed in a removable block which can be inserted into any one of nine frames. These nine frames represent one for each of the three rotor blade rows (R1-R3) and each of the three tip clearance configurations (TC1-TC3). The removable sensing block and one of the nine frames are shown in Figure 2.11(a).

The instrumentation block was designed to maximize the number of sensors which can fit within the space defined by the instrumentation access location over

Rotor 1, which features the least axial space of the three rotors. Because the same fixed sensor locations are implemented for Rotor 2 and Rotor 3, whereas the axial chord of the rotors increases slightly moving from Rotor 1 to Rotor 3, the positions of the sensors change with respect to the leading and trailing edges of the blades for the three rotor rows. These sensor positions are presented for the three rotors in Table 1 as a percentage of axial chord.

Table 2.5: Flush-mounted sensor positions for each rotor as a percentage of axial chord.

Blade Row	Minimum Sensor Location [$\%c_x$]	Maximum Sensor Location [$\%c_x$]	Sensor Separation [$\%c_x$]
Rotor 1	-14.0	114.0	5.33
Rotor 2	-12.8	113.6	5.26
Rotor 3	-11.9	113.2	5.21

The excitation and amplification for these fast-response pressure sensors were provided by a Precision Filters 28000 chassis with four 28118 full bridge amplification cards, each of which is capable of managing eight channels for a total of 32 simultaneous operating sensors. Each of the channels in the Precision Filters system is independently managed through a manufacturer-designed GUI to adjust the DC offset, gain, and on-board analog filter characteristics. The sensor signals were then digitized using an NI PXIe-1073 chassis utilizing two 16-channel PXIe-6358 modules, each capable of simultaneous sampling of up to 1.25 MHz per channel, via NI BNC-2110 connector blocks.

(a) (b)

Figure 2.11: Over-rotor static pressure measurement system. (a) Removable sensing block and frame; (b) Calibration chamber.

Immediately prior to installation and operation in the compressor, the fast-response pressure sensors were calibrated in a custom-designed calibration chamber (Figure 2.11(b)) by prescribing a known pressure to the device. For each calibration, up to 15 data points were prescribed over the full sensing range of 0 to 5 psi. From these measurements, a least-squares linear fit was applied to the calibration data with a typical R^2 value of 1.00000, where R^2 represents the coefficient of determination as calculated from the residual sum of squares and the total sum of squares. The channels were zeroed prior to each calibration and again prior to testing, although thermal compensation and a stable measurement system reduce the day-to-day drift of a representative channel to 1 mV or less over (after amplification), which corresponds to a pressure of less than 8×10^{-4} psi.

For each rotor and each tip clearance configuration, data were acquired at several loading conditions on the 100% corrected speedline. In all cases, 500 revolutions of data were simultaneously sampled, thereby allowing phase-locked ensemble averaging and other pertinent statistics to be calculated.

2.4.2. Total Pressure Measurements at Rotor Exit

In addition to the steady total pressures measured at positions downstream of the stator vane rows, time-resolved total pressure measurements were also acquired at the rotor exit planes. A custom-designed fast-response total pressure probe incorporates a Kulite LQ-062 subminiature pressure transducer embedded in a miniature Kiel head with a 0.083 in. outer diameter and a 0.067 in. inner diameter (Figure 2.12). The sensor has a 5 psi maximum range with an electronically sealed gage reference condition. As with the surface-mounted pressure sensors described in Section 2.4.1, this transducer also includes a standard B-type protective screen, therefore reducing the frequency response of the sensor to approximately 20 kHz. A separate pressure chamber designed for this probe provided the ability to calibrate the sensor at prescribed intervals over the 0-5 psi, range and a least-squares linear fit was applied to the calibration results with an R^2 value of 1.00000. The sensor was balanced with the acquisition of a zero gage pressure reading prior to each calibration, and similarly before and after each test. As with the detailed steady total pressure measurements, these time-resolved rotor exit total pressures were acquired at two loading conditions on the 100% corrected speedline for the smallest and largest tip clearance configurations (TC1 and TC3).

Figure 2.12: Fast-response total pressure probe.

2.4.3. Thermal Anemometry

Hot-wire anemometry was used for this study to acquire time-resolved velocity and flow angle measurements throughout the compressor. For all measurements, a Dantec Dynamics StreamLine Pro frame was used with 91C10 constant temperature anemometer (CTA) bridges. A computer interfaces with the bridge frame through a PC operating the Dantec Dynamics StreamWare software. The sensor voltages output from the CTA bridges are digitized using an NI PXIe-1073 chassis through a NI BNC-2110 connector block and an eight-channel NI PXIe-6356 module. A custom-designed NI LabVIEW GUI operates the L.C. Smith precision probe positioner holding the sensor, as well as the data acquisition procedures.

The hot-wire sensors utilized for this project were calibrated using the hot-wire calibration facility in the Purdue Compressor Research Laboratory, which features a low-turbulence heated jet with three-dimensional directional sensitivity and precision control of flow conditions. The facility, shown schematically in Figure 2.13, is fed from a reservoir of dry compressed air maintained at a nominal pressure of 300 psig. A digital pressure regulator (UP) adjusts the upstream pressure of the system to control the velocity via a proportional-integral-derivative (PID) control loop. The flow passes through two in-line flow heaters (H1, H2), and a separate PID control sequence maintains the jet temperature to within 0.5 degrees Fahrenheit of the desired set point. The heaters ensure that the hot-wire calibration data are acquired at a constant temperature to avoid calibration uncertainties due to temperature changes. After flowing through the two heaters, the air is diverted around a flow spreader and then passes through a series of honeycomb and screens for flow conditioning. A nozzle with a diameter of 1 in. accelerates the flow to the desired velocity, which is determined by a combination of stagnation plenum pressure and static pressure at the nozzle exit. The system maintains the jet exit velocity within 0.2 percent of the desired set point. An attachment to the calibration nozzle (Figure 2.14) provides the capability to vary the position of the probe with respect to the jet, effectively changing the pitch angle of the flow with respect to the probe. Additional information about the calibration jet facility is available from Morrison (2013).

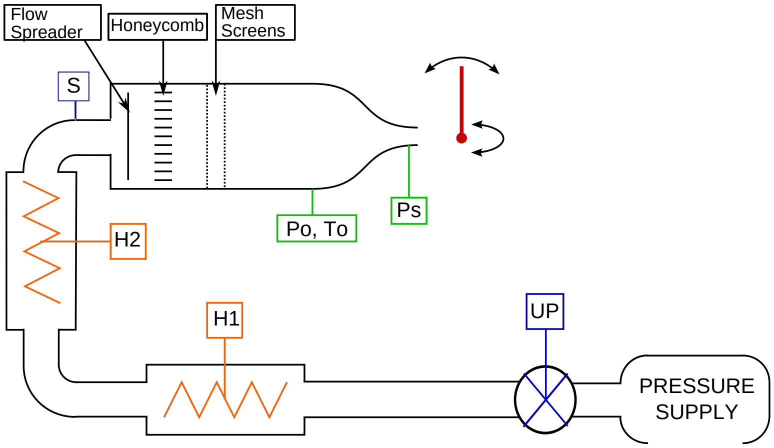

Figure 2.13: Purdue Compressor Research Laboratory hot-wire calibration facility schematic (Morrison, 2013).

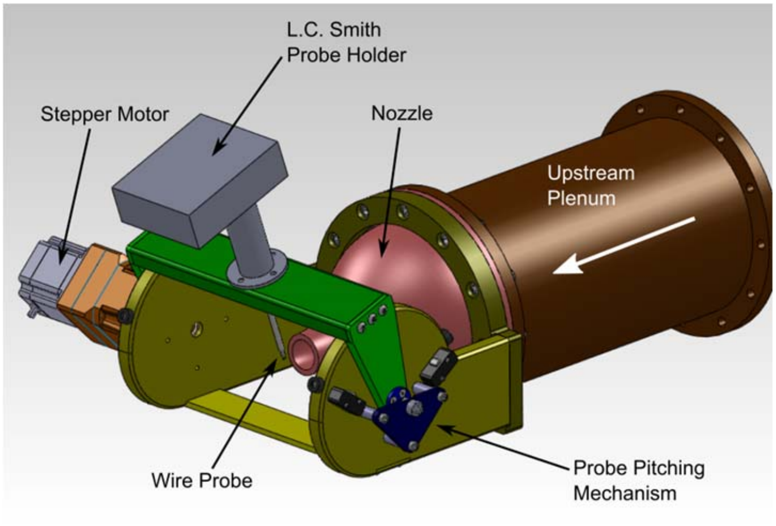

Figure 2.14: Hot-wire cailibration facility optional three-dimensional calibration feature. Adapted from Morrison (2013).

2.4.3.1. Velocity and Flow Angle Measurements

The velocity and flow angles throughout the compressor were evaluated for axial measurement planes 2 through 8. These data were acquired at two loading conditions on the 100% corrected speedline for the two extreme tip clearance configurations (TC1 and TC3). These tests were conducted using a Dantec Dynamics 55R02 fiber-film sensor with an inclination angle of 45 degrees with respect to the probe support axis. For this sensor, the manufacturer specifies a sensing film length of approximately 1.25 mm and a nickel film diameter of 70 μm. The selection of the slanted probe for this project provides the opportunity to investigate three velocity components, with a particular emphasis on the tip leakage flow features. For these measurements, the 55R02 sensor was operated in a standard 20:1 CTA bridge mode. In the CTA control software, the overheat ratio (OHR) of the bridge was adjusted to the manufacturer-optimized value of 1.8, as defined the resistance of the wire, R_w, under heated ("hot") and ambient ("cold") conditions:

$$\mathrm{OHR} = \frac{R_{w,\mathrm{hot}}}{R_{w,\mathrm{cold}}}. \tag{2.5}$$

The fiber-film sensor technology is offered as an option which provides a more robust design than traditional thin wires, thereby reducing susceptibility to damage from the high-shear flows present in compressor applications, without the degradation of frequency response which is typically observed with traditional film sensors. Throughout this document, however, the term ‘wire’ will be used interchangeably to also describe the fiber-film sensor.

The 55R02 sensor was calibrated over a range of velocities and flow angles, as prescribed in Table 2.6. The response of the fiber-film sensor was optimized near the upper end of the velocity calibration range (400 ft/s) using a square wave test signal. Using this method, the frequency response of the sensor was optimized to be approximately 85 kHz – nearly 30 times the blade passing frequency of the rotor blades in the desired compressor application. For each test campaign, a calibration was performed prior to the data collection, and a separate calibration was performed after the completion of the campaign for comparison of measurement drift. The jet temperature for these calibrations was always maintained at a constant 100 ºF.

Table 2.6: Hot-wire calibration matrix.

Parameter	Velocity, V[ft/s	Yaw angle, α[deg]	Pitch angle, ϕ[deg]
Min. value	100	-90	-20
Max. value	450	+90	+20
Increment	50	5	5

To evaluate three components of phase-locked ensemble averaged velocity, a minimum of three separate wire positions is required. At each test condition and radial plunge position, the sensor was aligned with the approximate mean flow angle, and then yawed to the three desired measurement angles using the precision probe positioner. Following the procedure outlined by Shin and Hu (1986), the sensor angles used for this study were -20 degrees, +20 degrees, and +60 degrees with respect to the null position, as defined by the coordinate system in Figure 2.15.

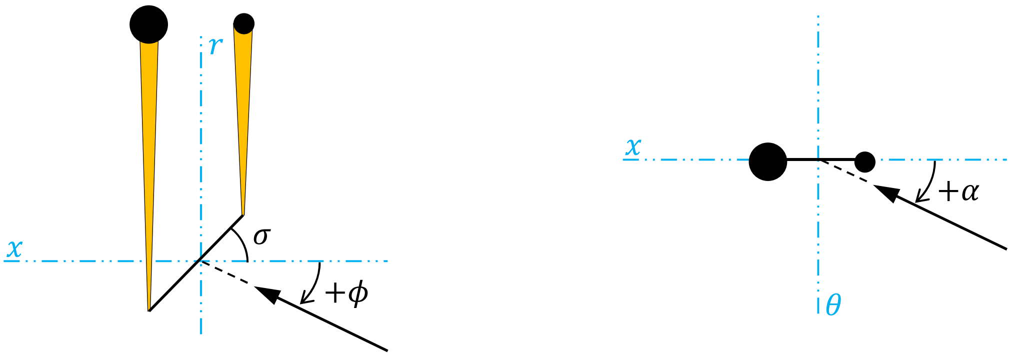

Figure 2.15: Angular definitions for slanted hot-wire sensor. The long prong is denoted by the large circle.

The measured wire voltages were converted to known velocities and flow angles using calibration data with a non-linear solver technique for data reduction. In this case, the Joule heating principle and King's law (1914) are applied to evaluate the voltage-velocity relationship. Next, a predetermined relationship between Nusselt number and Reynolds number proposed by Collis and Williams (1959) accounts for variations of flow properties between calibration and test conditions. When required, REFPROP was used to calculate thermodynamic properties for use in the non-dimensional Nusselt and Reynolds numbers. The effective Reynolds number, $\mathrm{Re}_{\mathrm{eff}}$, is determined from the effective velocity, defined as any velocity which does *not* appear as a normal velocity with respect to the wire orientation (i.e., ±90 degrees yaw and 0 degrees pitch). Finally, the desired non-linear relationship:

$$\frac{\mathrm{Re}_{\mathrm{eff},j}}{\mathrm{Re}} = C_0 + C_1\,\alpha + C_2\,\phi + C_3\,\mathrm{Re} + C_4\,\alpha\,\phi + C_5\,\alpha\,\mathrm{Re} + C_6\,\phi\,\mathrm{Re} + C_7\,\alpha^2 + C_8\,\phi^2 + C_9\,\mathrm{Re}^2\,, \tag{2.6}$$

is developed for ten coefficients C_i determined from the calibration data, which must apply for all three wire orientations, $j = 1..3$. This equation is based on the method utilized by Schmidt and Okiishi (1976).

An example comparison of the non-linear equation fit from Equation (2.6) with the discrete calibration points, Figure 2.16, represents this functional relationship for one of the calibration sets used in this study at a velocity of 300 ft/s. For this study, the slanted wire was found to be asymmetric about the null (zero degrees yaw) position. As a result, a separate coefficient set was defined for each half of the curves in Figure 2.16. The coefficient fit for the example data in Figure 2.16 has an R^2 value greater than 0.98.

Once wire voltages are measured in the compressor, the effective Reynolds numbers are calculated, and the three equations, Equation (2.6), are solved simultaneously using the pre-determined coefficients to calculate the true Reynolds number and the flow angles, which are geometrically related to the pre-defined wire positions of -20, +20, and +60 degrees.

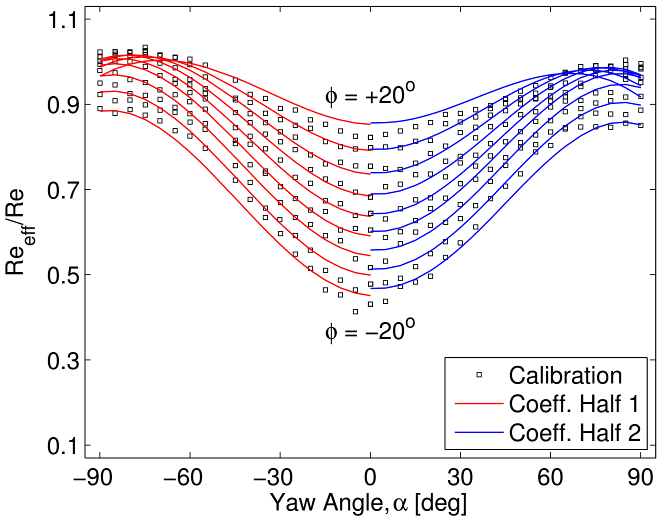

Figure 2.16: Example slanted hot-wire coefficient fit at 300 ft/s.

2.4.3.2. Thermal Anemometry Uncertainty

The uncertainty of the calibration data collected from the Purdue calibration jet facility has been evaluated previously by Morrison (2013). To evaluate the accuracy of the processing algorithm implemented for the velocity and flow angles measurements, a series of data were collected at known wire positions, velocities, and conditions in the calibration jet which represent the compressor operating conditions for each test campaign. Specifically, the temperature and density of the jet were adjusted to match the flow conditions determined from the steady total temperature and total pressure rakes (and wall static pressure), as measured simultaneously with the hot-wire. Furthermore, a representative velocity was also calculated from these rake measurements to select the operating velocity of the calibration jet. Using this method, the accuracy of the measurements at each axial measurement position (i.e., Rotor 1 exit, Stator 3 exit, etc.) and compressor loading condition was separately identified, Figure 2.17.

The results in Figure 2.17 show that the calculated velocity from the hot-wire processing algorithm is a strong function of the operating condition in the compressor, whereas the calculated yaw and pitch angles are less dependent on operating conditions. An investigation of an alternate processing method (Berdanier and Key, 2015b-c; Appendix C) has shown that the velocity can be greatly affected if the conditions of the measured flow vary significantly from the calibration conditions. However, the calculated flow angles are much less sensitive to these temperature effects due to their greater dependence on the geometry of the probe itself. Indeed, analysis of the results in Figure 2.17 shows that the test conditions which yield the most significant velocity difference are the same conditions for which the temperature at the wire location was most different from the calibration temperature. In the same manner, the test conditions which show the least difference (closest to zero) are those for which the temperature at the location of the wire in the compressor was nearly identical to the calibration temperature. For reference, in this figure, the velocity difference on the order of -60 ft/s is representative of a temperature 40 ºF lower than calibration conditions, and the velocity difference on the order of +20 ft/s is representative of a temperature 30 ºF higher than calibration conditions.

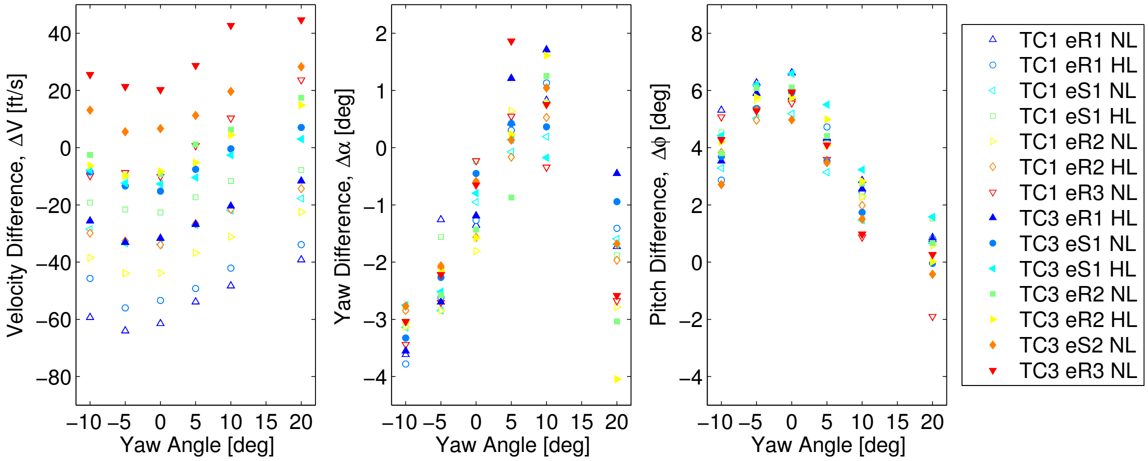

Figure 2.17: Approximate accuracy of hot-wire processing algorithm for test-representative conditions at several known flow angles.

Although the velocity errors shown in Figure 2.17 appear significant, they are predictable and trend linearly with the temperature difference, ΔT_o:

$$\Delta T_o = T_{o,\text{test}} - T_{o,\text{cal}} \,. \tag{2.7}$$

This linear relationship between velocity error and temperature difference is shown in Figure 2.18. As a result, the velocities are easily adjusted to reduce velocity error less than 15 ft/s (within approximately 5% relative error) at all test conditions.

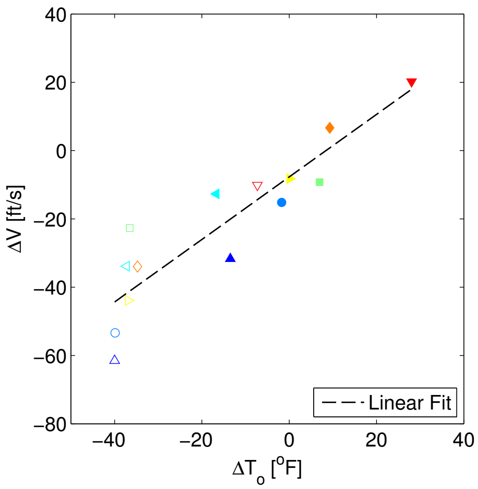

Figure 2.18: Trend of velocity error with temperature difference for velocity adjustment.

The reason for the velocity discrepancy outlined in Figure 2.17 and Figure 2.18 is related to the correction proposed by Collis and Williams (1959). Previous studies have shown that the Collis and Williams correction relating the Nusselt number and the Reynolds number deviates for Mach numbers above approximately 0.3 (Shin, 2015). In these cases, compressibility effects begin to become more significant for the hot-wire measurements. Referring again to the results in Figure 2.17, the rotor exit measurements are the locations at which the absolute flow velocity is expected to be the largest (due to the diffusion of flow in the relative reference frame causing acceleration in the absolute reference frame). Furthermore, as the temperature decreases, the Mach number will increase. As a result, the measurements at Rotor 1 exit for TC1 at NL with a velocity difference on the order of -60 ft/s represent a Mach number on the order of 0.35. All of the tested conditions in Figure 2.17 with a velocity difference beyond approximately ±25 ft/s represent flow conditions with an average Mach number greater than or equal to 0.30.

This processing method of solving a set of non-linear equations represents the most accurate of two methods evaluated for these data. The other method implemented a look-up table approach, for which the temperature and density variations are independently accounted using known relationships, as discussed by Berdanier and Key (2015b-c).

Aside from developing new relationships to accommodate temperature variations with compressibility considerations, future hot-wire measurements such as these may benefit from a more controlled selection of inlet conditions which more closely resemble calibration conditions, or several calibration sets for different temperature ranges. However, neither of these recommendations is particularly advantageous: (i) A judicious selection of compressor operating conditions comparable to calibration conditions can only be achieved with temperature-controlled compressor inlet conditions. This is especially true for test campaigns which span several days in the midwest United States, where weather patterns can be particularly difficult to predict. (ii) Extended calibration time poses an increased potential to experience a broken sensor. The fragility of hot-wire sensors makes them particularly prone to breakage, and additional operating time (in a calibration jet, for example) greatly increases this potential for failure.

To further evaluate the robustness of the hot-wire calibration and processing algorithm, two separate calibration data sets (one before the test campaign and another after the test campaign, each approximately one week apart) were used to process the same experimentally-collected data. Specifically, data collected at the exit of Stator 1 for TC1 at two loading conditions were processed using the two sets of coefficients (Equation (2.6)). This axial measurement position at Stator 1 exit was selected because it represents a data set which was collected with approximately equal time between the pre-calibration an the post-calibration data (about four days between the collected data and either calibration). The results from this comparison, Figure 2.19, show the differences between the results processed with the two calibrations are much smaller than the differences which may be observed due to operating temperature and density changes, as shown in Figure 2.17. For the nominal loading (NL) condition in Figure 2.19, the velocities show a constant offset between the two calibrations. The yaw angles are least affected in the wake region, but the pitch angles show the most difference in the wake region. Separately for the high loading (HL) operating condition, the velocities show little effect in the wake region, with a more noticeable change for the undisturbed mean flow. At this same HL condition, the yaw and pitch angles in the mean flow are largely unchanged, but the flow angles in the wake region are most different. The average differences across one vane pitch from Figure 2.19 are summarized in Table 2.7.

Table 2.7: Average differences across one stator pitch for data processed with two calibration sets. Data collected at Stator 1 exit for TC1.

Loading	$\Delta(V/U_t)$ [%]	ΔV [ft/s]	$\Delta\alpha$ [deg]	$\Delta\phi$ [deg]
NL	2.0	10.3	0.9	0.4
HL	1.7	9.0	0.7	0.1

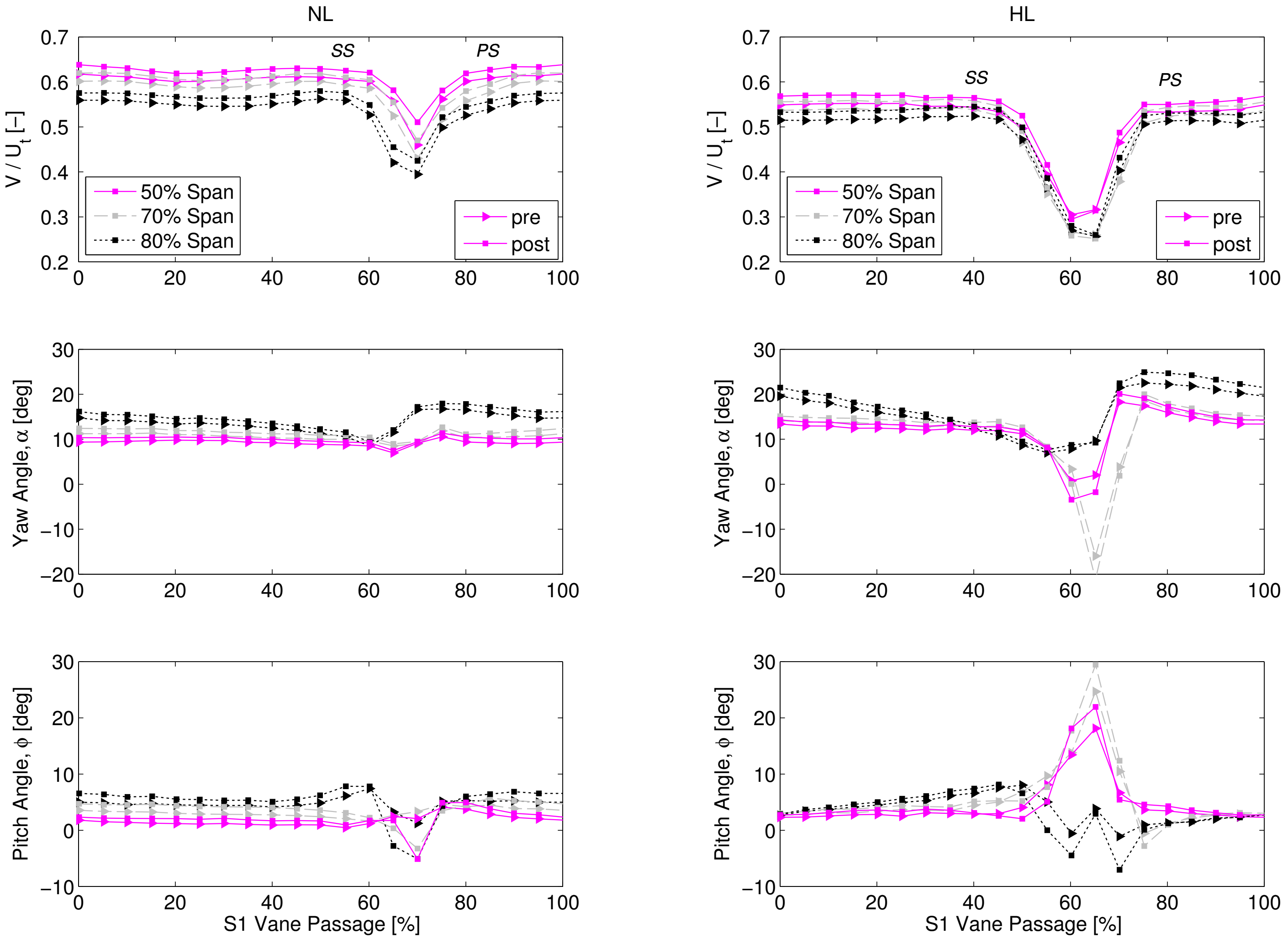

Figure 2.19: Processed hot-wire data at Stator 1 exit for TC1 using two separate calibrations.

CHAPTER 3: STEADY COMPRESSOR PERFORMANCE

3.1. Compressor Performance Maps

For this study, a series of steady compressor performance data were collected at four corrected operating speeds (100%, 90%, 80%, and 68%) for each of the three tip clearance configurations (TC1-TC3). The 68% corrected speedline was selected instead of the 70% corrected speed to avoid a Campbell diagram crossing corresponding to a rotor first torsion (1T) vibratory mode, as analyzed by Murray (2014). In all cases, the corrected speed and corrected mass flow rate were calculated according to the procedure outlined in Section 2.2.1. For each of the four speedlines, data from different tip clearance configurations were collected at equivalent corrected mass flow rates for direct comparison.

3.1.1. Total-to-Total Pressure Rise Characteristics

Benchmark compressor map data are presented in Figure 3.1. Each measurement point in Figure 3.1 is calculated from area-averaged rake measurements collected from the seven-element total pressure rakes at 20 equally-spaced vane positions across one vane pitch. In this figure, the overall total pressure ratio (TPR) across the compressor is calculated as the ratio of radially and circumferentially area-averaged total pressures from axial planes 1 and 9 in the Figure 2.6 schematic:

$$\mathrm{TPR} = \frac{P_{o,9,\mathrm{AA}}}{P_{o,1,\mathrm{AA}}}. \tag{3.1}$$

In Figure 3.1, five operating points from the 100% corrected speedlines have been designated for comparison throughout this document: a low loading (LL) condition which represents a high flow rate; a nominal loading (NL) condition representing an operating point at a mass flow rate slightly higher than the peak efficiency point; a peak efficient (PE) point; a high loading (HL) condition which represents a low flow rate, high incidence operating point; and a set of conditions near the stall point (NS) which have a stall margin of approximately 5%. For this study, the stall margin (SM) is defined as follows:

$$\mathrm{SM} = \frac{\left(\frac{\mathrm{TPR}}{\dot{m}_c}\right)_{\mathrm{stall}} - \left(\frac{\mathrm{TPR}}{\dot{m}_c}\right)}{\left(\frac{\mathrm{TPR}}{\dot{m}_c}\right)} \times 100\%\,. \tag{3.2}$$

On the abscissa of Figure 3.1, the corrected inlet mass flow rates have been normalized by the value at the nominal loading point. For reference, the calculated relative uncertainty of the overall total pressure ratio in Figure 3.1 is 0.16% (within the symbol size in the figure). The maximum relative uncertainty of the normalized inlet corrected mass flow rate using the ASME-standard (ASME PTC 19.5, 2004) set of equations is 1.4% and occurs at the near-stall loading condition. Nearly 60% of this calculated measurement uncertainty is contributed by the ASME-standard uncertainty for discharge coefficient, which will be reduced in the future upon calibration of the Venturi flow meter. However, the repeatability of the mass flow rate measurements for a fixed throttle position at the same loading condition is typically on the order of 0.2%.

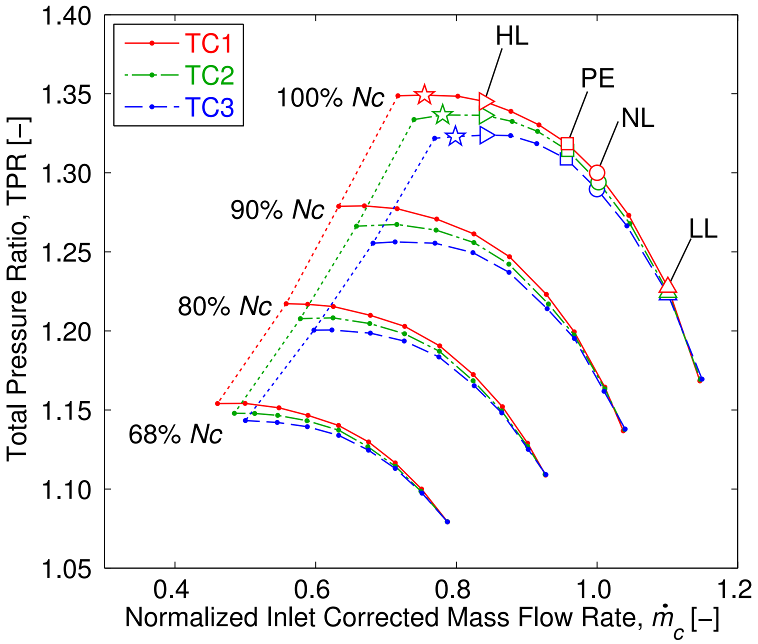

Figure 3.1: Compressor total pressure ratio map.

In Figure 3.1, the final point at the top of each speedline (the lowest flow rate condition) is not a 20-point traversed point, but rather a representative location of the stall point for the compressor at that operating speed. Once the stall point is identified in a preliminary run, it is subsequently approached slowly through incremental throttle movements to determine the mass flow rate and pressure rise locating the stall point. An approximate representation of the stall point with respect to the traversed points on the rest of the speedline can be determined by a comparison with the last (NS) traversed point and by stalling the compressor in several stator vane positions with respect to the fixed rake positions. The dotted line connecting these points represents a stall line for the specific tip clearance configuration. Comparing these results, an increase of rotor tip clearance leads to a decrease of overall total pressure rise and moves the stall point to a higher flow rate (the stall margin is reduced). Additional discussion about the stall characteristics of the compressor is given in Chapter 4.

3.1.2. Operating Tip Clearance Measurements

The operating points defined in Figure 3.1 can be characterized by their nominal (design intent) rotor tip clearance height, as listed in Table 2.2. However, several environmental factors can influence the physical components of the facility and, in turn, introduce variations of the operating tip clearance. These factors include, but are not limited to, centrifugal effects related to rotational speed changes and corresponding blade elongation, thermal effects due to temperature rise through the compressor, and pressure forces resulting from the pressure rise through the compressor. In a previous study guided toward modeling tip clearance changes in a multistage axial compressor, Dong et al. (2014) separated the potential contributions of operating tip clearance changes into several categories, as suggested above:

$$\begin{aligned}\tau_{\text{model}} = \tau_{\text{static}} - \left[(\Delta\tau)_{B,\text{thermal}} + (\Delta\tau)_{B,\text{centrif}}\right] + \left[(\Delta\tau)_{S,\text{thermal}} + (\Delta\tau)_{S,\text{pressure}}\right] \\ - \left[(\Delta\tau)_{D,\text{thermal}} + (\Delta\tau)_{D,\text{centrif}}\right]\end{aligned} \tag{3.3}$$

where the subscripts B, S, and D represent tip clearance change contributions from the blade, shroud (casing), and disk, respectively. This equation calculates the operating "model" clearances, τ_{model}, based on the static (cold) build clearance, τ_{static}. Equation (3.3) shows a thermal expansion or centrifugal growth of the blade or disk will decrease the clearance height, whereas a thermal expansion or pressure force acting on the shroud will increase the clearance height.

This model has been applied specifically to the Purdue three-stage axial compressor to compare measured tip clearances with model predictions (Berdanier and Key, 2015a), and the outcome showed that the predicted model clearances are driven primarily by the thermal growth terms, which yield clearance change contributions several orders of magnitude larger than the pressure or centrifugal components. Ultimately, this previous study (Berdanier and Key, 2015a), in combination with the original model analysis presented by Dong et al. (2014), has confirmed that considerable changes in operating tip clearance height can be achieved as the loading condition is changed along a given speedline or between speeds.

The operating tip clearances for this project were measured using the capacitance probe system outlined in Section 2.3. Beginning with the baseline tip clearance configuration (TC1), the measured operating tip clearances for the steady operating points defined in Figure 3.1 are presented in Figure 3.2 as a function of the normalized inlet corrected mass flow rate for each of the four identified speeds. These clearance data have been determined using the RMS calculation method, although an arithmetic mean of the blade-by-blade DNS data is similar. In Figure 3.2, the three circumferentially-distributed probes for each rotor row have been averaged to yield one representative tip clearance value for each rotor row.

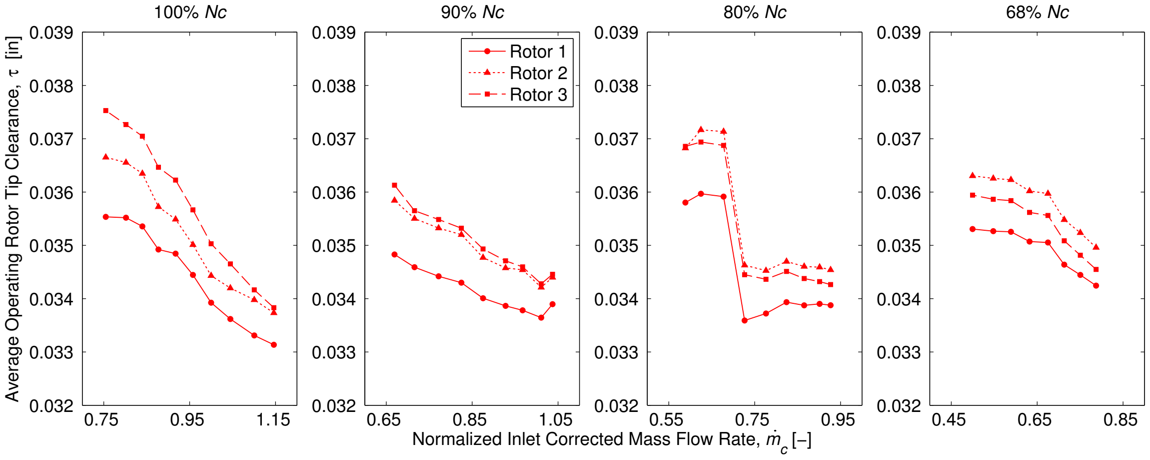

Figure 3.2: Operating tip clearances measured using capacitance probes for TC1.

Considering Figure 3.2, these operating points were collected in immediate succession moving from left to right across the four parts of the figure. In this way, the results display the variation of rotor tip clearance height as the operating point changes with minimal point-to-point effect from ambient temperature changes. However, there are several noticeable effects of changes in ambient conditions. First, the final high flow rate condition for the 90% corrected speedline moving into the 80% corrected speed conditions represents a period of time at the beginning of a day when the ambient temperature was increasing; Second, there is a significant drop of measured tip clearances between the third and fourth points (from left to right) in the 80% speedline. A period of severe weather forced a stop of the experimental campaign after the completion of the third point in this line, and the data collection process resumed on the 80% speedline, beginning with the fourth point on the following day. This discontinuity represents a change of approximately 2.5×10^{-3} in., which represents an 8% change of operating tip clearance for the nominal value of 0.030 in., and it is attributable to a change in ambient temperature of approximately 28 ºF. It is important to note here that there is no measureable change of performance parameters at this speed and for this loading condition (away from the stall point at part-speed) due to this small measured tip clearance change, whereas a high loading point on the 100% corrected speedline may be more likely to show a measurable performance change (see Smith et al. (2015a)). Third, the 80% and 68% speed curves in Figure 3.2 show less relationship between measured tip clearance and loading condition (compared to 100%, e.g.) as the temperature rise through the compressor is significantly reduced in this part-speed operating regime. Thus, a majority of the observed decrease of tip clearance with loading conditions in the 68% corrected speed range is due to a decrease in ambient temperature that occurred in the evening.

Similar measurements are presented for the two larger tip clearance configurations, TC2 and TC3 in Figure 3.3 and Figure 3.4. As with the TC1 results in Figure 3.2, these larger tip clearance measurements were also collected in succession, but without the discontinuity in the 80% speedline discussed for TC1. Although the mean weather conditions were extremely similar between measurements collected for the three different tip clearances, the TC2 and TC3 data collection processes began at a different time of day than TC1. As a result, a comparison of the results in Figure 3.3 and Figure 3.4 show a very similar trend which differs slightly from the observed trends for TC1. In particular, the 100% speedline data for TC2 and TC3 began in the early morning hours prior to sunrise and, therefore, the high-loading, low flow rate operating points which showed the highest tip clearance values for TC1 display a less discernable trend as the highest static temperature rise conditions are affected slightly by the slow temporal variation of temperature through the day.

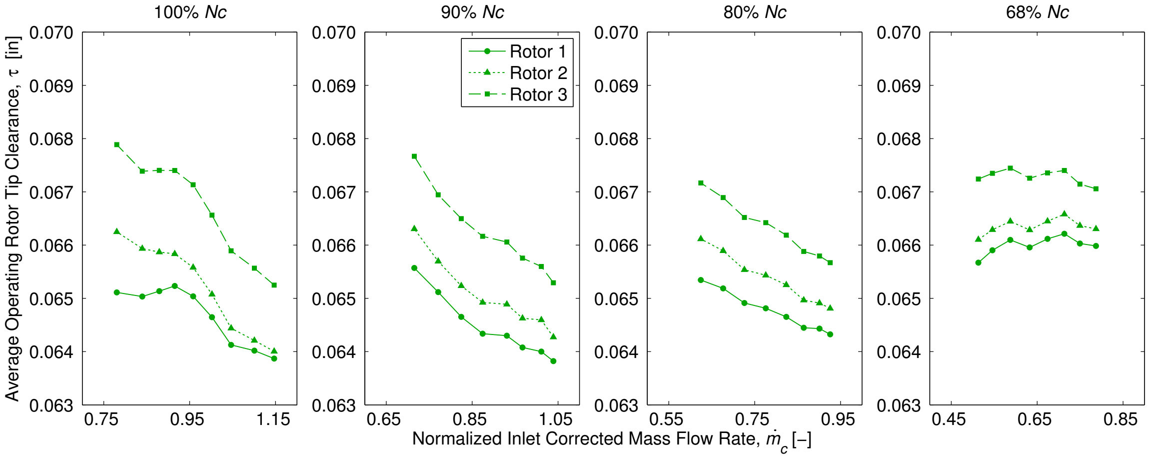

Figure 3.3: Operating tip clearances measured using capacitance probes for TC2.

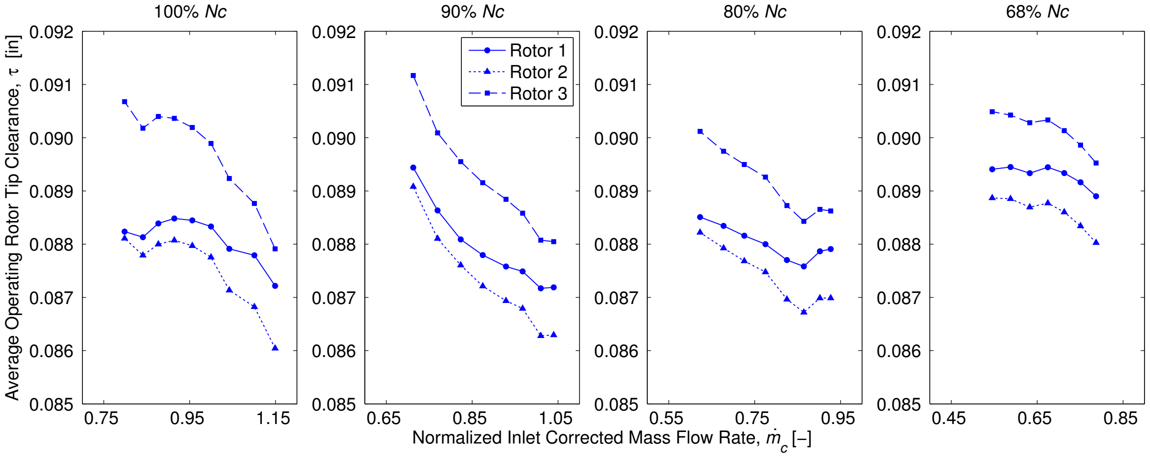

Figure 3.4: Operating tip clearances measured using capacitance probes for TC3.

The operating tip clearance measurements in Figure 3.2, Figure 3.3, and Figure 3.4 are a crucial component of this overall measurement campaign. In particular, these results have shown the potential extent to which even a small variation of ambient temperature can impact the tip clearance height. Furthermore, it is entirely insufficient to report the design intent tip clearance heights, as in Table 2.2, as a result of the potential variations in clearance height between operating conditions alone. For absolute consistency, these measured operating tip clearance values are used throughout the remainder of the document whenever clearance values at a specific operating condition are required.

Additional research summarized by Smith et al. (2015a) further highlights the importance of measuring tip clearance when performing detailed performance measurements. In light of the results shown in Figure 3.2, it should be noted here that the 28 ºF envelope shown for the 80% speedline of TC1 represents the largest discrepancy of temperatures for all points shown in the compressor map of Figure 3.1. More specifically, the 100% speedline data points for all tip clearances were all collected for compressor inlet temperatures within a 19 ºF envelope to ensure the best possible comparison of measurements and avoid the discrepancies outlined by Smith et al. (2015a).

3.1.3. Stall Margin

Using Equation (3.2), the stall margin has been calculated for each of the primary identified points on the 100% corrected speedline. These results, Figure 3.5, are presented with the average measured tip clearance on the abscissa, as described in Section 3.1.2. In Figure 3.5, the Rotor 2 chord has been selected to normalize the clearance values due to the relationship between stall and blade boundary layer separation. Thus, stalling trends typically correlate to τ/c, whereas efficiency correlates to τ/H (Wisler, 1998). The chord changes slightly through the machine for the three rotors, but the Rotor 2 chord is a representative average of the three rotor rows (see Table 2.1).

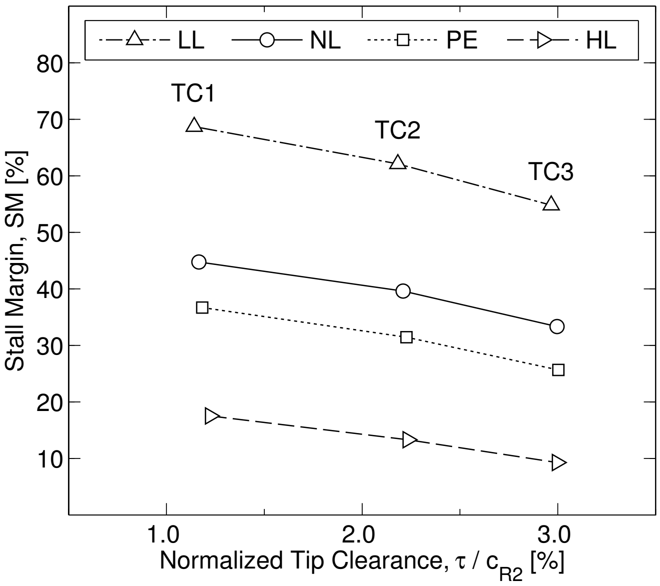

Figure 3.5: Stall margin and stalling flow coefficient effects with tip clearance height for specified loading conditions on the 100% corrected speedline.

Based on the results in Figure 3.5, the stall margin follows a slight non-linear trend with increasing tip clearance for each of the four chosen loading conditions: the decrease of stall margin is more significant moving from TC2 to TC3 than from TC1 to TC2 at the same corrected mass flow rate. This difference increases more noticeably at higher flow rates (lower loading conditions) than at the lower flow rates (higher loading conditions). This observed trend also exists for other definitions of stall margin (i.e., based solely on corrected mass flow rates or based on the total pressure ratios in Equation (3.1)).

Previous studies of tip clearance effects on overall compressor performance have identified the loss of operability range using a percent loss of flow coefficient instead of stall margin (Wisler, 1985b; McDougall et al., 1990), for which the flow coefficient is defined by the ratio of the axial flow velocity, V_x, to the rotor tip speed, U_t:

$$\Phi = \frac{V_x}{U_t}. \tag{3.4}$$

The same quantities can be compared with these data, using a percent difference of the flow coefficient at the stall point as a percent difference from the baseline tip clearance (TC1):

$$\Delta\Phi_{\text{stall}} = \frac{\Phi_{\text{stall}} - \Phi_{\text{stall,TC1}}}{\Phi_{\text{stall,TC1}}} \times 100\%\,. \tag{3.5}$$

The results using this equation are presented in Figure 3.6 along with a comparison of the results from Wisler and McDougall. The smallest clearance studied by McDougall (0.5% chord) is not shown here because it is well outside the range of clearances for the present study. As before, the clearance heights for the present study in Figure 3.6 are evaluated using measured operating tip clearance heights normalized by Rotor 2 chord.

Wisler introduces the concept of a “clearance derivative” for stall margin, which evaluates the stall margin penalty incurred for a one percent change in tip clearance height [24]:

$$\delta = \frac{\Delta\phi_{\text{stall}}}{\Delta(\tau/c)}. \tag{3.6}$$

These clearance derivatives for stall margin have been calculated for the present study and the canonical studies, and these values are indicated in Figure 3.6. The derivatives calculated from Wisler (1985b) and McDougall (1990) are both larger than the results from the present study. Specifically, McDougall shows a clearance derivative for stall margin which is nearly 50% larger than the present study for nearly the same clearance-to-chord values (TC1 to TC3). Also indicated in Figure 3.5, the derivative for the change from TC2 to TC3 is more than 1.5 times greater than the change from TC1 to TC2.

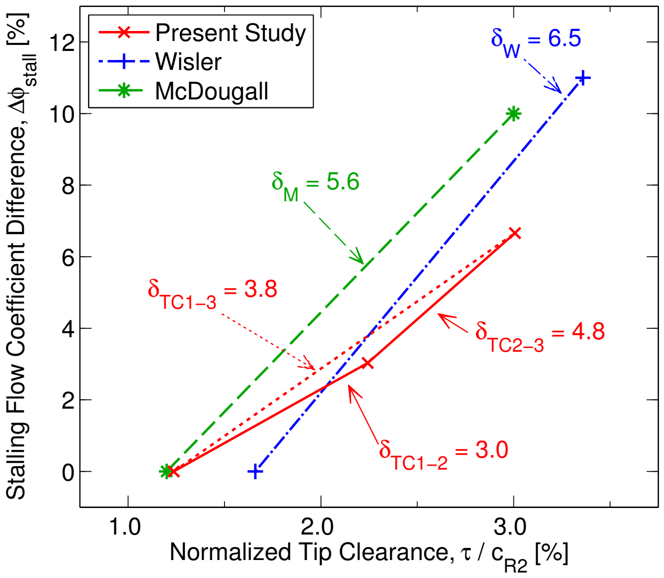

Figure 3.6: Trends of flow range change with rotor tip clearance.

Despite the differences shown in Figure 3.6, the clearance derivatives for stall margin are nearly all in agreement with the published value of 3-6% for 1% increase of clearance-to-chord by Wisler (1998). There are several important differences between these studies which may contribute to the spread of data in Figure 3.6. Of note, the rotor blade sections for the present study (DCA) differ from McDougall (1990) (C4) and Wisler (1985b) (GE E^3). Furthermore, the aspect ratio for the rotors in this study is on the order of 0.7, compared with 1.4 for McDougall and 1.2 for Wisler. Studies analyzing the effects of low aspect ratio blades on compressor performance have shown that lower aspect ratio blades are more resistant to stall as the a more significant portion of the blade span is influenced by three-dimensional endwall flows (Wennerstrom, 1989). Thus, these data supplement the existing literature to provide stall margin clearance derivatives for very low aspect ratio blading with specific applicability to rear stages of modern high pressure compressors.

Similar conclusions can also be related to the solidity of the machines presented in Figure 3.6. The solidity of the rotors in Wisler’s (1985b) study are reported to be 1.16, whereas the McDougall (1990) rotor and the rotors in the present study have solidities on the order of 1.3 at mid-span (the present study is slightly larger than McDougall). The increased solidity represents decreased loading for each blade, increasing the stall resistance compared to the results from Wisler.

3.1.4. Total-to-Static Pressure Rise Characteristics

As an alternative to the total pressure ratio as a metric for achieved pressure rise, some authors (Hutton, 1956; Wisler, 1985b; McDougall, 1990) have discussed the total-to-static pressure rise coefficient, defined as:

$$\Psi = \frac{P_9 - P_{o1}}{\frac{1}{2}\rho U_t^2}. \tag{3.7}$$

Figure 3.7 shows this total-to-static pressure rise coefficient, presented as a function of the flow coefficient, Φ, for each of the three tip clearance configurations at all four corrected operating speeds. As with Figure 3.1, the point at the lowest inlet mass flow rate for each of the curves represents the stall point of the compressor. The results in Figure 3.7 show the expected result of decreasing total-to-static pressure rise coefficient as the tip clearance is increased. Another observation from Figure 3.7 is for the 100% corrected speedline of TC3, which has a location in the characteristic at a flow coefficient of approximately 0.5 where the slope of the curve changes sharply to become less negative (approaching zero). This location of the characteristic also corresponds to a region of the curve which has a slight positive slope in the speedline from Figure 3.1. This is the only speedline from the 12 presented lines which features a total pressure rise decrease prior to the stall point, which may explain the unique feature of this characteristic in Figure 3.7. Also in this figure, the results for different speeds with a given tip clearance configuration do not collapse to one single line, alluding to the significance of compressibility effects in the Purdue three-stage compressor.

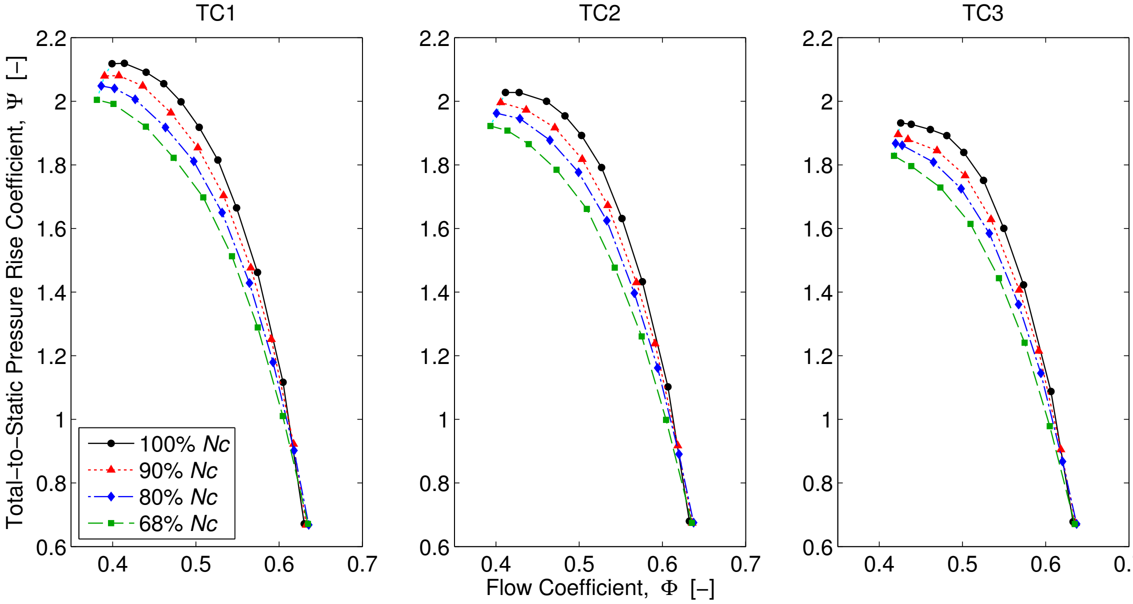

Figure 3.7: Total-to-static pressure rise characteristics for three tip clearance configurations.

To evaluate the relationship between peak pressure rise capability and rotor tip clearance, the pressure rise coefficient defined in Equation (3.8) is compared. Specifically, Figure 3.8 presents this parameter using a percent difference of the peak pressure rise for a given tip clearance with respect to peak pressure rise coefficient for the smallest clearance (TC1 for the data from the present study),

$$\Delta\Psi = \frac{\Psi - \Psi_{\mathrm{TC1}}}{\Psi_{\mathrm{TC1}}} \times 100\%\,, \tag{3.8}$$

presented as a function of average measured tip clearance. A study by Koch (1981) comparing data collected in the same LSRC utilized by Wisler (1985b) showed that peak pressure rise can be correlated with clearance-to-staggered-spacing, τ/s, to yield results independent of aspect ratio. As a result, this length scale has been implemented to normalize the clearance values in Figure 3.8. Here also, the Rotor 2 staggered spacing is used as a representative average of the three rotor rows in the machine.

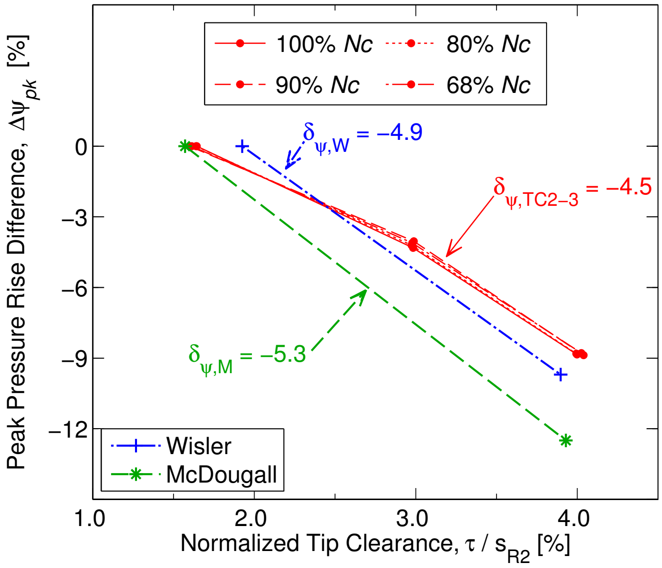

Figure 3.8: Peak total-to-static pressure rise coefficient as a function of tip clearance height.

Figure 3.8 shows that the decrease of peak pressure rise for the results from the present study is not consistent between the two clearance ranges – there is a greater decrease of peak pressure rise from TC2 to TC3 than from TC1 to TC2. This observation is important because it further highlights a trend which can only be observed with three or more tip clearance heights and may be unknown for a study with only two clearance heights. However, Figure 3.8 does show that the reduction of peak pressure rise is independent of rotational speed, as shown by the collapsed results for the four speeds.

Here, a clearance derivative for peak pressure rise difference is defined using the clearance-to-staggered-spacing ratio:

$$\delta_{\psi} = \frac{\Delta\psi_{pk}}{\Delta(\tau/s)}. \tag{3.9}$$

A comparison of these clearance derivative results for peak pressure rise between the present study with the canonical results show good agreement between Wisler (1985b) and the change from TC2 to TC3. The results from McDougall (1990), however, show a clearance derivative magnitude which is slightly larger than the other data sets presented.

3.1.5. Isentropic Efficiency

As explained earlier, the isentropic efficiency of the compressor has been evaluated using the formal definition from Equation (2.3). The required stagnation enthalpies for this equation are calculated using the thermodynamic equation program REFPROP (Lemmon et al., 2013) through the use of measured conditions (stagnation temperature, stagnation pressure, static pressure, and relative humidity) at axial positions 1 and 9 – in agreement with the measurement planes used to define total pressure ratio in

Equation (3.1). Using Equation (2.3), the isentropic compressor efficiency has been calculated for each of the measurement points shown in the overall compressor total pressure ratio map of Figure 3.1 (neglecting the stall points). These efficiencies, shown in Figure 3.9, are presented for each of the four corrected rotational speeds as a function of the normalized inlet corrected mass flow rate.

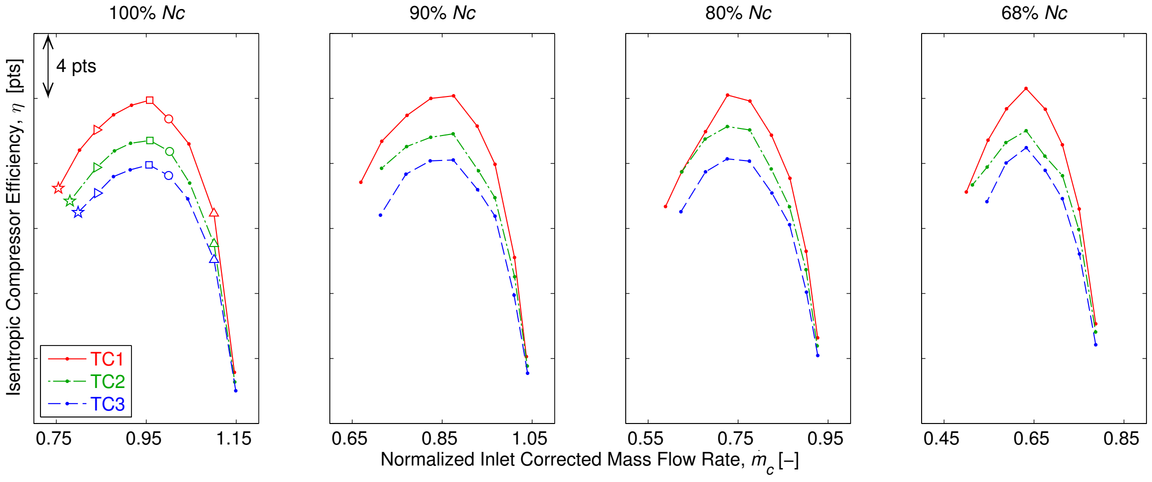

Figure 3.9: Overall isentropic compressor efficiency at four corrected rotational speeds.

The uncertainty of the efficiency values in Figure 3.9 can be influenced by uncertainty contributions from measured pressures, temperatures, and humidity. Great care has been taken to ensure that the respective uncertainty for each of these measured parameters is as small as possible (see Section 2.2). With this in mind, the efficiency uncertainty has been carefully evaluated using the *T*-*s* region technique implemented by Lou et al. (2013). The uncertainty values for the 100% corrected speedlines in Figure 3.9 are on the order of 5 points across the entire flow range for all tip clearances. Similarly, the 90% corrected speedline data have efficiency uncertainties of approximately 6 points across the entire flow range. At the lower speeds of 80% and 68% corrected speed, however, the reduced pressure rise is associated with a reduced temperature rise (although still measurable and appreciable), especially at high flow rate conditions. As a result, the uncertainties for the 80% corrected speedline data vary from approximately 6 points at low flow, high loading conditions to as much as ten points for the high flow, low loading conditions. At the 68% speed conditions, the uncertainties vary from approximately 8 points at low flow conditions to more than 15 points at high flow conditions.

These relatively large uncertainty values are primarily due to the propagation of measurement uncertainty when calculating enthalpies, especially h_{09s}, as explained by Lou et al. (2013). Indeed, the data for this project also show that h_{09s} is the largest component of the efficiency uncertainty. Despite the large measurement uncertainties, however, the repeatability of the efficiencies shown in Figure 3.9 is typically on the order of 0.5 points – an order of magnitude improvement over the calculated uncertainty.

As an additional consideration, measurement variability due to machining tolerances, blade row interactions, and more, can also influence calculated performance parameters such as isentropic efficiency. The measurement locations for data presented here were carefully selected to avoid these effects as much as possible based on prior knowledge of the machine. Nonetheless, a vane wake variability study characterizing the circumferential variation in the wakes shed from a particular stator row was recently conducted by Methel et al. (2015). The results from this study, combined with a similar investigation of passage-to-passage variations in total temperature, have shown that the circumferential variation in the flow field is small (on the order of measurement uncertainty) yet repeatable. Thus, efficiencies calculated by combining pressure and temperature measurements from different sectors of the machine can be influenced by this variation. The only way to avoid this error in the absolute value of efficiency would be to use a measurement rake with combined total pressure and total temperature sensors. However, the measured changes in efficiency between different configurations are valid and meaningful.

Beginning with the data presented in Figure 3.10, the compressor efficiency is separately considered for each of the three tip clearance configurations at the four operating conditions of primary interest on the 100% corrected speedline: LL, NL, PE, and HL. Figure 3.10 shows the expected result of decreased compressor efficiency with increased rotor tip clearance, as discussed in earlier studies for isolated rotors and multistage machines. Similar to the stall margin analysis, a clearance derivative can also be defined for the change in efficiency associated with a one percent increase of clearance-to-height:

$$\delta_\eta = \frac{\Delta\eta}{\Delta(\tau/H)}. \tag{3.10}$$

Figure 3.10 shows small, but discernable changes of clearance derivatives when comparing different clearance ranges in the present study. The most significant differences are observed at the LL operating condition (-1.2 from TC1 to TC2 versus -0.8 from TC2 to TC3), but the other three loading conditions shown here yield a δ_η standard deviation of 0.1 with respect to the mean value. For these results, a representative mean clearance derivative for efficiency based on the data in Figure 3.10 is on the order of -1.3. There is also a slight non-linear trend for the efficiencies in Figure 3.10, aligning with other results from this study, which was also observed by Ruden (1944) and Tschirner et al. (2006), and more recently in a computational study by Sakulkaew et al. (2013).

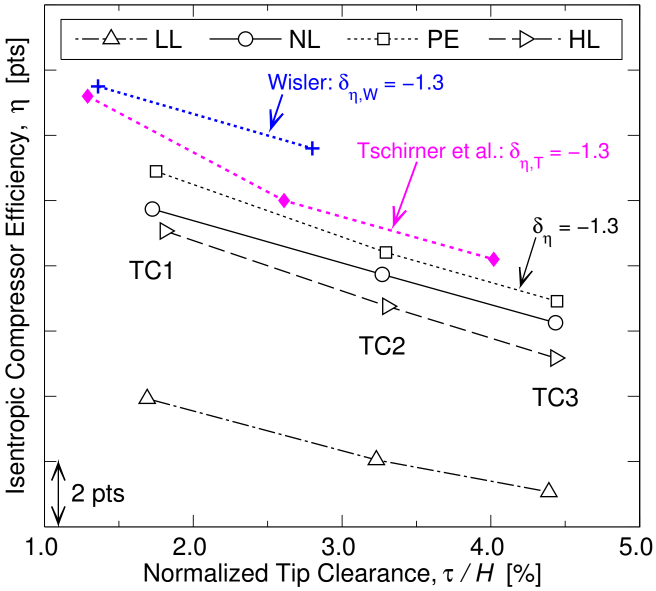

Figure 3.10: Isentropic compressor efficiency for specified 100% $N_c$speedline points as a function of tip clearance height.

Figure 3.10 compares results measured from the present study with efficiency changes measured by Wisler (1985b) and a similar four-stage low-speed compressor with repeating stages used by Tschirner et al. (2006). In this figure, the tip clearances for the comparison studies represent the values reported by the authors (as-built values are provided by Tschirner et al.), and the low-speed operation of the facilities (1000 rpm or less) suggests a minimal change of the clearances from the “cold” static measurements.

Wisler’s canonical observation showed a peak efficiency decrease of 1.5 points with increased tip clearance. However, the author also showed the peak efficiency moved to a different flow coefficient (that was not the case for the present study – see Figure

3.9). Thus, if a comparison is made between the peak efficiency point at the small clearance and the same flow coefficient at a larger clearance for Wisler's results, a larger efficiency change exists, leading to an efficiency clearance derivative of -1.3 – identical to the value observed for many of the segments for the present study in Figure 3.10. A similar comparison for the peak efficiency point between the two larger clearance heights tested by Tschirner et al. also leads to an efficiency clearance derivative of -1.3 points for a 1% change of clearance-to-height. The results from Tschirner et al. show a larger efficiency clearance derivative magnitude (beyond -2) between their TC1 and TC2 configurations, but this effect may be attributed to cantilevered stator hub clearances which were not present for Wisler's tests or the present study. These results agree well with rules-of-thumb suggested by Freeman (1985) and Wisler (1998) of approximately 1.2 to 2 efficiency points lost per 1% increase of tip clearance height based on linear fits of data collected from several engine tests and research compressor studies.

3.1.6. Stator 3 Seal Leakage Flow Measurements

To adequately define boundary conditions for computational models, the leakage flow paths for the compressor have been carefully evaluated. At the inlet of the compressor, the air paths are all sealed, but a potential leakage path exists under the Stator 3 labyrinth (knife) seals to atmospheric pressure. Ball (2013) considered these leakage flow paths and the related knife seal geometry for computational models. Ball determined that whether the Stator 3 seal flow was allowed to exit to ambient pressure, or if the respective flow paths were plugged, the effect on overall compressor pressure rise was negligible. However, a measureable change of overall compressor efficiency was observed, likely due to a localized heating of the rear bearing and other components at the rear of the compressor in the absence of the Stator 3 leakage flow path.

For this study, the leakage pathways remained open to the atmosphere, but the air was connected to a manifold through four tubes at the rear of the compressor, Figure 3.11, to capture the leakage flow. These tubes delivered the leakage flow to a Wyatt Engineering orifice plate with a discharge coefficient of 0.6042 and a diameter ratio of 2.294 (as provided by the manufacturer). The pressure drop across the orifice plate was measured by a Rosemount 3051C differential pressure transmitter with a calibrated range of 0-13 inH_2O. The representative overall relative uncertainty of mass flow rate measurement for this orifice plate system is less than 2.4%.

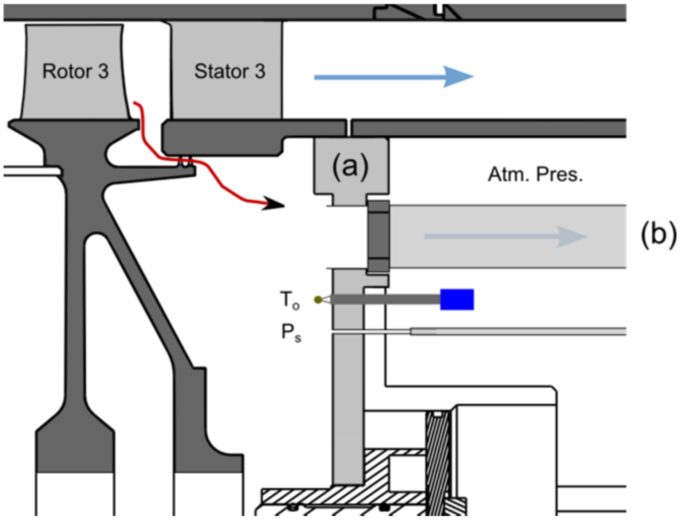

Figure 3.11: Stator 3 seal leakage flow path and manifold tubes from (a) the rear bearing plate to (b) an orifice plate run (Brossman, 2012).

The measured Stator 3 seal leakage mass flow rates for each of the measured points in Figure 3.1 (seal leakage flow rate data for the stall point were not collected) are shown in Figure 3.12, normalized as a percentage of the inlet corrected mass flow rate:

$$\dot{m}_{\mathrm{LN}} = \frac{\dot{m}_{\mathrm{leak},c}}{\dot{m}_c} \times 100\%\,, \tag{3.11}$$

for which the measured leakage mass flow rate is first corrected using the inlet conditions of the compressor using Equation (2.2) to yield $\dot{m}_{\mathrm{leak},c}$. The increase of leakage flow rate at lower inlet mass flow rate conditions in Figure 3.12 suggests that the leakage mass flow rate is affected by the pressure rise through the compressor (increased loading and pressure rise at low flow rates leads to increased leakage flow rate as the pressure differential with respect to ambient pressure increases). However, the curves in Figure 3.12 are independent of tip clearance configuration, showing that the leakage flow rate is influenced more by the flow rate through the compressor than the overall pressure rise through the machine (in which case, the leakage flow rates would change more significantly for different tip clearance configurations). The one potential exception to this is the final two to three points on the 100% speedline for TC3, which appear to roll over (unlike the two smaller tip clearances, TC1 and TC2). This observation aligns with the previous discussions about total pressure ratio and total-to-static pressure rise characteristics.

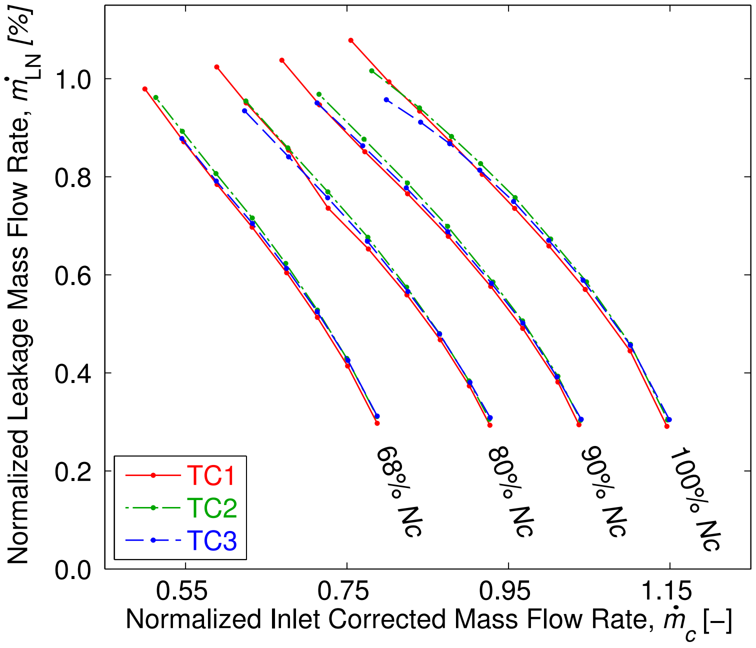

Figure 3.12: Stator 3 seal leakage mass flow rate as a percentage of inlet corrected mass flow rate for each of the traversed data points in Figure 3.1.

3.1.7. Casing Outer Surface Temperature Measurements

Often, turbomachinery system analyses assume that the machine operates adiabatically. This assumption is based on the difference in orders of magnitude between the work imparted to the fluid by the rotor and the heat flux from the machine. However, an analysis of the total temperature profiles through the compressor (see Section 3.3.2) shows an increase of the fluid total temperature in the tip region near the compressor casing, especially for the front stages. In this case, the more significant temperature of the aft section of the compressor conducts through the aluminum casing and influences the flow at the front of the machine. As a result, alternative boundary condition techniques may be better suited for computational analyses, such as the isothermal wall boundary condition discussed by Bruna and Turner (2013) or a conjugate heat transfer analysis.

Several surface-mounted T-type thermocouples were installed on the outside of the compressor casing to isolate these temperature measurements. One thermocouple was installed over each of the seven blade rows at the circumferential position noted in Figure 2.9. A separate analysis of the circumferential uniformity of the casing temperatures showed the circumferential variations are less than 1.8 ºR. Prior to collecting data at each operating point, an additional surface-mounted K-type thermocouple installed over Rotor 3 was allowed to reach a steady operating condition to prevent any transient temperature effects in the collected data.

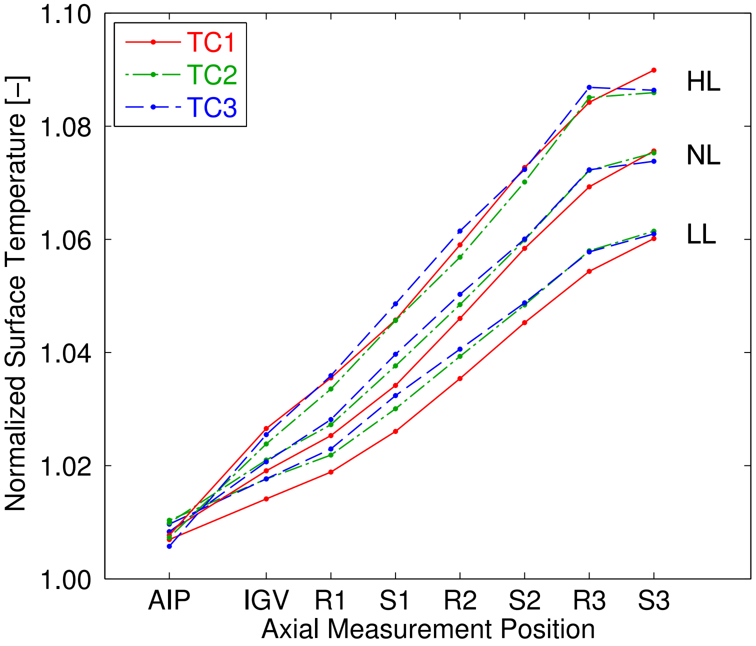

Figure 3.13: Normalized surface temperatures for three loading conditions on the 100% corrected speedline.

Beginning with Figure 3.13, the casing outer diameter surface temperature trends are shown at three selected loading conditions (LL, NL, and HL) for all three tip clearance configurations. These temperatures are presented as a normalized temperature ratio with respect to the area-averaged temperature measured by the total temperature rakes at the AIP (plane 0 in Figure 2.6). As the work imparted to the fluid by the rotor increases with loading condition, the temperature of the outer compressor casing also increases through the compressor. Figure 3.14 shows the same normalized temperature ratio, but for the final "near-stall" traversed operating point, at each of the four speeds and all three tip clearance configurations. Figure 3.13 and Figure 3.14 both show that the TC1 data continue to experience temperature rise, even at the Stator 3 measurement position, whereas the larger tip clearance configurations (TC2 and TC3) appear to level off more significantly comparing the surface temperatures over Rotor 3 and Stator 3.

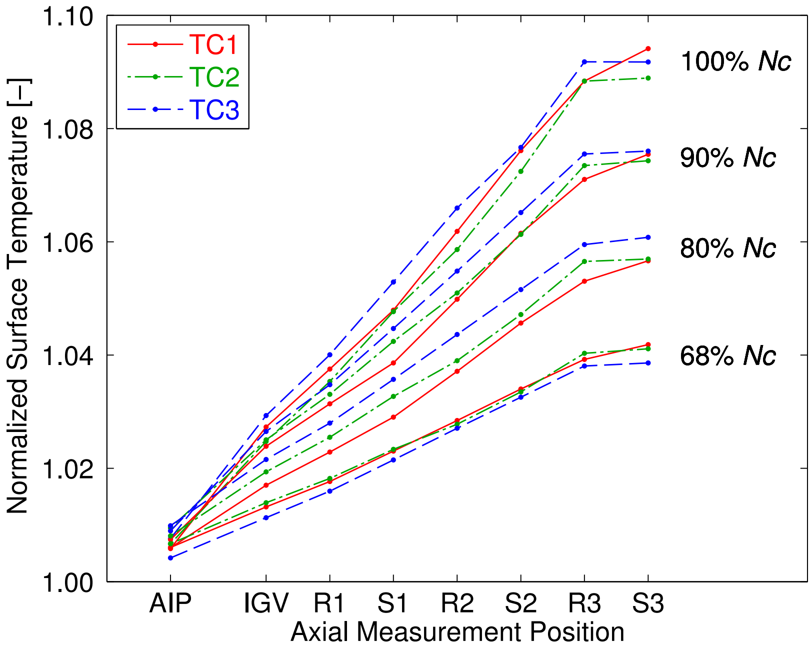

Figure 3.14: Normalized surface temperatures for the final "near-stall" traversed operating point at all four operating speeds.

3.2. Stage Performance Characteristics

3.2.1. Total-to-Total Pressure Rise Characteristics

In addition to the overall performance, the stage-by-stage compressor performance has also been considered for this study. The stage total pressure ratios are shown in Figure 3.15 as a function of the stage inlet corrected mass flow rate. For this figure, the stage inlet corrected mass flow rate uses the same equation for the inlet corrected mass flow rate, Equation (2.2), but the values for stagnation density and stagnation speed of sound are selected to represent the measured parameters at the inlet to the stage. Stage 1 is defined for axial positions 1 to 4, Stage 2 is defined for axial positions 4 to 6, and Stage 3 is defined for axial positions 6 to 9. By these definitions, the combination all three stages results in the overall total pressure ratios from Figure 3.1.

Figure 3.15 allows several important observations regarding the performance of the three-stage compressor, particularly relating to off-design performance and stage matching. Of note, each of the three stages has distinctly different characteristic shapes at all speeds and tip clearance configurations. The Stage 1 characteristics show the total pressure rise turns to a positive slope near the top of the curve as the compressor approaches stall. The Stage 2 curves all show a position where the slope of the curve changes sharply. This location appears at the peak efficiency point of the compressor for each curve – these characteristics could be approximated by two linear regions. Finally, the Stage 3 curves have a curvature which more closely resembles Stage 1 than Stage 2, but with less total pressure rise.

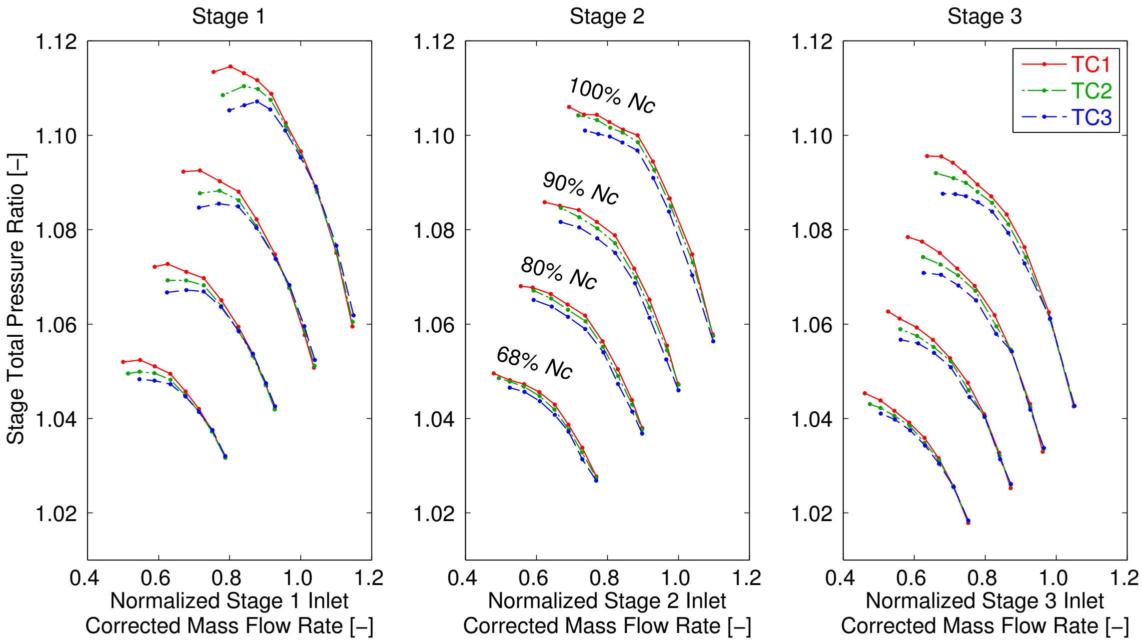

Figure 3.15: Stage total-to-total pressure rise characteristics for the traversed map points.

For Stage 1 and Stage 3, the operating points closest to the stall point (the actual stall points are not shown in Figure 3.15) show a noticeable and consistent decrease of total pressure rise with increased tip clearance height. A similar observation may be made for the 100% corrected speedline of Stage 2, but the part-speed operating conditions (90%, 80% *Nc*, and 68% *Nc*) for Stage 2 show a more consistent offset of results across the entire speedline. Figure 3.15 also shows that the individual stage total pressure rise may actually increase by a small amount for the larger tip clearance configurations (TC2 and TC3) at the highest flow rate position on the 100% speedline for Stage 1. An analysis of the individual rake pressure measurements which combine to create the area-averaged total pressure ratios shown in Figure 3.15 reveals that the lower 60% annulus height performs at a slightly higher total pressure exiting Stator 1 – at the expense of a more significant endwall blockage and total pressure loss in the tip region. Although the magnitudes of these differences for Stage 1 are greater than the repeatability of the measurements, they are on the order of the uncertainty of the measurements, so no definitive conclusions can be attributed to the observations.

3.2.2. Total-to-Static Pressure Rise Characteristics

In addition to the total-to-total pressure rise characteristics, the total-to-static pressure rise characteristics are also considered here. These data, Figure 3.16, assess the traversed measurement points from the overall total pressure ratio map for 100% corrected speed (the stall point is not included). The shape of these curves shows that Stage 1 is likely the limiting stage for the machine as its characteristic rolls over more than the other stages at low flow rates. Also, Stage 2 does not show the same dependence of pressure rise coefficient to tip clearance height that is observed for Stage 1 and Stage 3. In fact, the TC1 and TC2 results for Stage 2 in Figure 3.16 are relatively indistinguishable.

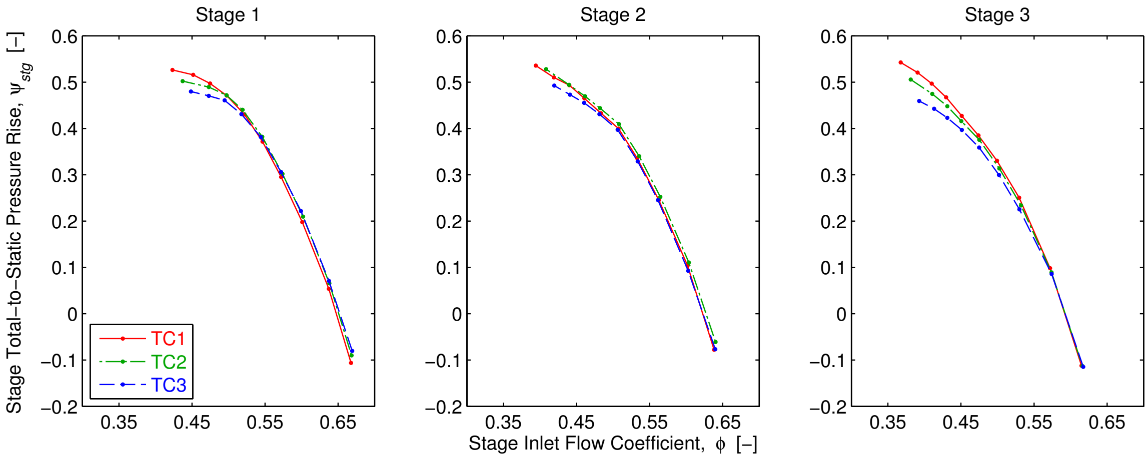

Figure 3.16: Stage total-to-static pressure rise characteristics at 100% corrected speed.

These stage pressure rise characteristics bring about a consideration of stage matching effects in the compressor. It is expected that the Purdue three-stage axial compressor is well-matched at the design speed with the design tip clearance configuration (TC1). Comparing the TC1 performance with TC2 throughout Figure 3.16, the trends of the curves are very similar – many of the characteristics overlap for significant portions of the flow range, especially for Stage 2. This suggests that the stage matching of the compressor may not be significantly altered by a change from 1.5% to 3.0% rotor tip clearance height. However, more distinct differences exist for the largest tip clearance configuration (TC3).

3.2.3. Stage Efficiency

These stage performance observations are further investigated by rotor and stage efficiency trends with tip clearance at the NL and HL operating conditions in Figure 3.17. At the NL operating condition, Rotor 1 has the highest efficiency of the three rotors regardless of clearance height, but the Stage 1 efficiency is nearly insensitive to clearance changes as the Stator 1 performance improves with increased tip clearance height. This observation agrees with a decreasing trend of calculated Stator 1 pressure loss coefficient at NL by approximately 8.7% from TC1 to TC3. Also in Figure 3.17, the large efficiency difference between the Rotor 3 and Stage 3 curves suggests that Stator 3 performs poorly at NL, which is supported by the presence of large recirculating flow regions in flow visualization photographs taken for Stator 3 at NL (Smith, 2015). In these photos, the separation region for Stator 3 NL covers more than twice the suction surface area compared to the Stator 1 and Stator 2 separation regions.

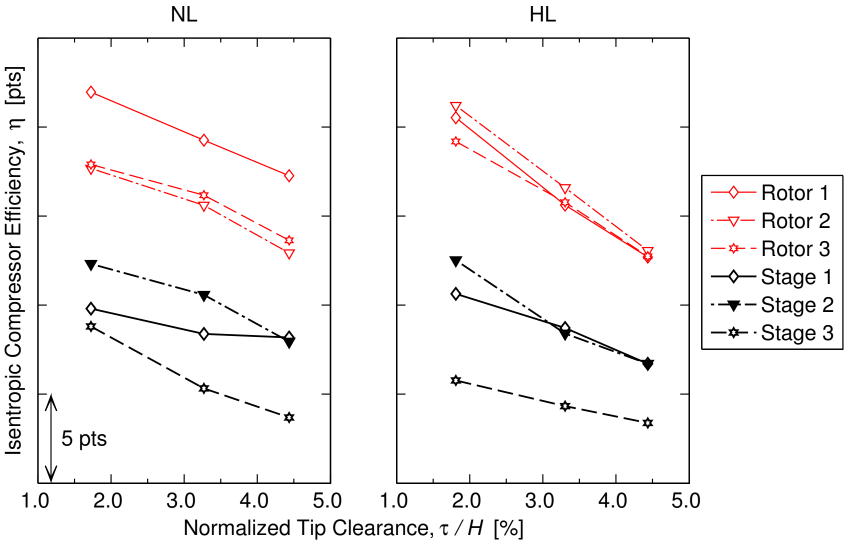

Figure 3.17: Comparison of rotor and stage efficiencies differences with tip clearance height at NL and HL.

At the HL condition in Figure 3.17, the three rotor rows show more similar magnitudes of isentropic efficiency as the rotor tip clearance height increases. For all three stages, the stage efficiencies decrease at a lower rate than the rotor efficiencies, suggesting the stator performance may be improving as the surface flow topologies change and the separated flow regions on the suction surface decrease (Smith, 2015). However, the most significant effect is observed in the change of the Stage 2 efficiency curve. Unlike the NL condition where the Stage 2 curve mirrors the Rotor 2 curve across the tip clearance range, the HL condition shows a distinct change of the clearance derivative for efficiency in Stage 2, δ_η, which is not observed in Rotor 2. This observation is further supported by a comparison of the total pressure loss coefficient for Stator 2 at HL, which shows a decrease of 6.2% from TC1 to TC2 but only an additional 2.4% decrease from TC2 to TC3. Ultimately, the results shown in Figure 3.17 motivate the importance of comparing stage performance in a multistage compressor without repeating stages as stage matching effects become increasingly important.

3.3. Inter-Stage Flow Measurements

In addition to the performance metrics discussed thus far, the inter-stage total pressure and total temperature measurements collected from the seven-element rakes provide valuable information regarding the radial distributions of measured flow properties. A direct comparison of these radial distributions for each of the three tip clearance configurations may be affected by the overall pressure rise (or temperature rise) through the compressor, therefore making it difficult to draw meaningful conclusions about the comparisons, especially near the rear of the compressor where discrepancies between tip clearance configurations may be large. As a result, these spanwise measurements must be normalized by some chosen value to accommodate comparison of the radial total pressure and total temperature profile shapes. The five selected loading conditions on the 100% corrected speedline have been chosen for comparison between the three tip clearance configurations.

3.3.1. Total Pressure

To effectively compare pressure profiles through the compressor, the normalized total pressure (NRP_o) is defined to represent the circumferential average at each radial position, normalized by the radial and circumferential area average at the same axial position:

$$\mathrm{NRP}_{o,i} = \frac{P_{o,i,\mathrm{CA}}}{P_{o,i,\mathrm{AA}}}. \tag{3.12}$$

Using this definition, any reductions in pressure rise due to an increase of rotor tip clearance at the same axial measurement plane are avoided, and the radial stagnation pressure profile shapes remain for comparison. Figure 3.18 shows this normalized radial total pressure shape comparison at the LL operating condition for each of the three tip clearances, TC1-TC3, at axial measurement planes 3 through 8 (as denoted by the schematic in Figure 2.6). For reference, the uncertainty of measurements presented in Figure 3.18 is smaller than the symbol size in the figure.

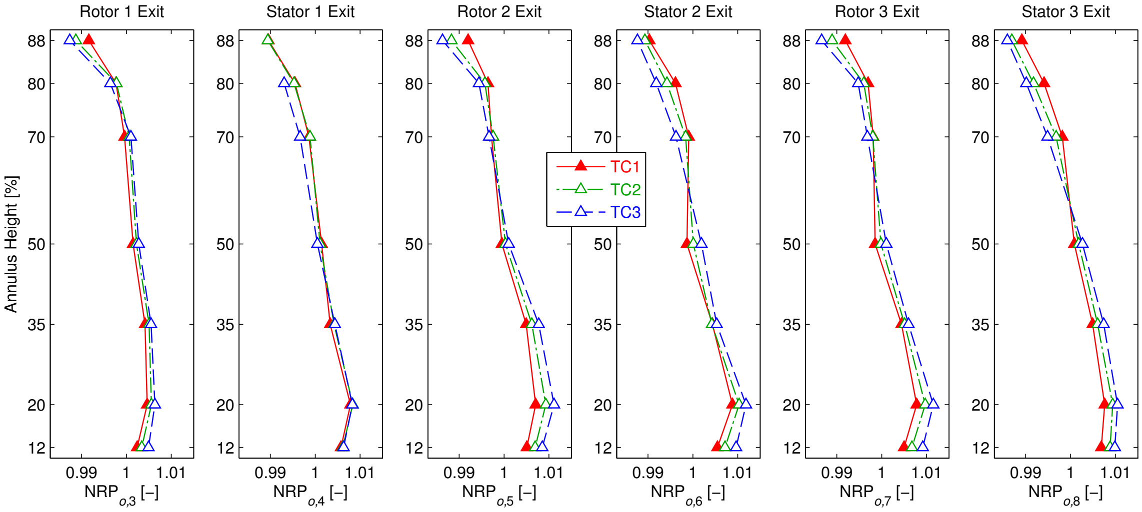

Figure 3.18: Radial total pressure profiles at LL.

As the tip clearance height is increased in Figure 3.18, the portion of the flow affected by the tip leakage flow grows in size. This effect is not significant for the low loading (LL) condition, which is expected from the lack of distinct difference in compressor overall total pressure ratio between tip clearance heights for high flow rate conditions in Figure 3.1. However, this effect becomes more apparent as the loading condition is increased up the speedline to the nominal loading (NL) and peak efficiency (PE) points in Figure 3.19 and Figure 3.20, respectively. In these figures, the increased blockage created by the tip leakage flow disturbance growth redistributes a portion of the flow from the tip region toward the hub region, as distinguished by the reduction of NRP_o at the tip and increase near the hub for all axial measurement positions. Also in these figures, it is possible to distinguish a set of similar profile shapes at the three rotor exit planes (axial positions 3, 5, and 7), which differ from a separate set of similar profiles shapes at the stator exit planes (axial positions 4, 6, and 8).

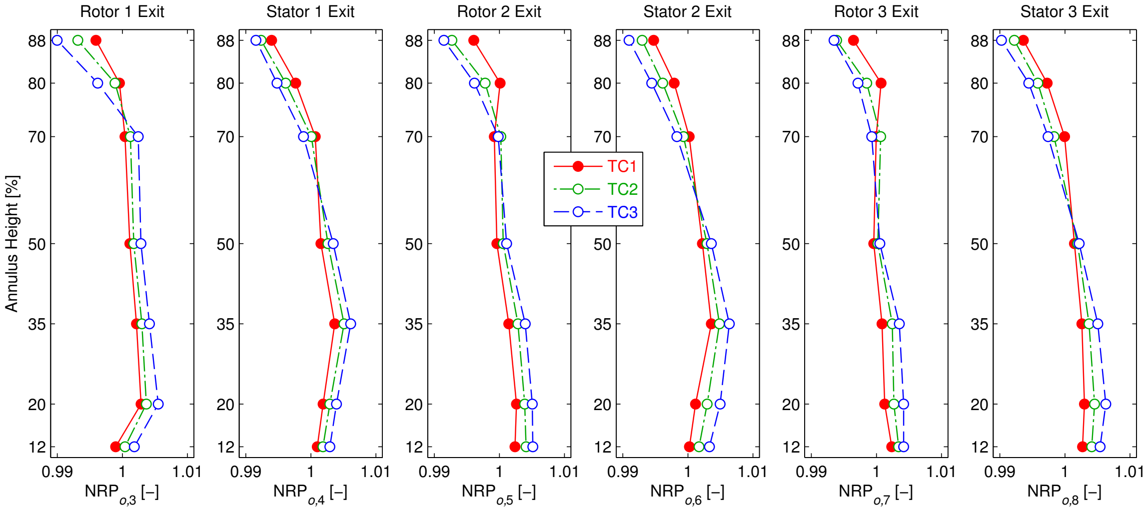

Figure 3.19: Radial total pressure profiles at NL.

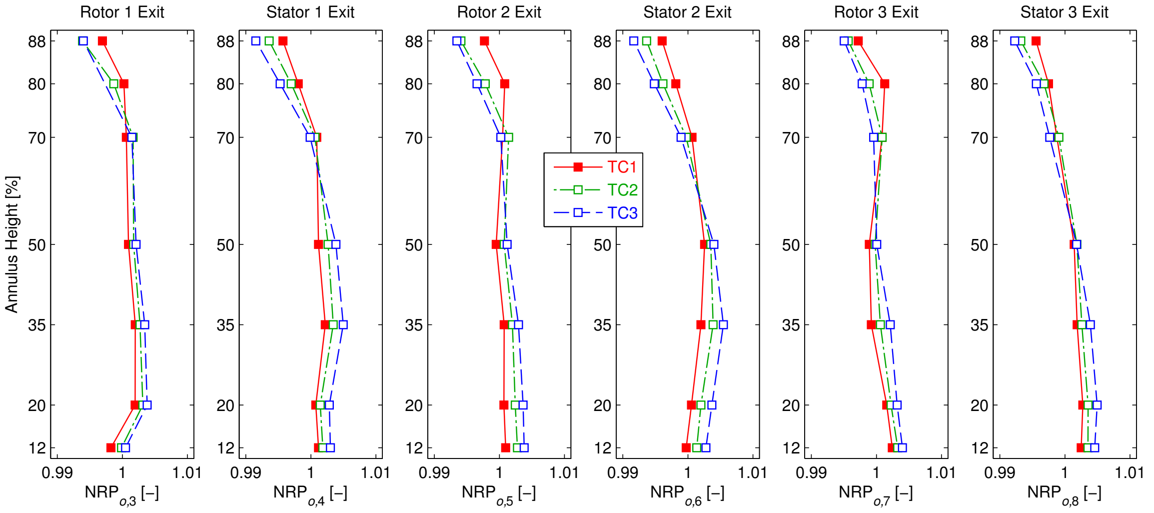

Figure 3.20: Radial total pressure profiles at PE.

As the loading condition is increased further up the speedline toward the stall point, these trends become more distinct. In particular, Figure 3.21 shows the same normalized radial pressure profile shapes at a high loading (HL) condition for the three tip clearance configurations. The same general trends of redistributed flow from the tip toward the hub with increased tip clearance persist in Figure 3.21, but there are more distinguishable characteristics between the axial positions. Of note, the difference between radial pressure profiles for the TC1 and TC3 configurations at Stator 2 Exit are more pronounced than for Stator 1 Exit or Stator 3 Exit. Specifically, a corner separation condition exists at the hub of Stator 2, which is energized by the redistributed flow from the tip region toward the hub to prevent the flow separation tendencies of the vane row. This observation will be further explained with detailed measurements in subsequent sections, and it is supported qualitatively by complementary flow visualization photographs (Smith, 2015).

Also in Figure 3.21, the tip region at Rotor 1 Exit portrays a repositioning of the minimum pressure from 88% span to 80% span as the tip leakage core extends radially downward into the flow path with increased tip clearance. This leaning-over of the radial profile in the tip region for TC2 and TC3 is indicative of a close proximity to the stall point which has not yet been reached for TC1 at the same corrected mass flow rate (see Figure 3.1). However, the same distinguishing characteristic is not present at Rotor 2 Exit or Rotor 3 Exit, suggesting a difference in overall performance for the embedded stages, which ingest the increased blockage from the upstream stage(s), compared to the first stage which is always met with the same clean inlet flow from the IGV.

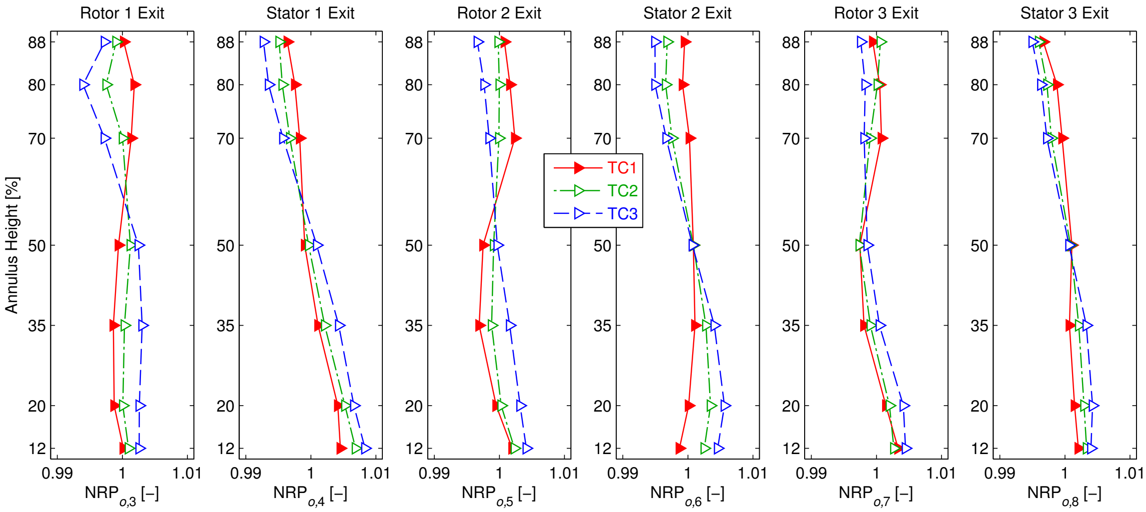

Figure 3.21: Radial total pressure profiles at HL.

As suggested earlier, the HL condition points compared in Figure 3.21 are located at proximities to the stall point which vary with tip clearance. Thus, an additional loading condition is considered which helps to overcome this inherent difference. The near-stall (NS) points denoted by the five-pointed stars in Figure 3.1 are representative of approximately 5% stall margin, as defined by Equation (3.2). By matching stall margin, the data comparison between the three tip clearance configurations should be more appropriate.

This comparison, shown in Figure 3.22, reveals interesting results: the Rotor 1 Exit profile shape for TC1 has leaned over in the same manner as TC2 and TC3; also, the normalized radial pressure profile shapes for the three tip clearance configurations appear to coalesce at Rotor 2 Exit and Rotor 3 Exit. These data at Rotor 2 Exit and Rotor 3 exit show a very slight difference for the TC3 results, but this is explained by the fact that the data for TC3 actually represent a stall margin closer to 4% instead of the desired 5% which was achieved for TC1 and TC2. Therefore, the TC3 data are expected to achieve slightly less pressure near the tip and slightly higher pressure near the hub, as shown in Figure 3.22. Despite this apparent insensitivity of profile shape with respect to clearance size at Rotor 2 Exit and Rotor 3 Exit in Figure 3.22, there is a more noticeable difference at Rotor 1 Exit, and the discrepancy between TC1 and TC3 at Stator 2 Exit is even more significant than in Figure 3.21.

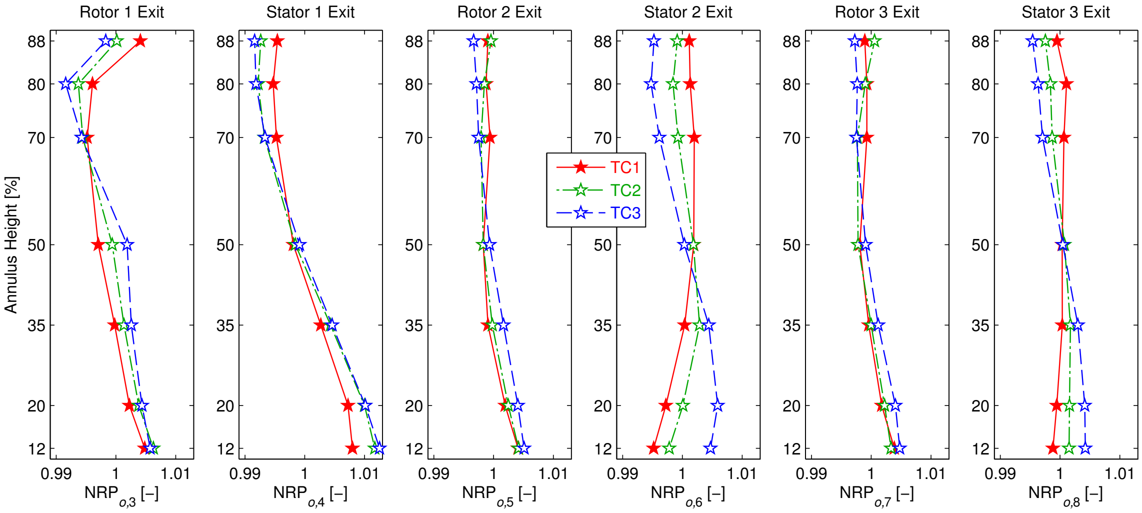

Figure 3.22: Radial total pressure profiles at NS.

3.3.2. Total Temperature

In the same manner as the radial total pressure profiles, the normalized total temperature (NRT_o) represents the circumferential average at each radial position, normalized by the area average (radial and circumferential) at the same axial position:

$$\mathrm{NRT}_{o,i} = \frac{T_{o,i,\mathrm{CA}}}{T_{o,i,\mathrm{AA}}}. \tag{3.13}$$

Figure 3.23 presents this normalized radial temperature distribution for the low loading (LL) condition on the 100% corrected speedline. At this operating point, the similarity of the pressure rise for the three tip clearance configurations leads to a largely insignificant difference between the three cases, with only minor differences downstream of each rotor row. For reference, the uncertainty of measurements presented in these figures is smaller than the symbol size in the figure.

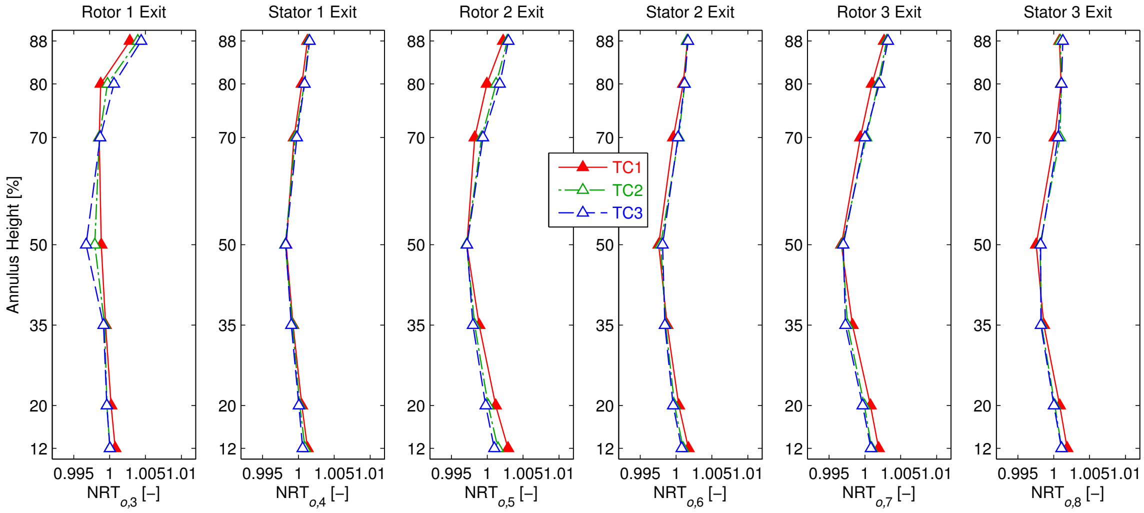

Figure 3.23: Radial total temperature profiles at LL.

As the loading of the compressor is increased, more significant differences appear in these normalized radial temperature profiles. Of note, the NL and PE operating points (Figure 3.24 and Figure 3.25, respectively) begin to show slight differences of the temperature distribution in the tip region at Rotor 1 Exit, denoting the difference of work distribution as the tip leakage flow affects the rotor performance. Also at these loading conditions, the Stator 1 Exit total temperature distributions are largely unaffected by the tip clearance changes, but Stator 2 Exit and Stator 3 Exit begin to show slight shape changes in these radial distributions.

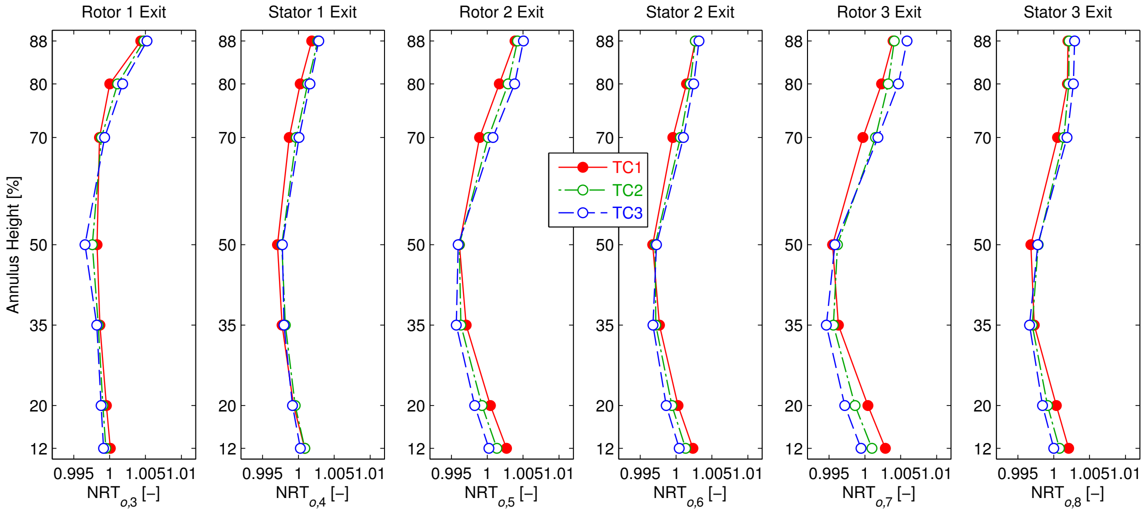

Figure 3.24: Radial total temperature profiles at NL.

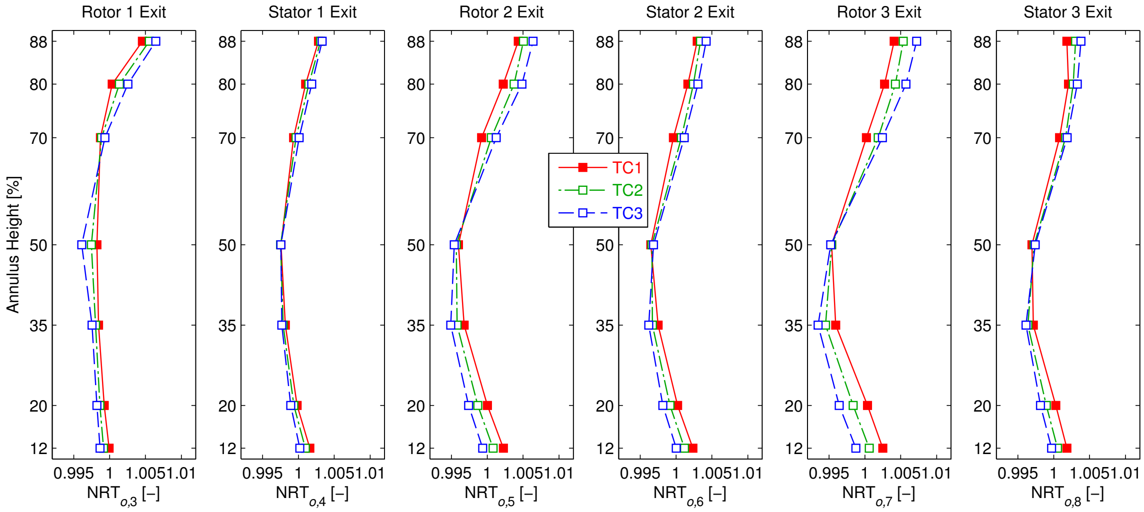

Figure 3.25: Radial total temperature profiles at PE.

As the compressor is further throttled toward stall, the HL (Figure 3.26) and NS (Figure 3.27) normalized radial total temperature distributions show the differences at the rotor exit planes identified for the other loading conditions persist. The Stator 1 Exit profiles remain relatively unaffected by tip clearance changes across the entirety of the

100% corrected speedline. The Stator 2 Exit profiles are largely unchanged from the NL condition to the NS condition, with only slight differences at the LL condition. However, the Stator 3 Exit profiles highlight a slight difference in work distribution for the TC1 configurations compared to the larger tip clearances (TC2 and TC3) at the near stall (NS) operating condition. In particular, the TC1 configuration shows more work distributed in the hub region of Stator 3, compared to TC2 and TC3 which are nearly identical for this normalized total temperature distribution shape.

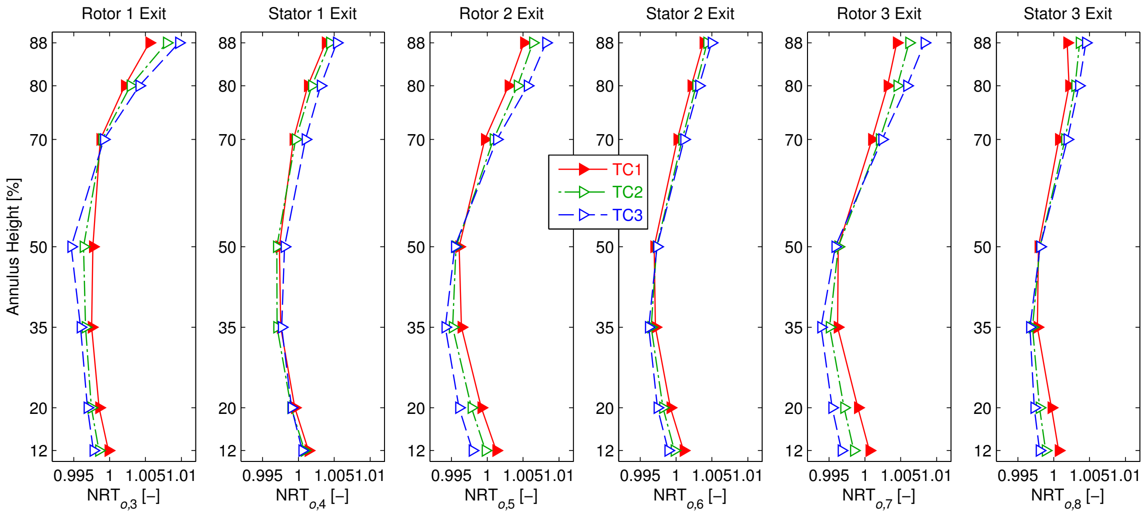

Figure 3.26: Radial total temperature profiles at HL.

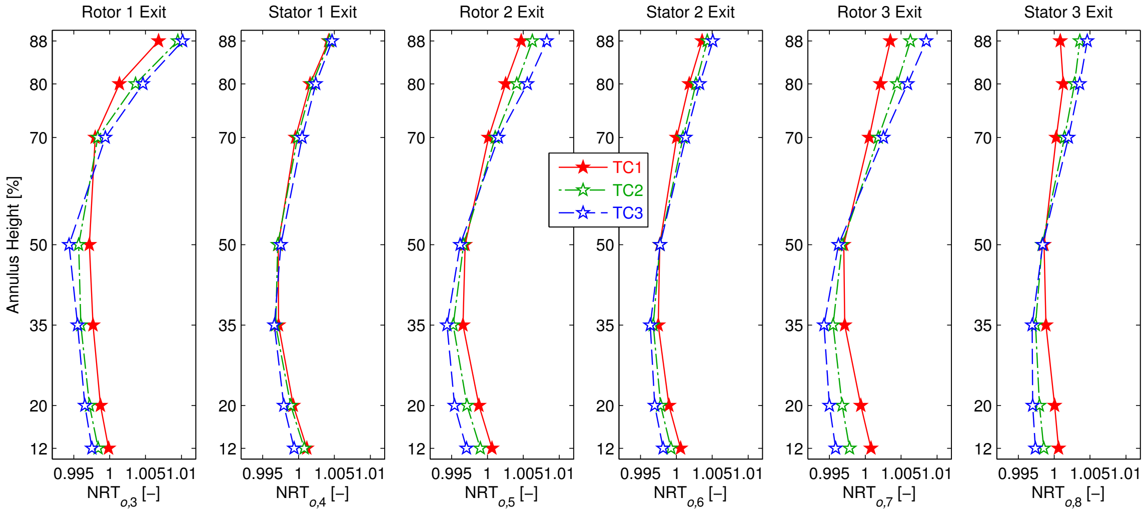

Figure 3.27: Radial total temperature profiles at NS.

3.4. Stator Wake Measurements

3.4.1. Steady Pressure and Temperature Rake Data

In addition to the circumferentially-averaged data presented in Section 3.3, the discrete measurements from the total pressure and total temperature rakes have also been considered in the circumferential direction across one vane pitch at the exit of each stator vane row. Beginning with data collected at Stator 1 exit, Figure 3.28 highlights measurements collected at three of the radial measurement positions: 50%, 70%, and 88% annulus height. These data have been normalized by the circumferential average of the data collected at 50% annulus height for each of the tip clearances.

At each of the three loading conditions in Figure 3.28, the Stator 1 total pressure wake shapes at 50% and 70% annulus height are relatively unchanged with tip clearance height. However, there are slight variations in the measurements collected at the 88% span position, where the flow is most directly affected by the tip leakage flow. At the low loading (LL) condition, the suction side of the wake increases in width at 70% and 88% annulus height.

The Stator 1 Exit wake shapes at nominal loading (NL) appear unaffected by rotor tip clearance height at 50% annulus height. The wake depths and widths at 70% are unchanged, but there is a slight decrease of pressure rise off the pressure surface edge of the vane – an effect which is greatest between the TC2 and TC3 tip clearance configurations. At this loading condition, however, the maximum effect is at 88% annulus height, where the change of rotor tip clearance from TC1 to TC3 shows a decrease of the normalized wake shape off the suction surface (near 40% vane passage) on the order of one percent.

At the high loading (HL) condition, the Stator 1 data in Figure 3.28 also show the thickness and minimum normalized pressure of the wake regions are unaffected by the change of rotor tip clearance. However, the pressure in the primary throughflow at 88% annulus height shows a constant offset in the flow adjacent to the suction surface of the vane. The one percent change observed in the small circumferential region from 30 to 50% vane passage at NL extends across the rest of the vane passage at the HL condition.

The normalized total temperature behind Stator 1 in Figure 3.28 shows the accumulation of high total temperature fluid off the pressure surface of the vanes. This region represents the fluid from the rotor wake which collects on the stator pressure surface, as described by Kerrebrock and Mikolajczak (1970). This same effect has been previously documented at the baseline tip clearance, TC1, by Key (2014). At the LL and NL conditions, Figure 3.28 shows no discernable change of the normalized circumferential total temperature distribution. However, the HL condition shows an increase of the peak normalized total temperature in the region off the vane pressure surface (associated with rotor wake fluid) with increased rotor tip clearance – the most significant of which is observed at 70% annulus height.

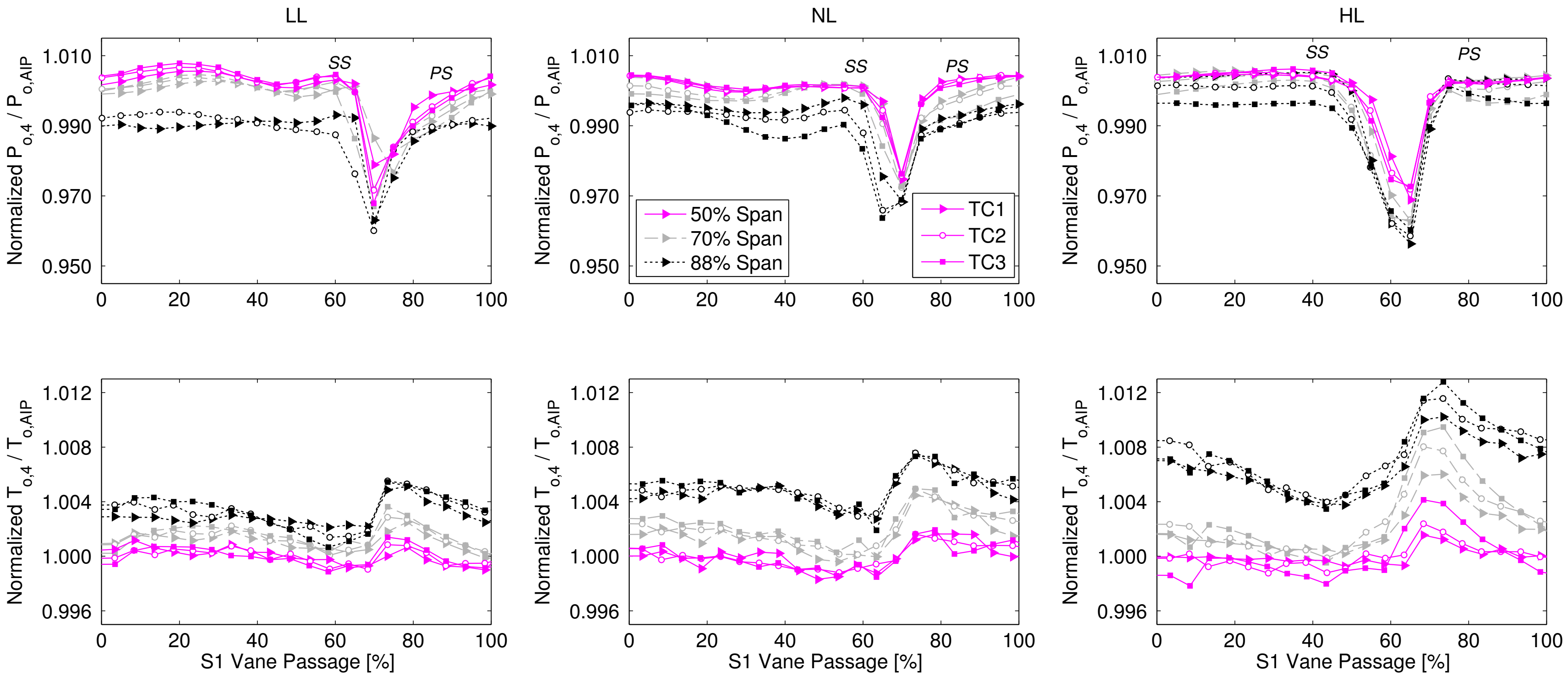

Figure 3.28: Stator 1 total pressure wakes and pitchwise total temperature distribution.

Measurements comparing total pressure and total temperature rake data are also included at Stator 2 exit for three rotor tip clearance configurations and three loading conditions, Figure 3.29. Whereas the Stator 1 exit results showed minimal effect at the LL operating condition, Stator 2 displays a more significant impact at the 88% measurement location: a nearly constant pressure across the bulk throughflow at 88% for TC1 develops into a pressure trough extending approximately 60% vane passage at a maximum depth of nearly two percent with respect to the bulk throughflow. The total temperature variations observed at HL at Stator 1 exit are not present at the Stator 2 exit.

The circumferential variations of Stator 3 exit pressures and temperature are shown in Figure 3.30. As with Stator 2, the most distinct effect of the pressure wake shapes with rotor tip clearance changes is observed at the low loading (LL) condition. At this condition, the increase from TC1 to TC2 creates a depression on the order of one percent with respect to the bulk throughflow, in a circumferential region extending across the majority of the throughflow area. In contrast, the increase from TC2 to TC3 shows the same depression depth, but the location of minimum pressure has moved approximately 20% vane passage toward the vane pressure surface.

Similar to the other stators, the Stator 3 results in Figure 3.30 show circumferential total temperature distributions which are largely unaffected by increased rotor tip clearance at LL and NL. At the high loading (HL) condition, there is an increase of normalized total temperature across the entire circumference at 88% span; this observation is in contrast to the slight increase of peak rotor fluid accumulation observed only near the pressure surface of Stator 1 (and most significantly at 70% span), and the Stator 2 measurements which were largely unaffected by rotor tip clearance.

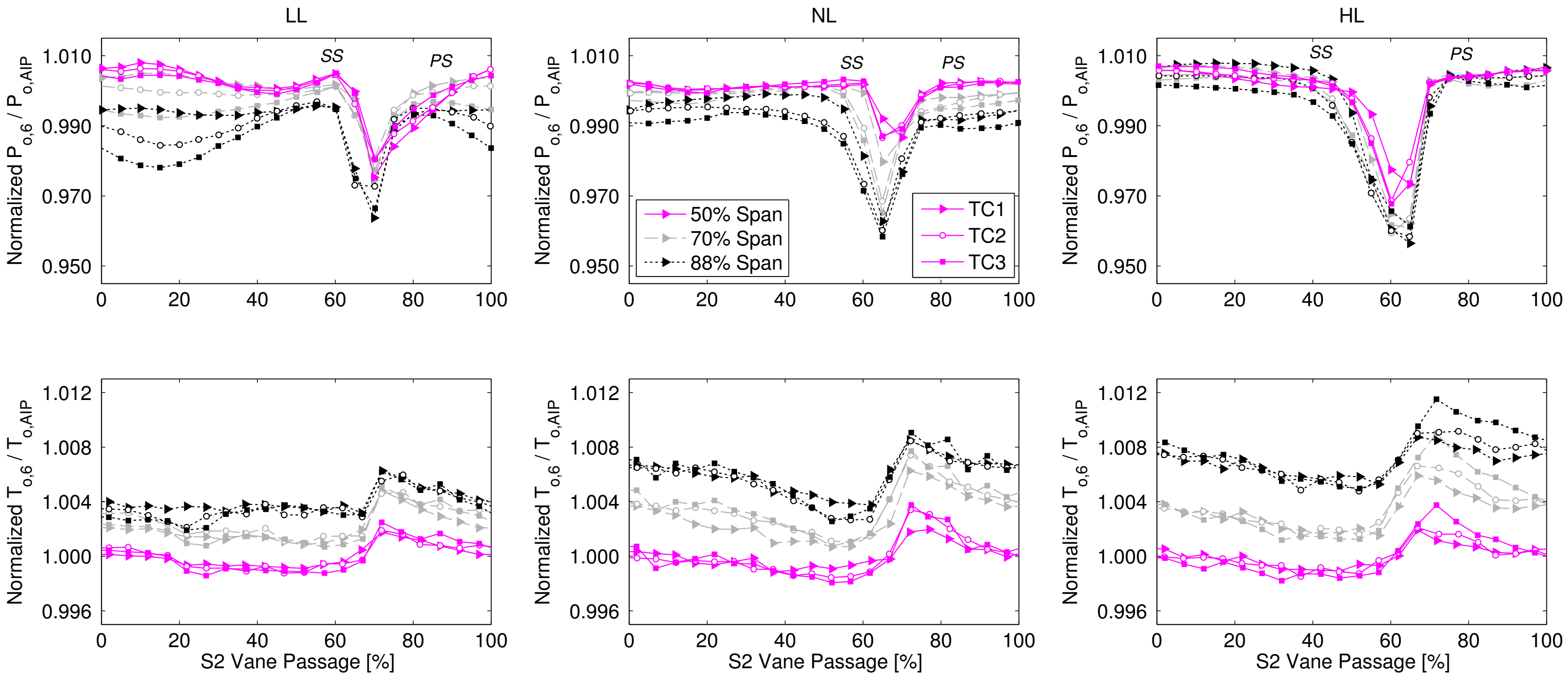

Figure 3.29: Stator 2 total pressure wakes and pitchwise total temperature distribution.

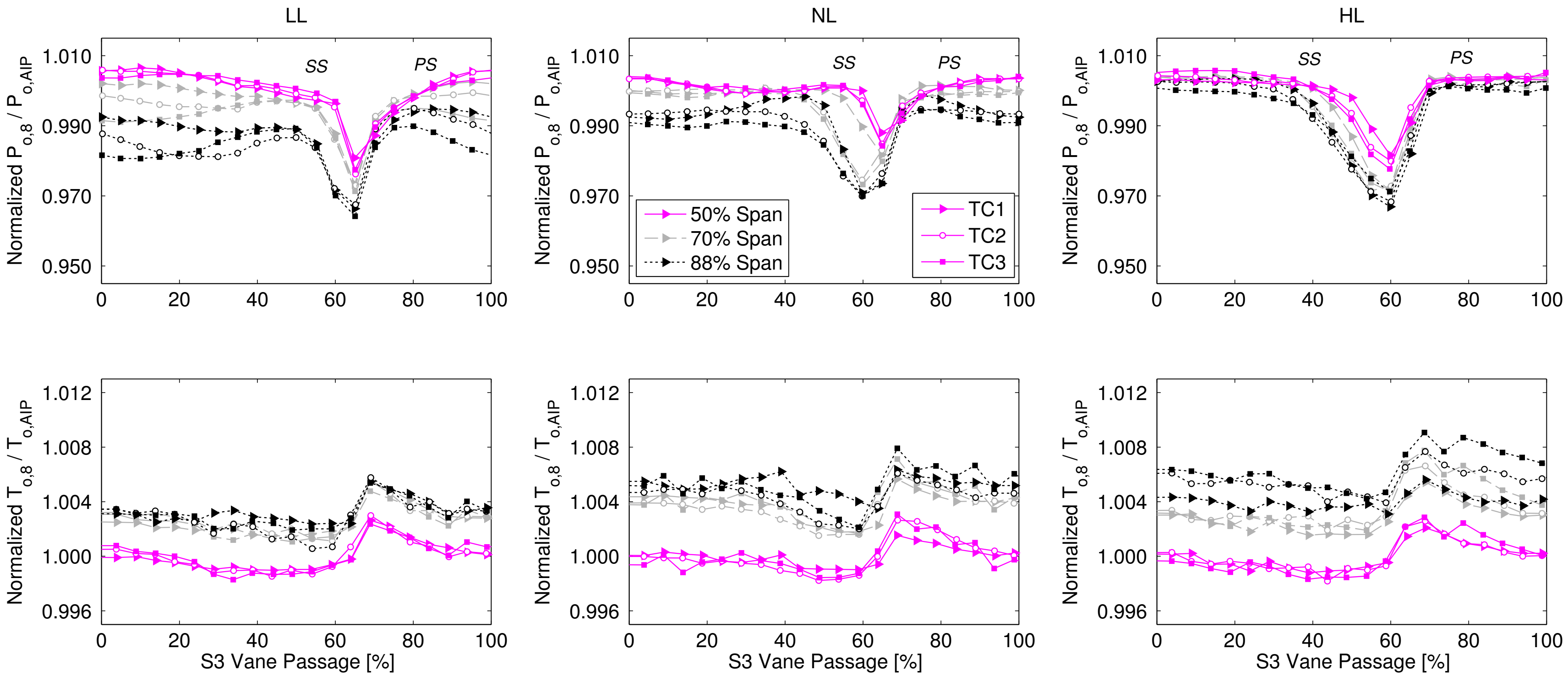

Figure 3.30: Stator 3 total pressure wakes and pitchwise total temperature distribution.

3.4.2. Detailed Steady Total Pressure Traverses

To supplement the measurements collected downstream of the stator vanes using the total pressure rakes, a series of detailed traverses were completed with a miniature Kiel head total pressure probe. These measurements consisted of up to 30 radial plunge positions (at least four times the resolutions from the rake), with an emphasis on capturing the flow features in the endwall regions, as well as a higher resolution of 25 pitchwise vane positions with respect to the fixed probe location. Due to the long-duration runs required for this measurement technique, these detailed measurement campaigns were conducted at the exit of each of the three stator vane rows, at two loading conditions (NL and HL), for the smallest and largest tip clearance configurations (TC1 and TC3).

As alluded to by the radial profiles in Section 3.3.1, an increase of rotor tip clearance height has the effect of producing increased blockage due to the leakage flow region in the outer area of the annulus. This corresponding redistribution of mass flow from the tip region toward the hub region unloads the hub region of the downstream stator to reduce the wake thickness in the lower region of the annulus and reduce the corner separation regions in the hub corner, as shown by Smith (2015). However, the reduced flow in the tip region leads to increased flow separation at the outer diameter of the stator vane. For measurements collected at Stator 1 exit for a nominal loading (NL) condition, Figure 3.31 shows this slight decrease of wake thickness at approximately 30% annulus height as the rotor tip clearance is increased from TC1 to TC3. In this same figure, the reduction of flow (and corresponding reduced total pressure) in the tip region is also apparent due the presence of the leakage flow from Rotor 1.

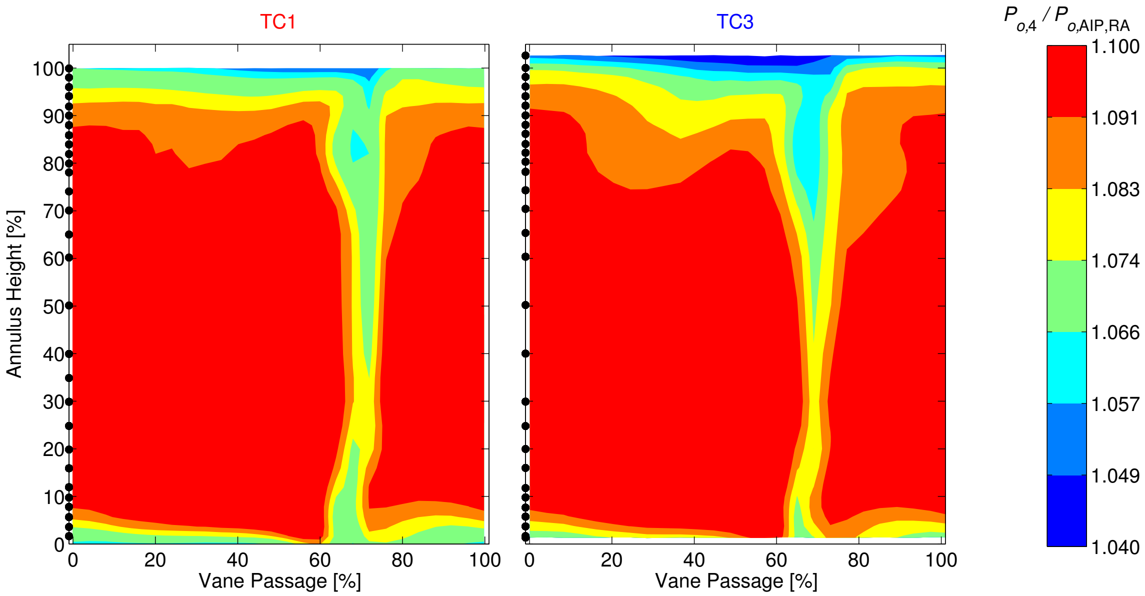

Figure 3.31: Detailed total pressure traverses at Stator 1 exit, NL.

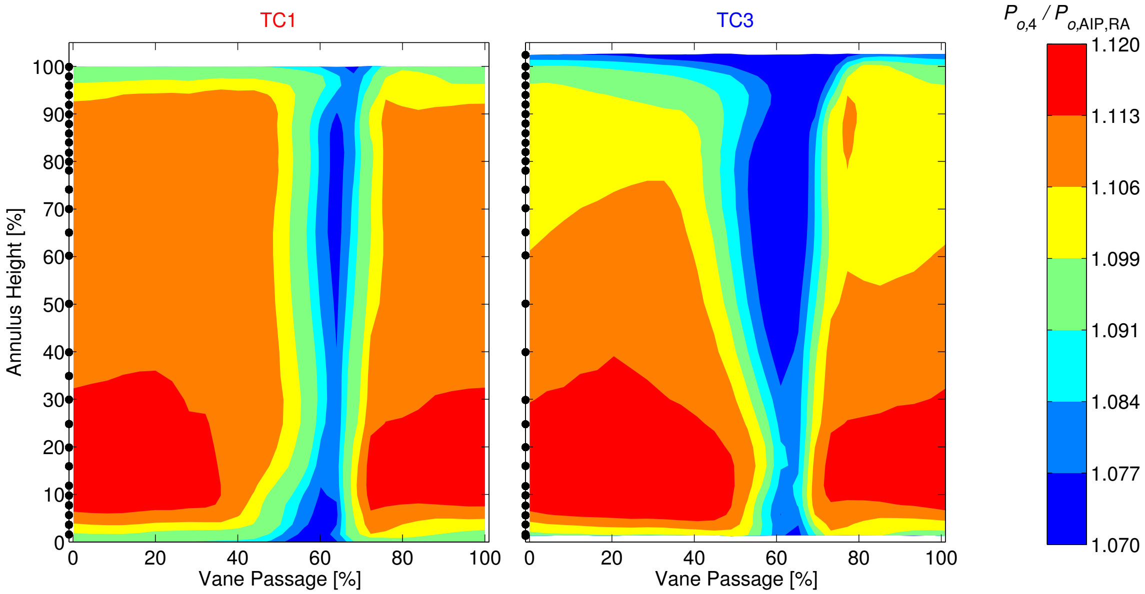

Figure 3.32: Detailed total pressure traverses at Stator 1 exit, HL.

For the same Stator 1 exit measurement plane, but at a high loading (HL) operating condition, Figure 3.32 shows that this effect is more noticeable at high loading. At this position closer to the stall point, the lower 30% of the annulus shows a benefit from the increased tip clearance, but the outer 70% annulus height presents a significant increase of stator wake width and depth. In this figure, the bulk flow outside the wake also shows a significant decrease of total pressure rise extending down to approximately 70% annulus height.

Similar comparisons can also be made between two tip clearance configurations at the exit of Stator 2. At the NL operating condition, Figure 3.33 shows a decrease of total pressure in the tip region as the increased tip leakage flow from Rotor 2 is ingested by the stator vane. The compounding effect of the increased tip clearance height is displayed by this embedded stage, making it more difficult to directly compare contour levels between the two tip clearance configurations. However, the effect of the increased blockage appears to affect the flow most significantly in the outer 20% of the annulus height.

For the high loading (HL) condition at Stator 2 exit, Figure 3.34, the most noticeable effect of the increased tip clearance height is observed. Referring back to the radial total pressure profiles at this same operating condition, Figure 3.21, a distinct shape difference is observed for the change from TC1 to TC3. The data in Figure 3.34 show that TC1 exhibits a significant hub corner separation at this high loading condition which extends up to approximately 30% annulus height; however, the wake thickness remains relatively constant across the remainder of the annulus. As the rotor tip clearance height is increased, the redistribution of mass flow from the tip toward the hub region has the expected result of energizing the hub region and decreasing the likelihood of flow separation, thereby reducing the hub corner separation zone. However, this benefit comes at the expense of a drastic increase of wake thickness, as observed for the upper 50% annulus height.

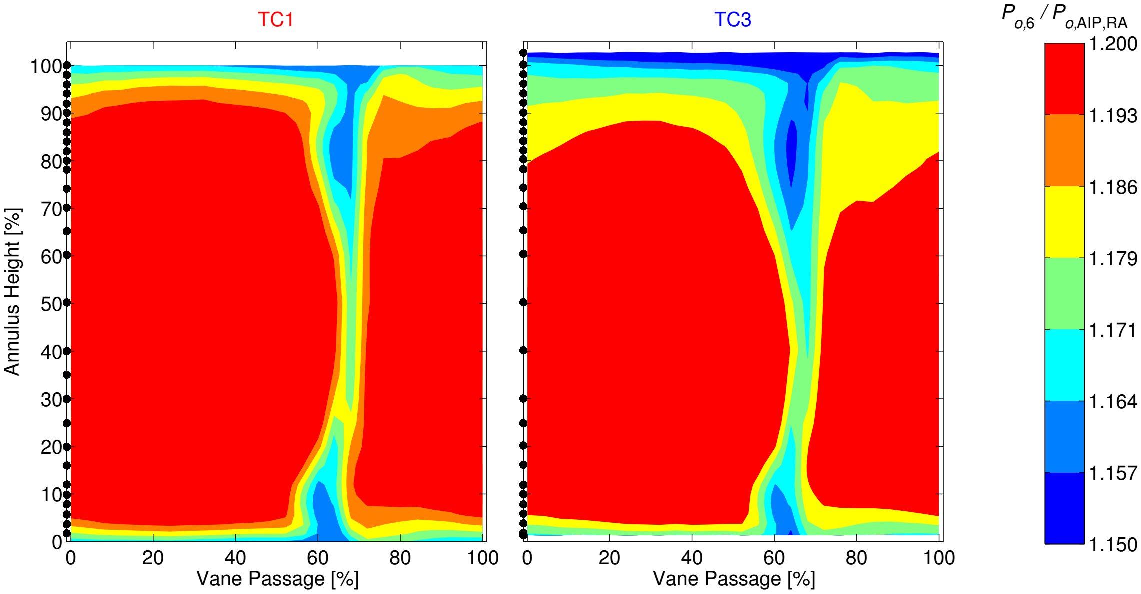

Figure 3.33: Detailed total pressure traverses at Stator 2 exit, NL.

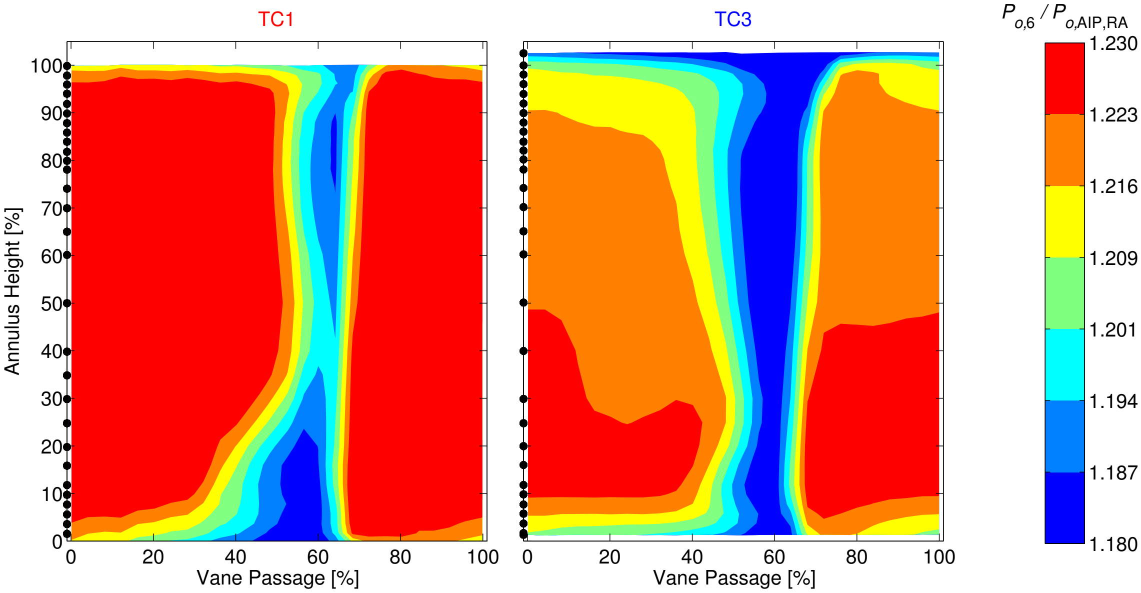

Figure 3.34: Detailed total pressure traverses at Stator 2 exit, HL.

The detailed total pressure measurements collected at Stator 3 exit are also shown for the same NL and HL operating conditions on the 100% corrected speedline in Figure 3.35 and Figure 3.36, respectively. At the high loading condition, Figure 3.36, the TC1 rotor tip clearance configuration exhibits the thickest wake of all three stators (relatively), but with the shallowest depth (see also Figure 3.30). As the tip clearance is increased to TC3, the observed effect is the same for Stator 3 as it was for the other two vane rows: the hub region (up to approximately 30% annulus height) shows a decreased wake thickness, but the outer 70% annulus height is negatively affected by the decreased flow in the tip region that has been redistributed toward the hub.

In addition to the high resolution of measurements, the increased quantity of data points from these detailed radial traverses provide the ability to compare with the calculated total pressure ratio determined from the seven-element total pressure rakes. On average, the total pressure ratios calculated as an area average of the detailed radial traverse data agree with the values evaluated from the pressure rakes within 0.04%, less than one-fourth of the uncertainty for the total pressure ratio.

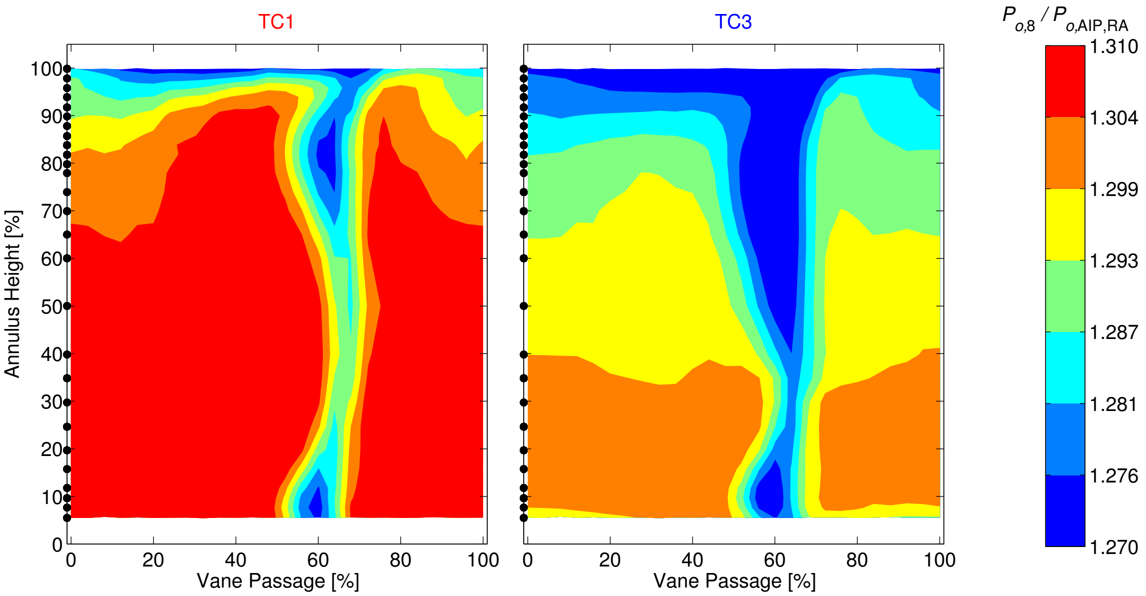

Figure 3.35: Detailed total pressure traverses at Stator 3 exit, NL.

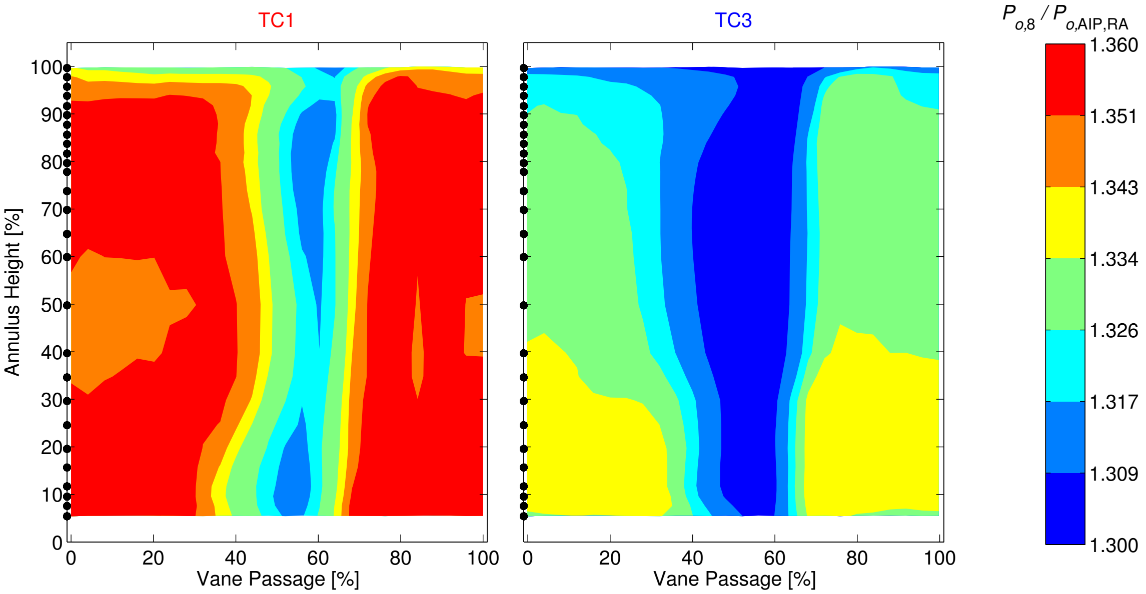

Figure 3.36: Detailed total pressure traverses at Stator 3 exit, HL.

CHAPTER 4: CHARACTERIZATION OF COMPRESSOR STALL INCEPTION

4.1. Measurement Technique

For this study, the stall inception mechanism for the compressor was systematically assessed for each of the three tip clearance configurations. In addition to the four corrected speedlines shown in Figure 3.1, the compressor stall behavior was also investigated for the 60% and 52% corrected speedlines. In each case, the stall point was determined by closing the throttle in incremental steps to slowly increase the loading of the compressor. At the onset of stall, a human-interface control mechanism was initiated to open the throttle and allow recovery to a stable operating condition. This process was repeated several times to determine a representative average of corrected mass flow rate and total pressure ratio for each test case. The previous statements regarding uncertainty of mass flow rate and overall total pressure ratio apply for these measurements as well. For a given operating speed and tip clearance configuration, the compressor was also stalled in up to five different vane positions with respect to the stationary instrumentation to develop a representative average for the overall map. During the stall inception tests, the full set of inter-stage measurement rakes was removed, and only the inlet and exit conditions of the compressor (axial measurement planes 0, 1, and 9 in Figure 2.6) were monitored for overall pressure rise information.

To detect the formation of stall events, a series of high-frequency response Kulite XTL-140 pressure transducers were installed throughout the compressor. These piezoresistive pressure transducers each have an outer diameter of 0.101 in. with a threaded mounting system to accommodate insertion and removal at several unique positions. As with the other fast-response pressure transducers used in this study, these XTL-140 sensors also featured a standard protective B-screen, reducing the frequency response of the sensors to approximately 20 kHz. For these stall tests, six circumferentially-distributed sensors were positioned approximately 15% axial chord upstream of each rotor blade row, following the design outlined by Houghton and Day (2010), for 18 total sensors. The measurements from these fast-response sensors were collected through the same data acquisition chain described in Section 2.4.1.

4.2. Stall Inception Analysis

Over the years, researchers (McDougall et al., 1990; Day, 1993) have identified two different stall inception mechanisms in axial compressors. The first type, modal oscillations, or "modes," represents long length-scale disturbances which affect the entire compressor. These modal oscillations are often observed for some time prior to the definitive stall point for the compressor. The second type, "spikes," appears as a short length-scale disturbance which develops as a result of a localized stalling, typically in one blade row. These spike signals may appear in high-frequency-response data collected from hot-wire velocity measurements or fast-response pressure transducers.

Camp and Day (1998) continued the discussion of these stall inception types and developed a model for predicting the stall inception mechanism of a given compressor, based on the shape of the total-to-static pressure rise characteristic for the machine. These authors concluded modal stall inception characteristics are expected to appear if the compressor reaches a peak total-to-static pressure rise prior to entering stall (i.e., a zero slope condition). On the other hand, if the compressor stalls prior to reaching a peak total-to-static pressure rise value, the corresponding stall inception mechanism will likely be a spike-type stall event.

The total-to-static pressure rise characteristics are shown for the Purdue three-stage compressor, with each of three tip clearance configurations at four operating speeds, in Figure 3.7. The characteristics in this figure show that there are three lines which potentially show a peak value has been reached: the 100% corrected speedlines for TC1 and TC2, and the 90% corrected speedline for TC1. Based on the model presented by Camp and Day (1998), it is expected that these three speedlines are the most likely candidates to portray modal stall inception traits. The other nine speedlines all appear to be continuing to rise at the stall point (the lowest flow rate point on each line) – typical signs of spike-type stall inception.

Beyond the predictive capabilities of the characteristics in Figure 3.7, time-resolved static pressure traces at several of these operating conditions are presented. First, measurements collected with the baseline tip clearance (TC1) are shown for the 100% corrected speedline, Figure 4.1. This figure presents the offset time-resolved pressure traces collected at each of the eighteen locations around the compressor (six circumferentially-distributed sensors at each rotor). As expected from the total-to-static characteristic, this speed and tip clearance configuration exhibits modal stall inception traits. Of note, the long length-scale disturbances are observed for several rotor revolutions prior to the onset of stall (approximately identified by the zero location on the abscissa). Tracking these “modal” oscillations through the compressor shows the mode speed is approximately one-fourth of the rotor rotational speed. At the onset of stall, the stall cell rotates at approximately one-half the rotor rotational speed.

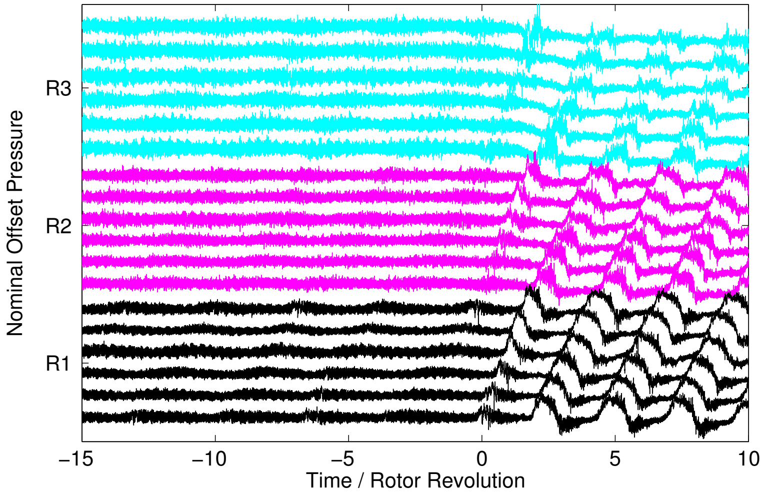

Figure 4.1: Time-resolved casing static pressure traces at the inception of stall for TC1 at 100% N_c.

Day (1993) showed that a change of rotor tip clearance may affect the stall inception mechanism of the machine. As previously discussed, the data acquired at 100% corrected speed for the intermediate clearance height (TC2) also suggests the existence of modal stall. The time-resolved static pressure traces for this speed and tip clearance configuration are presented in Figure 4.2. This figure may show weak long length-scale modal propagations (also at a rotational rate on the order of one-fourth the rotor speed) in the measurements upstream of Rotor 1, as suggested from the total-to-static pressure rise characteristic. However, the distinct modal traits from Figure 4.1 are certainly less apparent (and nearly absent in the Rotor 2 or Rotor 3 data). Further, some spikes can also be identified in the Rotor 1 pressure traces. Of note, one spike develops in the first sensor upstream of Rotor 1 at eight revolutions prior to the onset of stall, and it rotates approximately at the rotor rotational speed. The traces in Figure 4.2 confirm Camp and Day's (1998) observations that these two stall inception mechanisms can occur simultaneously in the same machine. In this case, however, Figure 4.2 appears to be dominated by spikes than the long length-scale modal fluctuations.

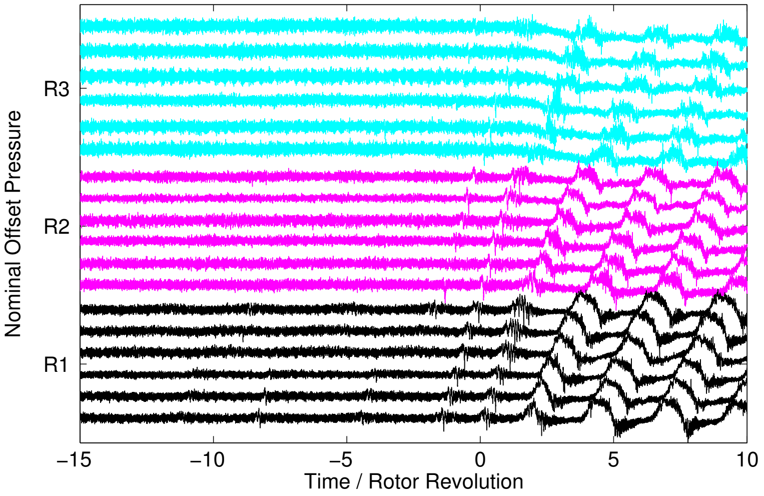

Figure 4.2: Time-resolved casing static pressure traces at the inception of stall for TC2 at 100% N_c.

Hoying et al. (1999) has previously identified that the trajectory of the tip leakage flow approaches a tangential angle as the blade loading increases, influencing the potential for an unstable condition in which the leakage flow may jump upstream of the adjacent rotor blade and cause spike-type stall behavior. This diagnosis from Hoying et al. would predict that the TC3 tip clearance configuration (and possibly also TC2) may display a near-tangential leakage flow trajectory for the near stall operating conditions on the 100% corrected speedline (based on the spikes observed emanating from the Rotor 1 pressure traces in Figure 4.2, e.g.), whereas the TC1 trajectory would be less inclined due to its modal stall tendencies (Figure 4.1). To investigate this further, time-resolved static pressures were measured over Rotor 1 using the removal instrumentation block described in Section 2.4.1. These data were collected at the near stall (NS) operating condition, defined by a position of 5% stall margin using Equation (3.2), as explained in Section 3.1. The results are analyzed in terms of root-mean-square (RMS) unsteadiness with respect to the ensemble average:

$$P_{\mathrm{RMS}}(t_i) = \sqrt{\frac{1}{N}\sum_{k=1}^{N}[P(t_i) - \langle P(t_i)\rangle]^2{}_{k}}\ , \tag{4.1}$$

for which the phase-locked ensemble average (EA) is defined by:

$$\langle P(t_i)\rangle = \frac{1}{N}\sum_{k=1}^{N}[P(t_i)]_k\ . \tag{4.2}$$

These NS results, Figure 4.3, show this predicted result by considering the over-rotor static pressure unsteadiness in terms of normalized RMS pressures.

More recent studies continuing the evaluation of spike-type stall inception suggested by Hoying et al. (1999) have suggested the development of spike-type stall may not be strictly dependent on the leakage flow, but rather a radial vortex which develops as a result of leading edge separation (Weichert and Day, 2014; Pullan et al., 2015). It is this radial vortex structure which propagates in front of the adjacent blade and leads to the spike. However, the increased incidence at the tip due to the leakage flow, especially with larger tip clearance heights, as shown in Figure 4.3, is expected to increase the likelihood of such leading edge separation.

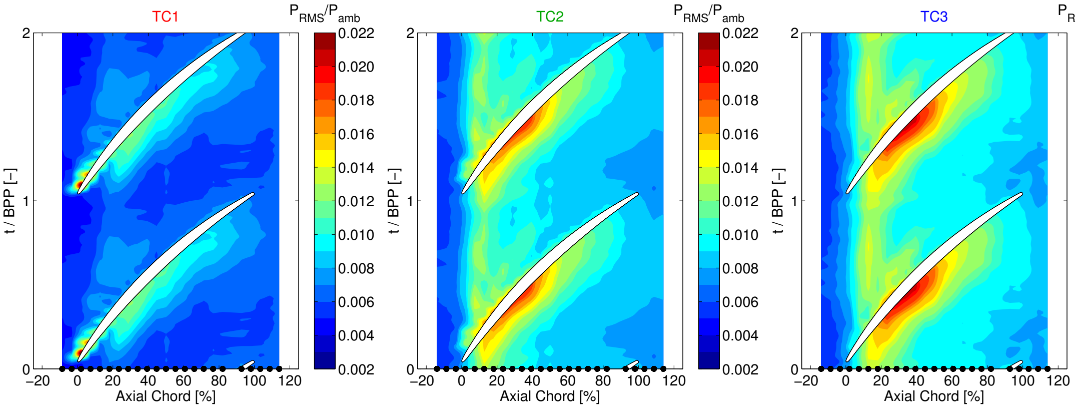

Figure 4.3: Static pressure unsteadiness over Rotor 1, presented as an RMS with respect to the EA, for each tip clearance configuration at NS.

Considering again the total-to-static pressure rise characteristics for the baseline tip clearance configuration (TC1), Figure 3.7, the 90% corrected speedline also appears to reach a maximum and begin to decrease – a sign of potential modal stall inception traits. The pressure traces for this case, Figure 4.4, reveal results which are more similar to TC1 at 100% corrected speed than TC2. In particular, Figure 4.4 presents long length-scale modal tendencies which persist through all three rotor rows. However, the spike-type signals are still present in the Rotor 1 pressure traces. Of note, there are spikes emanating from the first sensor of Rotor 1 at 13, 11, and five revolutions prior to the onset of stall, all of which fall in the troughs of the modal waves. Relative to Figure 4.2, these results for TC1 at 90% corrected speed represent more modal stall inception traits than spikes; however, both mechanisms are certainly present for this condition as well.

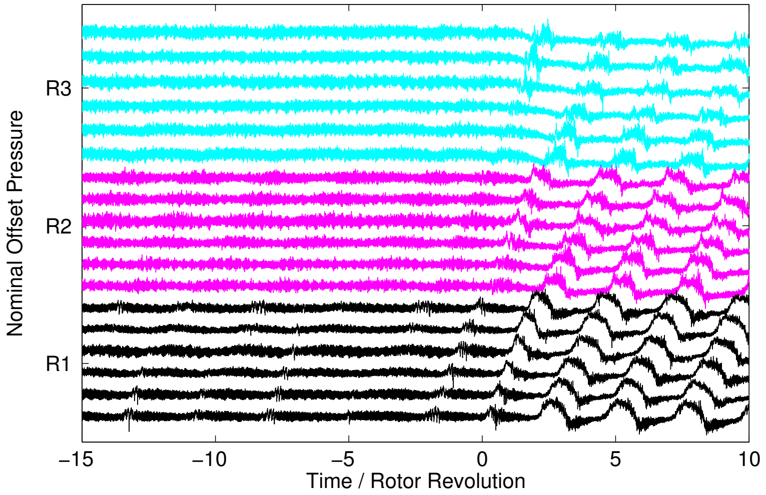

Figure 4.4: Time-resolved casing static pressure traces at the inception of stall for TC1 at 90% N_c.

In contrast with the results presented thus far, the part-speed results for TC1 (68% corrected speed) are shown in Figure 4.5. These fast-response pressure traces are dominated by spike-type stall inception traits originating from Rotor 1. The spikes travel circumferentially around Rotor 1 at a rate approximately equal to the rotor rotational speed, and they are likely the result of localized separation regions related to high incidence angles for Rotor 1. However, it is interesting to note in this case that it appears to be Rotor 2 which first trips the compressor into stall, suggesting that the rear stages of the compressor could be attempting to "assist" Rotor 1 until they are no longer capable of doing so. The data in Figure 4.5 are shown on the same scale as the previous 100% and 90% speedline traces for consistency. Although it may not be clear from the scale, if the results in Figure 4.5 were shown on a larger scale, modal stall characteristics would still not be present.

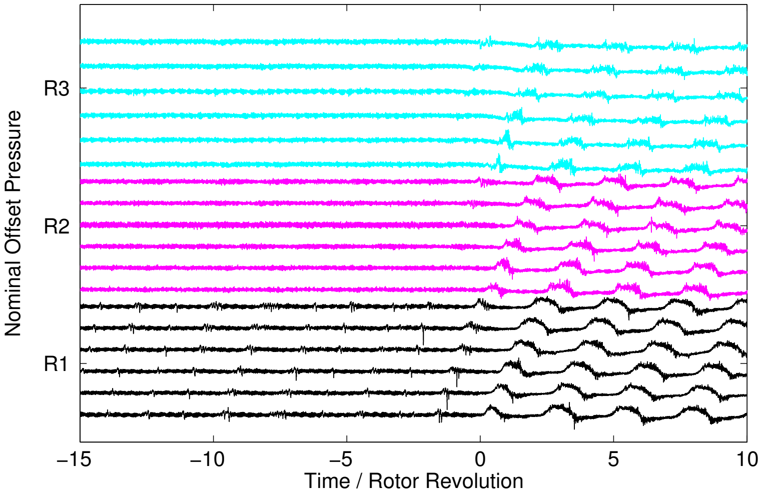

Figure 4.5: Time-resolved casing static pressure traces at the inception of stall for TC1 at 68% N_c.

Although not all of the test cases have been presented here, these four selected results represent the observed trends in the compressor at different speeds and with different tip clearance configurations. A summary of all test cases, Figure 4.6, highlights several regions of a tip clearance vs. speed matrix; the four cases presented thus far are noted by black dots in Figure 4.6. As suggested by Figure 3.7 and shown in Figure 4.1, the 100% corrected speedline for TC1 portrays distinctly modal stall inception traits. This test case is representative of the original design conditions for the compressor, suggesting the compressor is likely well-matched, and it stalls via long length-scale perturbations. The 90% corrected speedline for TC1 and the 100% corrected speedline for TC2 exemplify a transitional range away from the distinct modes to also incorporate spike-type stall inception traits. Ultimately, though, the compressor exhibits clear spike-type stall inception mechanisms (i.e., Figure 4.5) for the conditions which depart most significantly from the original design intent of the machine.

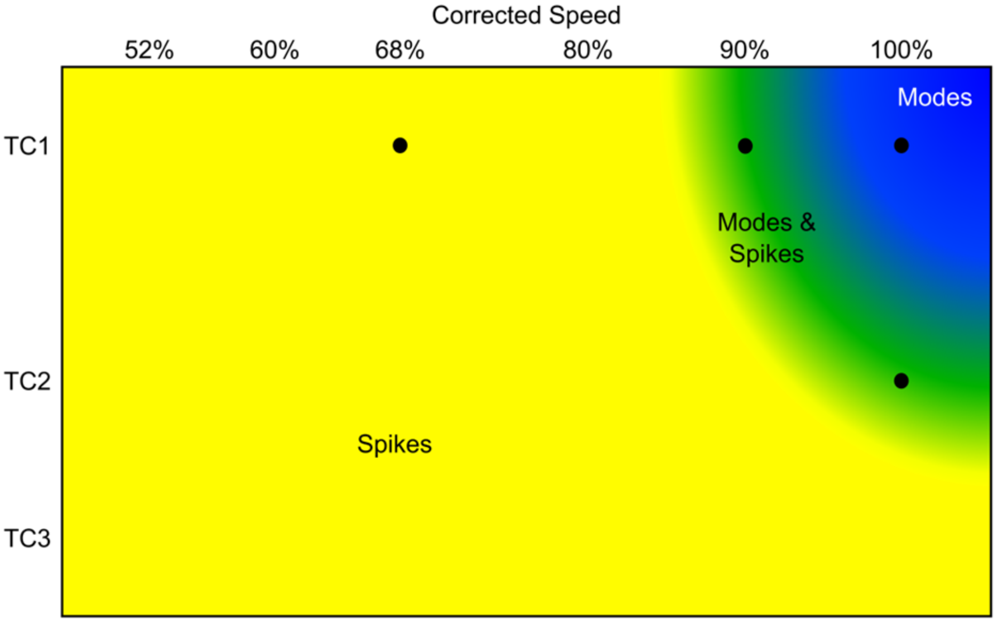

Figure 4.6: Summary of stall inception trends for all tip clearance configurations at all investigated operating speeds. Pressure traces shown herein are identified by black dots.

CHAPTER 5: TIME-RESOLVED FLOW FIELD MEASUREMENTS

5.1. Over-Rotor Static Pressures

5.1.1. Tip Leakage Flow Characterization

The tip leakage flow trajectory can be tracked using the time-resolved static pressure measurement system described in Section 2.4.1. These data have been collected at a sampling frequency of 100 kHz with a low-pass filter cut-off frequency of 40 kHz for a total of 500 revolutions, as defined by the 1/rev signal from the laser tachometer. The large number of revolutions makes it possible to represent an average of the measured pressures using the phase-locked ensemble averaging (EA) technique:

$$\langle P(t_i) \rangle = \frac{1}{N}\sum_{k=1}^{N}[P(t_i)]_k \,, \tag{5.1}$$

defined for each revolution k and each time i. Using Equation (5.1), the ensemble average wall static pressures over Rotor 1 at NL is shown for each of the three tip clearance configurations in Figure 5.1. The data presented in Figure 5.1 represent a mean rotor tip flow, calculated by dividing the ensemble-averaged signal into the 36 separate rotor blade passages, and averaging across the 36 passages. This average result is shown twice, assuming periodicity, to more easily discern the applicable flow features. Also in Figure 5.1, the axial position of the utilized sensors is shown at the bottom of each figure by a series of black dots. For these initial comparisons, the data were collected at one position with respect to the upstream and downstream vane rows. However, these static pressure data were all collected at the same position with respect to the stator vanes and the measurement location was selected to ensure that the sensors were not positioned in the wake from the upstream stator vane. Further consideration is given to the variability of the tip leakage flow due to interaction with the adjacent vane rows in the next section.

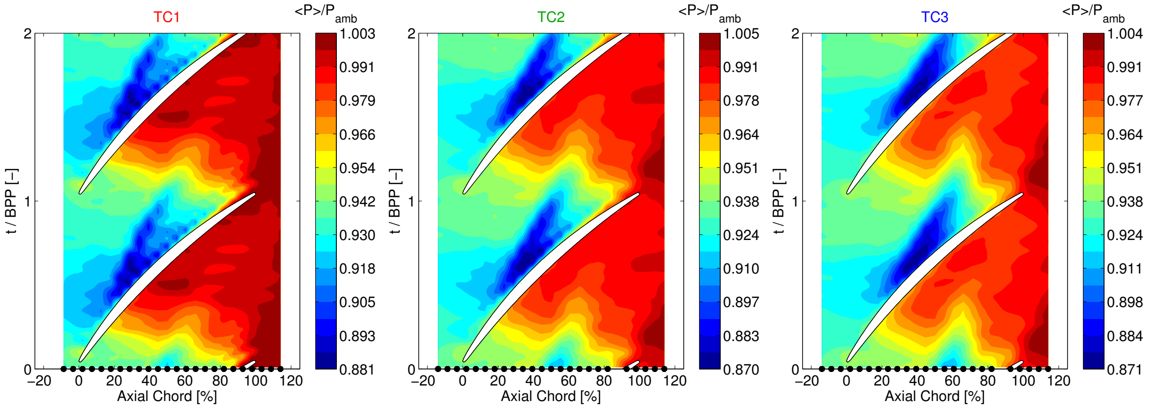

Figure 5.1: Ensemble-average static pressure over Rotor 1 for each tip clearance configuration at NL.

The phase-locked ensemble average data in Figure 5.1 identify a low pressure region, representing the tip leakage flow. However, the leakage flow trajectory becomes less distinct downstream of approximately 60% axial chord. As an alternative method for identifying the leakage flow path, previous authors have also used the root-mean square (RMS) unsteadiness with respect to the ensemble average:

$$P_{\text{RMS}}(t_i) = \sqrt{\frac{1}{N}\sum_{k=1}^{N}[P(t_i) - \langle P(t_i)\rangle]^2{}_k} \ . \tag{5.2}$$

This definition of RMS unsteadiness provides the ability to more easily identify regions of pressure fluctuation. For example, the same data from Figure 5.1 (previously presented as an ensemble average) are recast in terms of the RMS with respect to the ensemble average in Figure 5.2. This figure shows that the RMS definition provides the capability to more easily distinguish the tip leakage flow trajectory up to nearly 80% axial chord.

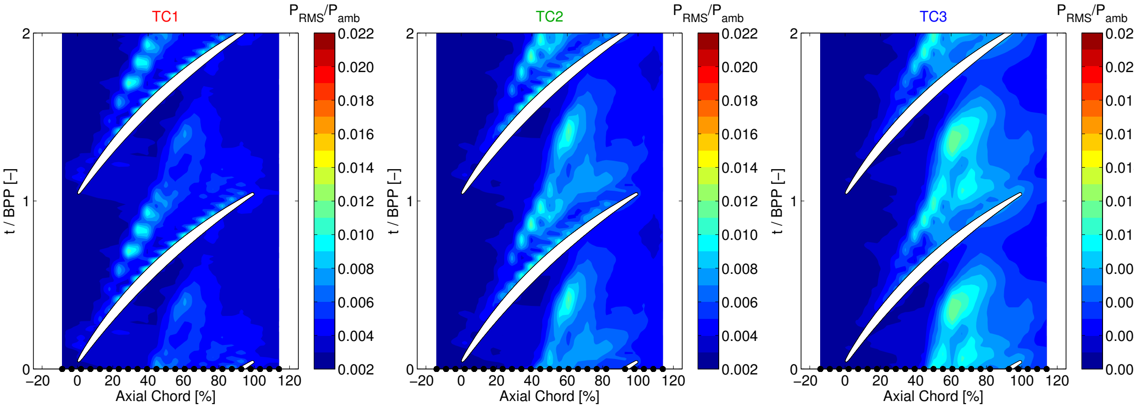

Figure 5.2: Static pressure unsteadiness over Rotor 1, presented as an RMS with respect to the EA, for each tip clearance configuration at NL.

Similar to the data presented at NL, an ensemble-average of the wall static pressures over Rotor 1 at a high loading (HL) operating condition is shown in Figure 5.3 for each tip clearance. Compared to the NL results, these HL data show that the tip leakage flow region has increased its trajectory angle across the rotor passage, as expected from the increased incidence angle on the rotor and the increased pressure difference across the blade tip. Initially, there is no discernable difference in the trajectory angle between these tip clearance configurations in Figure 5.3, although the RMS with respect to the ensemble average can again be used to more easily track the leakage flow trajectory across the rotor passage.

These RMS data, Figure 5.4, highlight flow patterns at the high loading operating condition which are not clearly identified in the ensemble average results of Figure 5.3. Of note, the trajectory angle of the tip leakage flow increases as the tip clearance height increases from TC1 to TC3. This observed trend can be attributed to the fact that the HL conditions for the three tip clearances represent operating points which are at varying proximity to the stall point for a particular tip clearance, as discussed in Section 3.1. In particular for the TC3 tip clearance configuration, Figure 5.4 shows the leakage flow approaches a tangential angle.

At the HL operating condition shown in Figure 5.4, the larger tip clearance configurations (TC2 and TC3) show regions of large unsteadiness (RMS) where the tip leakage flow disturbance impinges on the adjacent blade. These data do not provide a definitive explanation for whether or not this machine displays the “double-leakage” discussed by Khalsa (1996). However, there is reason for speculation, particularly related to the region of high unsteadiness on the suction side of the rotor blade in the region of 30 to 60% axial chord for TC2 and 20 to 50% axial chord for TC3. A follow-on campaign focused on implementing non-intrusive measurements techniques (such as PIV or LDV) inside the blade passage could provide more insight into this phenomenon.

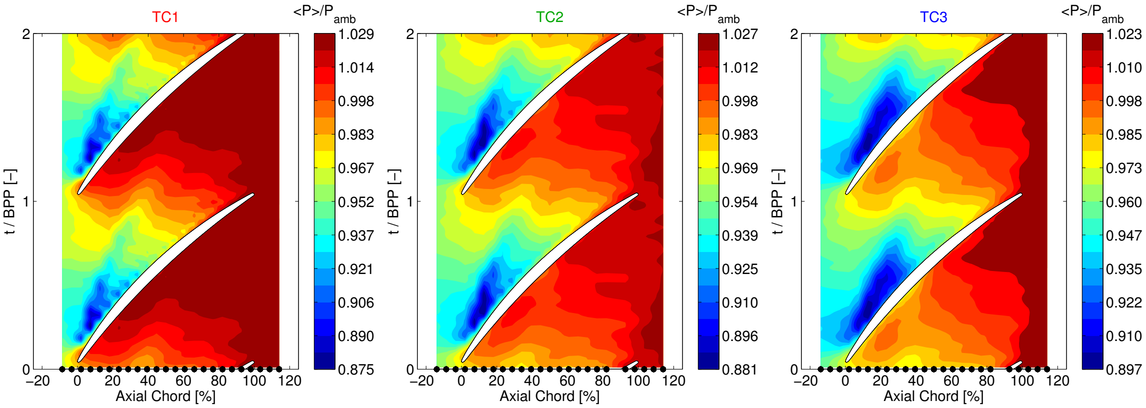

Figure 5.3: Ensemble-average static pressure over Rotor 1 for each tip clearance configuration at HL.

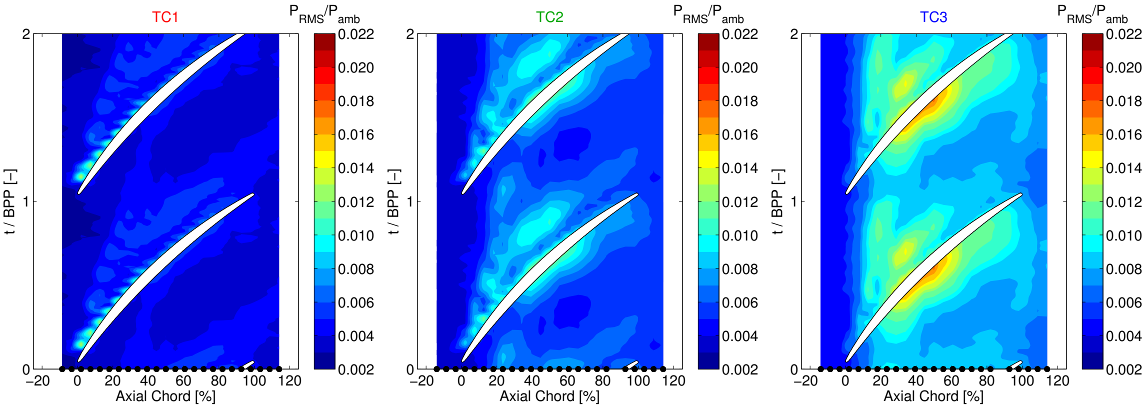

Figure 5.4: Static pressure unsteadiness over Rotor 1, presented as an RMS with respect to the EA, for each tip clearance configuration at HL.

Using the RMS pressures shown in Figure 5.2, Figure 5.4, and a similar figure for the low loading condition, the effect of the tip leakage flow trajectory on loading condition and tip clearance height can be determined. These trajectories, shown in Figure 5.5, have been identified as the locus of the peak RMS values. The comparison for these trajectories has been specifically selected for the Rotor 1 data because they represent comparisons of tip leakage flow trajectories which are less affected by upstream flow conditions. In all cases, Rotor 1 experiences the same “clean” inlet flow exiting the IGV, whereas the rotors in the aft stages of the compressor experience more flow unsteadiness and non-uniformities due to ingestion of the upstream flow disturbances.

For the two high flow rate conditions, NL and LL, Figure 5.5 shows an increase of tip clearance height has the effect of moving the leakage flow trajectory closer to the blade suction surface. This figure also more clearly reveals a non-linear leakage flow trajectory, which is especially apparent for the TC3 tip clearance configuration at the high flow rate conditions, LL and NL. This observation was also noted by Yoon et al. (2006) near mid-chord, but the results shown here represent a less drastic turn of the leakage flow than was observed by those authors. Chen (1991) theoretically predicts this non-linear trajectory, but not until the end of the passage, where the image vortices required to satisfy kinematic constraints change with the absence of the blade as an effective wall.

In addition to these observed trends at high flow rate operating conditions, Figure 5.5 also depicts a noticeable change of the leakage flow trajectory concavity at the high loading condition as the tip clearance height increases. The discussion of Figure 5.4 noted the change of the leakage flow trajectory angle between the three tip clearance configurations, but the locus of peak RMS values shows the two larger tip clearance heights turn more noticeably toward the adjacent blade. It is likely that this observed change of flow trajectory path is also due to the relative proximity of the HL points to the stall condition with different tip clearance heights.

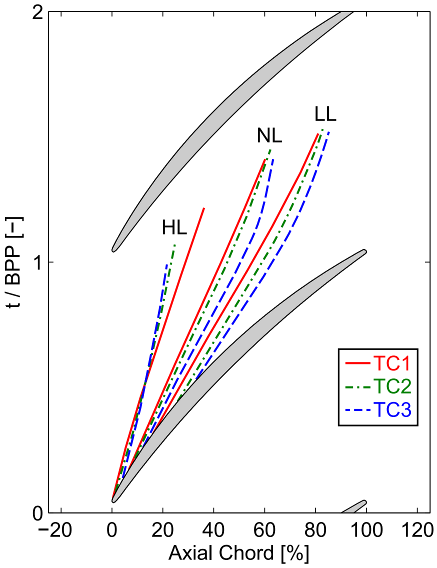

Figure 5.5: Rotor 1 tip leakage trajectories for all three tip clearance configurations at three loading conditions on the 100% corrected speedline.

The over-rotor static pressures presented thus far have compared the results for one rotor with three tip clearance heights. In contrast, Figure 5.6 shows the RMS unsteadiness of the static pressures over each of the three rotor rows at the NL condition for TC2. As with the Rotor 1 results shown above, these figures represent a mean passage, for which the data have been separated into the number of blades in the row (36, 33, or 30 for Rotor 1, Rotor 2, and Rotor 3, respectively) and subsequently averaged. These averaged data are then repeated (assuming periodicity) to more clearly distinguish the flow features in the blade passages.

In Figure 5.6, a clear distinction can be made between the data for Rotor 1 and the data for Rotor 2 or Rotor 3. As shown above in Figure 5.5, the trajectory of the Rotor 1 tip leakage flow is non-linear, but this is less present in Rotor 2 or Rotor 3. Furthermore, the Rotor 2 and Rotor 3 results portray a wider region of high flow unsteadiness (RMS), indicating a different shape of the leakage flow at these positions.

In the same manner, Figure 5.7 shows the RMS unsteadiness over each rotor for TC2 at HL. As with the nominal loading condition, a clear distinction can be drawn between the Rotor 1 data and the results for Rotor 2 or Rotor 3. Although the angle of the leakage flow trajectory is similar for the three rotors, a wider region of high flow unsteadiness is present for the Rotor 2 and Rotor 3 results, representing a larger leakage flow disturbance for these rotors.

The measurements in the fixed frame of reference for the data in Figure 5.6 and Figure 5.7 are nearly identical in position with respect to the upstream stator vane row and the associated low-pressure wake region. Thus, the results in these figures further emphasize the differences measured over Rotor 1, which always ingests the same clean inlet flow from the IGV. This compares with the latter Rotor rows, which are subject to flow disturbance ingestion from the upstream rotor rows, especially the flow in the outer region near the rotor tip affected by the tip leakage flow.

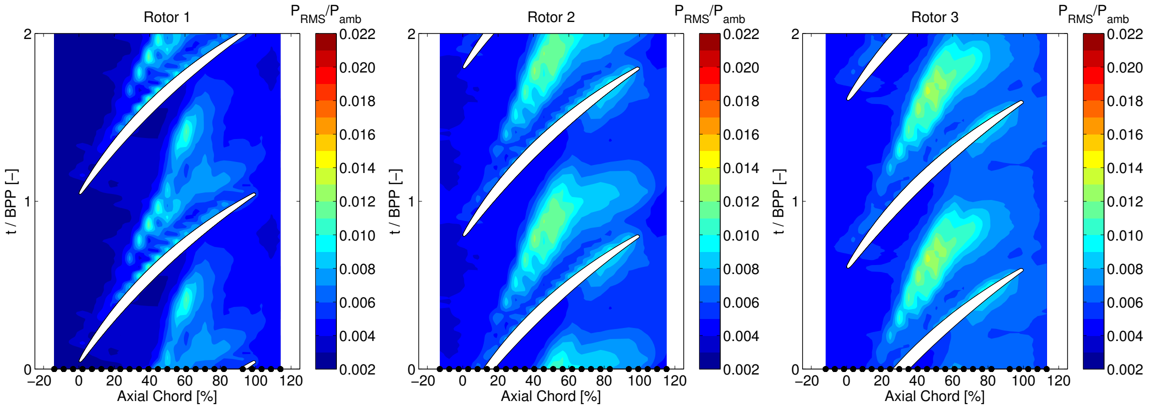

Figure 5.6: Static pressure unsteadiness, presented as an RMS, over each rotor for TC2 at NL.

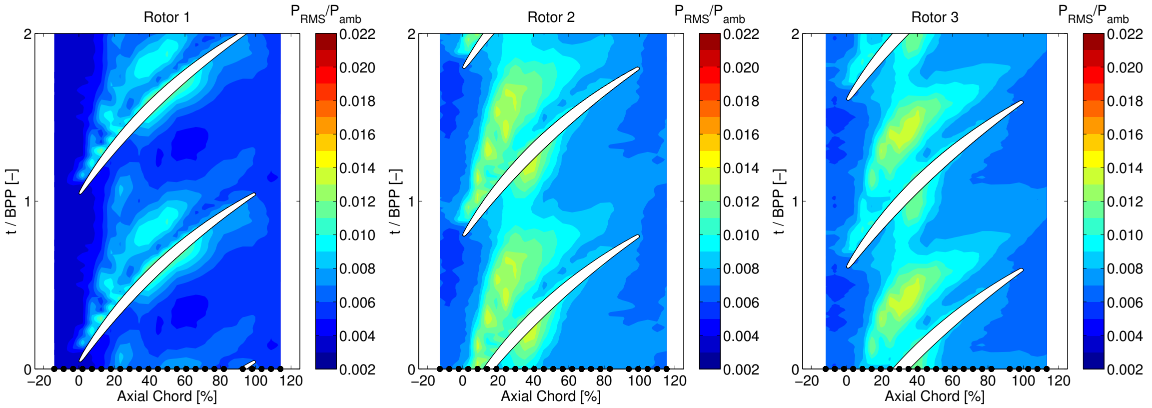

Figure 5.7: Static pressure unsteadiness, presented as an RMS, over each rotor for TC2 at HL.

5.1.2. Influence of Stator Wakes on Leakage Flow

The wealth of data presented so far for this project have suggested the loading condition of the compressor can affect the overall influence of the tip leakage flow. In particular, the over-rotor static pressure time series have shown the trajectory of the leakage flow through the rotor passage changes significantly as the compressor loading is increased toward stall. With this understanding, the rotor tip leakage flow can also be noticeably affected due to position with respect to the upstream stator vanes.

In the wake of a stator vane (i.e., Stator 1), the absolute velocity deficit creates a corresponding increase of incidence into the downstream rotor row (i.e., Rotor 2). The local increase of incidence angle loads up the front of the rotor, affecting the strength and trajectory of the tip leakage flow (Smith et al., 2015b). As a result, the location of the probe in the stationary frame of reference will dictate whether or not the measured flow parameter (pressure, velocity, etc.) will be affected by the rotor passing through the upstream vane wake.

This phenomenon is illustrated in Figure 5.8 with respect to the rotor passing through the upstream stator wake. In Figure 5.8(a), the rotor leading edge (Rotor 2, in this case) is positioned between stator wakes, and a corresponding velocity triangle is shown. At this location, the leakage flow propagates through the rotor passage and is measured by a series of probe locations at the rotor exit plane. In Figure 5.8(b), the rotor leading edge is located in the wake of the upstream stator, and the associated velocity triangle appears as a deficit of velocity in the absolute frame of reference. In this case, as the rotor loading increases, the leakage flow region increases in size, and the trajectory changes as its inception point moves upstream toward the rotor leading edge. The modulation of the tip leakage flow due to an interaction with the upstream stator wake has also been exemplified qualitatively using flow visualization photographs on the compressor casing endwall (Smith, 2015).

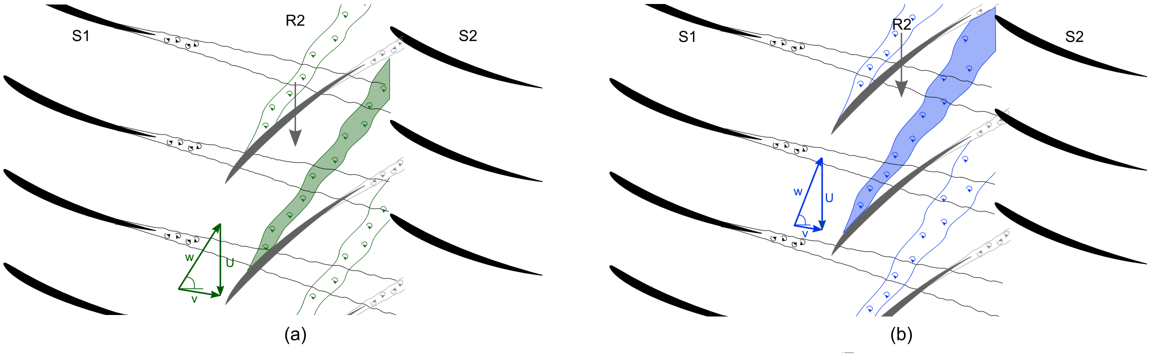

Figure 5.8: Schematic of the interaction between rotor tip leakage flow and upstream stator wake. (a) R2 passing in the middle of the S1 passage, (b) R2 passing through the S1 wake. Adapted from Smith et al. (2015b).

As suggested by the cartoon schematic in Figure 5.8, when the rotor passes through the upstream stator wake (in the absolute reference frame), the velocity deficit causes the position of leakage flow inception to move axially upstream. The strength of this modulation changes for Rotor 1 compared to Rotor 2 or Rotor 3 due to the difference of the IGV wake compared to wake of Stator 1 or Stator 2. The fundamentals of this rotor-stator interaction have been documented by few authors in the past (Moyle et al., 1996; Mailach et al., 2008; Krug et al., 2015), but a more in-depth analysis is desired to outline the effects of different tip clearances. The following measurements expand upon the findings of a recent study at part-speed operating conditions in the Purdue three-stage axial compressor (Smith et al., 2015b).

5.1.3. Stator Wake Effects on Leakage Flow Trajectory

As described above, the over-rotor static pressure measurements presented in preceding sections were all acquired at one fixed position with respect to the upstream and downstream vane rows. However, the interaction of the rotor tip leakage flow and the upstream stator wakes suggested by previous authors, and alluded to in the photographs from Smith (2015), motivates additional analysis. Thus, over-rotor static pressure measurements were repeated with the baseline tip clearance, TC1, at several loading conditions for each rotor.

The cartoon schematic in Figure 5.9 outlines the measurement process conducted using the over-rotor static pressure measurement array. The sensors for these measurements are in fixed positions in the compressor casing, but the stator vanes can be moved (either together or independently) relative to these sensors. Thus, Figure 5.9 shows representative measurements that may be measured at two vane positions with respect to the fixed measurement locations: (a) the sensors are located between the upstream stator wakes and measure the freestream flow, or (b) the sensors are approximately in the upstream stator wake. In each case, the time-resolved measurements are phase-locked with the rotor rotation, so the shaded measurement region identifies one blade passage of time-resolved static pressure data for each of the two vane positions. The cartoons in Figure 5.9 show measurements over Rotor 2 for which Stator 1 and Stator 2 are moved together, but similar measurements were collected over Rotor 1 and Rotor 3, and some data were also collected over Rotor 2 when Stator 1 and Stator 2 were moved independently from one another.

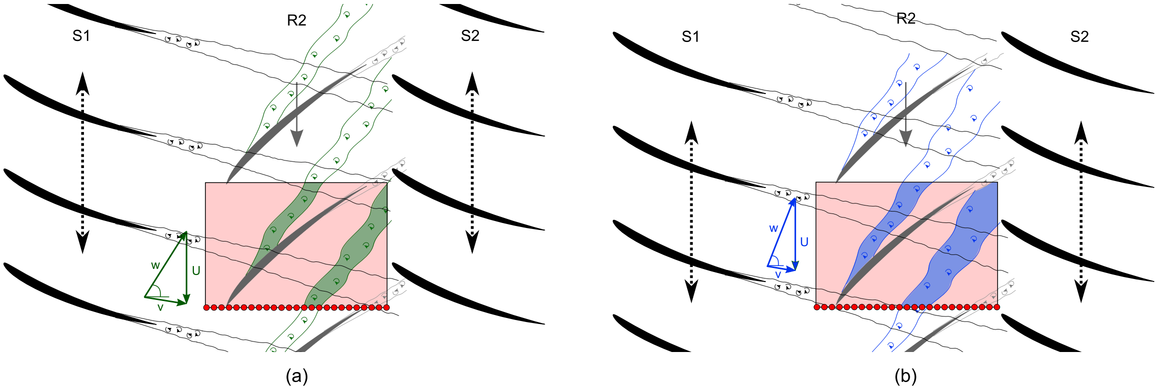

Figure 5.9: Schematic of leakage flow measurements over the rotor for two vane wake-leakage flow interaction positions, (a) and (b). A boxed region identifies a representative snapshot of the leakage flow identified by the static pressure measurements. Adapted from Smith et al. (2015b).

The first of these measurements, Figure 5.10, highlights the Rotor 1 leakage flow variations when moving all of the stator vanes simultaneously to 25 unique equally-spaced pitchwise positions with respect to the fixed high-frequency-response sensor positions for the nominal loading (NL) condition. Figure 5.10 shows the unsteadiness represented by the RMS with respect to the ensemble average. For each representation of the pressure measurements, the diagrams may be followed in a clockwise direction, as identified by the directional arrow.

To more clearly separate the modulation of the leakage flow from the 25 pitchwise positions shown in Figure 5.10, two of the pitchwise vane positions have been selected for comparison. These positions, identified in Figure 5.10 as vpA and vpB, are located approximately 50% vane passage out of phase from one another.

The RMS unsteadiness results for these two discrete vane positions are enlarged and compared in Figure 5.11(a-b). For these data, the leakage flow trajectories have been identified by connecting the locus of peak unsteadiness positions. The comparison of trajectories, Figure 5.11(c), shows an identifiable difference between the trajectories for the two vane positions, vpA and vpB. This difference may seem small, but it is significant, especially compared to the effects observed for different tip clearances and loading conditions – as will be shown in further analyses.

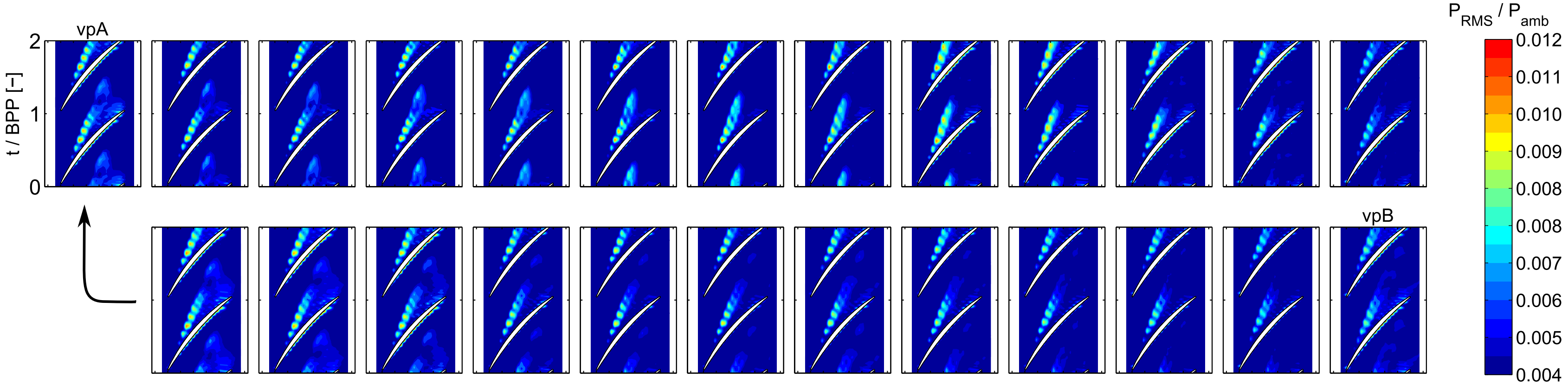

Figure 5.10: Static pressure over Rotor 1, averaged for all 36 blades, in terms of RMS static pressure, at each pitchwise position across one vane passage (clockwise) for TC1 at NL.

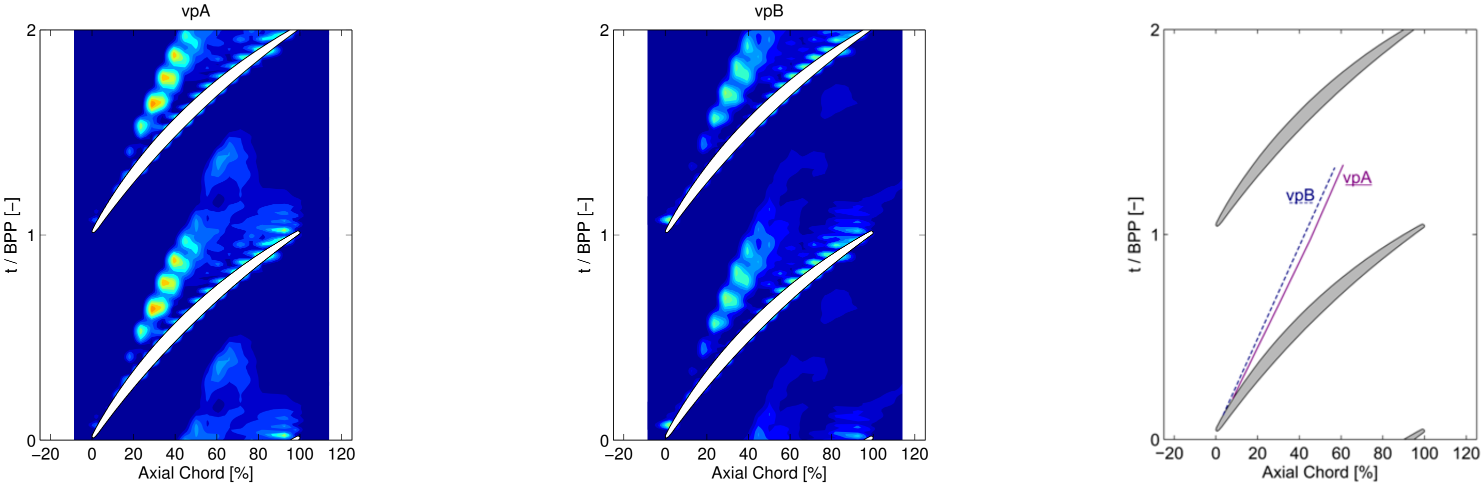

(a) (b) (c)

Figure 5.11: Static pressure unsteadiness (RMS) over Rotor 1 for vpA (a) and vpB (b) from Figure 5.10, and the trajectories (c).

The results from Figure 5.10 and Figure 5.11 identified a modulation of the leakage flow trajectory which agrees with flow visualization photographs (Smith, 2015). However, the IGV wake is expected to have a smaller effect on the leakage flow for Rotor 1 than the Stator 1 or Stator 2 wakes for Rotor 2 and Rotor 3, respectively. Furthermore, it is important here to more clearly distinguish the effects of the upstream vane row from those of the downstream vane row to ensure that the downstream potential field does not significantly impact the leakage flow development. Thus, the static pressures over Rotor 2 were chosen to investigate both of these hypotheses.

To address these questions, two separate vane movement processes were introduced – effectively clocking the position of the IGV and Stator 1 with respect to Stator 2 and Stator 3. (Recall that IGV, Stator 1, and Stator 2 all have the same vane count of 44, which allows vane clocking studies in this facility.) Specifically, the first method moved IGV and Stator 1 simultaneously to the same 25 pitchwise positions as for Figure 5.10, while Stator 2 and Stator 3 were maintained in fixed locations. In the second method, Stator 2 and Stator 3 were moved simultaneously to the 25 pitchwise positions while the IGV and Stator 1 were held fixed.

The calculated RMS unsteadiness pressures from this two-movement process are presented in Figure 5.12 at NL. This figure shows results for the first movement (Move IGV & S1, Fix S2 & S3) for the 25 pitchwise positions. As before, two of these positions are identified as vpA and vpB, and the results for those two vane positions are shown in Figure 5.13(a-b). Comparing the RMS unsteadiness from these two pitchwise vane positions, there is a region of high unsteadiness appearing for positions greater than 70% axial chord for vpB which does not appear for vpA. Referring to Figure 5.12, this region of high unsteadiness appears and disappears while moving clockwise around the 25 pitchwise positions. In addition, the trajectory is also compared for these two identified vane positions, in Figure 5.13(c). For this first vane movement process, the trajectory of the leakage flow modulates between vpA and vpB. In this case, the relative trajectories of vpA and vpB are opposite from the results shown in Figure 5.11(c). The positions of the IGV and Stator 1 with respect to the measurement sensors are nearly identical, but it is expected that the IGV wake will affect Rotor 1 differently than the effect of Stator 1 on Rotor 2 due the nature of the IGV as an accelerating vane row. This first vane movement process has isolated the upstream vanes from the downstream vanes for Rotor 2 to emphasize the effect of the upstream vane row on the leakage flow development.

A similar analysis of RMS unsteadiness is also presented for the second vane movement process (Move S2 & S3, Fix IGV & S1), Figure 5.14. For this case, the 25 positions in Figure 5.14 may identify a slight change of the static pressure unsteadiness near the trailing edge of the rotor blades where the downstream vane row may affect the flow, but there is no appreciable change of the leakage flow pattern or trajectory throughout the 25 positions. This becomes more apparent by selecting the same two relative positions, identified as vpA and vpB for comparison in Figure 5.15(a-b). The RMS unsteadiness for these two positions is nearly identical, and the trajectories traced in Figure 5.15(c) reinforce this invariability. Ultimately, these results in Figure 5.12 through Figure 5.15 highlight the effect that the upstream vane wakes may impose on the tip leakage flow (as suggested in the schematic of Figure 5.8), and they separate observations from the potential field associated with the downstream vane row.

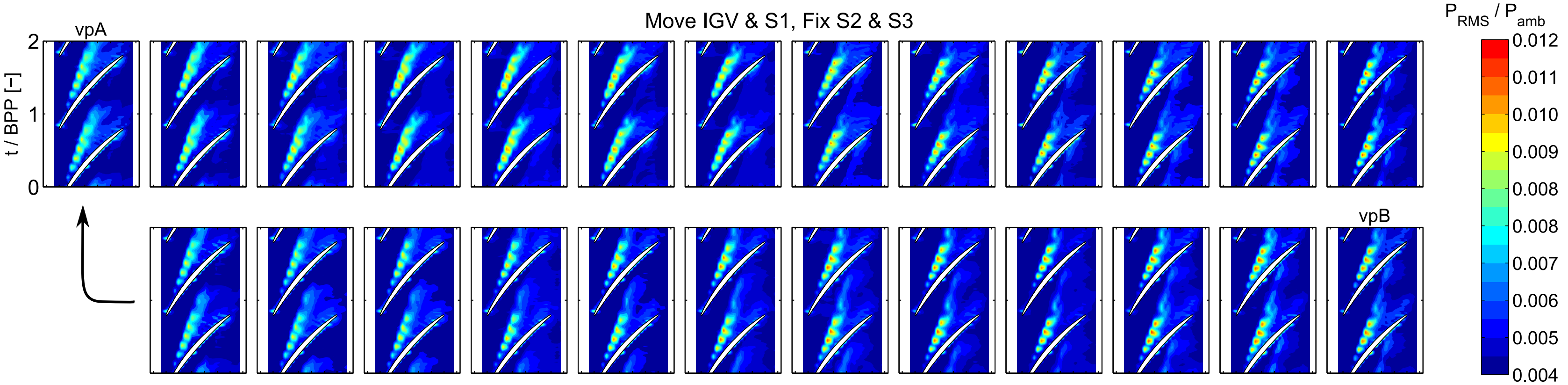

Figure 5.12: Static pressure over Rotor 2, averaged for all 33 blades, in terms of RMS static pressure, at each pitchwise position across one vane passage (clockwise) for TC1 at NL. Only IGV and S1 are moved, S2 and S3 are fixed.

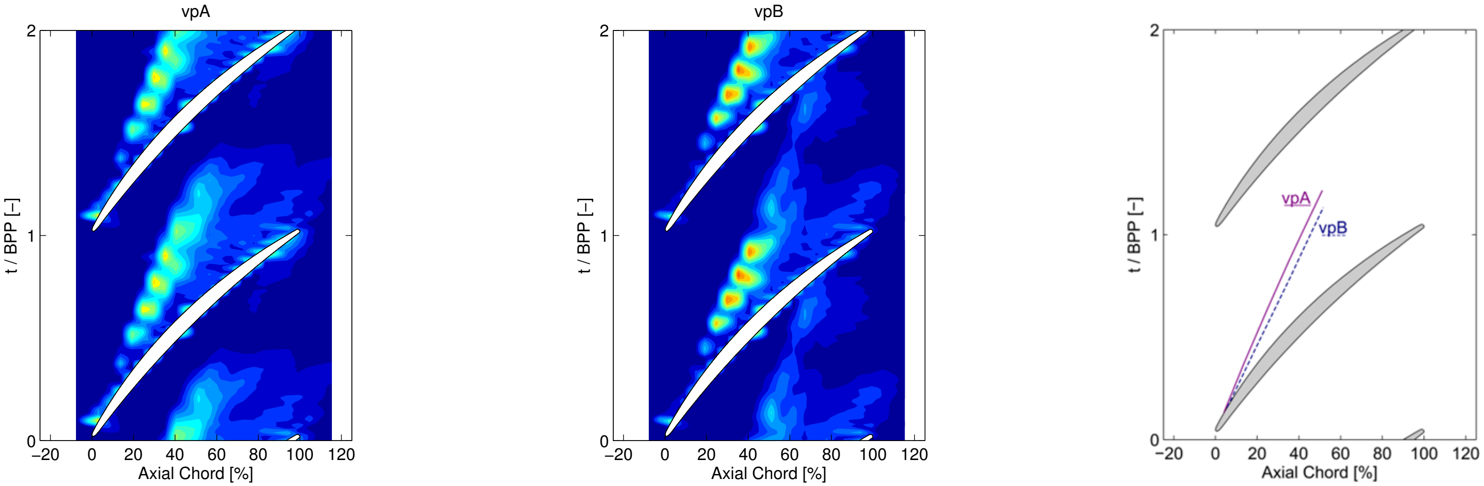

(a)

(b)

(c)

Figure 5.13: Static pressure unsteadiness (RMS) over Rotor 2 for vpA (a) and vpB (b) from Figure 5.12, and the trajectories (c).

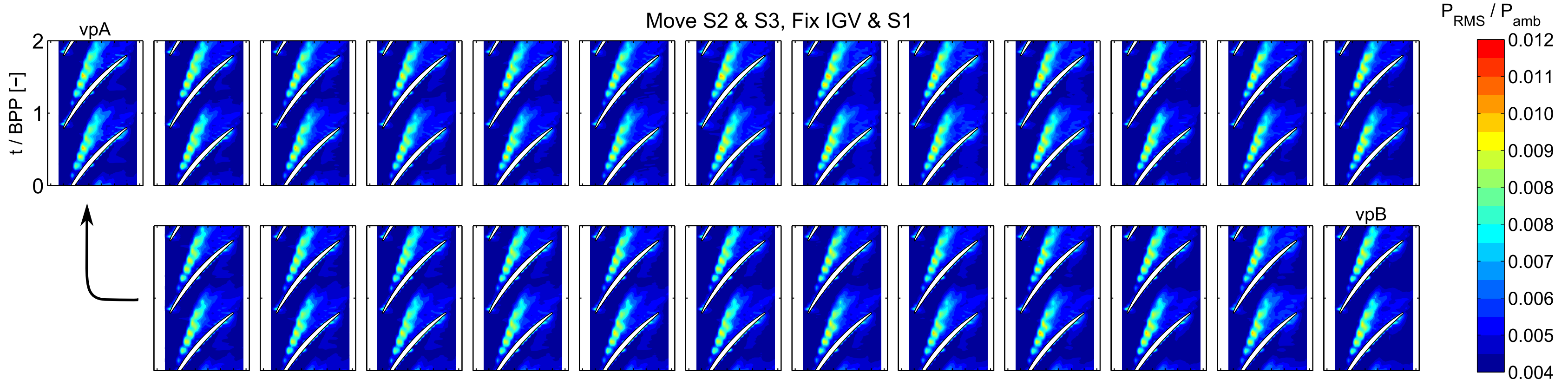

Figure 5.14: Static pressure over Rotor 2, averaged for all 33 blades, in terms of RMS static pressure, at each pitchwise position across one vane passage (clockwise) for TC1 at NL. Only S2 and S3 are moved, IGV and S1 are fixed.

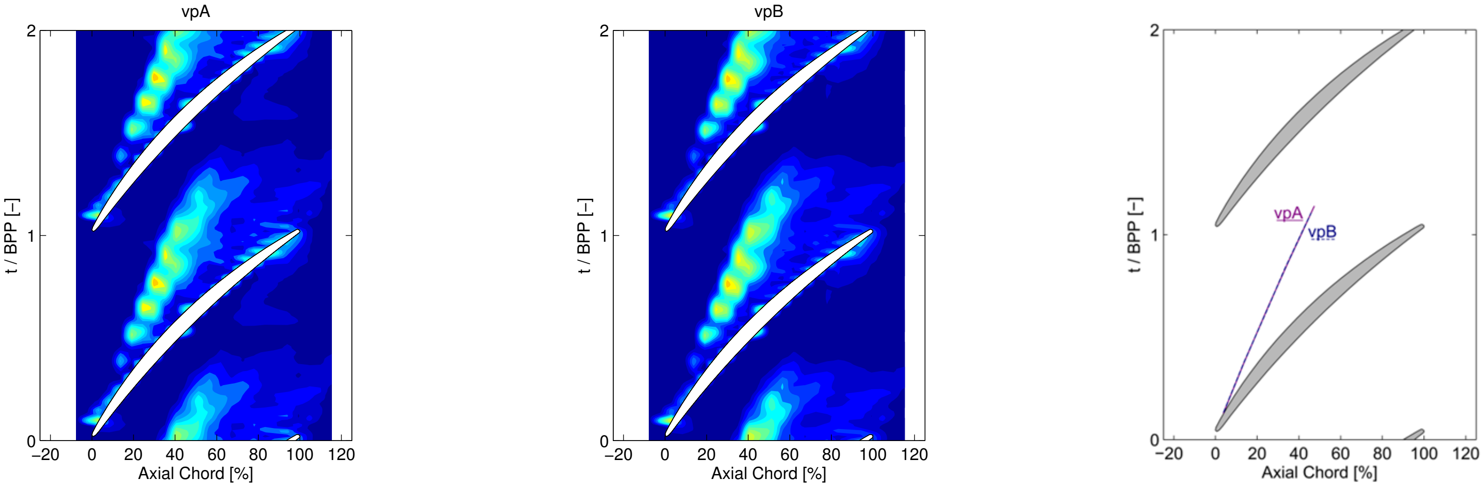

(a)

(b)

(c)

Figure 5.15: Static pressure unsteadiness (RMS) over Rotor 2 for vpA (a) and vpB (b) from Figure 5.14, and the trajectories (c).

To this point, the Rotor 1 leakage flow trajectory modulation was identified at the nominal loading condition. However, the IGV is expected to affect the Rotor 1 flow field differently than the downstream stators will affect the rotors of the latter stages. As a result, the static pressures over Rotor 2 were analyzed using two separate vane movement processes to investigate the embedded stage and separate the effects of the upstream vane wakes from the downstream potential field. At this point, further analysis is warranted to evaluate the effect of changing loading condition, and Rotor 3 was selected as the vehicle for this analysis.

Figure 5.16 identifies a modulation of the leakage flow trajectory for Rotor 3 using the simultaneous movement of all vane rows described previously for Figure 5.10. In Figure 5.16, the Rotor 3 unsteadiness data at the nominal loading (NL) condition show the modulation of the leakage flow for the 25 vane positions. Considering the pitchwise position identified as vpA, highlighted in Figure 5.17(a), the locations of high RMS are identified to approximately mid-chord, and then attenuate slightly prior to reappearing as a high-intensity region at the intersection with the trailing edge of the adjacent blade. In contrast, for vpB (Figure 5.17(b)), the high RMS regions begin to attenuate further forward in the passage (near 60% axial chord), but the high-intensity region at the trailing edge also moved forward in the passage to approximately 80% axial chord. For Rotor 3 at this NL condition, the trajectories identified in Figure 5.17(c) vary less than the results shown previously for Rotor 1 or Rotor 2 at the same loading condition.

At the high loading (HL) operating condition for Rotor 3 in Figure 5.18, a similar trend can also be identified. The comparison of vpA and vpB at this HL condition in Figure 5.19(a-b) shows a more dramatic difference than for the NL condition. At HL,

Figure 5.19(a) shows the high unsteadiness region of the leakage flow attenuates at approximately 40% axial chord before reappearing as a region of high unsteadiness at its intersection with the adjacent blade, near 65% axial chord. In contrast, Figure 5.19(b) shows for vpB that the same attenuation occurs near 40% axial chord, but the "island" of high unsteadiness can then be identified near 55% axial chord, but not in contact with the adjacent blade. However, Figure 5.19(b) also shows a region of high unsteadiness in contact with the adjacent blade centered near 85% axial chord which does not align with the trajectory path connecting the locus of high unsteadiness for the rest of the passage. The leakage flows in Figure 5.19(a-b) are clearly different, and their approximate trajectories are traced in Figure 5.19(c).

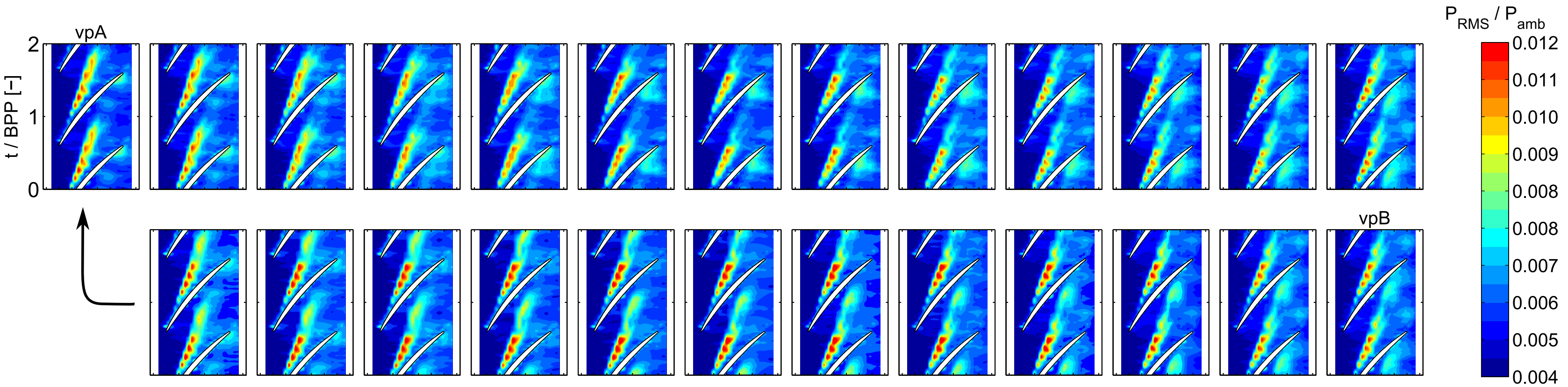

Figure 5.16: Static pressure over Rotor 3, averaged for all 30 blades, in terms of RMS static pressure, at each pitchwise position across one vane passage (clockwise) for TC1 at NL using two separate vane movement techniques.

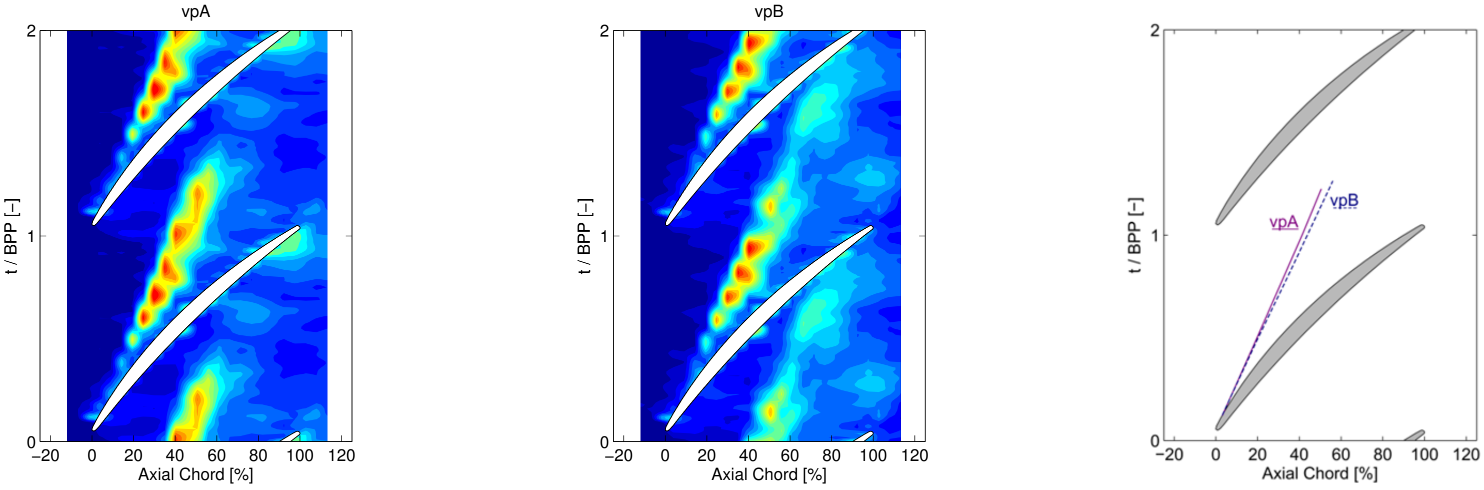

(a)

(b)

(c)

Figure 5.17: Static pressure unsteadiness over Rotor 3 for vpA (a) and vpB (b) from Figure 5.16, and trajectories (c) (TC1, NL).

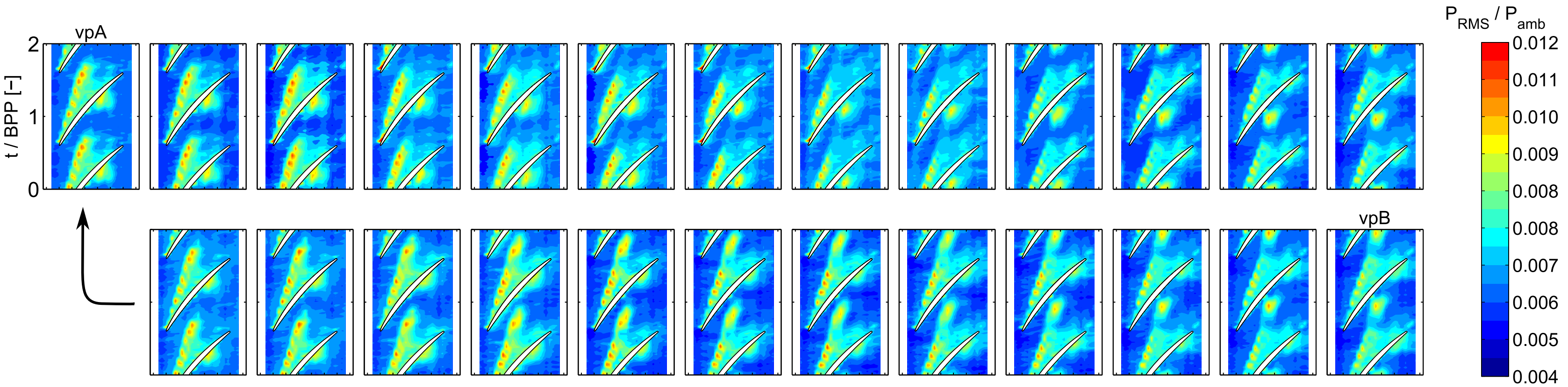

Figure 5.18: Static pressure over Rotor 3, averaged for all 30 blades, in terms of RMS static pressure, at each pitchwise position across one vane passage (clockwise) for TC1 at HL.

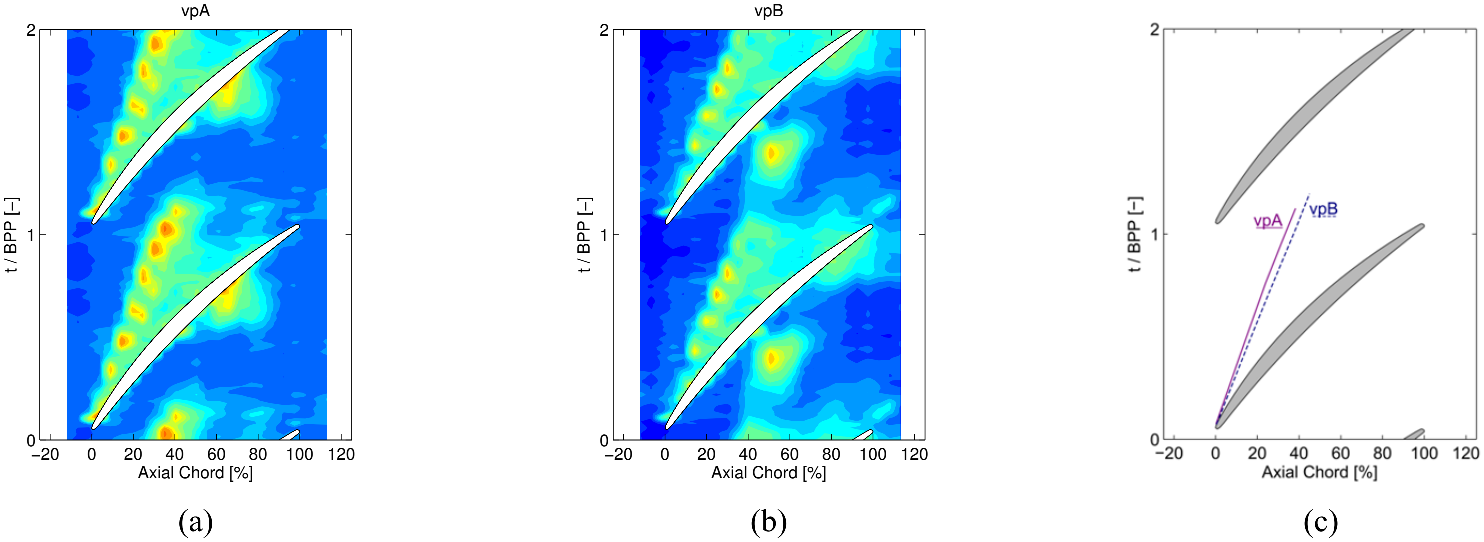

(a) (b) (c)

Figure 5.19: Static pressure unsteadiness over Rotor 3 for vpA (a) and vpB (b) from Figure 5.18, and trajectories (c) (TC1, HL).

5.1.4. Blade-to-Blade Leakage Flow Variability

In general, compressor measurements associated with the rotor are often considered in an average form, neglecting variations which may exist from one blade to the next – similar to the results presented in Figure 5.1 and Figure 5.2. However, small manufacturing defects in the blade hardware and blade row interactions within the machine can create substantial variations which must be considered, as identified in rotor wake variability studies by previous authors (Sherman et al., 1996; Boyd and Fleeter, 2003; Key et al., 2010; Smith et al., 2015b). As a result, in addition to the influence of upstream stator vane wakes on the tip leakage flow, it is also desirable to investigate blade-to-blade variations of the tip leakage flow.

As explained earlier, the runout of the rotor blade tips has been evaluated to discern the blade-to-blade variation of static tip clearance. This information (Figure 2.8) shows that the blade-to-blade tip clearance varies on the order of 3×10^{-3} to 5×10^{-3} in. (depending on rotor row) around the circumference of the rotor. However, there is also a particularly large discrepancy for Blade 9 of Rotor 3, which shows a significant increase of tip clearance of approximately 1×10^{-3} in. compared to its adjacent blades.

Based on this blade-to-blade variability information, it is expected that a discernable change of tip leakage flow pattern may be identified for Blade 9 of Rotor 3. Indeed, if the RMS results for Rotor 3 are maintained as 30 separate data sets (one for each blade) instead of an “average blade” representing the entire row, Figure 5.20 shows that Blade 9 can be easily identified by its leakage flow pattern which differs noticeably from its adjacent blades. In this case, the local tip clearance increase for Blade 9 creates a larger region of high unsteadiness identified by the RMS which is dispersed throughout the blade passage, compared with the more localized trajectories crossing the blade passage for the other blades. This phenomenon can be qualitatively compared with the change of leakage flow pattern with increased clearance height in Figure 5.2.

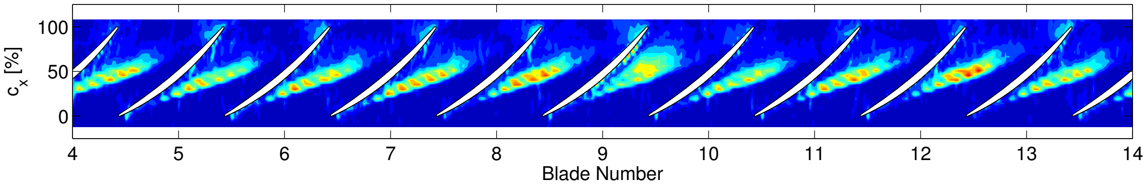

Figure 5.20: Blade-to-blade leakage flow pattern variability for Rotor 3 with TC1 at NL.

Aside from the differences for Blade 9 identified in Figure 5.20, blade-to-blade variations of the tip leakage flow are also visible for other blades which do not necessarily correlate with the clearance variations in Figure 2.8. Figure 5.21 shows a similar comparison of blade-to-blade leakage flow variability, but for all 30 blades from the Rotor 3 row at the larger tip clearance TC3. In Figure 5.21, the 30 blades have been segmented into three 10-blade series.

For this facility, the difference of blade counts between Rotor 1, Rotor 2, and Rotor 3 (36, 33, and 30, respectively) introduces a 3/rev modulation of the flow field for both Rotor 2 and Rotor 3. Figure 5.21 highlights the effect of this 3/rev modulation on the tip leakage flow. If the EA static pressure signals are assessed, troughs of this 3/rev modulation exist at blade numbers of approximately 3, 13, and 23, and peaks are located at blade numbers of 8, 18, and 28. The data in Figure 5.21 identify these same trends as the 3/rev troughs at Blades 3, 13, and 23 show lower leakage flow intensities than the peaks at Blades 8, 18, and 28.

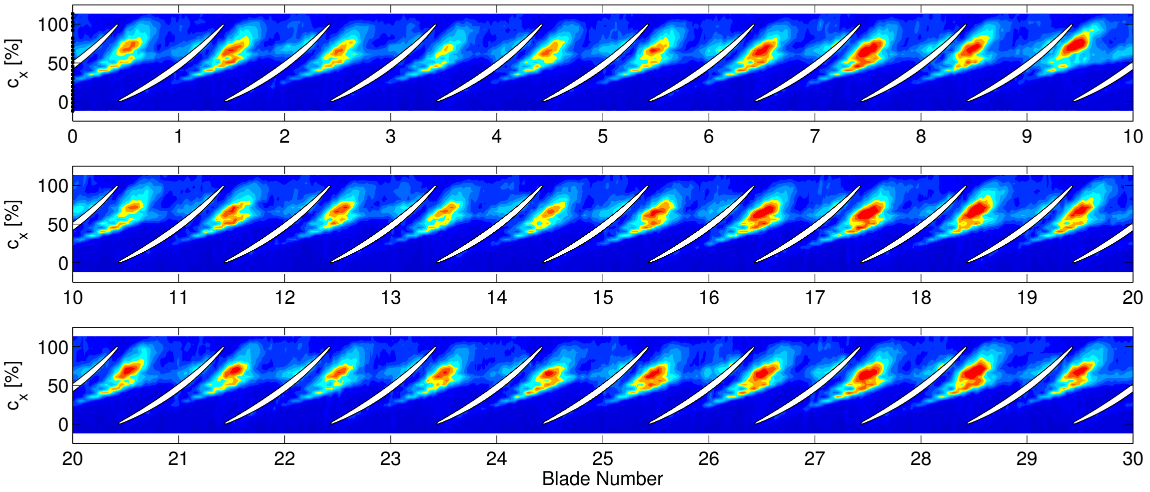

Figure 5.21: Blade-to-blade leakage flow pattern variability for Rotor 3 with TC3 at NL.

However, the results in Figure 5.21 tell an additional story as the 3/rev modulation is superimposed with the 1/rev tip clearance variations identified for Rotor 3 in Figure 2.8. A specific comparison of the leakage flow pattern for Blades 3, 13, and 23 (the troughs of the 3/rev modulation) shows highest intensity in the leakage flow for Blade 23 and lowest intensity (with more dispersed unsteadiness) for Blade 3. Referring to Figure 2.8, this aligns with an observation that larger clearance heights lead to decreased unsteadiness intensity in the leakage flow region as it is more dispersed through the blade passage.

Based on the data shown in Figure 5.20 and Figure 5.21, it is determined that the effect of small blade-to-blade tip clearance variations, such as the one identified for Blade 9 from Rotor 3, are most noticeable in the leakage flow unsteadiness if the tip clearance height is small (i.e., TC1 instead of TC3). This observation is due to the fact that a 1×10^{-3} in. change represents a larger fraction of the overall clearance height for TC1 (nominally 0.030 in.) than for TC3 (nominally 0.080 in.).

An in-depth investigation of the spectral content for these over-rotor static pressures uncovers additional information. The Fourier transforms are shown in Figure 5.22 for frequencies up to the 50 engine order (EO) based on the rotor revolution frequency. The data in Figure 5.22 correspond to measurements at the 9% axial chord position, which was selected in this case because it represents the approximate position of inception for the tip leakage flow. As the rotor tip clearance is increased from TC1 to TC3 in Figure 5.22, these Rotor 3 measurements show additional energy in the 36/rev component propagating from the Rotor 1. This is expected as the larger tip clearance leads to a more intense (as measured by the flush-mounted sensors) tip leakage flow structure from each rotor (with the same frequency as the blade passing frequency of the rotor) which persists through the downstream blade rows.

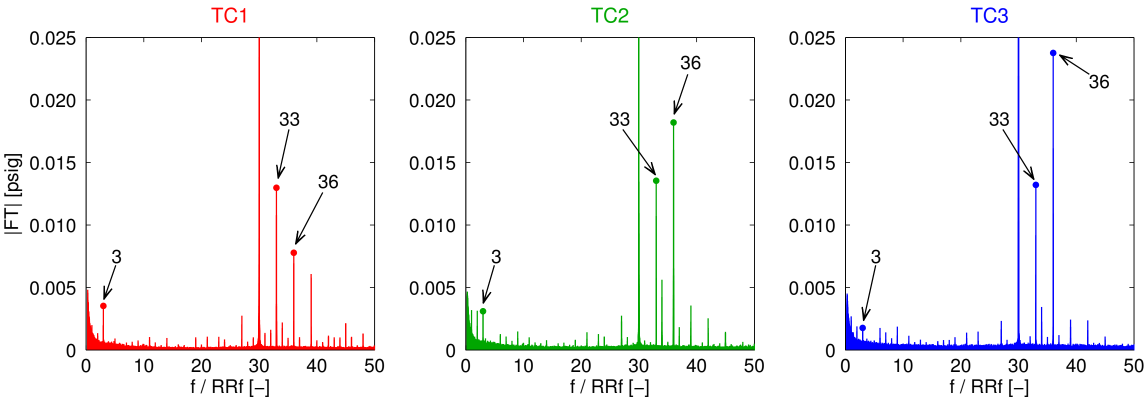

Figure 5.22: Spectral magnitudes of Rotor 3 pressure measurements at 9% axial chord for NL condition.

The spectral magnitudes from each sensor are also shown for the 3/rev, 30/rev, 33/rev, and 36/rev components in Figure 5.23. Figure 5.21 identified a rotor-rotor interaction of the tip leakage flow with an apparent frequency of 3/rev which is more pronounced for TC3 than TC1. However, the spectral content in Figure 5.22 and Figure 5.23 show that the 3/rev magnitudes decrease as the tip clearance is increased. For these larger tip clearance configurations, the 3/rev energy appears to be redistributed to other frequencies (e.g., 6/rev and 9/rev). Here, the 3/rev modulation of the leakage flow identified in Figure 5.21 is caused by the incoming wakes, and the corresponding frequency content is not necessarily expected to be sensed by the static pressure sensors.

As shown in Figure 5.22, the 36/rev component associated with Rotor 1 increases with tip clearance at the leading edge of Rotor 3, but the three tip clearances become more uniform as the 36/rev magnitudes decrease toward the trailing edge. In contrast, the 33/rev magnitudes are nearly uniform near the leading edge, whereas the larger tip clearance shows magnitudes increasing toward the trailing edge.

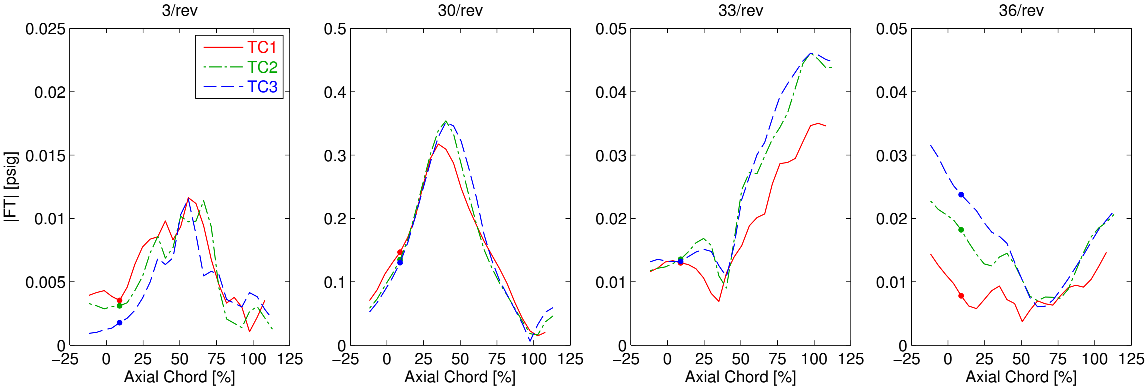

Figure 5.23: Spectral magnitudes from each sensor for selected frequency components from Figure 5.22.

Understandably, the observed change in the 36/rev content could be due to a combination of the 33/rev + 3/rev or the 30/rev + 6/rev content. In this case, though, the 33/rev magnitude is constant across all tip clearances while the 3/rev decreases, and the

6/rev magnitudes do not change significantly enough to cause the observed effect of the 36/rev magnitude. Although the 30/rev peaks are not shown in the scale of Figure 5.22, the trends in Figure 5.23 show the relative change of magnitude at the 30/rev frequency is less than 10% of the changes noted for the 36/rev peaks.

Based on these results in Figure 5.22 and Figure 5.23, an increase of tip clearance appears to cause the spectral magnitude from an upstream rotor blade passing frequency to increase only after propagating through a second rotor blade. In this case, the increased tip clearance causes an increase of the Rotor 1 frequency content sensed by Rotor 3.

Similar to the stator wake interactions highlighted in Section 5.1.3, the blade-to-blade variations identified in Figure 5.20 and Figure 5.21 are also important for quantifying changes of the tip leakage flow angle. In this case, the leakage flow angle, ξ, is defined with reference to an axial reference datum, as shown in Figure 5.24. In Figure 5.24, two leakage flow trajectories are shown for Rotor 1 and Rotor 3 at each loading condition, NL and HL. The minimum and maximum traces define the envelope of trajectory angles representing the blade-to-blade variations. This angular envelope for Rotor 1 is 1.8 degrees for both NL and HL. The blade-to-blade variation of trajectory angle shows no discernible trend with the tip clearance height, and no rotor-rotor interactions are expected for the Rotor 1 results.

However, several differences exist for the Rotor 3 results in Figure 5.24 compared to Rotor 1. In particular, the envelope of blade-to-blade trajectory angle variation for Rotor 3 is 1.5 degrees for NL, but increases to 2.2 degrees for HL. Also, the axial location of leakage flow inception and the leakage flow trajectory angle are more similar between the NL and HL positions for Rotor 3 than for Rotor 1. In this case, although a weak trend of trajectory angle with blade-to-blade tip clearance variation exists, there is no discernible trend associated with the other engine-order frequencies introduced previously. Although not shown here, the Rotor 2 envelopes are identical to the Rotor 3 trends (1.5 and 2.2 degrees for NL and HL respectively).

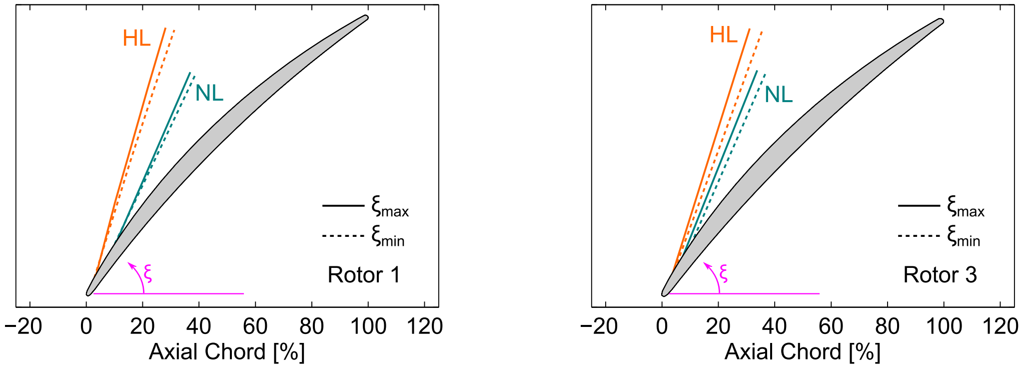

Figure 5.24: Maximum and minimum leakage flow angle variations for Rotor 1 and Rotor 3 (TC1).

5.1.5. Quantifying Tip Leakage Flow Trajectory

Using the leakage flow trajectory identification techniques presented herein, the angle of the leakage flow trajectory can be determined. Because the sensors are flush-mounted with the casing inner diameter, the distance between the sensors and the blade increases with tip clearance. As a result, the pressure and RMS levels will not have the same magnitude across tip clearances. Thus, the trajectory angle provides a unique method for assessing differences associated with different tip clearances.

The results from the present study are shown for each of the three rotors at the four loading conditions in Figure 5.25. Several of the NL and HL data points for TC1 in

Figure 5.25 also include range bars which identify the variations of tip leakage trajectory angle associated with the modulation of the tip leakage flow due to the upstream vane wakes (as calculated using information similar to Figure 5.13). The data in Figure 5.25 are again presented as a function of averaged measured tip clearances instead of the "nominal" design values. These operating clearances account for thermal growth differences related to changes in loading and ambient temperature discussed by Berdanier and Key (2015a).

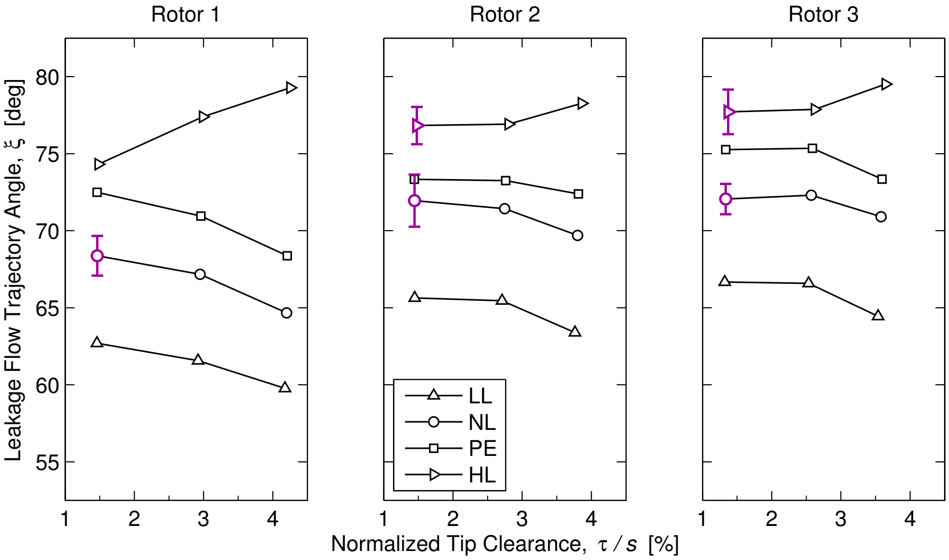

Figure 5.25: Leakage flow trajectory angle versus normalized clearance height. Range bars identify change of trajectory angle due to interaction with the upstream vane wake.

The results in Figure 5.25 highlight several important trends. In particular, the leakage flow trajectory angles appear to change differently for Rotor 1 than for Rotor 2 and Rotor 3, both of which show similar trends at all four loading conditions. In general, though, there is a consistent trend of decreasing trajectory angle with increasing tip clearance for LL, NL, and PE, but an increasing trend for the HL condition. This observation aligns with the observation that all rotors experience loading levels for HL which are at closer proximity to the stall point as the tip clearance height is increased.

The results for Rotor 1 in Figure 5.25 show that the leakage trajectory angles vary almost linearly with increasing rotor tip clearance for the range of clearances investigated in the present study. In contrast to these Rotor 1 observations, the data for Rotor 2 and Rotor 3 show insignificant changes of leakage flow trajectory angle for a tip clearance change from TC1 to TC2. This noted difference for Rotor 2 and Rotor 3 is crucial to this study because it shows a trend which would be otherwise overlooked if only two tip clearances were studied. This difference of leakage flow trajectory angles between Rotor 1 and the other two rotor rows agrees with previous observations in this facility noting a difference of Rotor 1 performance with increased tip clearance.

Results similar to the measurements presented in Figure 5.25 have also been collected by Yoon et al. (2006) over Rotor 3 in a four-stage low-speed research compressor with repeating stages. A comparison of the Rotor 3 results from the present study with the measurements collected by Yoon et al. is shown in Figure 5.26.

Previous authors have introduced the clearance derivative as a method for evaluating the change of a particular parameter with changes in tip clearance. In this case, a clearance derivative for leakage flow trajectory angle is defined with respect to the clearance-to-pitch ratio:

$$\delta_{\xi} = \frac{\Delta\xi}{\Delta(\tau/s)}. \tag{5.3}$$

In Figure 5.25 and Figure 5.26, the clearance-to-pitch ratio was selected instead of the clearance-to-chord ratio used by Yoon et al. (2006) (or clearance-to-span, which is typically used as a metric for efficiency changes) to present trajectory angle changes. The clearance-to-pitch ratio was chosen to avoid discrepancies of aspect ratio between the two facilities compared in Figure 5.26. A comparison between the four-stage low-speed research compressor used by Yoon et al. with the machine used for the present study shows a difference of aspect ratio from approximately 1.2 to approximately 0.7, respectively.

The relationship between pitch and blade loading, as well as the contribution of pitch as a representative length scale in the measurement plane over the rotor, combined to guide the selection of clearance-to-pitch as the representative metric for comparison. However, the relative dissimilarity of blade pitch for Yoon et al. (2006) and the present study creates an opportunity to evaluate the dependence of observed trends to a particular compressor design.

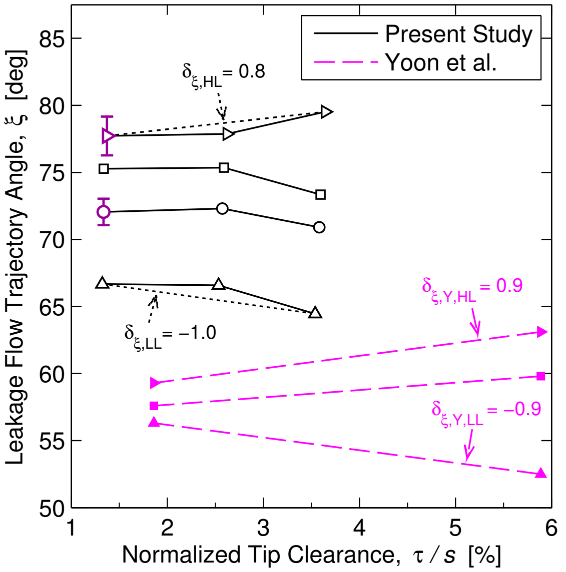

Figure 5.26: Rotor 3 leakage flow trajectory trends compared with results from Yoon et al. (2006).

A comparison of the results from the present study in Figure 5.26 with the data presented by Yoon et al. (2006) shows good agreement using the clearance-to-pitch ratio on the abscissa. Especially at the LL and HL conditions, the clearance derivatives are nearly identical when the widest tip clearance range is considered for the present study (TC1 to TC3). However, the absence of a third tip clearance configuration for Yoon et al. makes it difficult to conclude whether the same non-linear trend is expected for any multistage compressor. For reference, if the Rotor 2 results from the present study are selected for comparison with Yoon et al. instead of Rotor 3, the results are also similar based on the nearly identical trends between Rotor 2 and Rotor 3 in Figure 5.25.

As a rule-of-thumb, these data suggest that the leakage flow trajectory angle will decrease approximately one degree for every one percent increase of clearance-to-pitch at high flow rates (when incidence is expectedly negative). Similarly, approximately one degree of trajectory angle increase is predicted for every one percent of clearance-to-pitch when rotor incidence is large and positive. Although these data show rules of thumb which may apply for large clearance changes, it is very important to observe that a critical clearance may exist, leading to significant differences of the clearance derivative for leakage flow angle assessed here. For the present study, the critical clearance represents the TC2 clearance height. By this proposed effect, a change from a “small” to a “moderate” clearance height (i.e., TC1 to TC2) may be met by little or no change of leakage flow angle, whereas a change from a “moderate” to “large” clearance height (i.e., TC2 to TC3) may incur significant changes.

Further comparison of the present study results in Figure 5.26 with the data from Yoon et al. (2006) also shows that the peak efficiency point from the comparison study has a positive clearance derivative which was not observed in the present study. Based on the rule-of-thumb trends suggested here, it is assumed that the rotor may operate at a higher loading at the peak efficiency point for the machine investigated by Yoon et al. than the compressor in the present study.

For all rotors, the range bars in Figure 5.26 show that the leakage flow modulation associated with the upstream vane wake has a profound influence on the leakage flow. In fact, the change of leakage flow angle due to this stator-rotor interaction is greater than the change due to a doubling of the tip clearance height (TC1 to TC2). Additional research may be required to determine whether the observed leakage flow angle ranges identified for the TC1 loading conditions in Figure 5.25 are similarly present for other clearance configurations and loading conditions. At this point, however, there is sufficient information to determine that the stator-rotor interaction plays a significant role in the development of the tip leakage flow, and this relationship must be considered when comparing experimental data with computational results.

5.2. Rotor Exit Total Pressures

5.2.1. Influence of Stator Wakes on Leakage Flow at Rotor Exit Planes

To further capture the effect of the upstream vane wake on the rotor tip leakage flow, the time-resolved total pressure measurements downstream of the rotor blade rows have been completed for up to 28 radial positions at each of the 26 pitchwise positions (pp) across one vane pitch. (Of these 26 positions, 25 are *unique* positions, since one pair of positions, pp1 and pp26, are periodic with respect to the vane pitch.) The cartoon schematic in Figure 5.27 shows the relative locations of the probe positions at the rotor exit plane for simultaneous movements of all vane rows as the rotor interacts with the upstream vane wake to modulate the rotor tip leakage flow.

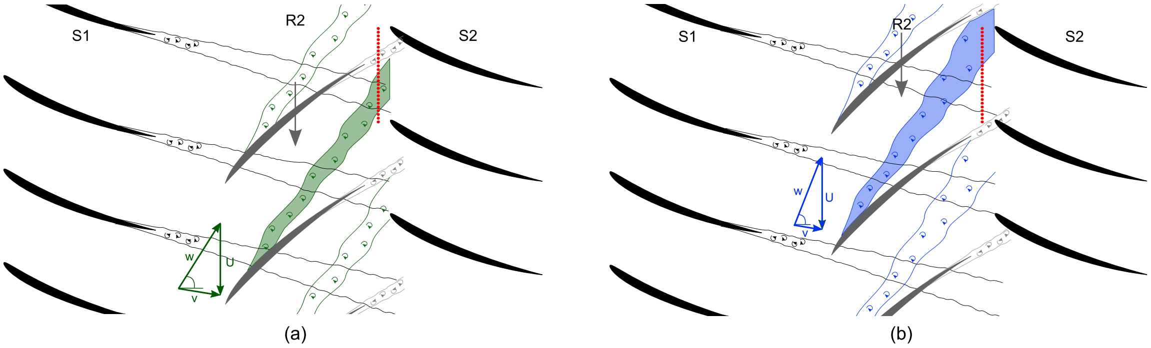

Figure 5.27: Schematic of leakage flow measurements at rotor exit planes for two vane wake-leakage flow interaction positions, (a) and (b). Adapted from Smith et al. (2015b).

The time-resolved total pressure measurements are presented here as an unsteadiness using the RMS with respect to the ensemble average, as defined in Equation (5.2). This presentation of results accommodates the identification of recirculating flow regions expected in the tip leakage flow disturbance, as well as the rotor wake. These RMS measurements are presented for the Rotor 1 exit plane at the NL and HL operating conditions in Figure 5.28 and Figure 5.29, respectively.

In these figures, the RMS with respect to the ensemble average (pertaining to 500 revolutions, for these data) has been calculated at each circumferential vane position, and then averaged across all rotor blades (36 blades for Rotor 1) to identify an averaged rotor passage. The IGV wake is very thin and has a minimal effect on the downstream rotor row. As a result, Figure 5.28 and Figure 5.29 show a weak modulation of the tip leakage flow across one vane pitch (following the figures in a clockwise direction, denoted by the titles pp1-pp26). However, an increased unsteadiness at the center of the leakage flow region is identifiable, particularly for the TC3 tip clearance configuration measurements at the NL operating condition in Figure 5.28. In addition to the pitchwise modulation of the flow field exemplified by the 26 circumferential measurement positions, a mean contour represents the rotor wake averaged across one vane pitch. The PS and SS of the rotor blade are also labeled in this mean contour to orient the figure.

At the nominal loading condition, Figure 5.28, a clear distinction can be made between the tip leakage flow regions for each of the tip clearance configurations, TC1 and TC3. For the smaller tip clearance, the unsteadiness due to the tip leakage flow occupies a region which extends down from the outer casing endwall to approximately 80% annulus height, whereas the larger tip clearance height shows a leakage flow region which reaches approximately 70% annulus height, as well as affecting a noticeably larger area in the pitchwise direction.

At the same Rotor 1 exit position for the HL operating condition, Figure 5.29 shows the TC1 leakage flow region no longer has a coherent circular shape, but rather fills a corner area adjacent to the pressure side of the rotor wake. The TC3 tip clearance configuration, on the other hand, maintains a shape which closely resembles the result from the NL condition in Figure 5.28. However, its size and relative intensity of the unsteadiness parameter are both increased at the higher loading condition. Also at the HL condition, both tip clearance configurations show a noticeable change as the hub corner separation off the suction surface, previously observed at NL, grows into a thick wake which extends above 50% annulus height.

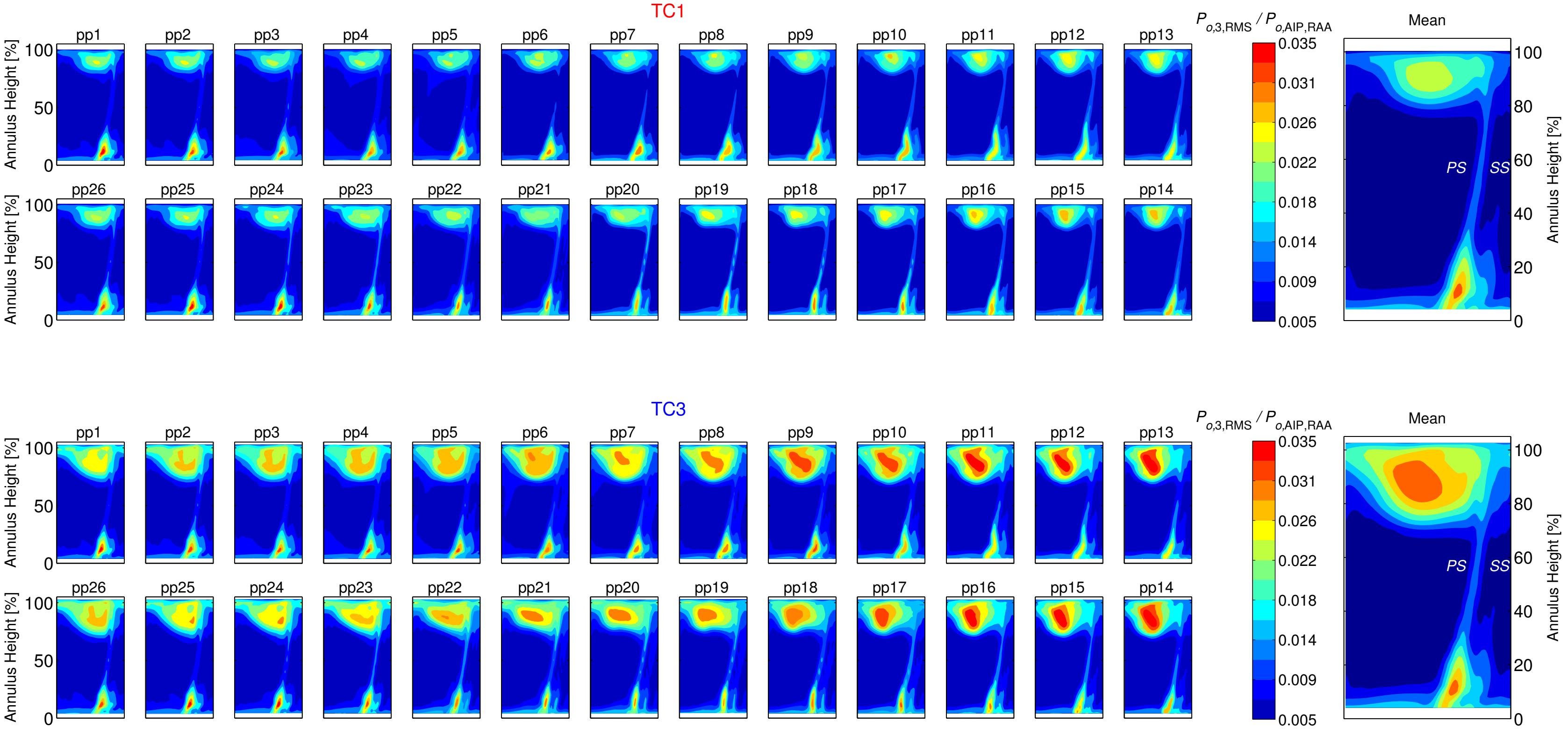

Figure 5.28: Average Rotor 1 exit flow field, in terms of RMS total pressure, at each circumferential location across one vane passage (clockwise) at NL.

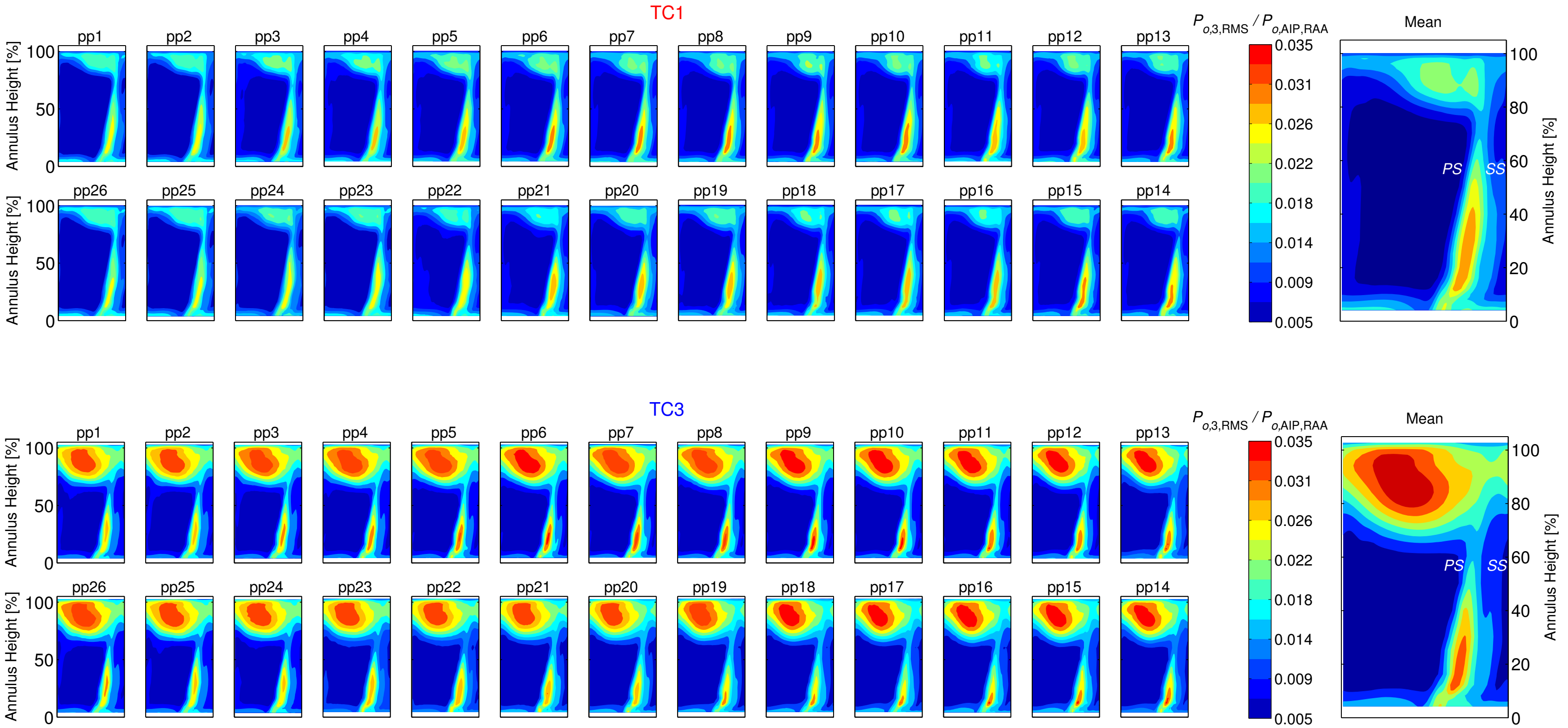

Figure 5.29: Average Rotor 1 exit flow field, in terms of RMS total pressure, at each circumferential location across one vane passage (clockwise) at HL.

Time-resolved total pressure measurements at Rotor 2 exit for the NL and HL operating conditions, Figure 5.30 and Figure 5.31, respectively, are also presented as the RMS unsteadiness with respect to the ensemble average. At Rotor 2 exit, the leakage flow modulation is more clearly denoted by following the measurements at each position across one vane pitch. For TC1 at the nominal loading condition, two adjacent high-intensity regions of flow unsteadiness are identifiable in the outer tip region for the measurements labeled pp1–pp7. These two regions compare with the results observed in Figure 5.6 (for TC2, although the figure for TC1 is similar), which is expected based on the position of the static pressure measurements falling in this same range with respect to the stator vanes. The strength of the two high-unsteadiness regions is also sufficiently significant to persist into the circumferential mean for TC1 in Figure 5.30. The TC3 results in Figure 5.30 position the extremes of the pitchwise leakage flow modulation in the same locations as for TC1. Further, the measurements are similar to the observations for Rotor 1, such that the radial extent of the leakage flow region for TC3 extends to approximately 70% annulus height, compared to 80% for TC1.

At the high loading condition for Rotor 2 presented in Figure 5.31, the unsteadiness of the flow identified by the RMS fluctuations shows less modulation than at the nominal loading condition (the RMS of the passage represents magnitudes which exist more in the middle of the prescribed contour range), especially for TC1. However, two regions of high pressure unsteadiness are still faintly present in the mean contour for TC1. Comparing the HL condition with the NL results for Rotor 2, the circumferential probe position which yields the most intense leakage flow structure is not the same. This result is expected as the width of the upstream stator wake is significantly changed between the two conditions. Furthermore, the trajectory of the leakage flow is expected to change as the rotor loading is increased.

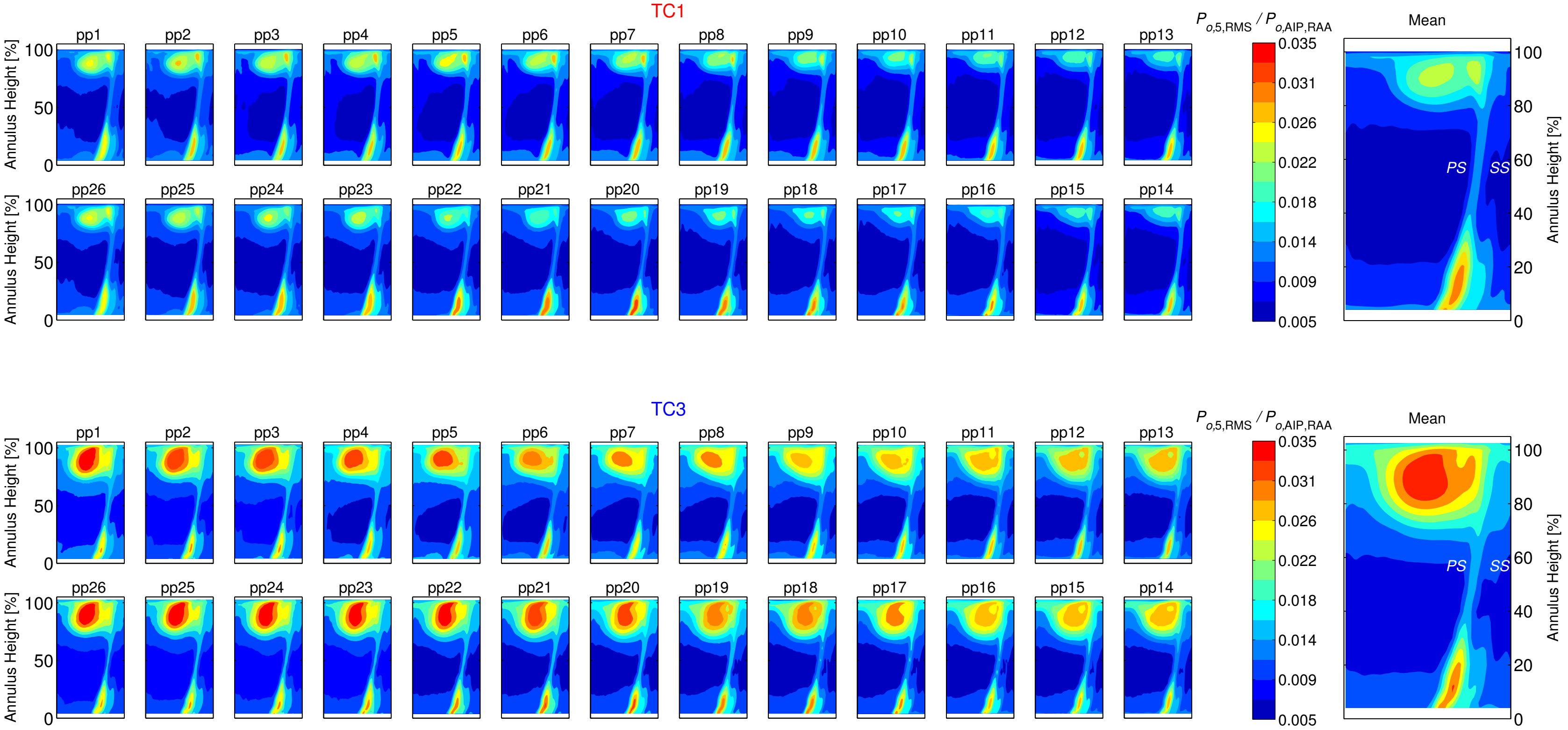

Figure 5.30: Average Rotor 2 exit flow field, in terms of RMS total pressure, at each circumferential location across one vane passage (clockwise) at NL.

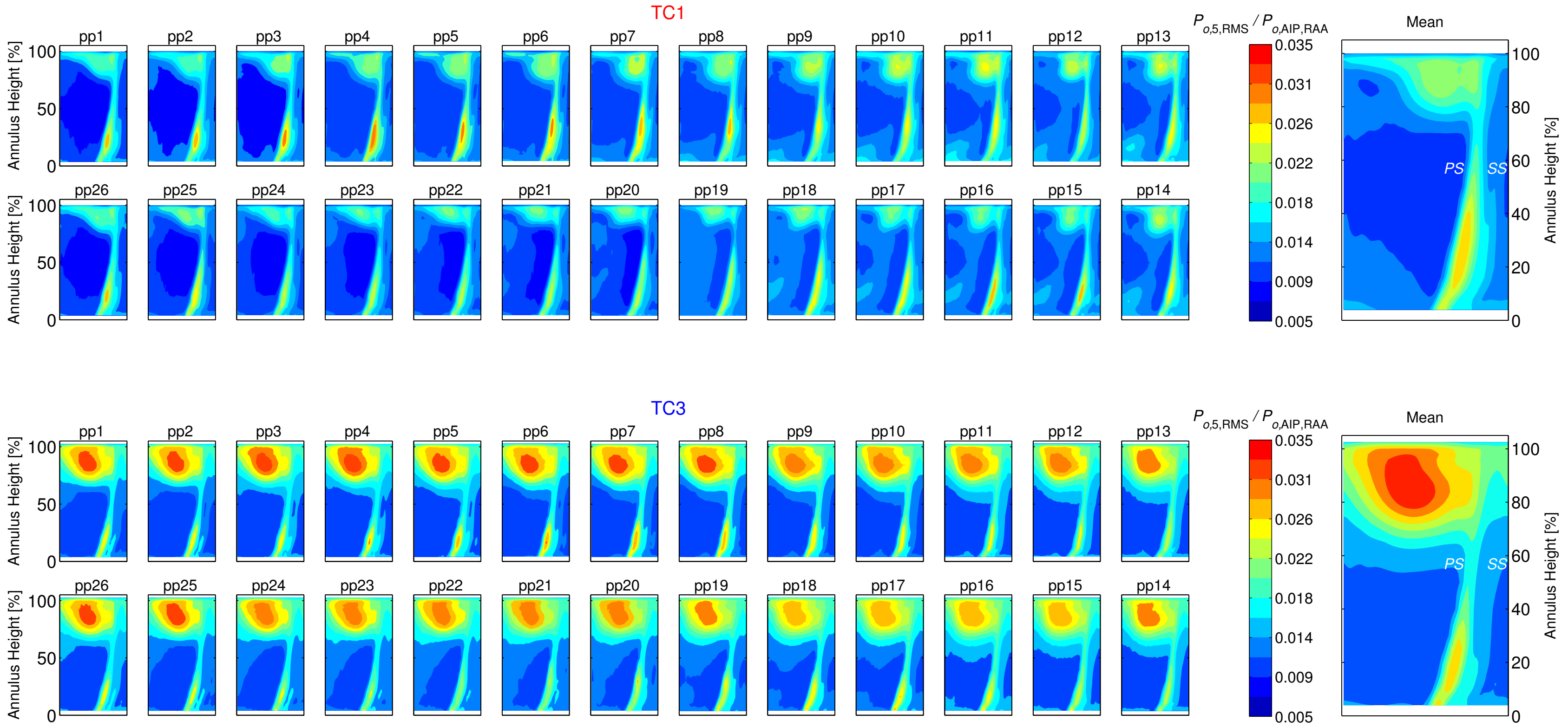

Figure 5.31: Average Rotor 2 exit flow field, in terms of RMS total pressure, at each circumferential location across one vane passage (clockwise) at HL.

Similar to the other rotor rows, the unsteadiness of the Rotor 3 exit total pressure is shown in Figure 5.32 and Figure 5.33 for the NL and HL operating conditions, respectively. At the NL condition, the results for TC1 identify two adjacent regions of high unsteadiness (in agreement with other results in this section of the document) – one in the middle of the passage and another adjacent to the blade pressure surface. As with Rotor 2, this observation compares with the over-rotor static pressures for TC2 at the NL condition (Figure 5.6). For the TC3 configuration, the circumferential modulation of the leakage flow in Figure 5.32 is less discernable compared to the TC1 measurements. This observation suggests the leakage flow region with the large tip clearance height is less sensitive to the influence from the upstream stator vane.

For the high loading condition, Figure 5.33, the TC1 unsteadiness is dominated by the rotor wake more than the leakage flow. Comparing the pitchwise modulation results, the location with the smallest or weakest leakage flow region corresponds to the most significant rotor wake, as the decreased leakage flow blockage provides less energizing benefit to the suction surface wake separation tendencies in the lower portion of the annulus. Similarly, the positions with the largest leakage flow regions show the least suction surface separation (i.e., the thinner rotor wakes). Also at the high loading condition, Figure 5.33 shows the leakage flow region for TC3 fills nearly the entire circumferential extent of the rotor passage, with radial extent down to approximately 70% annulus height. In contrast, the region of high unsteadiness identified as the leakage flow for TC1 only affects approximately half of the rotor passage (in the circumferential direction) with radial extent to just below 80% annulus height, but with a more significant rotor wake.

Ultimately, these rotor exit total pressure measurements provide valuable insight into the rotor tip leakage flow structure as it enters the downstream vane passage. Furthermore, the influence of the upstream stator wake can play an important role in the size, shape, and trajectory of the leakage flow through the rotor passage – particularly for Rotor 2 and Rotor 3. In combination with the over-rotor static pressure measurements, these rotor exit data can provide bounding planes which could be used to guide future measurements in the rotor passage collected using non-intrusive measurement techniques.

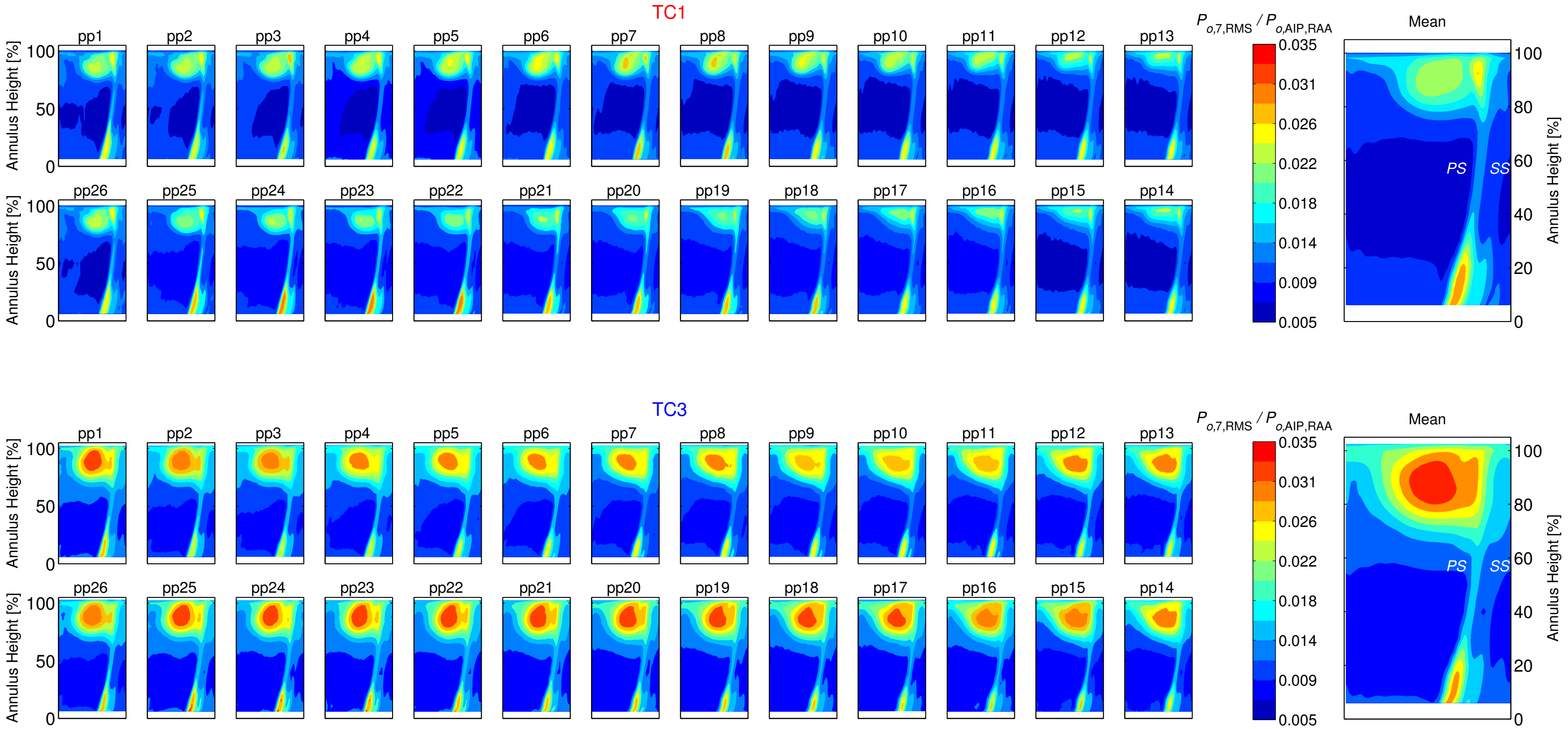

Figure 5.32: Average Rotor 3 exit flow field, in terms of RMS total pressure, at each circumferential location across one vane passage (clockwise) at NL.

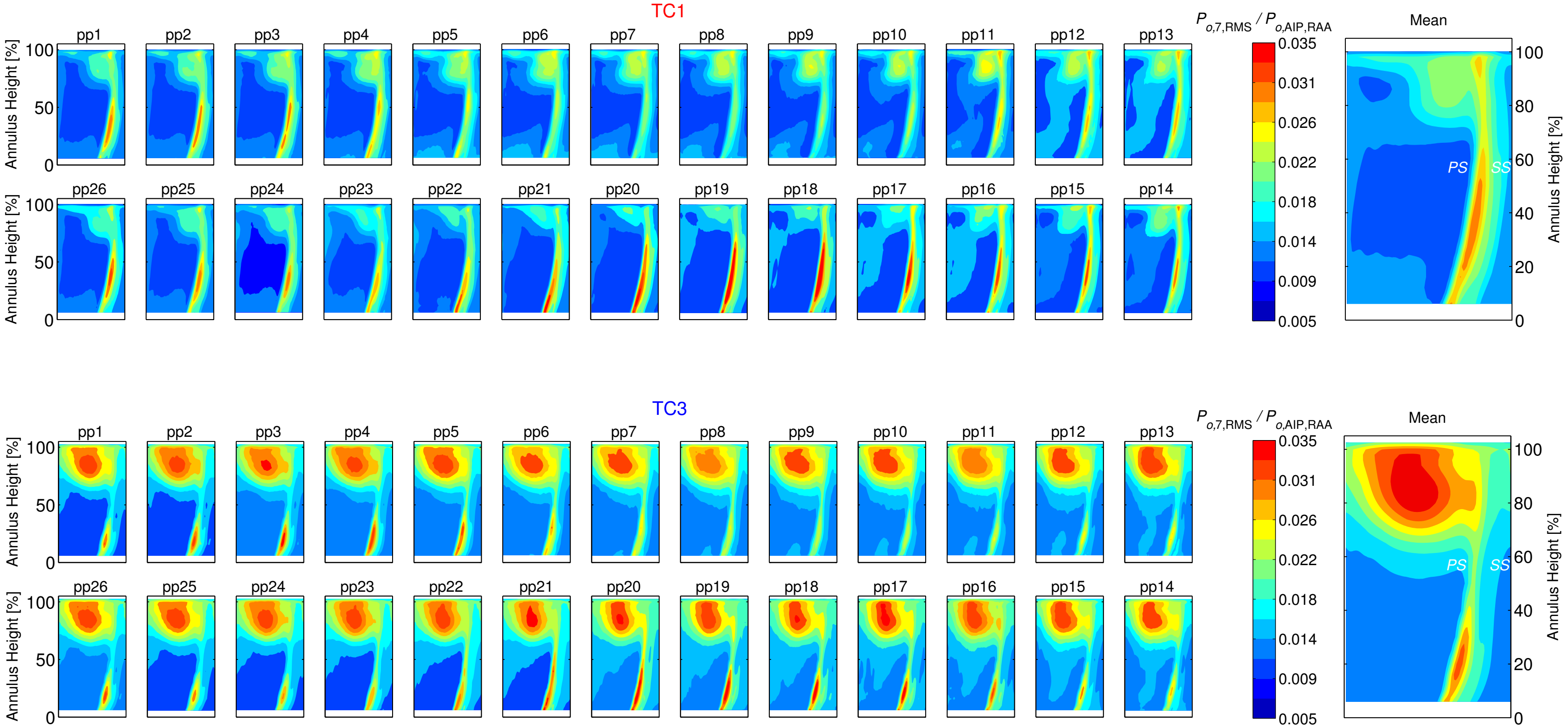

Figure 5.33: Average Rotor 3 exit flow field, in terms of RMS total pressure, at each circumferential location across one vane passage (clockwise) at HL.

5.2.2. Quantifying the Size of the Leakage Flow

The RMS unsteadiness of these rotor exit total pressure data provides an opportunity to quantify the size of the leakage flow region at the rotor exit measurement planes. Suder (1998) used the calculation of axial velocity gradients to identify a defect region for quantifying flow blockage. A similar method has been implemented with these RMS total pressures to identify a defect region. Specifically, the gradient of RMS pressure was calculated in the radial and circumferential directions, and a cutoff value was assigned to determine the defect region, as exemplified in Figure 5.34. Once the defect region was identified, a human-guided selection tool in the plotting GUI manually separated the points from the defect region associated with the leakage flow from those associated with the rotor wake or the hub endwall boundary layer. These separated leakage flow points are also highlighted for the example in Figure 5.34. The points identified to be associated with the leakage flow disturbance region were then integrated across the passage to determine the percentage of the rotor exit flow passage which is influenced by the tip leakage flow.

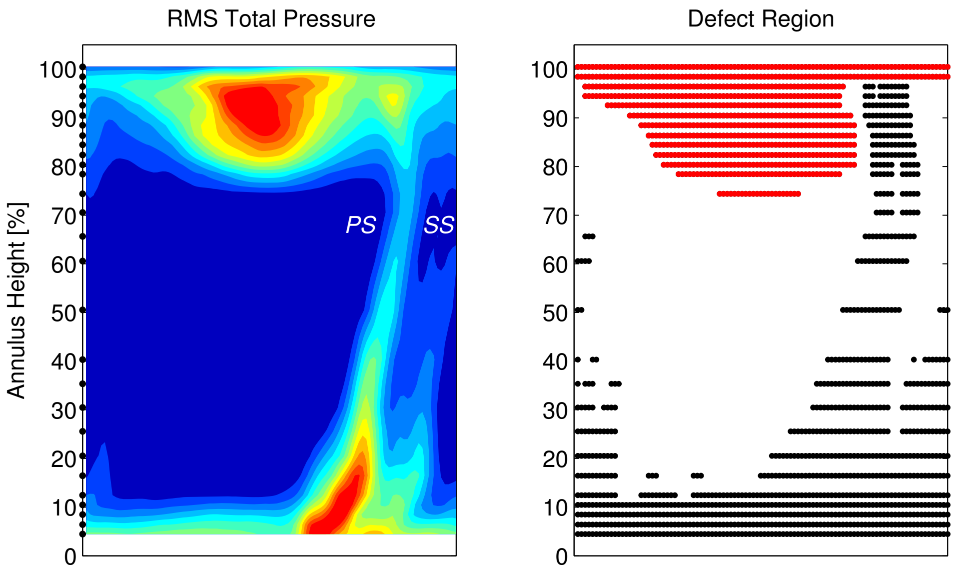

Figure 5.34: Identification of defect region associated with leakage flow unsteadiness.

This process was repeated for each of the 26 pitchwise measurement positions presented in Figure 5.28 through Figure 5.33. Because there is a potential effect of the calculated value associated with the human-guided identification technique, the identification process was repeated three times for all of the data sets. This repetition facilitates the calculation of pertinent statistics related to human-introduced variability. The average of these leakage flow areas was then calculated at each pitchwise position for each measurement condition.

A passage-averaged value was calculated for each measurement condition, as shown by the filled bar plots in Figure 5.35. From the figures above, the leakage flow region can change significantly for the different pitchwise measurement positions. Thus, the minimum affected area and maximum affected area are noted in Figure 5.35 by range bars about the passage-averaged value. For reference, and in the context of the results shown in Figure 5.35, the human-introduced variability may be represented by the standard deviation with respect to the sample mean. The calculated disturbed areas yield a standard deviation of less than 2% of the passage area for all conditions with the TC1 configuration. The TC3 data have a standard deviation of less than 2.5% of the passage area for Rotor 1 and Rotor 2 data, but approaching 5% of the passage area for the Rotor 3 data.

The information in Figure 5.35 shows the expected result of increased leakage flow disturbed area as the rotor tip clearance height is increased. Rotor 2 shows the lowest percentage of affected area for both tip clearances and both loading conditions, which is perhaps unexpected given the knowledge presented thus far about latter stages ingesting the high-loss leakage flow from the upstream rotor(s). Figure 5.35 also shows that Rotor 1 has the least pitchwise variability of the leakage flow size, which aligns with the fact that the IGV has a thinner wake than Stator 1 or Stator 2. This result can be referred to flow visualization photographs highlighting the leakage flow variability for TC1 from Smith (2015), which shows the significant difference of leakage flow modulation for Rotor 1 compared to Rotor 2 or Rotor 3. Furthermore, Figure 5.35 shows a similarity between Rotor 1 and Rotor 2 (compared to Rotor 3). To this point, the similarities between rotor rows or stages in the facility have been noted between Rotor 2 and Rotor 3, whereas Rotor 1 has performed differently.

At the NL condition, the increase of leakage flow affected area between TC1 and TC3 is an identical 10.5% for both Rotor 1 and Rotor 2, whereas Rotor 3 shows a smaller increase of 7.6%. At the HL condition, the same comparison is echoed as Rotor 1 and Rotor 2 show an identical increase of 15.3% between Rotor 1 and Rotor 2, whereas Rotor 3 shows a smaller increase of 10.4%. Based on these data, Rotor 3 shows a consistent trend of 30% less increase of leakage flow area between TC1 and TC3 compared to Rotor 1 and Rotor 2 for these loading conditions. These results, combined with previous observations suggesting the importance of evaluating three tip clearances instead of two, motivate follow-on work measuring these same phenomena for the intermediate clearance, TC2.

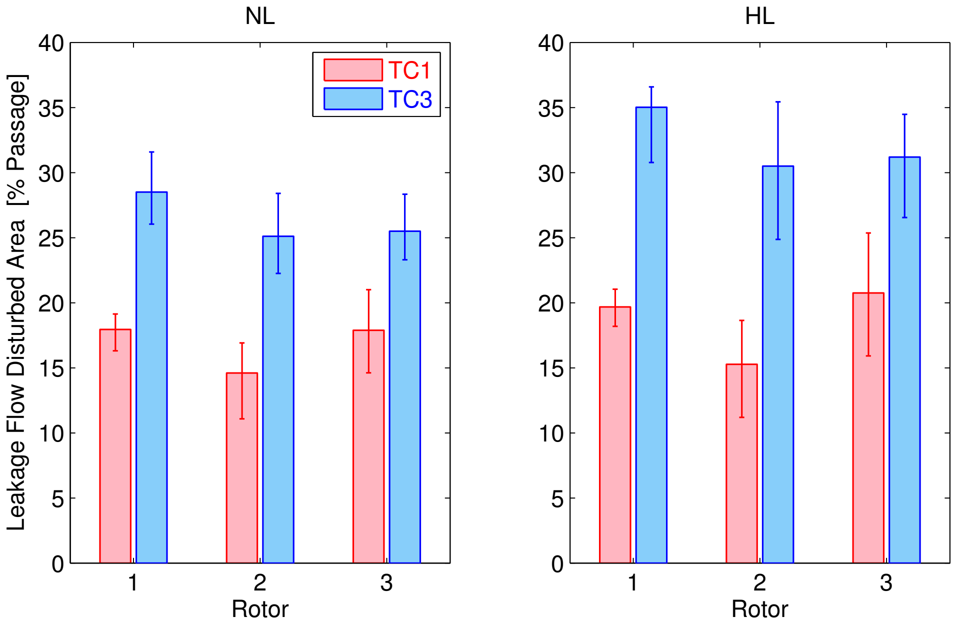

Figure 5.35: Percentage of rotor passage affected by tip leakage flow: passage-averaged value and range.

5.3. Thermal Anemometry

The steady pressure and temperature measurements presented in Chapter 3, combined with the time-resolved pressure measurements above, provide valuable insight into the overall performance of the Purdue three-stage compressor, as well as the underlying flow physics governing the tip leakage flow disturbance with different rotor tip clearance conditions. However, a quantification of the flow angles provides an additional method by which to evaluate the overall effect of the rotor tip leakage flows and validate computational tools. The slanted hot-wire technique implemented for these measurements provides valuable three-component velocity information about the flow features, as described in Section 2.4.3. At each of the axial measurement planes 2 through 8 (see Figure 2.6), hot-wire data were collected at up to 28 radial positions across the annulus height and a series of circumferential positions across one vane pitch. Data were sampled at a rate of 1 MHz for 200 rotor revolutions. Several methods for evaluating the results are presented here which feature results to complement the measurement techniques already introduced.

5.3.1. Time-Averaged Flow Angles and Velocity

To analyze the flow angles output from the slanted hot-wire processing technique, the radial profiles at each axial measurement plane are considered for two tip clearance configurations (TC1 and TC3). For these results, the passage-averaged flow angles were calculated using data collected at several measurement positions with respect to the fixed vanes (13 circumferential positions for rotor exit planes and 20 circumferential positions for stator exit planes).

The absolute flow angles for both tip clearance configurations at the nominal loading (NL) operating condition are shown in Figure 5.36. As the tip leakage flow passes from the rotor pressure surface to the suction surface, its trajectory across the rotor passage is interpreted in the flow angles as underturning in the rotor relative frame of reference. However, the corresponding decrease of local flow velocity in the endwall region as a result of the flow blockage due to the tip leakage flow is significant enough to cause the absolute flow angles to increase in the tip region at the rotor exit (Lakshminarayana and Pandya, 1984; Goto, 1992). This effect is clearly observed at the rotor exit planes in Figure 5.36. As the rotor tip clearance height is increased, the increased flow blockage from the larger leakage flow region is noted as the absolute flow angle at the rotor exit planes also increases.

In Figure 5.36, the Rotor 1 exit angles are distinctly different than those for the Rotor 2 and Rotor 3 exit angles. In fact, a comparison of the Rotor 2 and Rotor 3 exit angles for either tip clearance configuration, TC1 or TC3, shows nearly identical radial profile shapes and magnitudes. This observation aligns well with the previous notes that Rotor 1 performs differently than Rotor 2 and Rotor 3 in the Purdue three-stage compressor.

At this same loading condition, the radial profiles of stator exit angle are less affected by tip clearance height than the rotor exit profiles for these passage-averaged, time-averaged results. The Stator 1 exit results present an increase of absolute flow angle in the outer 40% annulus height as the rotor tip clearance height is increased, indicating that the decreased flow velocity in this region causes the stator loading to increase and the stator is less capable of performing the same amount of flow turning when the Rotor 1 tip clearance height is increased. At the Stator 2 and Stator 3 exit planes, the curvature of the absolute flow angle profile changes as the rotor tip clearance height is increased, and both stators (most notably Stator 3) show a slight decrease of flow angle in the outer 15% annulus height near the tip region. Referring to the steady detailed total pressure contours for Stator 2 and Stator 3 at the NL operating condition, Figure 3.33 and Figure 3.35, respectively, this change of flow angle is due to the slight shift of the location of maximum wake thickness toward the hub.

The same passage-averaged, time-averaged radial profiles of absolute yaw angle are also considered at the high loading (HL) operating condition, Figure 5.37. Similar to the observations at the NL operating condition, these HL data echo the difference between the results at Rotor 1 exit and those at Rotor 2 or Rotor 3 exit. At all three rotor exit planes for HL, however, the shift between the two tip clearance configurations is nearly twice that observed for NL. As the leakage flow region overtakes a more significant area at the high loading condition, Figure 5.37 shows a decrease of absolute yaw angle at Rotor 1 exit (due to the redistribution of mass flow) for the lower 70% annulus height which was less noticeable at the NL operating condition. Also at the HL condition, Figure 5.37 shows the reduction of the Stator 2 hub corner separation for TC3 compared to TC1 has a profound effect on the radial yaw angle profile in the same region occupying the lower 35% annulus height. This observation compares well with the results in Figure 3.34.

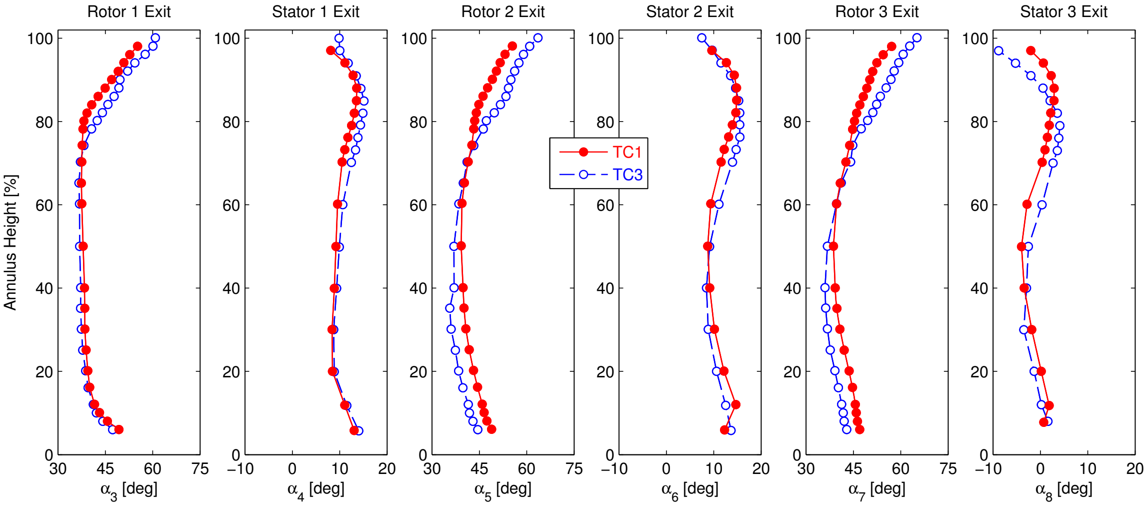

Figure 5.36: Radial profiles of absolute yaw angle at NL.

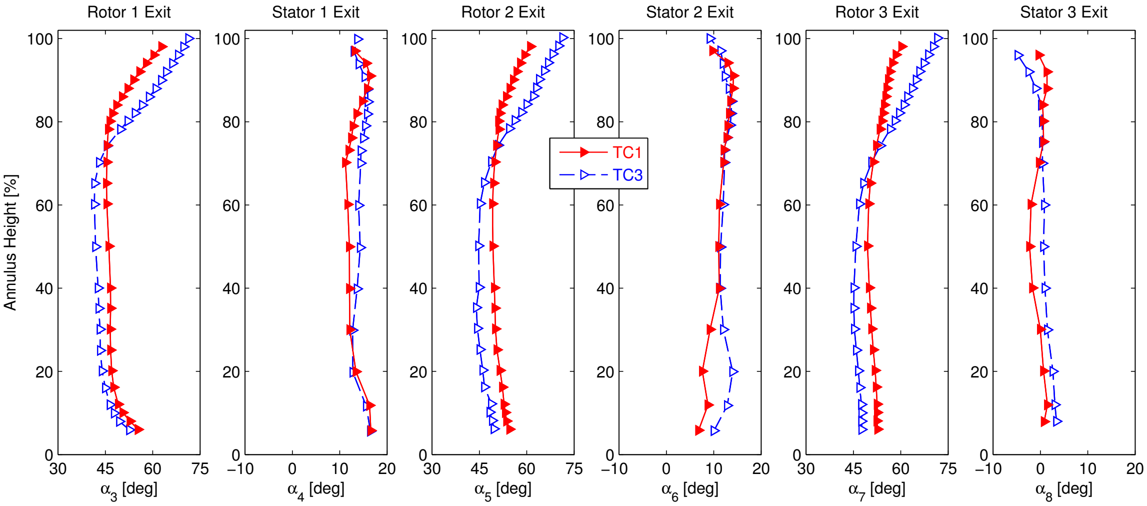

Figure 5.37: Radial profiles of absolute yaw angle at HL.

The constant annulus height of the Purdue three-stage compressor lends itself to a simplified parallel streamline assumption, suggesting the contributions of radial flow (i.e., pitch angles) are predicted to be small. However, the centrifugal effect imparted to the fluid by the rotors has the effect of pushing fluid outward in the radial direction. As a result, the flow may be expected to have a slight positive trend of pitch angles across the annulus height. Indeed, the NL results of passage-averaged, time-averaged pitch angle profiles, Figure 5.38, show a slight positive profile across the entire annulus for TC1. For TC3, Figure 5.38 further identifies the redistribution of flow from the tip toward the hub as the pitch angles in the flow regions unaffected by the leakage flow (i.e., less than 70% annulus height) decrease on the order of five degrees. This net change of pitch angles between TC1 and TC3 confirms flow redistribution from the tip toward the hub.

At the HL operating condition, Figure 5.39, similar trends of pitch angle with annulus height are observed as the rotor tip clearance height is increased from TC1 to TC3. Especially for the Stator 2 exit results, the considerable decrease of hub corner separation with increased tip clearance height is also noted in the pitch angles.

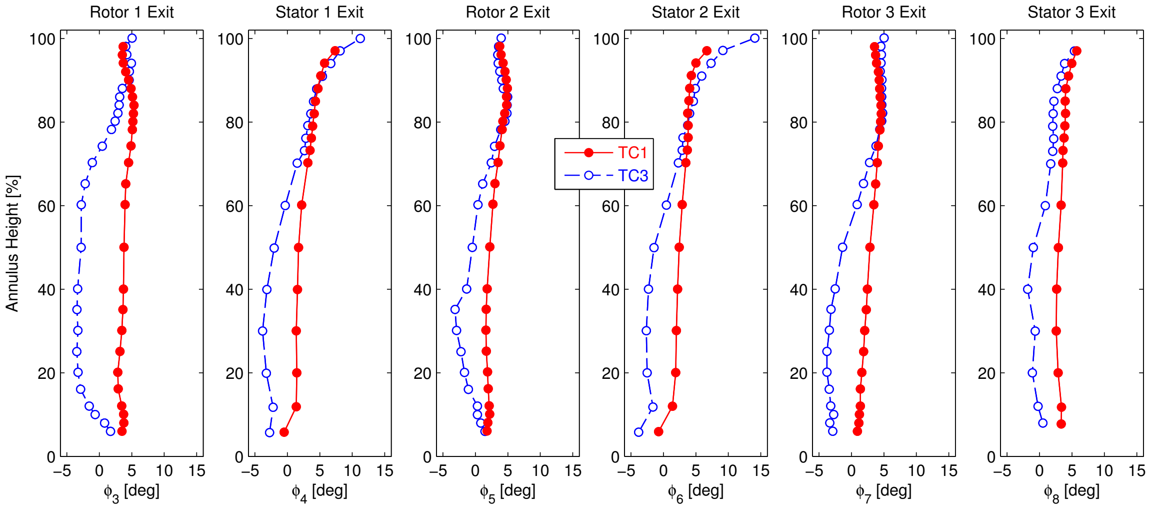

Figure 5.38: Radial profiles of pitch angle at NL.

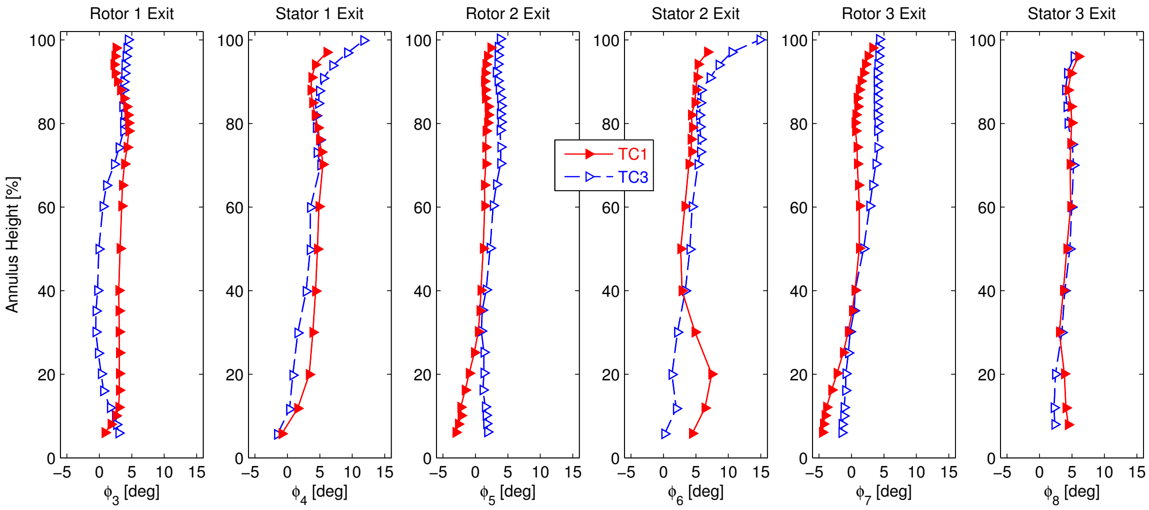

Figure 5.39: Radial profiles of pitch angle at HL.

The measured steady and time-resolved pressures have shown the redistribution of normalized pressure rise with increased tip clearance, and corresponding flow visualization photographs (Smith, 2015) have shown the effect that the increased flow near the hub can have on the separated flow regions for the stationary vane rows. The absolute flow angles shown here in Figure 5.36 and Figure 5.37 provide further evidence of this trend. However, the axial velocity profiles can provide a more definitive representation of the mass flow rate through the machine to confirm the statements about redistributed mass flow suggested throughout this report.

These axial velocity profiles are shown in Figure 5.40 for the axial measurement planes at the exit of Rotor 2 and Rotor 3, which show the specific effect of the tip leakage flow on the rotor exit flow fields including the important multistage effects. The profiles in Figure 5.40(a-b) correspond to the nominal loading and high loading conditions, respectively, and the data have been normalized in all cases by the corresponding tip speed, U_t.

The results in Figure 5.40 show important trends at both loading conditions. In particular, a comparison of the two rotors at NL or HL shows qualitatively similar profiles for each of the two tip clearance configurations. At the NL condition, Figure 5.40(a), there is a noticeable decrease of axial velocity in the tip region for both rotors and both tip clearances. However, the velocity profile has a profile across the span which resembles a parabolic profile. This contrasts with the HL condition, Figure 5.40(c), which shows a noticeable decrease of axial velocity near the tip (outer 20-30% span), but a more constant axial velocity profile across the lower 70-80% span. A comparison with the time-resolved total pressure measurements in Figure 5.30 through Figure 5.33 shows that this change of velocity profile is due to the thicker rotor wake at the high loading conditions, for which the separation off the suction surface of the rotor blade becomes more significant across a more substantial portion of the span.

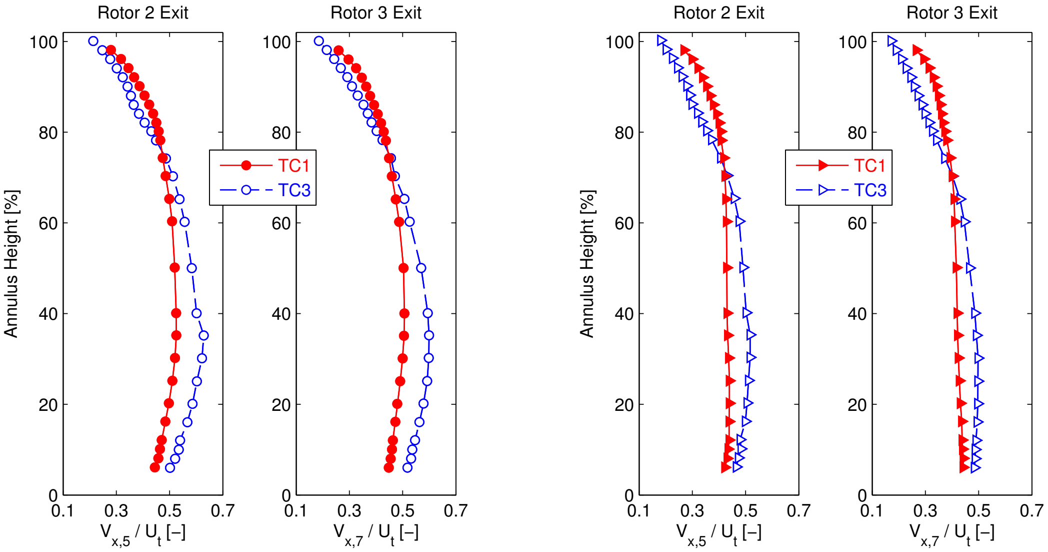

(a) NL (b) HL

Figure 5.40: Radial profiles of normalized axial velocity at Rotor 2 and Rotor 3 exit.

5.3.2. Blockage

In addition to the flow angles presented in the previous section, the flow blockage at each axial measurement plane has been quantified using the method outlined by Suder (1998). The blockage quantification method is defined for an effective reduction in flow area:

$$B = 1 - \frac{\text{effective area}}{\text{geometric area}}. \tag{5.4}$$

This equation is further defined by evaluating the effective area as a function of the velocity-density deficit in the flow region, δ^*:

$$B = 1 - \frac{A - \int \delta^* dr}{A}, \tag{5.5}$$

for which A represents the geometric flow area. The velocity-density deficit is analogous to the displacement thickness introduced through fundamental boundary layer theory:

$$\delta^* = \int_0^{2\pi/\mathrm{NB}} \left(1 - \frac{\rho u}{(\rho u)_{\mathrm{inviscid}}}\right) r d\theta\ , \tag{5.6}$$

where NB is the number of blades (or vanes) in the row of interest.

For these data, the blockage can be calculated at the rotor exit planes by analyzing time-series measurements. The time series is first phase-locked ensemble-averaged, then passage-averaged across one vane pitch, and finally averaged over each of the blades in one row; this final product represents a mean rotor wake at the given measurement plane and loading condition. Similarly, the same blockage parameter can be calculated in a spatial reference frame (instead of a time series) at stator exit planes, for example. At these locations, the hot-wire signal is time-averaged and then presented as a function of pitchwise location.

In either case, the physical method described by Suder (1998) is the same: determine a defect region via axial velocity gradients and the selection of an arbitrary cutoff value. For this study, the cutoff value was chosen to be 3 s^{-1} for all conditions. In agreement with Suder's conclusion, the arbitrary selection of the cutoff values has a negligible effect on the result (less than 5% change of calculated blockage values). Several cutoff values in the range of 1-5 s^{-1} were considered for these data. Examples of the axial velocity data and the corresponding defect region are shown in Figure 5.41 and Figure 5.42 for rotor exit data and stator exit data, respectively.

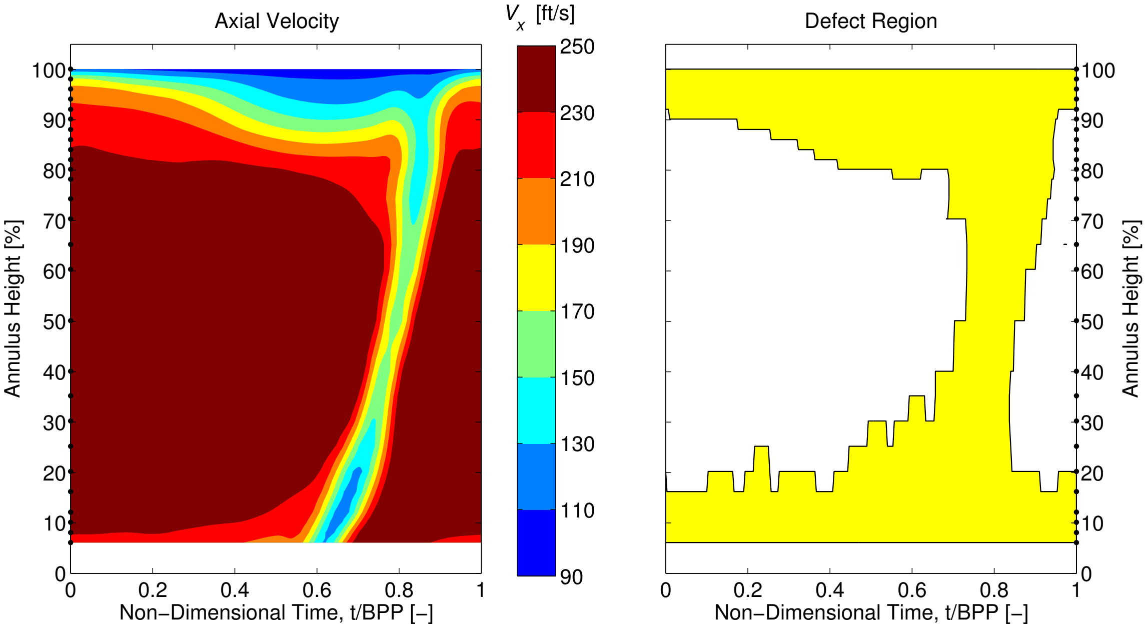

Figure 5.41: Example of defect region identification for Rotor 2 exit (TC1, NL).

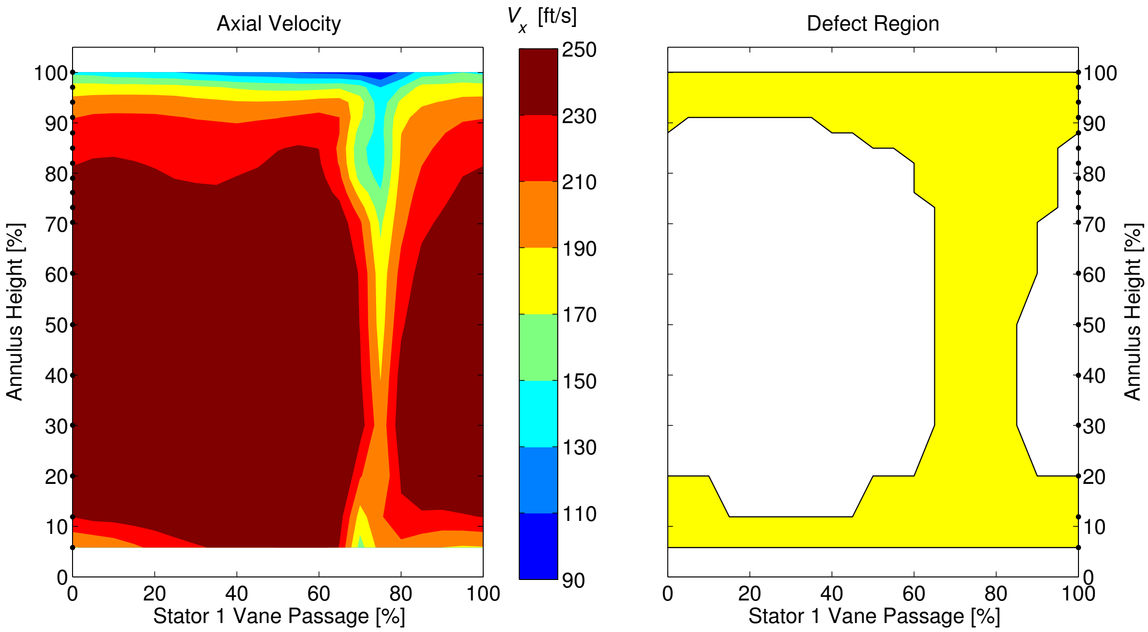

Figure 5.42: Example of defect region identification for Stator 1 exit (TC1, NL).

The calculated blockage values are presented in Figure 5.43 for the nominal loading (NL) condition and Figure 5.44 for the high loading (HL) condition. A summary of these results is also listed in Table 5.1 as a representative one-dimensional blockage value for each axial measurement position, loading condition, and tip clearance configuration. A preliminary analysis of the results in Figure 5.43 shows the most significant changes in blockage are observed in the tip region at Rotor 1 exit, Stator 2 exit, and Stator 3 exit for the two tip clearance configurations investigated here (TC1 and TC3). Considering the total pressure measurements at Rotor 1 exit in Figure 5.28, it is not surprising that a more significant blockage region flow is present due to the increased tip leakage. However, it is particularly interesting that the same disturbance does not appear as significantly in the calculated blockage for the Rotor 2 and Rotor 3 exit data. Although the Rotor 2 exit data show an increase of blockage on the order of 10% in the region from

80 to 90% annulus height, the Rotor 1 exit data are nearly 20% different between the two tip clearance configurations across the region spanning 80 to 100% annulus height.

The Stator 2 exit total pressures, Figure 3.33, reveal that the increased blockage in the tip region at the same location in Figure 5.43 is largely due to low pressure regions near the wall, not the wake itself. On the other hand, the Stator 3 exit total pressures (Figure 3.35) show a thicker wake in the outer 50% of the flow annulus between the two tip clearance configurations. However, this blockage effect is only identified for the outer 30% of the flow annulus.

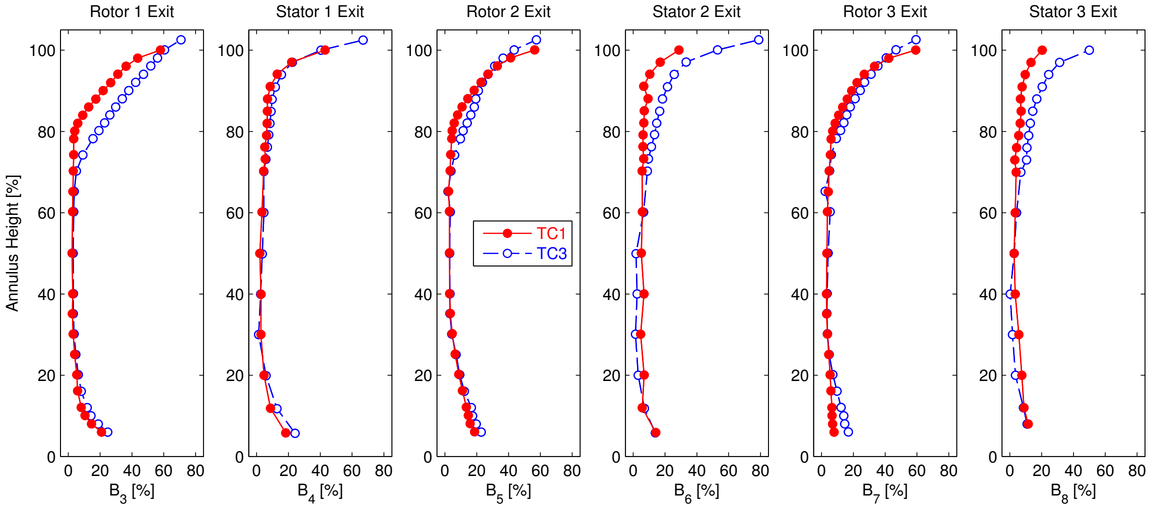

Figure 5.43: Radial profiles of blockage at NL.

As the compressor is throttled toward stall, the similarity between the observed blockage trends at each rotor exit plane increases, Figure 5.44. Of the three rotors, Rotor 3 shows a decrease of blockage in the tip region with increased loading for TC1, a result which is not surprising considering the difference of Rotor 3 exit measurements at the same conditions presented earlier. In Figure 5.32 and Figure 5.33, the mean wake contours of RMS total pressure show the leakage flow region is decreased at high loading, but at the expense of a very thick wake at HL which extends across a majority of the passage. Based on the calculated values in Table 5.1, the more intense fluctuating wake region extending across the blade span is significant enough to offset the blockage created by the leakage flow at NL (and more). Also at the three rotor exit planes, the blockage differences between the two tip clearance configurations approach 30% and the radial extent begins at approximately 70% annulus height for all rotors – a similarity which was not observed as clearly for the three rotors at the NL condition.

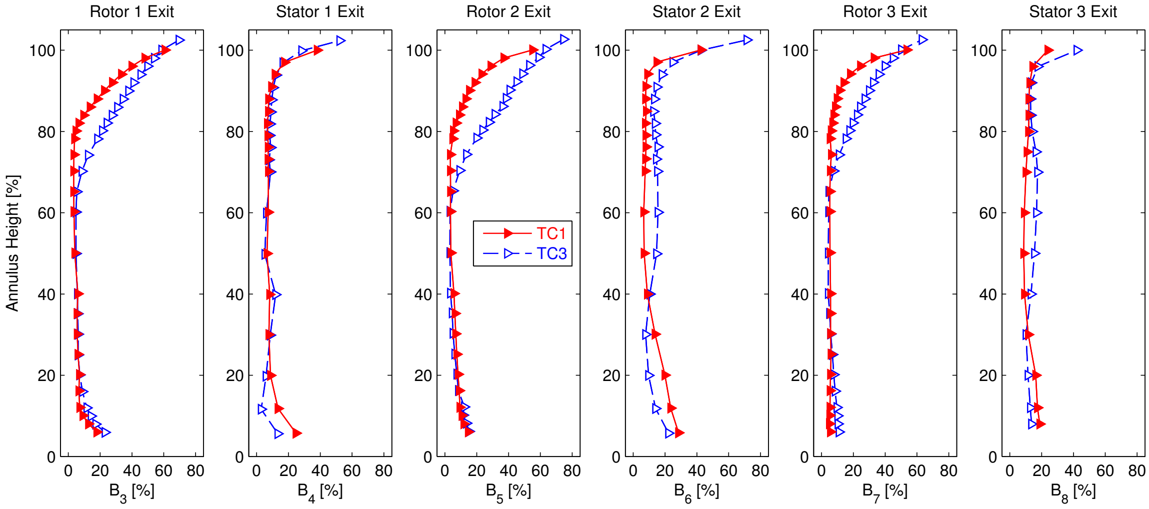

Figure 5.44: Radial profiles of blockage at HL.

For the high loading condition, a comparison of the two tip clearance configurations at Stator 2 exit confirms the expectations from the steady total pressure traverses shown previously in Figure 3.34 and flow visualization photographs. Although the Stator 2 exit blockage in Figure 5.44 increases across the outer 60% annulus height (on the order of 10% increased blockage), the reduction of the corner separation region off the suction surface of the vane is represented by the decrease of blockage in the lower 40% annulus height (on the order of 10% decreased blockage).

Table 5.1: Summary of one-dimensional blockage parameters, listed in percent flow area.

TC Config.	Loading	R1 Exit	S1 Exit	R2 Exit	S2 Exit	R3 Exit	S3 Exit
TC1	NL	9.1	6.8	9.3	7.4	8.4	6.2
	HL	10.2	10.0	11.8	12.4	11.8	12.3
TC3	NL	15.5	9.4	9.0	10.9	7.6	8.5
	HL	16.6	9.4	16.4	15.4	13.3	14.2

5.3.3. Streamwise Vorticity

The streamwise vorticity provides an additional method for evaluating the leakage flow region once the three-dimensional velocity vectors are known. Because the ensemble-average technique has been used to calculate the velocity vectors, the presence of an instantaneous vortex cannot be evaluated. However, this technique can still determine the average rotational motion in the leakage flow region.

Inoue et al. (1986) define the streamwise vorticity by calculating the projection of two vorticity components on the streamwise flow direction (defined by the relative flow angle, β):

$$\omega_{st} = \left[\frac{1}{r}\frac{\partial(rV_\theta)}{\partial r} - \frac{1}{r}\frac{\partial V_r}{\partial \theta}\right]\cos\beta - \left[\frac{1}{r}\frac{\partial V_r}{\partial x} - \frac{\partial V_x}{\partial r}\right]\sin\beta\,, \tag{5.7}$$

where the first bracketed terms represents the axial vorticity, ω_x, and the second bracketed term represents the tangential vorticity, ω_θ. Unlike the measurements collected by Inoue et al., the data collected in this study were only captured at one axial survey plane downstream of each rotor. As a result, the gradient of radial absolute velocity, $\partial V_r/\partial x$, cannot be evaluated for these measurements. Future studies may build in the ability to evaluate this change in the axial flow direction. However, if the contributions from this gradient are assumed to be small with respect to the other components, they can be neglected. Under this assumption, the streamwise vorticity is simplified:

$$\omega_{st} = \left[\frac{1}{r}\frac{\partial(rV_\theta)}{\partial r} - \frac{1}{r}\frac{\partial V_r}{\partial \theta}\right]\cos\beta - \left[-\frac{\partial V_x}{\partial r}\right]\sin\beta\,. \tag{5.8}$$

The derivatives needed for Equation (5.7) were numerically calculated using a central differencing scheme, with exception to the edges of the data region, which were calculated as single-sided differences.

Figure 5.45 shows contours of streamwise vorticity, as calculated from Equation (5.7), for two different tip clearance configurations and two loading conditions at the Rotor 1 exit plane. The calculated vorticity results in Figure 5.45 are normalized by the angular velocity of the rotor, Ω. The leakage flow structures identified in Figure 5.45 are very similar to the regions identified by the passage-averaged time-resolved total pressure measurements in Figure 5.28 and Figure 5.29. Specifically, the leakage flow for TC1 extends downward to approximately 80% span, whereas the leakage flow for TC3 extends to approximately 70% span for NL and 65% span for HL. However, Figure 5.45 also shows that the regions of high vorticity typically associated with the averaged tip leakage vortex (recall, these data are ensemble-averaged and passage-averaged, so they do not represent an instantaneous vortex) does not stay attached to the wall, but moves radially downward into the passage. These results suggest that, although the total pressure unsteadiness (RMS) at the rotor exit plane is an adequate method for identifying the leakage flow region, those results may not sufficiently represent any true vortex structures.

Further analysis of the contours in Figure 5.45 shows the difference of the wake region for TC1 versus TC3. Inoue et al. (1986) also identified these regions of positive and negative vorticity associated with the passing rotor wake, an observation which was attributed to the radial velocities induced by the centrifugal effects of the passing rotor. However, there is a significant reduction of both the positive and negative regions of vorticity in the rotor wake as the tip clearance height is increased from TC1 to TC3. This observation can be linked to the redistribution of flow velocity toward the hub, which energizes the separation-prone fluid on the rotor suction surface and effectively reduces the strength of the wake region (although comparisons of the yaw angle wake profiles at several spanwise locations, not shown here, suggest the width of the wake may not necessarily become narrower). Indeed, a deeper investigation of the contribution from each of the three velocity gradients in Equation (5.7) shows that the $\partial V_r/\partial\theta$ component of the streamwise vorticity has a peak value which not only changes magnitude, but also its circumferential position, leading to the change of the wake vorticity. This observed trend is in contrast to the other two components in Equation (5.7) which have peak values that are unaffected in their circumferential position and show a change only in their magnitude.

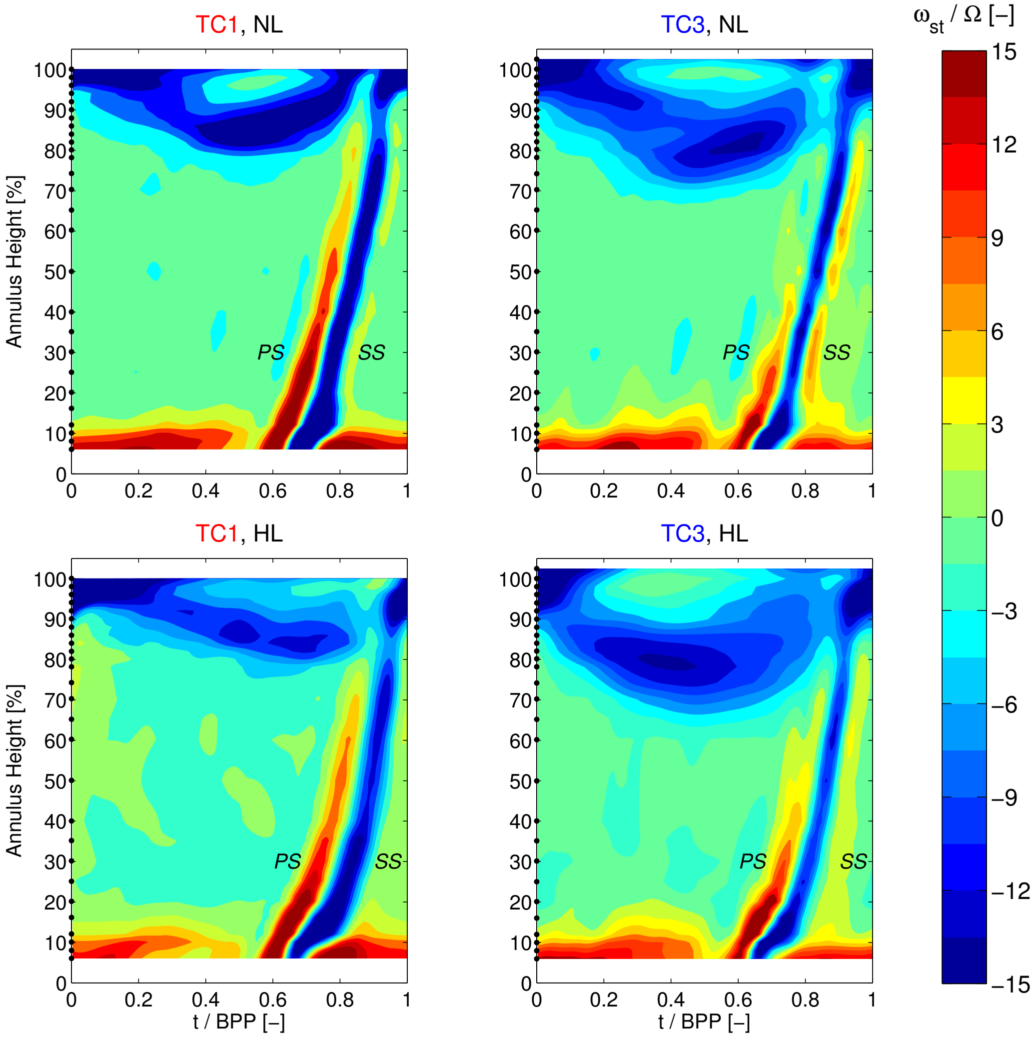

Figure 5.45: Contours of streamwise vorticity at Rotor 1 exit for TC1 and TC3.

In addition to these results for Rotor 1, the streamwise vorticity is also presented for TC1 at the exit of Rotor 2 and Rotor 3 in Figure 5.46. These results confirm many of the previous analyses suggesting the Rotor 2 and Rotor 3 may behave similarly to each other, but differently from Rotor 1. In particular, a qualitative comparison of the streamwise vorticity contours in Figure 5.46 shows leakage flow vorticity structures which are similar in size and shape. A primary difference here is the results at Rotor 3 exit for both NL and HL extend downward approximately 5% deeper into the passage than the results at Rotor 2 exit. This difference compares well with the leakage flow regions identified by high unsteadiness in the time-resolved total pressures, Figure 5.30 through Figure 5.33, and similar comparisons can be drawn between the rotor wake shapes at the two measurement locations.

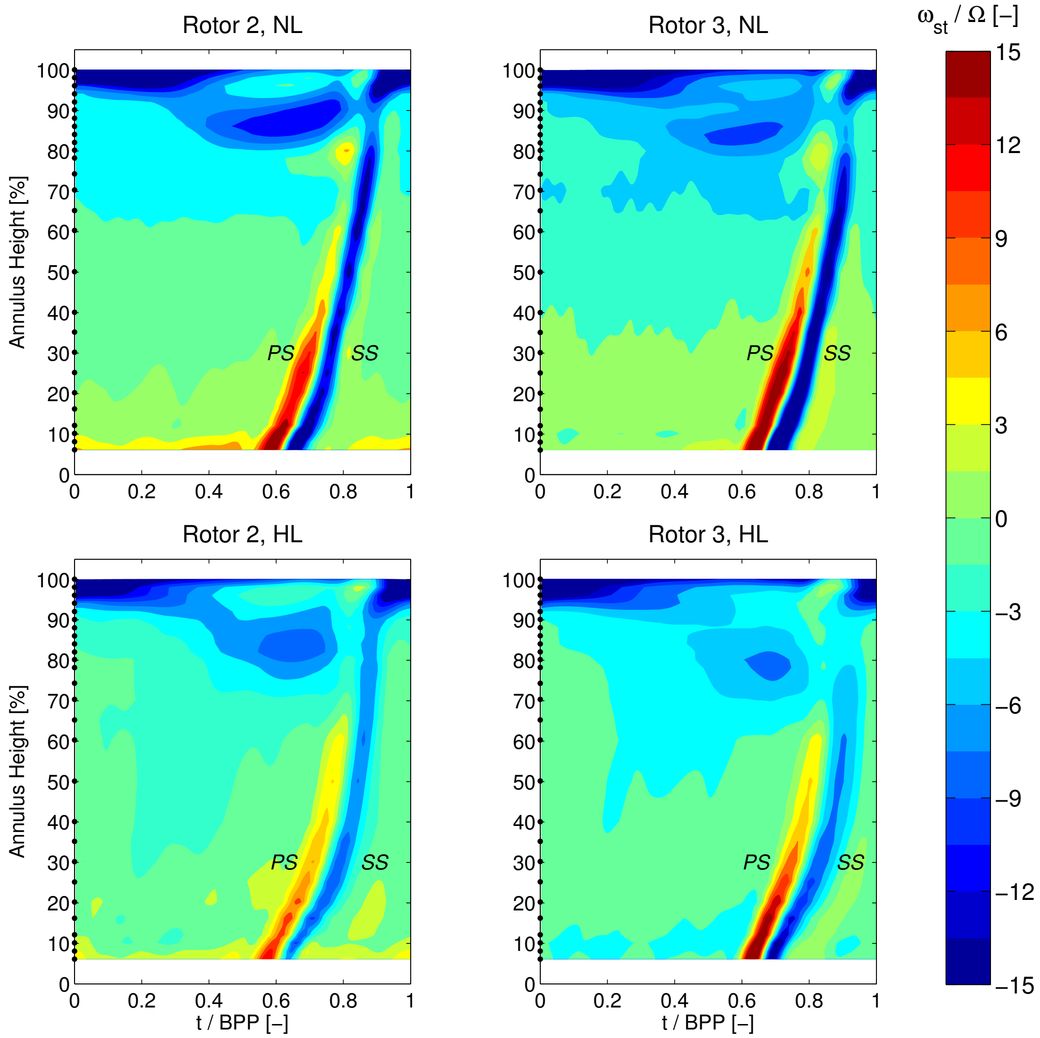

Figure 5.46: Contours of streamwise vorticity at for TC1 at Rotor 2 and Rotor 3 exit.

To supplement the streamwise vorticity contours shown here, the maximum vorticity strength has been quantified for each of the test conditions. The vorticity contour plots (e.g, Figure 5.45 and Figure 5.46) were used to locate the region of the blade passage which corresponds to the leakage flow. In this region, a search tool identified the largest negative value (based on the coordinate system in the above figures).

This information, presented in Figure 5.47, summarizes the streamwise vorticity results from all of the test conditions to one-dimensional values for comparison. In this figure, the maximum vorticity strength is shown for the passage-averaged vorticity field by the filled bars. Similar to the leakage flow size quantification shown in Figure 5.35, the same maximum vorticity strength was also determined for each of the unique pitchwise measurement positions with respect to the fixed vanes. From this, the ranges of maximum vorticity strength dependent on pitchwise position are noted in Figure 5.47 by range bars about the passage-averaged value.

These data show that as the rotor tip clearance is increased from TC1 to TC3, the maximum vorticity strength in the leakage flow region increases for Rotor 2 and Rotor 3, but decreases for Rotor 1. A comparison of the Rotor 1 vorticity contours for TC1 in Figure 5.45 shows that the change of the shape of the high negative vorticity region identified as the leakage flow from NL to HL is more dramatic than any of the other conditions shown here. This change of the leakage flow shape may contribute to the different for Rotor 1 at NL in Figure 5.47. Finally, as the loading condition changes from NL to HL, there is a consistent decrease of maximum streamwise vorticity strength. This trend shows an inverse proportionality of leakage flow size (Figure 5.35) with maximum vorticity strength in the leakage flow region which holds for a change in loading condition, but not a change in tip clearance height.

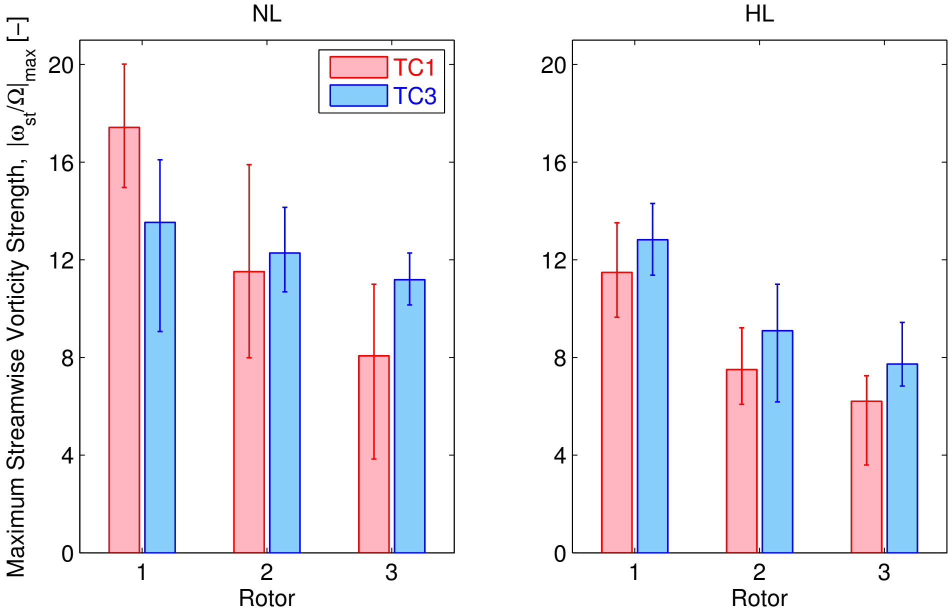

Figure 5.47: Passage-averaged maximum streamwise vorticity strength.

CHAPTER 6: SUMMARY AND CONCLUSIONS

The effect of rotor tip clearances on axial compressor performance has been a focus of research for several decades. In general, studies have found that pressure rise capability, efficiency, and operability range all decrease as the rotor tip clearance height is increased. However, the future of gas turbine engine engineering is moving toward designs which will incorporate smaller blade heights in the rear stages of high pressure compressors. As a result, a decrease in blade heights and a corresponding increase in relative rotor tip clearances are expected in the rear stages of these next-generation compressors. Therefore, a better understanding of the fundamental flow physics and multistage performance effects related to large tip clearance heights in axial compressors is a necessity.

6.1. Overview of Methods and Findings

This work has investigated the effects of large rotor tip clearances on the performance of a three-stage axial compressor at Purdue University. A series of experimental measurement techniques has been implemented to evaluate compressor performance and interrogate the tip leakage flow for three rotor tip clearances: 1.5%, 3.0%, and 4.0% based on annulus height.

Benchmark compressor performance measurements showed the overall pressure rise capability and isentropic compressor efficiency of the machine decrease linearly with rotor tip clearance height. Specifically, the results from this study showed the stalling flow coefficient is expected to increase by approximately 4% for a one percent increase of clearance-to-chord; the peak total-to-static pressure rise coefficient decreases by 4.5% for a one percent increase of clearance-to-pitch; and the isentropic efficiency decreases by 1.3 points for a one percent increase of clearance-to-span. Additional measurements with seven-element total pressure and total temperature rakes inserted at inter-stage locations in the compressor showed a redistribution of flow from the tip toward the hub as the tip clearance height was increased. This effect was shown to be due to the increased blockage related to the tip leakage flow.

Stall inception was evaluated using piezoresistive pressure transducers distributed circumferentially around the compressor, approximately 10% axial chord upstream of the rotor leading edges. These measurements showed the compressor stalls as a result of long length-scale modal disturbances for the 100% corrected speedline with the 1.5% tip clearance configuration. Previous research has suggested modal stall characteristics may be expected when the individual stages of a multistage compressor are well-matched. At part-speed operating conditions, or when the tip clearance height was increased, however, the compressor was more likely to exhibit spike-type stall inception mechanisms emanating from Rotor 1.

Time-resolved measurements of static pressure from piezoresistive transducers distributed axially over the rotors were used to assess the leakage flow trajectory angle through the rotor passage. These data showed changes of trajectory angle as a result of increased tip clearance are dependent on the loading condition and the proximity to the stall point. The results from this study confirmed that the observed effects are due to wakes from upstream vanes, whereas downstream stator vanes have a negligible effect on the tip leakage flow trajectory.

Quantitatively, the trajectory angle change due to this stator-rotor interaction can be more significant than the trajectory change due to a doubling (1.5% increase) of rotor tip clearance height, especially if tip clearance heights are small. This observation is especially true for Rotor 2 and Rotor 3, both of which showed little or no change of the trajectory angle between the smallest and intermediate clearance heights for all loading conditions. Results from Rotor 3 showed that the trajectory angle will increase approximately one degree for every one percent increase of clearance-to-pitch at a high loading point, whereas a low loading operating condition will result in a decrease of trajectory angle on the order of one point for a one percent increase of clearance-to-pitch.

Additional time-resolved measurements of total pressure at the rotor exit planes and hot-wire measurements of three-dimensional flow velocities were collected for two tip clearance configurations at two loading conditions on the 100% corrected speedline. By casting these data in terms of an unsteadiness parameter (the RMS with respect to the ensemble average), the radial and circumferential extent of the tip leakage flow region was evaluated for the smallest and largest clearances. For the nominal loading condition, the portion of the rotor passage affected by the tip leakage flow increased by approximately 10.5% from TC1 to TC3 for Rotor 1 and Rotor 2, whereas the affected area for Rotor 3 increased by only 7.6% (30% less); at high loading, these numbers were 15.3% for Rotor 1 and Rotor 2, and 10.4% for Rotor 3 (also 30% less). These measurements further helped to quantify the tip leakage flow modulation related to the upstream stator wakes, including the effects of leakage flow size and spanwise penetration into the main flow, for which the range of affected flow areas due to stator wake interactions increased as the loading increased.

Time-resolved velocity data were used to quantify the blockage at each measurement plane and correlate the calculated blockage with the observed tip leakage flow region. The most significant increases of overall passage-averaged blockage were observed at the exit of Rotor 1. Considerable increases of blockage between the smallest and largest clearances were noted in the outer 30% span at the exit of all rotors for the high loading condition. The three-component velocity measurements also facilitated calculations of phase-locked streamwise vorticity. These data were used to characterize the strength of the leakage flow from each rotor. An increase of maximum streamwise vorticity with tip clearance in the passage-averaged leakage flow “core” was identified for all rotors and loadings, with exception to Rotor 1 at the nominal loading condition, for which a decrease was noted. Variations of streamwise vorticity relative to vane position were also noted, with more significant modulations occurring at nominal loading than the high loading condition.

The measurements collected for this project represent a unique data set which contributes to an improved overall understanding of the tip leakage flow and its associated loss mechanisms. These data will serve the community as a method for validating computational tools, especially at off-design conditions. Through this process, the results presented herein will aid in the development of new blade designs which could be desensitized to rotor tip leakage flows and their associated performance decrements.

6.2. Recommendations for Future Research

The results from the present study provide a wealth of data which builds upon an understanding of tip leakage flow effects in axial compressors. However, additional processing will continue to glean valuable information from the collected data. For the time-resolved measurements, in particular, a majority of the results shown here have only analyzed the time domain, and further analysis of the frequency content may unveil more information, particularly relating to the multistage effects of the machine and any potential changes of aeromechanical forcing.

The uncertainty for calculated overall efficiency has been carefully evaluated for this project. One of the most significant driving factors of this uncertainty for efficiency is related to the relative uncertainty of the associated temperature measurements. For the data presented herein, a single conservative value was selected for the uncertainty of all temperature measurements based on independent calibration of the thermocouple channels. However, because the thermocouple measurement uncertainty correlates with the absolute value of the measured temperature, future analysis may accommodate a reduction of uncertainty propagation through the use of an uncertainty value chosen for each specific thermocouple channel and the absolute value of the measured temperature.

The detailed flow traverses (steady total pressure, time-resolved total pressure, time-resolved velocities) were conducted only for the smallest and largest tip clearance configurations at the nominal loading and high loading operating conditions. Thus, there is a multitude of additional data which could be collected at additional loading conditions (i.e., low loading condition) or at the intermediate tip clearance height. The measurements collected from a third tip clearance could accommodate a more thorough analysis of trends associated with vorticity, leakage flow size, and more as they relate to changing tip clearance.

The velocity and flow angle measurements collected in this study utilized the single slanted hot-wire technique. However, the potential utility of a multi-sensor probe for capturing instantaneous three-dimensional velocities and, potentially, turbulence statistics, is significant. As a result, comparison measurements using a three-dimensional measurement technique from a triple-wire probe with the results presented herein will provide useful information regarding the relative errors from these techniques for turbomachinery applications.

The significant dependence of hot-wire measurements on changing thermodynamic conditions was assessed in this document. A linear relationship of velocity error with temperature difference (from calibration to test conditions) was proposed and implemented. However, future hot-wire measurements may benefit from the development of new relationships to accommodate temperature variations with compressibility considerations. Aside from this, a more controlled selection of ambient inlet conditions which more closely resemble calibration conditions (on the order of ten degrees Fahrenheit or less), or several calibration sets for different temperature ranges, are also recommended for future hot-wire measurements.

Finally, the understanding of the rotor tip leakage flow and its impact on the compressor performance developed through this study has created a unique opportunity to investigate leakage flow control techniques (such as casing treatments) and blade design methodologies aimed toward desensitization of detrimental tip leakage flow effects. Ultimately, it is these technologies that will help to drive the future of robust compressor designs.

LIST OF REFERENCES

LIST OF REFERENCES

Adkins, Jr., G.G. and Smith, Jr., L.H., 1982, “Spanwise Mixing in Axial-Flow Turbomachines,” *Journal of Engineering for Power*, **104**(1), pp. 97-110.

American Society of Mechanical Engineers, 2004, “Flow Measurement,” ASME PTC 19.5-2004, pp. 19-27.

Ball, P.R., 2013, “An Experimental and Computational Investigation on the Effects of Stator Leakage Flow on Compressor Performance,” Purdue University, West Lafayette, IN, Master Thesis.

Berdanier, R.A. and Key, N.L., 2015a, "Experimental Investigation of Factors Influencing Operating Rotor Tip Clearance in Multistage Compressors," *International Journal of Rotating Machinery*, Article ID 146272 (14 pages).

Berdanier, R.A. and Key, N.L., 2015b, “Data Processing Techniques for Measurements Collected from a Single Slanted Hot-Wire,” Presented at the AIAA Fluid Dynamics Conference, Dallas, TX, June 22-26, 2015.

Berdanier, R.A. and Key, N.L., 2015c, “Utilization of a New Data Reduction Technique for Single Slanted Hot-Wire Measurements Used to Study Compressor Tip Leakage Flows,” Submitted to *Experiments in Fluids*.

Berdanier, R.A., Smith, N.L., Fabian, J.C., and Key, N.L., 2015, “Humidity Effects on Experimental Compressor Performance—Corrected Conditions for Real Gases,” *Journal of Turbomachinery*, **137**(3), 031011 (10 pages).

Boyd, D.M., and Fleeter, S., 2003, “Axial Compressor Blade-to-Blade Unsteady Aerodynamic Variability,” *Journal of Propulsion and Power*, **19**(2), pp. 242-249.

Brossman, J.R., 2012, “An Investigation of Rotor Tip Leakage Flows in the Rear-Block of a Multistage Compressor,” Purdue University, West Lafayette, IN, PhD Dissertation.

Bruna, D. and Turner, M.G., 2013, “Isothermal Boundary Condition at Casing Applied to the Rotor 37 Transonic Axial Flow Compressor,” *Journal of Turbomachinery*, **135**(3), 034501 (4 pages).

Camp, T.R. and Day, I.J., 1998, "A Study of Spike and Modal Stall Phenomena in a Low-Speed Axial Compressor," *Journal of Turbomachinery*, **120**(3), pp. 393-401.

Chen, G.-T., 1991, "Vortical Structures in Turbomachinery Tip Clearance Flows," Massachusetts Institute of Technology, Cambridge, MA, PhD Dissertation.

Collis, D.C. and Williams, M.J., 1959, "Two-dimensional convection from heated wires at low Reynolds numbers," *Journal of Fluid Mechanics*, **6**(3), pp. 357-384.

Courtiade, N. and Ottavy, X., 2012, "Experimental Study of Surge Precursors in a High-Speed Multistage Compressor," ASME Paper GT2012-68321, pp. 1-10.

Cumpsty, N.A., 1986, "Annulus Wall Boundary-Layer Measurements in a Four-Stage Compressor," *Journal of Engineering for Gas Turbines and Power*, **108**(1), pp. 2-6.

Cumpsty, N.A., 2004, *Compressor Aerodynamics*, Krieger: Malabar, FL.

Day, I.J., 1993, "Stall Inception in Axial Flow Compressors," *Journal of Turbomachinery*, **115**(1), pp. 1-9.

Denton, J.D., 2010, "Some Limitations of Turbomachinery CFD," ASME Paper GT2010-22540, pp. 1-11.

Dickens, T. and Day, I., 2011, "The Design of Highly Loaded Axial Compressors," Journal of Turbomachinery, **133**(3), pp. 1-10.

Dong, Y., Xinqian, Z., and Qiushi, L., 2014, "An 11-stage axial compressor performance simulation considering the change of tip clearance in different operating conditions," *Proceedings of the IMechE Part A: Journal of Power and Energy*, **228**(6), pp. 614-625.

Erwin, J.R., 1964, "Experimental Techniques," *Aerodynamics of Turbines and Compressors*, W.R. Hawthorne ed., Princeton University Press, Princeton, NJ, pp. 167-269.

Freeman, C., 1985, "Effect of Tip Clearance Flow on Compressor Stability and Engine Performance," VKI Lecture Series, 1985-05.

Gallimore, S.J. and Cumpsty, N.A., 1986, "Spanwise Mixing in Multistage Axial Flow Compressors: Part I – Experimental Investigation," *ASME Journal of Turbomachinery*, **108**(1), pp 2-9.

Gieseke, T.J. and Guzennec, Y.G., 1993, "An Experimental Approach to the Calibration and Use of Triple Hot-Wire Probes," *Experiments in Fluids*, **14**, pp. 305-315.

Goto, A., 1992, "Three-Dimensional Flow and Mixing in an Axial Flow Compressor with Different Rotor Tip Clearances," *Journal of Turbomachinery*, **114**(3), pp. 675-685.

Gupta, A., Khalid, S.A., McNulty, G.S., and Dailey, L., 2003, "Prediction of Low Speed Compressor Rotor Flowfields with Large Tip Clearances," ASME Paper GT2003-38637.

Heidmann, J.D., 2009, "NASA Turbomachinery Technical Working Group Technology Assessment," *Mechanical Engineering: Global Gas Turbine News*, **49**(4), pp. 5-6.

Houghton, T. and Day, I., 2010, "Stability Enhancement by Casing Grooves: The Importance of Stall Inception Mechanism and Solidity," ASME Paper No. GT2010-22284, 9 pages.

Hoying, D.A., Tan, C.S., Vo, H.D, and Greitzer, E.M., 1999, "Role of Blade Passage Flow Structures in Axial Compressor Rotating Stall Inception," *Journal of Turbomachinery*, **121**(4), pp. 735-742.

Hunter, I.H. and Cumpsty, N.A., 1982, "Casing Wall Boundary-Layer Development Through an Isolated Compressor Rotor," *Journal of Engineering for Power*, **104**(4), pp. 805-817.

Hutton, S.P., 1956, "Three-Dimensional Motion in Axial-Flow Impellers," *Proceedings of the Institute of Mechanical Engineers*, **170**, pp. 863-873.

Inoue, M., Kuroumaru, M., and Fukuhara, M., 1986, "Behavior of Tip Leakage Flow Behind an Axial Compressor Rotor," *Journal of Engineering for Gas Turbines and Power*, **108**(1), pp. 7-14.

Kanevce, G. and Oka, S., 1973, "Correcting hot-wire readings for influence of fluid temperature variations," DISA Info., **15**, pp. 21-24.

Key, N.L., 2007, "Vane Clocking Effects in an Embedded Compressor Stage," Purdue University, West Lafayette, IN, PhD Dissertation.

Key, N.L., Lawless, P.B., and Fleeter, S., 2010, "Rotor Wake Variability in a Multistage Compressor," *Journal of Propulsion and Power*, **26**(2), pp. 344-352.

Khalid, S.A., 1994, "The Effects of Tip Clearance on Axial Compressor Pressure Rise," Massachusetts Institute of Technology, Cambridge, MA, PhD Dissertation.

Khalid, S.A., Khalsa, A.S., Waitz, I.A., Tan, C.S., Greitzer, E.M., Cumpsty, N.A., Adamczyk, J.J., and Marble, F.E., 1999, "Endwall Blockage in Axial Compressors," *Journal of Turbomachinery*, **121**(3), pp. 499-509.

Khalsa, A.S., 1996, "Endwall Blockage in Axial Compressors," Massachusetts Institute of Technology, Cambridge, MA, PhD Dissertation.

King, L.V., 1914, “On the Convection of Heat from Small Cylinders in a Stream of Fluid: Determination of the Convection Constants of Small Platinum Wires with Applications to Hot-Wire Anemometry,” *Philosophical Transactions of the Royal Society A*, **214**, pp. 373-432.

Koch, C.C., 1981, “Stalling Pressure Rise Capability of Axial Flow Compressor Stages,” *Journal of Engineering for Power*, **103**(4), pp. 645-656.

Krug, A., Busse, P., and Vogeler, K., 2015, “Experimental Investigation Into the Effects of the Steady Wake-Tip Clearance Vortex Interaction in a Compressor Cascade,” *Journal of Turbomachinery*, **137**(6), 061006 (10 pages).

Lakshminarayana, B. and Pandya, A., 1984, “Tip Clearance Flow in a Compressor Rotor Passage at Design and Off-Design Conditions,” *Journal of Engineering for Gas Turbines and Power*, **106**(3), pp. 570-577.

Lakshminarayana, B., Pouagare, M., and Davino, R., 1982a, “Three-Dimensional Flow Field in the Tip Region of a Compressor Rotor Passage—Part I: Mean Velocity Profiles and Annulus Wall Boundary Layer,” *Journal of Engineering for Power*, **104**(4), pp. 760-771.

Lakshminarayana, B., Davino, R., Pouagare, M., 1982b, “Three-Dimensional Flow Field in the Tip Region of a Compressor Rotor Passage—Part II: Turbulence Properties,” *Journal of Engineering for Power*, **104**(4), pp. 772-781.

Lemmon, E. W., Huber, M. L., and McLinden, M. O., 2013, NIST Standard Reference Database 23: Reference Fluid Thermodynamic and Transport Properties—REFPROP, Version 9.1, National Institute of Standards and Technology, Standard Reference Data Program, Gaithersburg, MD.

Levis, W.R., 2006, “Unsteady Casewall Pressure Measurements in a Transonic Compressor,” Naval Postgraduate School, Monterey, CA, Master Thesis.

Leylek, J.H. and Wisler, D.C., 1991, “Mixing in Axial-Flow Compressors: Conclusions Drawn from Three-Dimensional Navier-Stokes Analyses and Experiments,” *Journal of Turbomachinery*, **113**(2), pp 139-160.

Liu, B., Wang, H., Liu, H., and Yu, H., 2003, “Experimental Investigation of Unsteady Flow Field in the Tip Region of an Axial Compressor Rotor Passage at Near Stall Condition with SPIV,” ASME Paper No. GT2003-38185, pp. 1-12.

Lou, F., Fabian, J., and Key, N.L., 2013, “Effects of Invoking Different Gas Models on Air Compressor Efficiency Calculation,” *Journal of Engineering for Gas Turbines and Power*, **136**(1), 012601 (8 pages).

Ma, H., 2001, “Three-Dimensional Unsteady Flow Field Due to IGV-Rotor Interaction in the Tip Region of an Axial Compressor Rotor Passage,” ASME Paper No. 2001-GT-0296.

Mailach, R., Lehmann, I, and Vogeler, K., 2008, “Periodical Unsteady Flow Within a Rotor Blade Row of an Axial Compressor—Part II: Wake-Tip Clearance Vortex Interaction,” *Journal of Turbomachinery*, **130**(4), 041005 (10 pages).

McDougall, N.M., 1990, “A Comparison Between the Design Point and Near-Stall Performance of an Axial Compressor,” *Journal of Turbomachinery*, **112**(1), pp. 109-115.

McDougall, N.M., Cumpsty, N.A., and Hynes, T.P., 1990, “Stall Inception in Axial Compressors,” *Journal of Turbomachinery*, **112**(1), pp. 116-123.

Methel, J.C., Smith, N.R., and Key, N.L., 2015, “Vane Wake Characterization for a Multistage Compressor Including Variability,” AIAA Paper No. 2015-1341, pp. 1-11.

Morrison, E.S.S., 2013, “Development of a Three Dimensional Compressible Flow Calibration Facility for Thermal Anemometry,” Purdue University, West Lafayette, IN, Master Thesis.

Moyle, I.N., Shreeve, R.P., Walker, G.J., 1996, “Case Wall Pressures in a Multistage Axial Compressor with Tip Clearance Variation,” *Journal of Propulsion and Power*, **12**(5), pp. 967-973.

Müller, D., Sheard, A.G., Mozumdar, S., and Johann, E., 1997, “Capacitive measurement of compressor and turbine blade tip to casing running clearance,” *Journal of Engineering for Gas Turbines and Power*, **119**(3), pp. 877-884.

Murray, W.L., 2014, “Experimental Investigation of a Forced Response Condition in a Multistage Compressor,” Purdue University, West Lafayette, IN, Master Thesis.

NACA Subcommittee on Compressors, 1950, “Standard Procedures for Rating and Testing Multistage Axial-Flow Compressors,” NACA TN-1138.

Peacock, R.E., 1982, “A review of turbomachinery tip gap effects. Part 1: Cascades,” *International Journal of Heat and Fluid Flow*, **3**(4), pp. 185-193.

Peacock, R.E., 1983, “A review of turbomachinery tip gap effects. Part 2: Rotating machinery,” *International Journal of Heat and Fluid Flow*, **4**(1), pp. 3-16.

Pullan, G., Young, A.M., Day, I.J., Greitzer, E.M., and Spakovszky, Z.S., 2015, “Origins and Structure of Spike-Type Rotating Stall,” *Journal of Turbomachinery*, **137**(5), 051007 (11 pages).

Reeder, J.A., 1968, "Tip Clearance Problems in Axial Compressors (A Survey of Available Literature)," Atomic Energy Commission R&D Report K-1682.

Ruden, P., 1944, "Investigation of Single Stage Axial Fans," NACA TM 1062.

Saathoff, H., Deppe, A., Stark, U., Rohdenburg, M., Rohkamm, H., Wulff, D., and Kosyna, G., 2003, "Steady and Unsteady Casingwall Flow Phenomena in a Single-Stage Low-Speed Compressor at Part-Load Conditions," *International Journal of Rotating Machinery*, **9**(5), pp. 327-335.

Sans, J., Dell-Era, G., Desset, J., Brouckaert, J.-F., and Hiernaux, S., "Time-Resolved Measurements of the Unsteady Flow Field in a Single Stage Low Pressure Axial Compressor," ASME Paper No. GT2013-94264, pp. 1-14.

Schmidt, D.P. and Okiishi, T.H., 1976, "Multistage Axial-Flow Turbomachine Wake Production, Transport, and Interaction," AFOSR-TR-77-0720.

Sherman, P.J., Dudley, R., and Suarez, M., 1996, "The Stochastic Structure of Downstream Pressure from an Axial Compressor – II. An Investigation of Blade-to-Blade Variability," *Mechanical Systems and Signal Processing*, **10**(4), pp. 423-437.

Shin, H.-W., 2015, Private communications.

Shin, H.-W. and Hu, Z.A., 1986, "Measurement of Swirling Flow Field Using the Single-Slanted Hot-Wire Technique," *International Journal of Turbo and Jet Engines*, **3**(2-3), pp. 139-146.

Shin, H.-W., Solomon, W., and Wadia, A., 2008, "Transonic fan tip-flow features revealed by high frequency response over-tip pressure measurements," ASME Paper No. GT2008-50279, pp. 1-9.

Sirakov, B.T. and Tan, C.-S., 2003, "Effect of Unsteady Stator Wake—Rotor Double-Leakage Tip Clearance Flow Interaction on Time-Average Compressor Performance," *Journal of Turbomachinery*, **125**(3), pp. 465-474.

Smith, L.H., 1970, "Casing Boundary Layers in Multistage Axial-Flow Compressors," in: *Flow Research in Blading*, L.S. Dzung, ed., Elsevier, Amsterdam, p. 275.

Smith, N.R., 2015, "An Experimental Study on the Effects of Blade Row Interactions on Aerodynamic Loss Mechanisms in a Multistage Compressor," Purdue University, West Lafayette, IN, PhD Dissertation.

Smith, N.R. and Key, N.L., 2015, "Flow Visualization for Investigating Stator Losses in a Multistage Axial Compressor," *Experiments in Fluids*, **56**(5), 94 (17 pages).

Smith, N.R., Berdanier, R.A., Fabian, J.C., and Key, N.L., 2015a, "Reconciling Compressor Performance Differences for Varying Ambient Inlet Conditions," *Journal of Engineering for Gas Turbines and Power*, **137**(12), 122603 (9 pages).

Smith, N.R, Murray III, W.L., and Key, N.L., 2015b, "Considerations for Measuring Compressor Aerodynamic Excitations Including Rotor Wakes and Tip Leakage Flows," ASME Paper GT2015-43508, pp. 1-11.

Storer, J.A. and Cumpsty, N.A., 1994, "An Approximate Analysis and Prediction Method for Tip Clearance Loss in Axial Compressors," *Journal of Turbomachinery*, **116**(4), pp. 648-656.

Suder, K.L., 1998, "Blockage Development in a Transonic, Axial Compressor Rotor," *Journal of Turbomachinery*, **120**(3), pp 465-476.

Suder, K.L. and Celestina, M.L., 1996, "Experimental and Computational Investigation of the Tip Clearance Flow in a Transonic Axial Compressor Rotor," *Journal of Turbomachinery*, **118**(2), pp 218-229.

Sakulkaew, S., Tan, C.S., Donahoo, E., Cornelius, C., and Montgomery, M., 2013, "Compressor Efficiency Variation With Rotor Tip Gap From Vanishing to Large Clearance," *Journal of Turbomachinery*, **135**(3), 031030 (10 pages).

Talalayev, A., 2011, "On the Renovation of the Three-Stage Axial Compressor Research Facility for Compressor Performance Research," Purdue University, West Lafayette, IN, Master Thesis.

Tan, D., Yuanchao, L., Wilkes, I., Miorini, R.L., and Katz, J., 2014, "PIV Measurements of the Flow in the Tip Region of a Compressor Rotor," ASME Paper No. FEDSM2014-21593, pp. 1-11.

Tschirner, T., Johann, E., Müller, R., and Vogeler, K., 2006, "Effects of 3D aerofoil tip clearance variation on a 4-stage low speed compressor," ASME Paper No. GT2006-90902, pp. 1-10.

Van Zante, D.E., Strazisar, A.J., Wood, J.R., Hathaway, M.D., and Okiishi, T.H., 1999, "Recommendations for Achieving Accurate Numerical Simulation of Tip Clearance Flows in Transonic Compressor Rotors," *Journal of Turbomachinery*, **122**(4), pp 733-742.

Walsh, P.P. and Fletcher, P., *Gas Turbine Performance*, Blackwell Science, Oxford, 2008.

Weichert, S. and Day I., 2014, "Detailed Measurements of Spike Formation in an Axial Compressor," *Journal of Turbomachinery*, **136**(5), 051006 (9 pages).

Wennerstrom, A.J., 1989, "Low Aspect Ratio Axial Flow Compressors: Why and What It Means," *Journal of Turbomachinery*, **111**(4), pp. 357-365.

Williams, R., Gregory-Smith, D., and He, L., 2006, “A Study of Large Tip Clearance Flows in an Axial Compressor Blade Row,” ASME Paper No. GT2006-90463, pp. 1-9.

Wisler, D.C., 1985a, “Aerodynamic Effects of Tip Clearance, Shrouds, Leakage Flow, Casing Treatment, and Trenching in Compressor Design: Blading Design in the Endwall Region,” VKI Lecture Series, 1985-05.

Wisler, D.C., 1985b, “Loss Reduction in Axial-Flow Compressors Through Low-Speed Model Testing,” *Journal of Engineering for Gas Turbines and Power*, **107**(2), pp. 354-363.

Wisler, D.C., 1998, “Axial-Flow Compressor and Fan Aerodynamics,” *Handbook of Fluid Dynamics*, R.W. Johnson, ed., CRC Press, Boca Raton, FL.

Wisler, D.C., Bauer, R.C., and Okiishi, T.H., 1987, “Secondary Flow, Turbulent Diffusion, and Mixing in Axial Flow Compressors,” *Journal of Turbomachinery*, **109**(4), pp 455-482.

Wisler, D.C. and Beacher, B.F., 1989, “Improved Compressor Performance Using Recessed Clearance (Trenches),” *Journal of Propulsion*, **5**(4), pp. 469-475.

Yoon, S.Y., Song, S.J., and Shin, H.-W., 2006, “Influence of Flow Coefficient, Stagger Angle, and Tip Clearance on Tip Vortex in Axial Compressors,” *Journal of Fluids Engineering*, **128**(6), pp. 1274-1280.

APPENDICES

Appendix A. Mean Rotor Wakes for the Embedded Stage (Stage 2)

A primary goal for this project is to investigate the effect of the rotor tip clearance and the associated tip leakage flow on the performance of an embedded stage. The embedded stage provides a unique opportunity to evaluate the influence of the upstream and downstream stages. Information in this document has noted the differences between the first stage and the other two stages as the aft stages ingest increased blockage due to the rotor tip leakage flow disturbance. At this point, the variations of the rotor wake will be evaluated with respect to a passage-average wake using the time-resolved flow angle measurements.

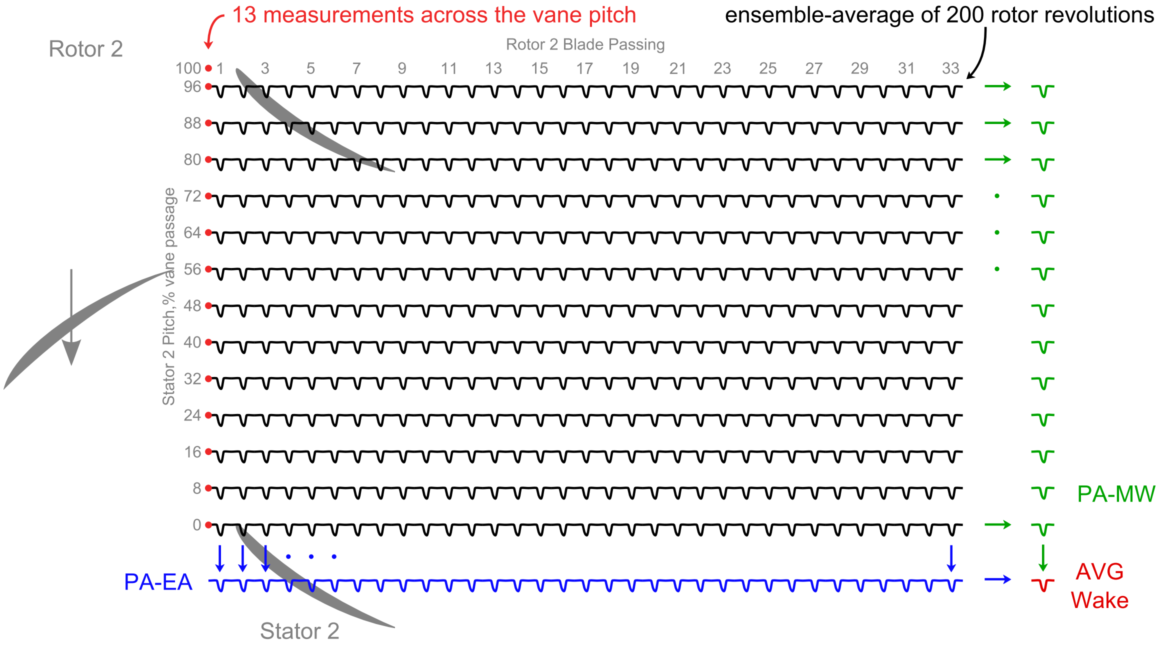

Figure A.1: Schematic outlining the two averaging methods used for hot-wire measurements at Rotor 2 exit. Adapted from Smith et al. (2015b).

The Rotor 2 exit flow angles for TC1 and TC3 have been evaluated using two different averaging techniques, as defined by Key (2007) and shown by the schematic in Figure A.1. The first method is the Passage Average Ensemble Average (PA-EA) technique. For these hot-wire measurements, this method begins with an EA of 200 rotor revolutions for data collected at each of the pitchwise measurement positions (at the Rotor 2 exit plane, 13 positions were investigated across one vane pitch). The 13 discrete EA signals from each of the pitchwise positions are then averaged to identify an EA revolution which is free from effects due to the upstream and downstream vane positions. This EA revolution could also be divided into 33 segments (for Rotor 2, e.g.) to analyze the blade-to-blade variations, but it will be considered in whole for this analysis.

The second method is the Passage Average Mean Wake (PA-MW) technique which was applied previously for the time-resolved pressure measurements. This method begins by calculating an ensemble average of 200 rotor revolutions at each pitchwise measurement location. Next, the PA-MW method divides the EA signal into the 33 separate blade wake signals (for Rotor 2), and the average of these 33 wakes is calculated to identify a separate "mean wake" for each of the circumferential pitchwise measurement positions. Similar to methods utilized previously in this study, this PA-MW averaging technique yields a variability of the wakes associated with the upstream and downstream vanes.

Figure A.2(a) shows the Rotor 2 PA-EA yaw angles measured at the nominal loading (NL) condition for four selected radial measurement positions (20%, 50%, 80%, and 88% annulus height). These selected radial positions highlight some of the flow features discussed in other locations throughout the report, as well as illuminating some additional important observations. At each of the radial positions, a three-per-revolution pattern can be identified in the measurements. This modulation occurs as the result of a blade count difference between Rotor 1 (36 blades) and Rotor 2 (33 blades). As the Rotor 1 wake persists through the compressor and interacts with Rotor 2, it influences the shape of the Rotor 2 wake. Specifically, when the Rotor 1 wake aligns with the Rotor 2 wake, it increases the depth of the Rotor 2 wake.

The PA-EA yaw angles are relatively unaffected at the 50% measurement position when the tip clearance height is increased from TC1 to TC3. In Figure 5.36, the slight decrease of time-averaged yaw angle at 50% annulus height with increased tip clearance is reflected through a decrease of the wake depth in Figure A.2(a). At 20% span, the overall wake depth is relatively unchanged as the tip clearance is increased, but the bulk mean flow shows a decreased absolute yaw angle. As the blockage increases with tip clearance, the redistribution of flow (increase of axial velocity) in the hub region leads to a decrease of yaw angle in the absolute frame of reference.

At the measurement locations closer to the tip, the 3/rev modulation of the PA-EA signal is more clearly identified and the presence of the Rotor 1 wakes may be identified between Rotor 2 wakes when the two are out-of-phase (i.e., normalized times 1, 12, and 23 at 80% annulus height). A significant change in the PA-EA yaw angles is also observed due to the influence of the tip leakage flow. In particular, at 80%, Figure A.2(a) shows the tip leakage flow is less present in these traces of flow angle for TC1. However, the tip leakage flow is clearly present for each blade with the TC3 tip clearance configuration. Comparing the two clearances for blade 3 (for example) shows the additional bump in the TC3 traces is due to a flow feature that was not present at TC1.

At 88% annulus height, the tip leakage flow appears in the measurements collected from both tip clearance configurations. Indeed, Figure 5.30 shows this is the approximate location of the center of the high-loss leakage flow region for both TC1 and TC3. Both tip clearances show that the yaw angle peak due to the tip leakage flow does not modulate much with the 3/rev beating pattern (on the order of 2 degrees), compared to the modulation of the wake peaks at 80% on the order of 5 degrees. For TC3, Figure A.2(a) suggests that the leakage flow contributes a peak flow angle which is greater than the actual rotor wake for nearly all 33 blades. As a result, the PA-EA signal appears to approach a full sine wave, instead of the "half-rectified" shape at 20% or 50%.

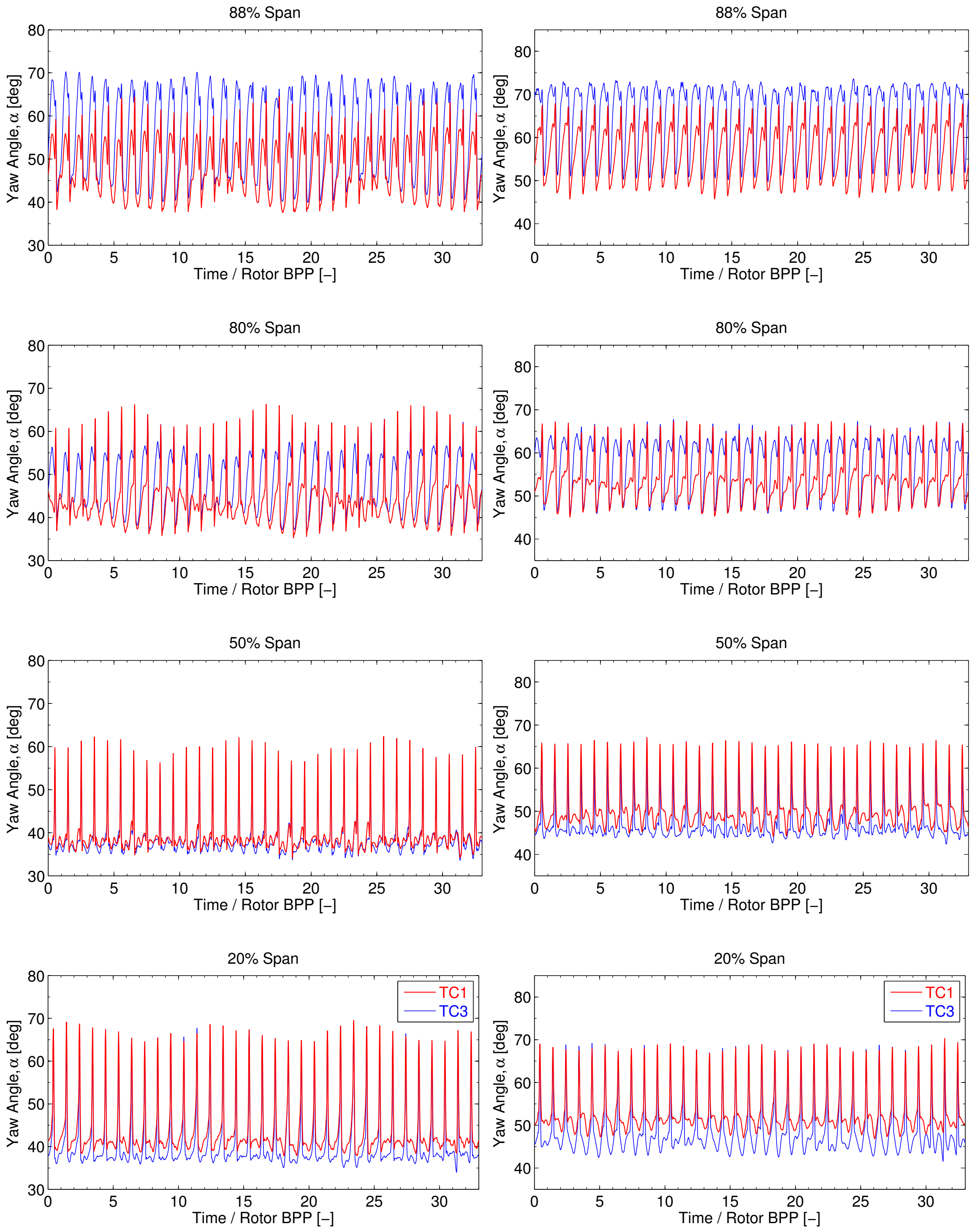

(a) (b)

Figure A.2: Average Rotor 2 revolution of yaw angle at select radial positions using PA-EA method. (a) NL; (b) HL.

A similar comparison of the PA-EA absolute yaw angle wakes at the high loading (HL) condition is also shown, Figure A.2(b). At 20% annulus height, the peak value of the yaw angle in the rotor wakes is unchanged from TC1 to TC3, but the mean flow angle decreases – as before, this is an artifact of the redistribution of flow toward the hub with increased tip clearance. Overall, this contributes to a deeper wake for TC3 at this measurement location. At 50%, there is a more noticeable difference between tip clearance configurations, compared with the NL condition in Figure A.2(a). Referring to the time-averaged results for HL, Figure 5.37, these data show a more distinct delta between the flow angles across the entire annulus, whereas the NL results, Figure 5.36, present flow angles which are less affected from 50% to 80% annulus height.

As discussed above for the NL condition, the measurements at 80% and 88% show more noticeable contributions of the tip leakage flow. At this HL condition, though, there is a considerable change in the influence and extent of the leakage flow. Referring to the time-resolved total pressure unsteadiness at the same condition, Figure 5.31, the mean leakage flow disturbance fills nearly the entire rotor passage (in the circumferential direction) at HL for TC3, whereas the leakage flow for TC1 only influences approximately half of the rotor passage. As a result, these PA-EA wakes at 88% in Figure A.2(b) reflect a much wider region of high absolute yaw angle.

As a separate analysis, the absolute yaw angles at Rotor 2 exit were also processed using the PA-MW technique at the same four radial measurement locations. As shown schematically in Figure A.1, the PA-MW method removes blade-to-blade variations and the 3/rev modulation due to the blade count difference between Rotor 1 and Rotor 2. Instead, this method highlights flow variations in the pitchwise direction.

In Figure A.3(a), the 13 separate PA-MW wakes for the NL condition are shown (thin lines), as well as the weighted average (thick lines) for each tip clearance configuration. At the 20% and 50% measurement locations, Figure A.3(a) shows minimal variation between the different pitchwise positions. In general, the variation is on the order of ±2 degrees for both radial measurement locations. The 80% and 88% locations, however, the leakage flow introduces a bump of absolute yaw angle, as suggested by the PA-EA results above. At these measurement locations near the rotor tip, the amplitude and position of this bump changes due to the modulation of the tip leakage flow. A comparison of the results in Figure A.3(a) with the time-resolved total pressure unsteadiness, Figure 5.30, confirms this observation – the increased blockage due to the tip leakage flow reduces the flow velocity and results in a corresponding increase of absolute yaw angle in these regions. For both 80% and 88% annulus height, however, the weighted average wake shows the location in the rotor passage of the bump off the blade PS is largely unaffected by the change of tip clearance from TC1 to TC3.

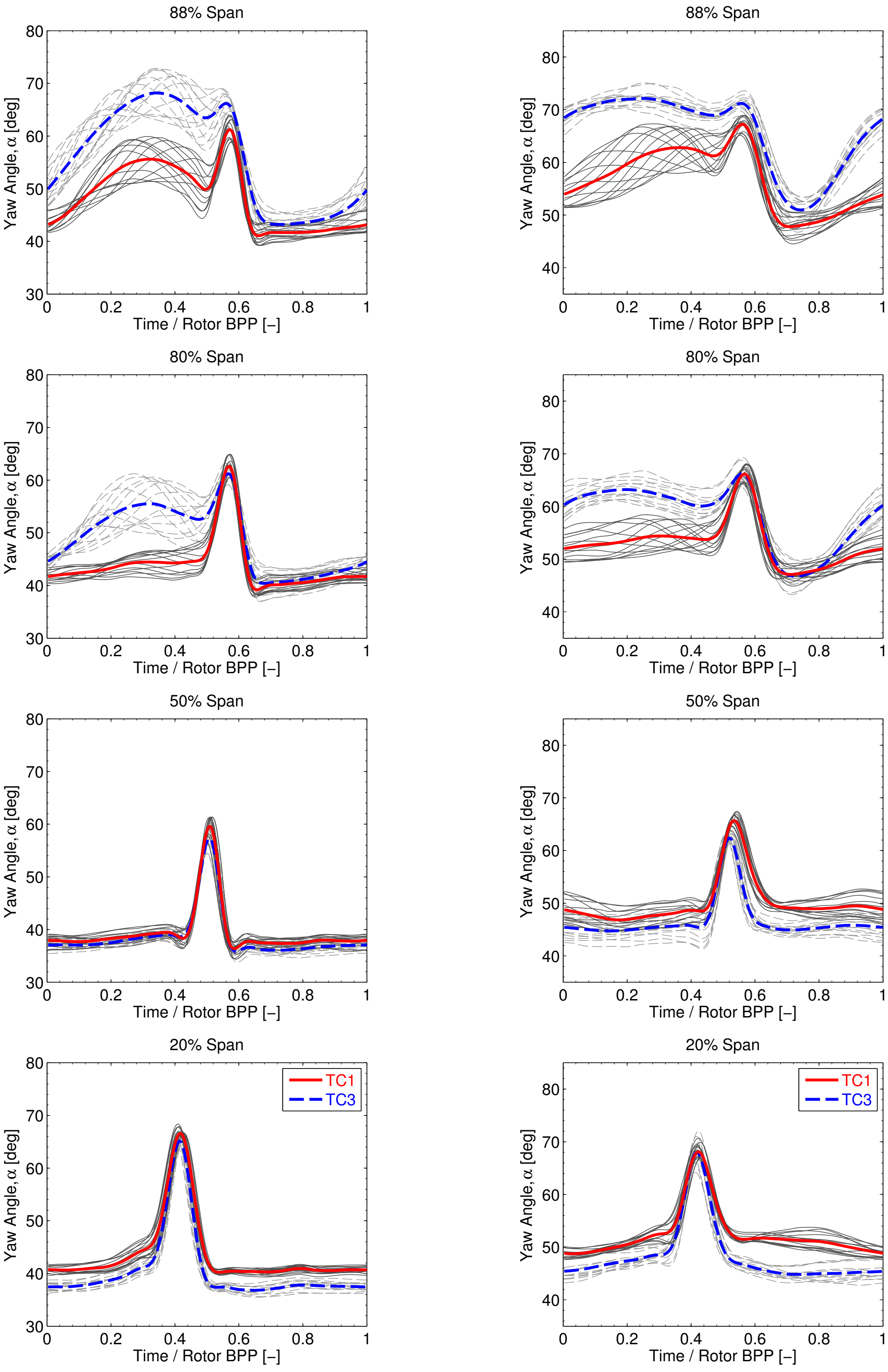

(a) (b)

Figure A.3: Average Rotor 2 wakes at select radial positions using PA-MW method. (a) NL; (b) HL.

Considering instead the high loading (HL) operating condition, Figure A.3(b), shows a different result in the PA-MW results at 80% and 88%. In particular, the 13 individual PA-MW curves for TC1 confirm the modulation of the tip leakage flow identified above. However, the TC3 results show less variability of the leakage flow. At this increased tip clearance height, the influence of the leakage flow region extends across a greater circumferential portion of the rotor passage. At these outer measurement positions, the circumferential extent of the tip leakage flow region is largely unchanged as the upstream and downstream stator vanes are moved; however, the depth of the leakage flow region does vary (as confirmed by the size and intensities of the tip leakage flow region in Figure 5.31).

Appendix B. Time-Averaged Stator Wakes

In addition to the rotor exit measurements, the pitchwise velocity and flow angles at the stator exit planes provide valuable information to supplement the total pressure wakes and pitchwise total temperatures shown in Section 3.4.1. For these figures, the time-average of the ensemble-averaged signal at each location is calculated to create a two-dimensional mesh of data in the radial-circumferential plane at the measurement location. Similar to the total pressure wakes and pitchwise total temperatures presented earlier, three discrete radial measurement locations were selected for comparison (50%, 70%, and 80% annulus height). The same hot-wire data used to present the radial profiles in Section 5.3.1 provide a comparison between two tip clearance configurations (TC1 and TC3) at two operating conditions on the 100% corrected speedline (NL and HL).

The Stator 1 wake data, Figure B.1, present absolute velocity as a ratio of the rotor tip speed, and normalized by the calculated value at the 50% annulus height measurement position. These velocity wakes compare well in shape to the pressure wakes presented at the same axial measurement position, Figure 3.28. A comparison of the two loading conditions in Figure B.1 shows a distinct change of the measured absolute flow angles at the three radial measurement positions, as well as across the wake in the pitchwise direction. Specifically, the NL operating condition illustrates an envelope of approximately ten degrees for absolute yaw angle and pitch angle; however, the same angles at the HL operating condition show values which extend beyond a 25 degree range. Evaluation of the same results at the Stator 2 exit plane, Figure B.2, and the Stator 3 exit plane, Figure B.3, yield similar results to those discussed for Stator 1. These results also compare well with the total pressure wakes and pitchwise total temperature profiles in Figure 3.29 and Figure 3.30 for Stator 2 and Stator 3, respectively.

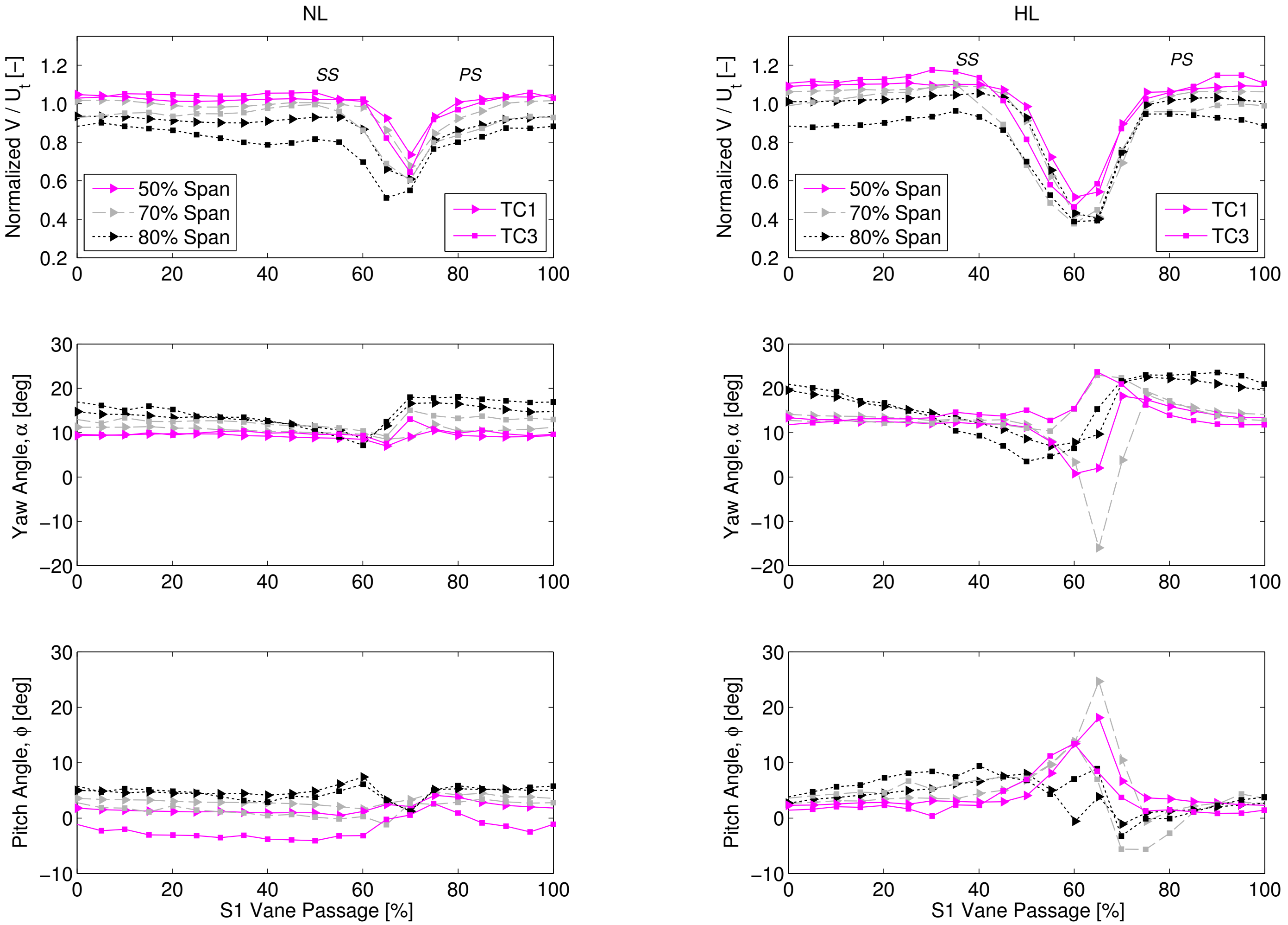

Figure B.1: Stator 1 time-averaged velocity and flow angle wakes.

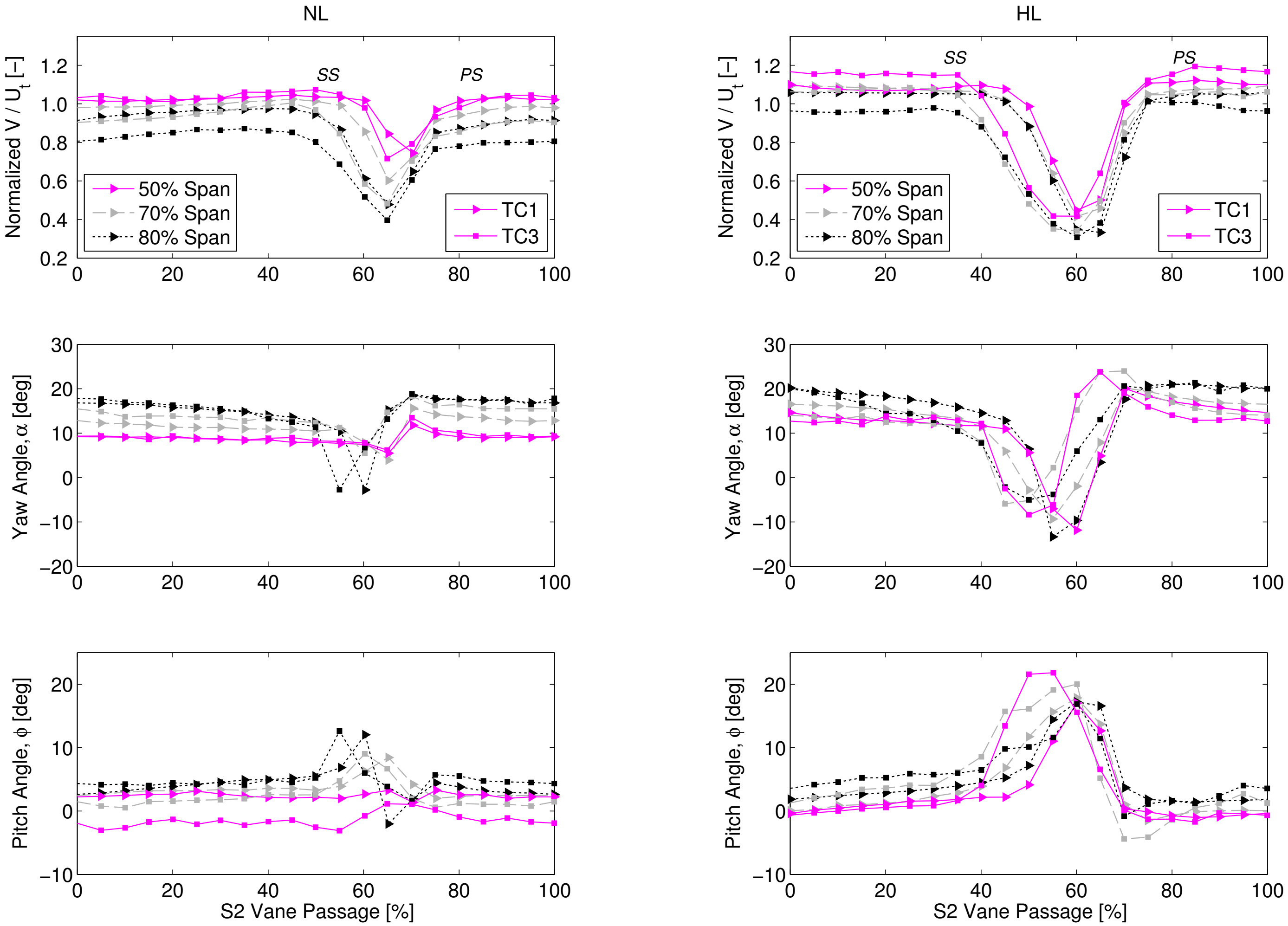

Figure B.2: Stator 2 time-averaged velocity and flow angle wakes.

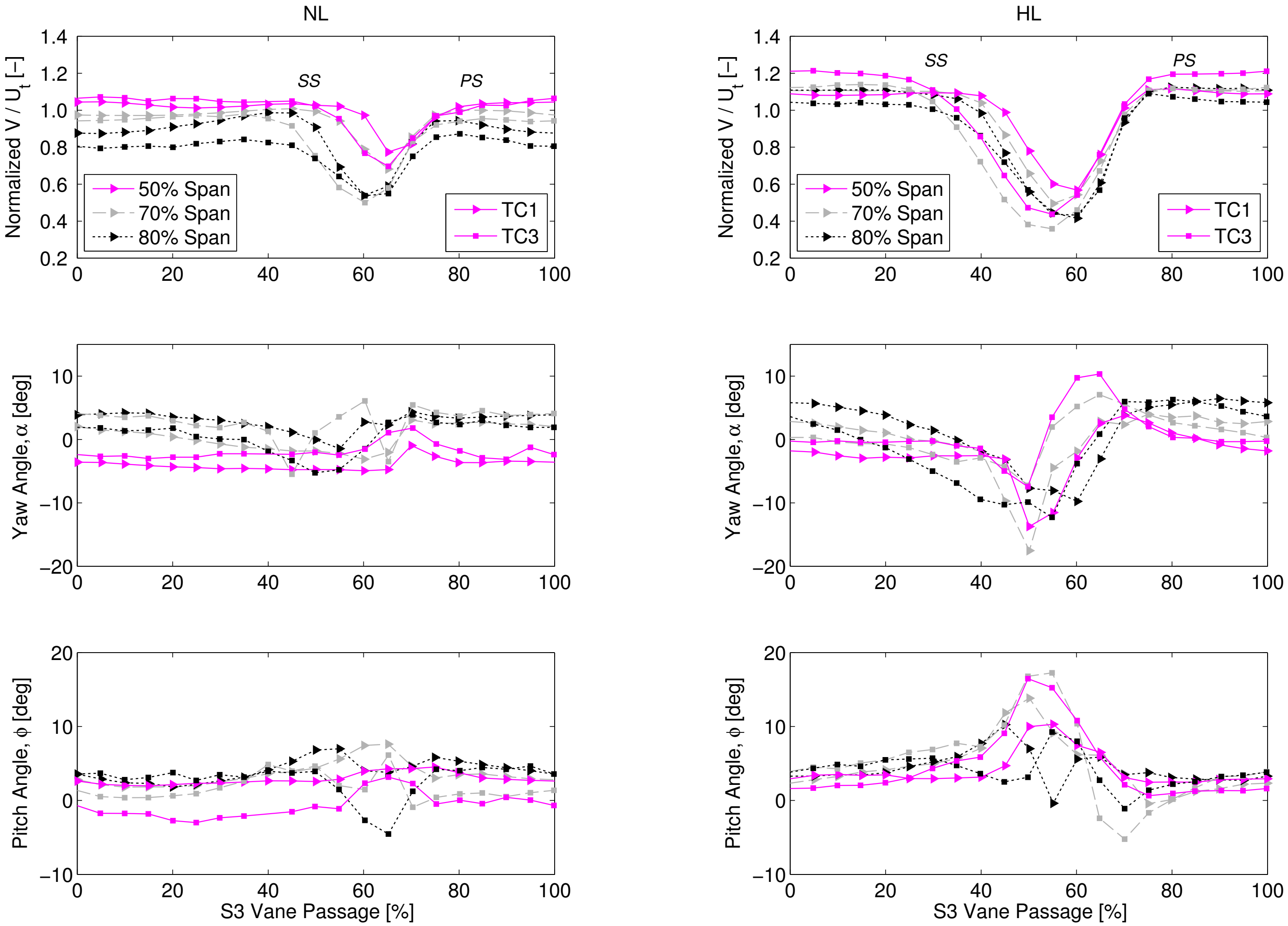

Figure B.3: Stator 3 time-averaged velocity and flow angle wakes.

Appendix C. A New Data Reduction Method for Slanted Hot-Wire Measurements

In addition to the non-linear solver (NLS) method for hot-wire data reduction discussed in this Chapter 2, a new method for processing data from a single slanted hot-wire for turbomachinery applications has been developed. This method, referred to as the 'look-up table' method (LUT), corrects measured voltages to the calibration data, thereby allowing a direct interpolation of data in a three-dimensional calibration space. The basis for a look-up table method has been introduced for X-wire configurations by previous authors in recent years (Key, 2007; Murray, 2014), and some authors have also extended this method to triple-wire probes (Gieseke and Guezennec, 1993; Morrison, 2013). However, the principle of utilizing a look-up table for data collected from a single slanted hot-wire is new. A graphical representation of the process for redistributing calibration data is given in Figure C.1.

If phase-locked ensemble-averaged data are collected in the method described herein for three wire orientations, a phase-locked triple-sensor probe can be simulated in the calibration data for processing purposes. It is important to note, though, that this look-up table method requires extreme precision during the probe positioning (data collection) process to be effective. If precision probe positioning is not achievable, the look-up table method is still possible, but a separate calibration space may be required for each set of three wire positions, which would significantly increase the computational expense. This differs fundamentally from the non-linear solver method which can accept any probe position in the equations.

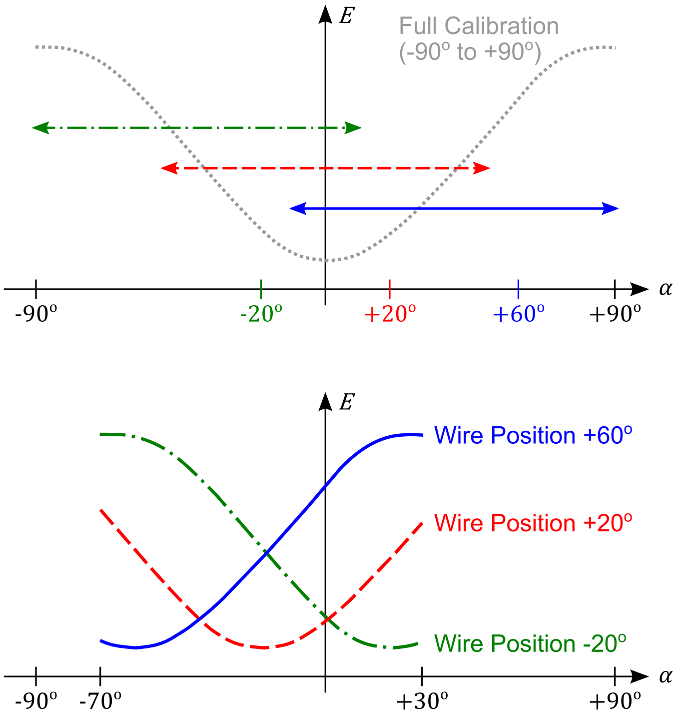

Figure C.1: Graphical representation of look-up table method for a slanted hot-wire.

Once the calibration data have been split and rearranged as shown in Figure C.1, a three-dimensional space is created corresponding to the calibration voltages. These calibration voltages are then combined with the `scatteredInterpolant` function in MATLAB to create Dalaunay triangulation matrices of velocity, yaw, and pitch for a given set of three wire voltages.

As with the NLS method, temperature and density variations in the fluid can introduce significant errors in the calculations if they are not properly considered. In this case, the following equation has been implemented to correct “test” voltages captured during compressor experiments back to the “cal” voltages which agree with the calibration temperature (Kanevce and Oka, 1973):

$$E_{\text{cal}} = E_{\text{test}} \left(\frac{T_w - T_{o,\text{cal}}}{T_w - T_{o,\text{test}}} \right)^{0.5} . \tag{C.1}$$

Similarly, a linearization process is applied to correct voltage effects due to density change back to the calibration space:

$$E_{\text{cal}} = E_{\text{test}} - \frac{\partial E}{\partial \rho} (\rho_{\text{test}} - \rho_{\text{cal}}) . \tag{C.2}$$

for which the voltage-density gradient, $\partial E / \partial \rho$, is determined through a separate calibration process with the calibration jet. Here, a correction based on mean density is sufficient because the density fluctuations in the flow are expected to be much less than the velocity fluctuations.

Typically, the voltage-density gradient is independent of wire orientation, but it may exhibit a strong dependence on the velocity, as shown in Figure C.2. As a result, an iterative solver scheme was implemented. By this process, an initial velocity "guess" based on an approximate velocity calculated from simultaneous pressure and temperature measurements was used to determine a value of the voltage-density gradient. The entire look-up table process (including density corrections using Equation (C.2)) was completed using this initial gradient, and the calculated mean velocity from the processed wire voltages was used to re-initialize the process with a new voltage-density gradient. This iterative process continued until a convergence criterion was achieved or a maximum number of iterations lapsed. Typical voltage-density gradient iterations affect the overall mean velocity by less than 3 ft/s.

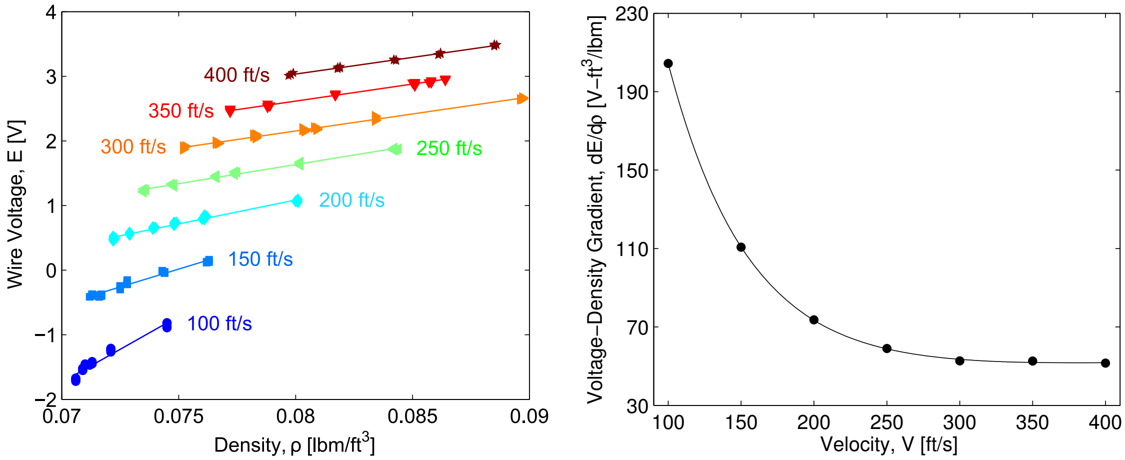

Figure C.2: Example calibration data for determining voltage-density gradient.

An assessment of processed results and associated errors from the non-linear solver and look-up table processing methods is provided in Berdanier and Key (2015c). However, an important consideration for the utility of a certain technique is related to the computational time required for the processing. There is no appreciable difference in the computational time required by the NLS method using one to two sets of calibration coefficients, but the relative simplicity of the look-up table interpolation method yields a computational expense which is one order of magnitude less than a solution of the non-linear equations. Based on these clock speeds, the look-up table approach has a significant advantage over the NLS algorithm. However, the implementation of an optimization algorithm with a compiled FORTRAN solver in place of the MATLAB solver can further improve the time required by the NLS algorithm to a value on the order of the LUT method.

VITA

VITA

Reid Adam Berdanier was born in Shelby, Ohio to parents Bruce and Melinda Berdanier on June 2, 1988. He has one brother, Aaron Berdanier. Reid grew up in Shelby, Ohio before moving to Rapid City, South Dakota, and then Ada, Ohio, where he graduated from Ada High School in 2006. In 2006, he began pursuing a degree in Mechanical Engineering at Syracuse University in Syracuse, New York. During his undergraduate studies, Reid was awarded a NASA-ASEE Aeronautics Scholarship, through which he worked as an intern at NASA Langley Research Center in Hampton, Virginia studying ultrasonic transducers in the nondestructive testing branch in 2009. He graduated Summa Cum Laude from Syracuse with a Bachelor of Science in Mechanical Engineering in May 2010. In the summer of 2010, Reid worked in the compressor aero design group at Siemens Energy in Orlando, Florida developing the preliminary design for a multistage axial compressor research facility. He began his graduate studies in August 2010 under the guidance of Professor Nicole L. Key in the School of Mechanical Engineering at Purdue University, where he designed the aerodynamic flowpath for a new three-stage axial compressor facility for investigating stator hub clearance flows. He received a Master of Science in Mechanical Engineering from Purdue in August 2012. Reid was awarded a National Science Foundation Graduate Research Fellowship to begin doctoral research at Purdue University in August 2012. As a PhD student at Purdue, he was awarded the Ward A. Lambert Teaching Fellowship from the School of Mechanical Engineering in 2014 and the Outstanding Graduate Student Research Award from the School of Mechanical Engineering in 2015. Reid will receive his PhD from the School of Mechanical Engineering in August 2015.